Targeted Synthesis of Functional Soft and Hard Carbons from Bio-waste and Natural Products for Supercapacitor and Battery Applications

Thesis Submitted to the AcSIR for the Award of the Degree of

DOCTOR OF PHILOSOPHY
In
CHEMICAL SCIENCES

Malik Abdul Wahid

Registration Number: 10CC11A26043

Under the guidance of

Dr. Manjusha V Shelke

(Research Guide)
and

Dr. Satishchandra Ogale

(Research co-guide)

CSIR-NATIONAL CHEMICAL LABORATORY
PUNE – 411 008, INDIA

2016

Targeted Synthesis of Functional Soft and Hard Carbons from Bio-waste and Natural Products for Supercapacitor and Battery Applications

Thesis Submitted to the AcSIR for the Award of the Degree of

DOCTOR OF PHILOSOPHY
In
CHEMICAL SCIENCES

Malik Abdul Wahid

Registration Number: 10CC11A26043

Under the guidance of

Dr. Manjusha V Shelke

(Research Guide)
and

Dr. Satishchandra Ogale

(Research co-guide)

CSIR-NATIONAL CHEMICAL LABORATORY
PUNE – 411 008, INDIA

2016

Thesis Certificate

This is to certify that the work incorporated in this Ph.D. thesis entitled **"Targeted Synthesis of Functional Soft and Hard Carbons from Bio-waste and Natural Products for Supercapacitor and Battery Applications"** submitted by **Mr. Malik Abdul Wahid** to Academy of Scientific and Innovative Research (AcSIR) in fulfillment of the requirements for the award of the Degree of **Doctor of Philosophy in Chemical Sciences,** embodies original research work under my supervision. I further certify that this work has not been submitted to any other University or Institution in part or full for the award of any degree or diploma. Research material obtained from other sources has been duly acknowledged in the thesis. Any text, illustration, table etc., used in the thesis from other sources, have been duly cited and acknowledged.

Research Guide

Dr. Manjusha V Shelke

Research Co-guide

Dr. Satishchandra Ogale

Declaration

I hereby declare that the thesis entitled **"Targeted Synthesis of Functional Soft and Hard Carbons from Bio-waste and Natural Products for Supercapacitor and Battery Applications"** submitted for the degree of **Doctor of Philosophy** in **Chemical Sciences** to the Academy of Scientific & Innovative Research (AcSIR), has been carried out by me at the Physical and Materials Chemistry Division of CSIR-National Chemical Laboratory, Pune, India, under the guidance of **Dr. Manjusha V Shelke and co-guidance of Dr. Satishchandra Ogale**. Such material which has been obtained by other sources has been duly acknowledged in this thesis. The work is original and has not been submitted in part or full by me for any other degree or diploma to other University.

Date: **Malik Abdul Wahid**

Physical & Materials Chemistry Division **(Research Student)**

CSIR-National Chemical Laboratory,

Pune - 411008, India


Dedicated to my Parents

Acknowledgements

Firstly, thanks to God, the praiseworthy, to guide my way towards this ultimate step of studentship. He indeed, honored human to be His agent, and to that end, endued him with understanding. I affirm His secret presence to elevate me to achieve this goal. Without His blessings no deed returns its deserved end.

At the outset, my earnest acknowledgement goes to my co-supervisor, ***Prof. Satishchandra B Ogale*** *for his meticulous guidance throughout my PhD tenure. It was really nice of him to accept my membership in his dynamic and self sufficient group. I am extremely thankful to him for allowing me to carry out my PhD under his guidance. His timely classes, specially organized for the group, on diverse subjects including quantum mechanics, condensed matter physics and electrochemistry were special and instrumental for young researcher like me, to build my basics. Dr. Ogale possesses an inspirational persona, positive attitude and amicable behavior. There is lot to emulate from him for successful research and successful life. Thanks sir for all the parties and fun. Thanks for making my stay comfortable and enjoyable.*

I am extremely grateful to my research supervisor ***Dr. Manjusha V Shelke*** *for her unfeigned and constant support. It was a gesture of extreme kindness from her part for accepting to be my supervisor towards the finishing stage of my PhD. I would like to thank her for all the research related suggestions and for all important signatures. I would also like to personally thank her for the help regarding an issue with SAC office, which otherwise could have swelled up to a deep problem. Thanks madam for being kind and nice.*

I feel it an ultimate opportunity to thank Dr. Saurav Pal, (former Director, CSIR-NCL), Dr. Ashwini kumar Nangia (Director, NCL), Dr. P A Joy, HOD, Physical and Materials Chemistry Division for maintaining the infrastructural and quality standards, NCL is known for. I sincerely thank my Doctoral Advisory Committee (DAC) members, Dr. C.P Gopinath, Dr. M.V. Badiger and Dr. M V Rode for their suggestions, directions, and detailed deliberations during DAC meetings. At this time it would be unfair if the AcSIR staff and SAC staff is not acknowledged for their selfless contributions; thanks

sirs and madams. I am equally thankful to the administrative staff and security guards, posted at the PAML gate and three main entry gates, for being friendly.

I would also like to pay special thanks to the people with whom I have collaborated for XPS analysis. Thanks to Dr. D M Phase, Dr R J Choudhary, Prof. D C Kothari and Dr.Rohan Fernandes for providing their valuable time and space. At this juncture I would also like to acknowledge my teachers from University of Kashmir, Govt. Degree College Anantnag, Govt. Higher Secondary School Doru, Govt. Boys High School Verinag and Govt. Middle School Bonagund for their valuable input.

My heartfelt thanks to my Kashmiri friends Dr. Manzoor, Saleem Dar, Waseem Mir, Saleem Bhat, Javaid Rashid, Ishtiyaq Khan, Zahid, Dr. Nayeem, Er. Akhter Rasool and Er. Showket Rasool, for making my stay joyful and home-like. It was nice time cooking, gossiping, discussing, shopping and occasionally fighting with you people. Manzoor and Saleem have been particularly special in being there whenever I was in need. Thanks guys for your long and playful company.

I acknowledge my former and current labmates, Dr.Mandakini, Dr. Sarika Phadke, Dr.Vivek Dhas, Dr.Subas Muduli, Dr. Abhimanyu Rana, Dr.Prasad Yadav, , Dr.Lily, Dr.Parvez, Dr.Datta, Dr.Shruti, Dr.Abhik, Dr.Rohan, Dr.Meenal, Dr.Onkar, Dr. Shraddha, Dr. Anil, Dr. Dhanya, Dr. Pradeep, Dr. Satish, Aniruddha, Vishal, Satywan, Yogesh, Rounak, Dr Dipti, Umesh, Dr. Sambhaji, Dr. Nilima, Dr.Supriya, Mukta, Divya, Pooja, Poonam, Srashti, Ishita, Swati, Shrreya, Dr Rami Reddy, Chaitanya, Indrapal,Pravin, Rupali, Vedi and Ashwini for creating a wonderful and scientifically viable laboratory environment. I would like to specially thank my intern students, Golu, Ajay, Harshita, Vikas, Naman, Amit for their honesty and obedience. They all have been very helpful and friendly.

A very special thanks to Karthika for being well above the friendship standard. She has been a keen listener and ardent helper. I would also like to thank Manoj Sharma (Mr. Resilient) for being a lovely friend for a while. I would also like to thank Dr. Parbhu for letting me be a witness to some of his dazzling dancing performances.

Finally, I would like to thank my family for being immensely supportive, loving and patient. I would like to pay my ultimate thanks to my father and mother for building me to what I am. It was because of their encouragement and motivation that I could think of

perusing higher education. I would like to thank my brother for being a strong support. It would all be worthless if I fail to pay my sincere and extra special thanks to my sisters for being extremely loving and caring. I am equally thankful to my brother-in-law and sister-in-law for their excellent comradeship. Very sincere thanks to my uncles and aunts for their love. Very special thanks to Papa and Babhi for sonly love, and for their constant remembrance through phone calls. I can't hold to specially mention my dear cousins (my lifelong friends) at this juncture, thank you all for always making every moment special and worth enjoyment. Lots of love to Musaib, Mueed, Haseeb, Mukeet and Salehah. At the end, I would also like to thank my late grandfather for his wise advices and bounteous love.

Malik Abdul Wahid

List of Abbreviations

1D	One-dimensional
2D	Two-dimensional
3D	Three-dimensional
AC	Activated Carbon
ACF	Activated Carbon Fibre
ACNF	Activated Carbon Nanofibre
BET	Brunauer–Emmett–Teller
CCD	Charge-Coupled Device
CD	Charge -Discharge
C_{dl}	Double- layer Capacitance
CF	Carbon fibre
CNC	Carbon nanocup
CNF	Carbon nanofibre
CNH	Carbon nanohorn
CNO	Carbon nanoonion
CNT	Carbon nanotube
CV	Cyclic Voltammogram
CVD	Chemical Vapor Deposition
DCB	Dichlorobenzene
DEC	Diethyl carbonate
DFT	Density Functional Theory
DMC	Dimethyl carbonate
E.D	Energy Density
EC	Ethylene Carbonate
EDLC	Electrochemical Double Layer Capacitance
EDS	Energy Dispersive Spectroscopy
EIS	Electrochemical Impedance Spectroscopy

EM	Electron Microscope
EMI	1-ethyl-3-methylimidazolium
ESR	Electrochemical Series Resistance
FEC	Fluoroethylene carbonate
FE-SEM	Field Emission Scanning Electron Microscopy
FWHM	Full Width Half Maxima
GO	Graphene Oxide
HPGC	Hierarchically Porous Graphitic Carbon
HPGCF	Hierarchically Porous Graphitic Carbon Fibre
HR-TEM	High Resolution Transmission Electron Microscopy
IHP	Inner Helmholtz Plane
IR	Infrared
LIB	Lithium Ion Battery
MWCNT	Multiwall Carbon Nanotube
NCS	nickel-cobalt sufide
NMP	n-methyl pyrrolidone
NMR	Nuclear Magnetic Resonance
O.P	Operating Potential
OHP	Outer Helmholtz Plane
P.D	Power Density
PAN	Polyacrylonitrile
PANI	Polyaniline
PC	Propylene Carbonate
PSD	Position Sensitive Detector
PVA	polyvinyl alcohol
PVDF	Polyvinylidene Fluoride
PVP	polyvinylpyrrolidone

PXRD	Powder X-ray Diffraction
R_{ct}	Charge Transfer resistance
rGO	Reduced Grapheme Oxide
RRS	Resonance Raman Spectroscopy
SAED	Selected Area Electron Diffraction
SEI	Solid Electrolyte Interface
SEM	Scanning Electron Microscopy
SERS	Surface Enhanced Raman Spectroscopy
SWCNT	Single- wall Carbon nanotube
TC	Templated Porous Carbon
TEM	Transmission Electron Microscopy
TEOS	Tetraethyl orthosilicate
TFSI	Bis(trifluoromethane) sulfoimide
TGA	Thermogravimetric Analysis
TMT	Thousand Metric Ton
TSEM	Thermionic Scanning Electron Microscopy
UV	Ultraviolet
XPS	X-ray Photon Spectroscopy
XRD	X-ray Diffraction

Contents

Chapter 2: Synthesis and Characterization techniques …..... 56-97

Abstract

Carbon materials are gaining special status as the low cost electrode materials for supercapacitor and batteries. This thesis projects the use of cheap and easily manoeuvrable carbon materials synthesized from bio wastes and natural products for energy storage applications. The carbon materials possessing the turbostratic graphitic structure possess suitable conductivities, surface areas and interplanar separations to be used as electrodes in super-capacitors and sodium ion batteries.

Synthesis of carbon materials from biowastes and natural products by pyrolysis at intermediate temperature (700^0C-1200^0C), under the inert atmospheres, leads to formation of carbonaceous products. The synthesizable carbonaceous products in presence of pore creating agents possess required porous architecture and pore dimensions for effective use as electrodes in supercapacitor. The carbonaceous products synthesised under similar conditions, but in absence of external and internal activating agents, lead to formation of low surface area carbon materials. The carbon materials of this type possess the turbostratic graphitic structure, having interlayer separation suitable for Na ion intercalation /de-intercalation, and hence use as anode material in Na-ion battery application.

First work projects the chemically activated carbon synthesized from sugar cane bagasse with a synthetic novelty of hydrothermal pre-treatment before activation pyrolysis as an efficient electrode material for a symmetric super capacitor. Further this carbon material is reported to exhibit the enhanced capacity retention of 72% and cycling stability with capacity retention of 90% after 10000 cycles.

Second work presents a non activation process for generation of porosity in a carbon material derived from a biogel, pectin. The gel infiltration inside the SBA-15 is achieved by simple dissolution which upon pyrolysis releases the interconnected carbon threads with sufficient meso/micro porosity to be used as electrode material in super capacitor. The capacitor furnishes an attractive performance with capacity of $285Fg^{-1}$ at $1Ag^{-1}$ and 96% retention of capacity after 2000 charge-discharge cycles.

Third work projects a chemically activated carbon derived from yogurt as an efficient negative electrode in the asymmetric super capacitor. The use of an asymmetric assembly with $NiCo_2S_4$ electrode grown on nickel foam as positive electrode has furnished wonderful results for this carbon with the enhancement in energy density ($21Whkg^{-1}$ in asymmetric assembly compared to $7Whkg^{-1}$ in symmetric one) by 3 folds.

Fourth work deals with the low surface area non activated carbon, the hard carbon, and its application as anode material in sodium ion battery. Hard carbon derived from walnut shell is being presented as an efficient performer as sodium ion anode. Direct pyrolysis of nutshell yielded desired carbon with the suitable interplanar separation. Sodium ion anode capacity of $257mAhg^{-1}$ was observed for the wall nut derived carbons with a remarkable stability upto 300 cycles.

Chapter 1

Introduction

This chapter presents the general perspective on different carbon materials with the focus on semi graphitic carbon forms of various types. A detailed discussion about the structure, properties and synthesis of different materials has been presented in this chapter. Besides a thorough description about the energy storage devices, their design, classification and mechanism of charge storage with the underlying electrochemistry has been presented. Finally the importance and indispensability of carbon materials, especially the semi-graphitic carbons, in the field of energy storage has been clearly established.

1.1 Introduction to carbon materials.

Nanoscale manipulations in carbon materials have attracted great research interest from different fields of science as in the case of materials other than carbon. Size confinement of electrons and high surface to volume ratio have bestowed astonishing properties to the nanomaterials as compared to their bulk counterparts.[1,2] Similar manipulations in carbon materials have rendered new and exciting properties to these materials which differ markedly from the two well-known allotropes of carbon i.e. graphite and diamond.[3–6] Discovery of fullerenes in 1985 was the first move towards the nanoregime.[7,8] Further, discovery of majestic carbon nanotubes (CNTs) by Iijima in 1991 opened a new gate of carbon nanoelectronics.[9] Remarkable mechanical properties of CNTs further broadened the scope of carbon materials as CNT proved to be a revolution in various engineering fields where toughness was a concern.[10–14] Discovery of graphene by scotch tape method by *Geim Andre* and *Konstantin Novoselov* in 2004 suddenly opened a broad spectrum of applications in electronics and chemical engineering fields.[15–17] Being a zero gap semiconductor and mechanically robust material graphene stays at the core of high performance microelectronic devices. Its remarkable mechanical stability has hugely benefitted in bringing to the market the more robust and very high performance devices.[18,19] Other forms of carbon like CNHs, CNFs, ACNFs, CNCs and NCSs are the other very interesting nano attractions of carbon domain.[20–22]

Other more common and more useful carbon forms which exist in the carbon domain may be categorized under the heading of engineered forms of carbon. These types of carbons can be considered to have evolved by nanoscale engineered defects in the bulk forms of carbon like graphite and diamond. Hard and soft carbon forms which are the subject matter of this thesis are categorised under this heading. [23,24]These carbon varieties are synthesized from polymer precursors by direct high temperature pyrolysis (in presence or absence of a defect inducing chemical) in inert atmosphere, laser induced pyrolysis or microwave assisted pyrolysis.[25–28] Complete discussion about their synthesis and properties will be undertaken in this chapter but we will begin with the basic introduction of chemistry of carbon materials and bonding. *Figure 1.1* shows

different application domains of carbon materials.

Figure 1.1 *Different applications of carbon materials in different fields of science and engineering.*

{ http://www.iop.org/resources/topic/archive/fuel/; http://www.kamerynasport.cz/ostatni/ 590-gopro-hd-hero2-li-ionbaterie.html;http://www.electronicsurplus.it/product/2441/350Farad-2,5V-Supercondensatore-Maxwell-Boostcap.html; http://pubs.rsc.org/en/content/articlehtml/2015/tb/c5tb01635e}

1.2 Bonding in carbon materials.

Carbon is unique element in the periodic table with its catenation property which allows it to bond with itself to form long chains. The attainment of this uniqueness can be attributed to its unique position in the periodic table. Carbon belongs to group 14 of periodic table possessing electronic configuration of $1s^2 2s^2 2p^2$ which is also exhibited by other group members i.e. Si, Ge, Sn, Pb and Fl. This very configuration implies the presence of four valence electrons for bonding because of which this group is also

referred to as tetrels and tetragens. Among other members of the group only Si retains the property of catenation but to a lesser extent compared to carbon. Because of more extensive catenation behaviour broad spectrum of carbon compounds have resulted which in turn has necessitated the separate subject of carbon chemistry referred to as organic chemistry. The ideal charge to size ratio and different possible hybridizations (sp, sp^2 and sp^3) allow carbon compounds to have different spatial dimensions. Carbon forms linear, planar and 3D molecules with itself and with other elements like oxygen, nitrogen, hydrogen and sulphur by exercising its different hybridizations. *Figure 1.2* shows the directional orientation of hybrid orbitals under different hybridization conditions. Overlap of linearly geometrized sp hybridized orbitals result into linear shape, sp^2 geometry leads to planar, and sp^3 to 3D shapes.

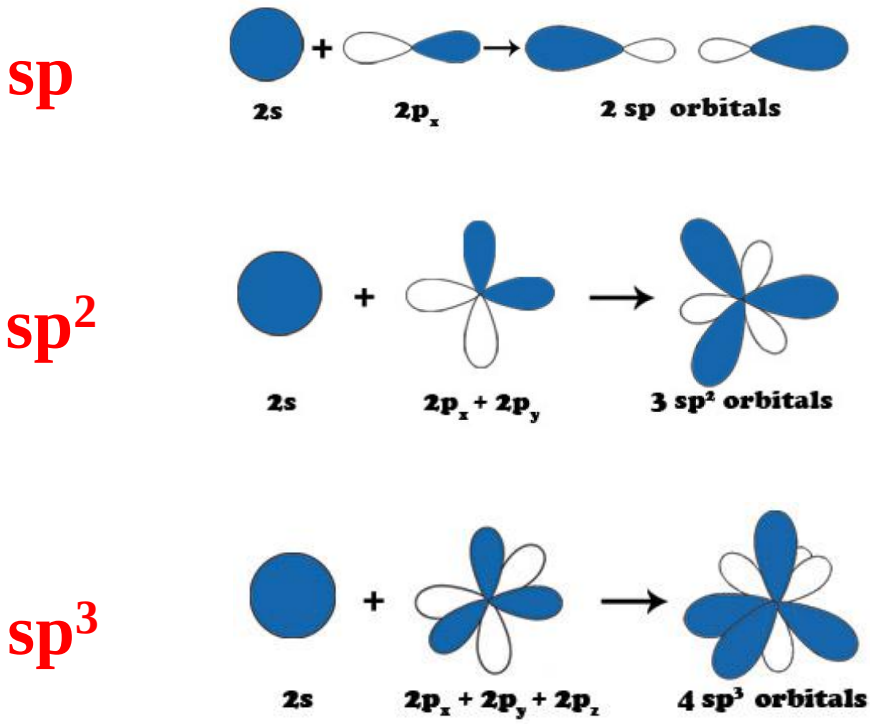

Figure 1.2 *Hybridization in carbon leading to different geometries. sp hybridisation leads to two hybrid orbitals of same energy at 180^0 to each other, sp^2 to three orbitals of same energy placed at 120^0 to each other and sp^3 hybridisation to four orbitals of located at 109.5^0.*

{http://asdn.net/asdn/chemistry/carbon_nanotubes.php}

A representative example of sp hybridised carbon forms where carbon has a linear

structure are linear carbon compounds like acetylenes, carbynes and carbolites. In acetylene, carbon exercises its sp hybridization with two sp orbitals pointed opposite to each other at 180^0 which gives linearity to the molecule while as the unhybridized orbitals participate in multiple bond formation. etc. The examples of carbon materials where sp^2 hybridization is operative are giant graphite, graphene, and some small molecules like naphthalene, anthracene, phenantherene etc. The sp^2 orbitals of carbon atoms are pointed at 120^0 to each other which leads to formation of giant network of hexagonal carbon rings while as the unhybridised orbitals participate in multiple bond formation. The sp^3 hybridization allows carbon to form 3D networks with all four directional orbitals, oriented at 109.5^0 to each other, available for bonding with carbon and other atoms. Diamond is an example of 3D sp^3 bonded lattice of carbon atoms. *Figure 1.3* shows bonding in linear (acetylene), planar (graphite/graphene) and 3D (diamond) carbon networks.

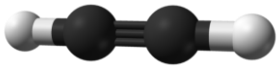

Linear Geometry of Acetylene

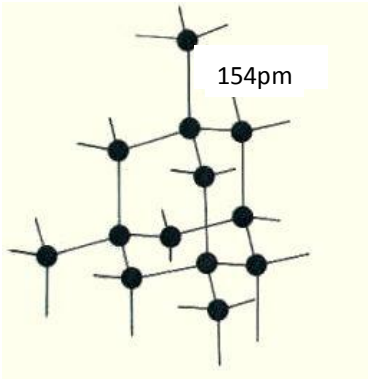

Tetrahedral geometry of Diamond (sp^3)

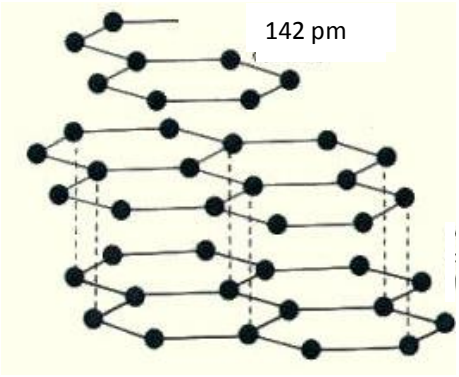

Triangular geometry of Graphite (sp^2)

Figure 1.3 *Bonding in linear, planar, and 3D carbon networks. Acetylene is linear because of sp hybridisation, extensive sp^2 hybridisation in graphitic network renders it planar with carbon-carbon in plane bond length of 1.42 A^0. Diamond on the other hand is a 3D solid because of sp^3 hybridisation throughout with strong C-C bond length of 1.54A^0.*

{http://sciencemadness.wikia.com/wiki/Acetylene; https://opentextbc.ca/geology/the-lattices-of-graphite-and-diamond/}

1.3 Different forms of carbon.

Carbon materials are exclusively made of carbon atoms with some functionalities of O, N, S, P etc. This broad spectrum of carbon materials can be categorized under three broad headings: 1) Bulk macrocrystalline carbons 2) Nanocarbons and 3) Nanoengineered carbons.

1.3.1. Bulk carbons: Under this heading we will discuss some well-known macro crystalline forms of carbon like diamond, graphite, lonsdaleite and carbynes. These are perfectly crystalline forms with crystallinity extending to micron to millimetre dimensions.

a) Diamond.

Diamond is a popular and valuable allotrope of carbon with high market and industrial value owing to its brilliant shine and extreme hardness. It mainly finds its use in jewellery (gemstones) and as an abrasive. By reason of its high refractive index (2.4) and high dispersive coefficient (0.04) diamond causes light to refract and re-refract (*total internal reflection*) which gives it sparkling shine and thus greatly interests opticians. Chemically diamond is a compound of sp^3 hybridized carbon atoms with crystallographic cubic shape (F3dm space group) following an *fcc* Bravais lattice. *Figure 1.4a* shows the crystal structure of diamond. The structure of diamond is zinc blend type with C-C bond length of 154 pm and packing fraction of 0.34%.[29,30] Because of sp^3 hybridization in operation, diamond can be called as all covalent solid. Extreme mechanical strength of diamond can be attributed to its cubic structure. It scores 10 on Mohs scale of material hardness, its toughness and tensile strength being 2MPa-$m^{1/2}$, 2.5–6.5×10^7 N-mkg^{-1} respectively.[29,30]

b) Graphite

Graphite is the other exciting allotrope of carbon much known for its excellent electrical properties and mechanical softness. Because of its high electric conductivity ($3x10^2$-$2x10^5$ Sm^{-1}) graphite has found application as electrodes in electric arch lamps. High in plane conductivity of graphite can be attributed to free pi- electron density. Chemically

graphite is also an all carbon covalent solid of sp^2 hybridized carbon atoms. As the sp^2 orbital overlap leads to a planar structure so it happens in graphite with all covalently bonded carbons forming the layered structure. The unhybridized p-orbitals participate in the pi bond formation throughout the crystal which enriches graphite with free de-localisable electrons hence high conductivity. Covalent bonds give graphite the inplane

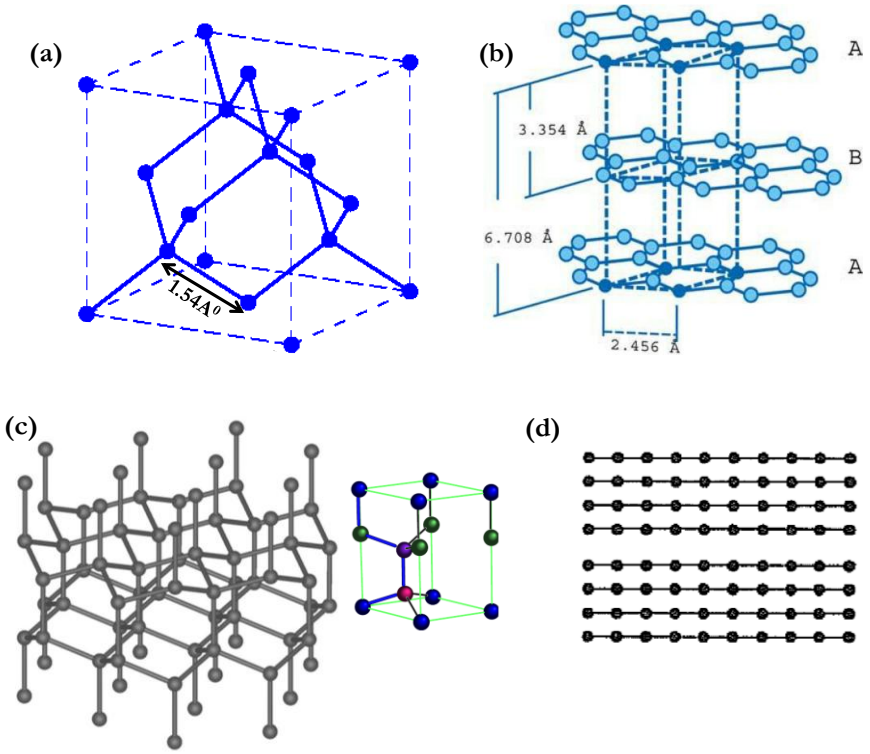

Figure 1.4 *Crystal structures of well-known bulk forms of carbon are listed here. a) Diamond displays an fcc lattice with typical zinc blende type structure. (source: http://www.iue.tuwien.ac.at/phd/karamitaheri/node13.html} b) Hexagonal crystal system of graphite with rhombohedrally centred lattice is exhibited.(Reprinted with permission of Journal of Power Sources @ Elsevier) c) Hexagonal crystal structure of lonsdaleite (chair conformation) with inset showing unit cell of hexagonal crystal family and hexagonal lattice.(Reprinted with permission of Diamond and Related Materials@ Elsevier) d) Crystal structure of carbynes having one dimensional order within a chain but lack long range planar and 3D order. {Source: Carbon material for advanced technology; Berchell T.D}*

2D order while as the 3D bulk structure of graphite is because of ordered stacking of these planar carbon sheets guided by van der Waals forces. The interplanar separation between these stacked layers is 0.33 nm. Crystallographically graphite is a hexagonal

system ($P6_3/mmc$ space group) possessing rhombohedrally centred Bravais lattice. *Figure 1.4b* shows the atomic arrangements and crystal structure of graphite.[29,30]

c) Lonsdaleite

It is just another but less known allotrope of carbon, also known as hexagonal diamond. Existence of this form of carbon was reported from the meteorites striking the Earth, first report being provided in 1967. It is proposed that under such high temperature and pressure graphite gets converted into diamond but retains its hexagonal structure. *Figure 1.4c* shows the crystal structure of Lonsdaleite.[29–32]

d) Carbynes.

Carbynes are linear allotropic form of carbon having a long chain of alternating single and triple bonds. Their discovery dates back to 1960 by *Goresy and Donnay* although some controversy shades the discovery. The well defined crystal of carbynes in sizable dimensions has not been reported yet. However, some small chain carbynes with chain length of 10-20 carbons has been synthesized. These intermediate size carbynes possessing sp hybridization in the constituent carbon atoms upon 3-D stacking gives them their crystal structure. The XRD pattern of synthetic carbynes shows some peaks which clearly distinguish it from diamond, graphite and other known allotropes thus confirming its status as a separate allotrope of carbon. Carbynes are claimed to be hardest carbon materials with tensile strength of $6.0–7.5\times10^7$ N-mkg^{-1} which is quite higher than other known carbon forms like graphene ($4.7–5.5\times10^7$ N-mkg^{-1}) , CNTs ($4.3–5.0\times10^7$ N-mkg^{-1}) and diamond ($2.5–6.5\times10^7$ N-mkg^{-1}). *Figure 1.4d* shows the crystal structure of carbynes obtained from ordering sp carbon chains.[29,30,33]

1.3.2. Nanocarbons: Nano domain has unravelled many exciting allotropes of carbon which has really broadened the scope of carbon materials for different applications. Confinement invoked quantum size effects in the nanomaterials make these materials much exciting than the bulk forms of carbons for applications like microelectronics, optics, environmental sustainability, robotics, energy conversion, energy storage and medicines.[34–37]

a) Fullerenes

The discovery of fullerenes (also called Bucky balls) dates back to 1985 when for the first time their existence was established by mass spectrography. It was proposed that molecule consists of 60 carbon atoms clustered into a closed football like structure of $6.8A^0$ diameter with 12 pentagonal faces and 20 hexagonal faces. The single ^{13}C NMR peak advocated chemically similar carbon throughout with a c-c bond length of $1.44A^0$ and sp^2 hybridization. Thus with this preliminary information fullerenes can be thought of as rolled up graphene sheets but the extensive characterization of C_{60} by neutron scattering and NMR has established a more clear structure(*figure 1.5*) with few single bonds ($1.455A^0$ by neutron scattering) located at the edge connecting a pentagon with a hexagon. Similarly presence of double bond ($1.39A^0$by neutron scattering) at the edge connection of two hexagons has been suggested. The *figure 1.5* shows the most accepted structure of C_{60} fullerene. Apart from C_{20} many other bulkier members of fullerene like C_{70}, C_{80}, C_{140}, C_{320} ,C_{380} up to C_{980} with varying symmetry have been isolated and have been assigned the structures. [29,30,38–44]

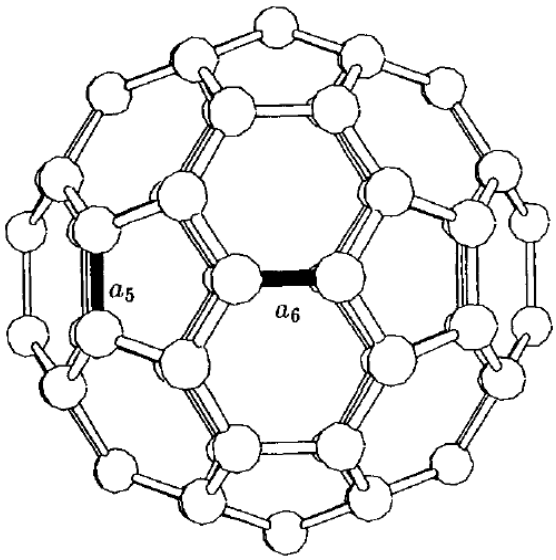

Figure 1.5 *C_{60} molecule showing single bond a_5 and double bond a_6. {Source: Carbon Materials for Advanced Technologies, 1st Edition; M.S Dresselhaus})*

Fullerenes are reported to have been synthesized by arc discharge and laser vaporization methods. Carbon arc has been used to prepare gram quantities of C_{60} and C_{70} fullerenes already.

Fullerenes (C_{60}) crystallize as a molecular crystal with a cubic crystal structure possessing the lattice constant of $14.2A^0$ and C_{60}-C_{60} distance of $10.02A^0$. The cubic phase is the low temperature phase and at elevated temperature various phase transitions are observed. The most exciting property of fullerenes which has compelled researchers to invest a considerable interest is the high temperature superconductivity observed in some metal doped forms of C_{60} and C_{70}. Apart from this, the useful applications in the field of nonlinear optics, micro electronics, photo resists, geology, and medicine is already well established.[29,30,38–44]

The multiwall counterparts of fullerenes have also been isolated and have been given an appropriate name as *carbon nanoonions (CNOs)*. For various applications and synthesis refer to Volker et al.[45–47]

b) Carbon nanotubes (CNTs)

CNTs are nano allotropes of carbon like fullerenes but with a high aspect ratio of ~1000000. The existence of carbon nanotubes was revealed by HR-TEM analysis of carbon soot obtained by arc discharge of graphite. Although reports of carbon nanotubes like structures were already in place but the credit of the discovery goes to Iijima for getting them the name and fame through his paper published in nature in 1991. In the Iijima's work and other observations till 1993, the nanotubes observed were composed of multiple layers of hexagonal carbon sheets (known as graphene now) folded in the form of concentric tubes as can be inferred from *figure 1.6.* These carbon structures with inner and outer diameters as shown were named as multi walled carbon nanotubes (MWCNTs). The MWCNTs have outer diameter of 2-20nm and an inner diameter of 1-3nm. The single cylindrical entity which can be considered as the basic building blocks being composed of single sheet of one atom layer thick carbon sheet have also been reported. These structures have been referred to as single walled carbon nanotubes (SWCNTs). The existence of SWCNT was seen inside arc furnace loaded with Fe, Co that act as catalysts for growth. The hexagonal carbon sheet can fold in three different ways as shown in *figure 1.6b* and hence three different types of SWCNTs are identified i.e. *arm-chair, zig-zag* and *chiral*.

The hybridization of the rolled sheets being sp^2, CNTs are expected to own high

conductivity and high mechanical strength. In its tensile strength it surpasses even steel with the tensile strength of 63-100 GPa. The strength of multiwall ones being little lower with values of 60 GPa. CNTs are also known for their exciting electronic properties which are very diverse and depend on the mode of rolling the graphene sheet might have undertaken. All arm chair type CNTs are metallic with an excellent conductivity of ~10^6 Sm^{-1} which is lower than graphene and most metals. But metallic

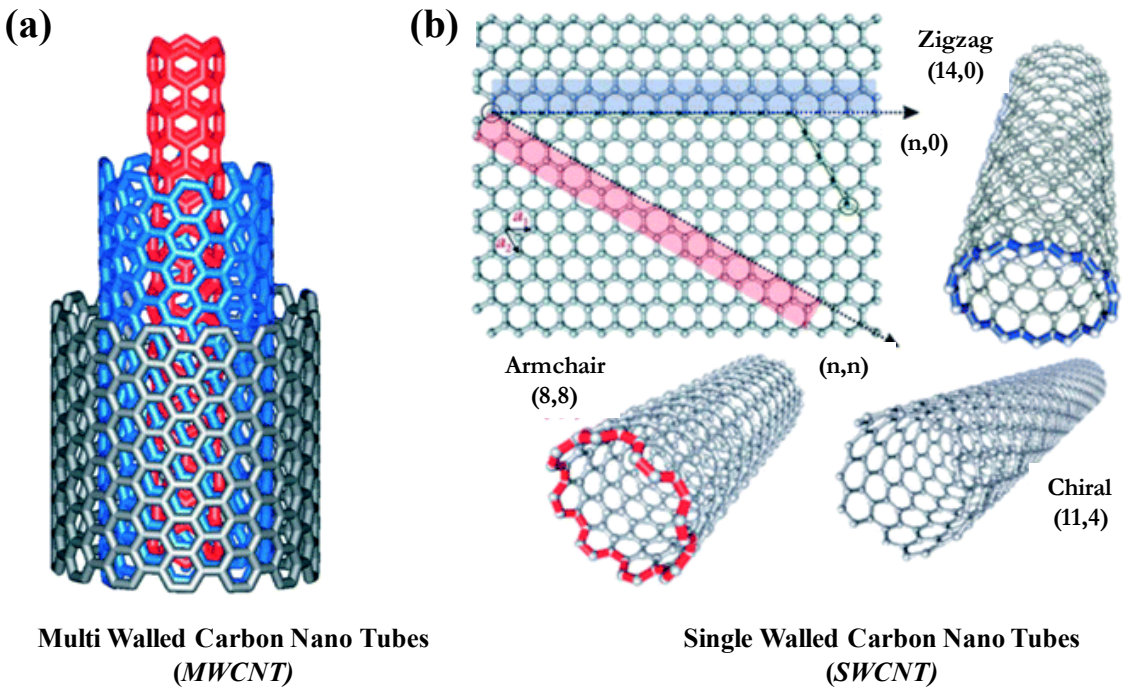

Figure 1.6 *a) Multiwalled carbon nanotube made up of rolling of three graphene sheets concentrically. b) Three types of CNTs resulting from three types of rolling mechanisms of a graphene sheet. (Reprinted with the permission of Royal chemical society @ Nanoscale)*

nanotube can carry a current of 4x$10^7$$Acm^{-2}$ which is 1000 times more than steel. The conductivity is one dimensional along the tube axis. Other type can be metallic or semi-conducting depending on the chirality of folding, discussion of which is not presented here. Besides this, CNTs are ballistic thermal conductors along the tube with conductivity of 3500$Wm^{-1}K^{-1}$. [14,48,48–50]

Because of these exciting and remarkable properties, CNTs find variety of modern applications. As hard coatings (on aeroplanes to prevent icing), micro motors, artificial

implants, conducting additives, microelectronics, heat transducers, biosensors, genetic engineering, diagnostic tools, catalysts and other biomedical applications.[48,51,52]

The synthesis of CNTs has been achieved by techniques like arc discharge, laser ablation, thermal synthesis, CVD, alcohol and plasma catalyzed CVD and hydrothermal synthesis. The other minor allotropes of carbon which can be considered as derivatives of and closely related to CNTs and fullerenes are carbon nanotorus, carbon nanobuds, and carbon nanohorns. *Figure 1.7* images these interesting but rare allotropes of carbon.[53,54]

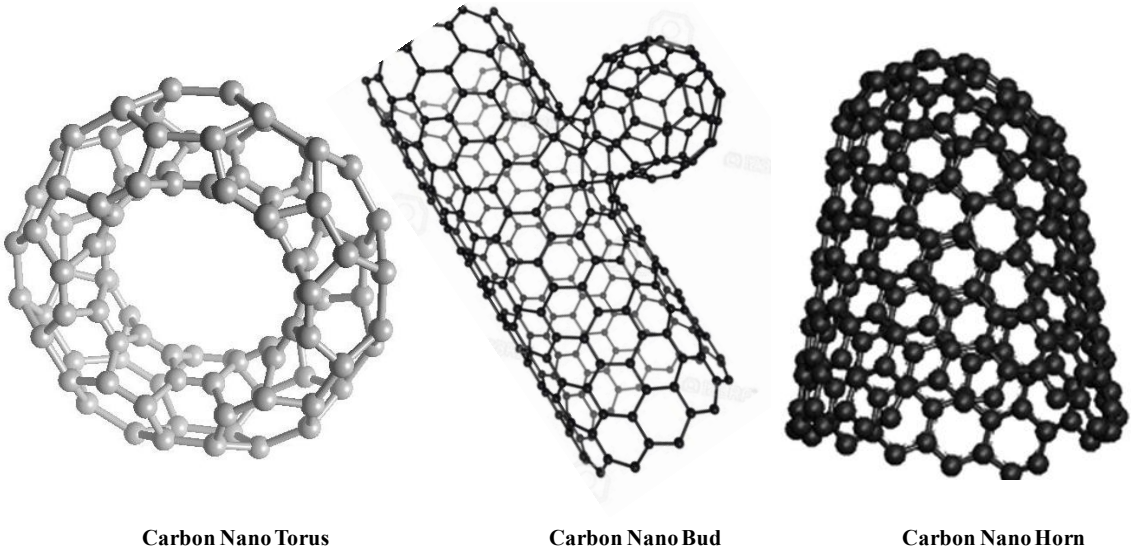

Figure 1.7 a) *Carbon nanotorus obtained by end joining of CNT.* ***b)*** *Carbon nanobud shown as a grown protuberance on the CNT.* ***c)*** *Carbon nanohorn resembling a one end closed CNT. {Source: CARBONLETT, vol. 15, no. 4, pp.219-237, 2014}*

c) Graphene

Graphene is one of the majestic nano allotropes of carbon which can be considered as the starting structural entity for the other allotropes of carbon. Theoretical prediction of existence of graphene and its practical use has already been there for few decades. But the rediscovery, characterization and isolation which really established its splendour is credited to *Geim Andre* and *Konstantin Novoselov* for their 2004 work.[55,56] Chemically graphene is a sheet of sp^2 hybridized carbon atoms forming a honey comb type hexagonal 2D lattice with carbon-carbon distance of $1.42A^0$. Also for a chemist

graphene is a continuous sheet of benzene rings with no out of plane bonds. Crystallographically, it can be thought of being made of two interpenetrating triangular lattices with lattice vectors a_1 and a_2 given by following equations:

$$\mathbf{a_1 = a\ /2\ (3, \sqrt{3}),\quad a_2 = a/\ 2\ (3, -\sqrt{3}),}$$

where *a* is length of carbon-carbon bond.[55,57–59] *Figure 1.8* shows the schematic, TEM image of a single layer graphene, and its crystal structure. The few layer graphene, which invariable result from most of the graphene synthesis are the three dimensional hexagonal lattice obtained from stacking of these individual sheets with c- axis stacking faults and hence referred to as turbostratic graphite. *Figure 1.9* shows derivation of some well known allotropes from graphene. This unique structure and bonding bestows

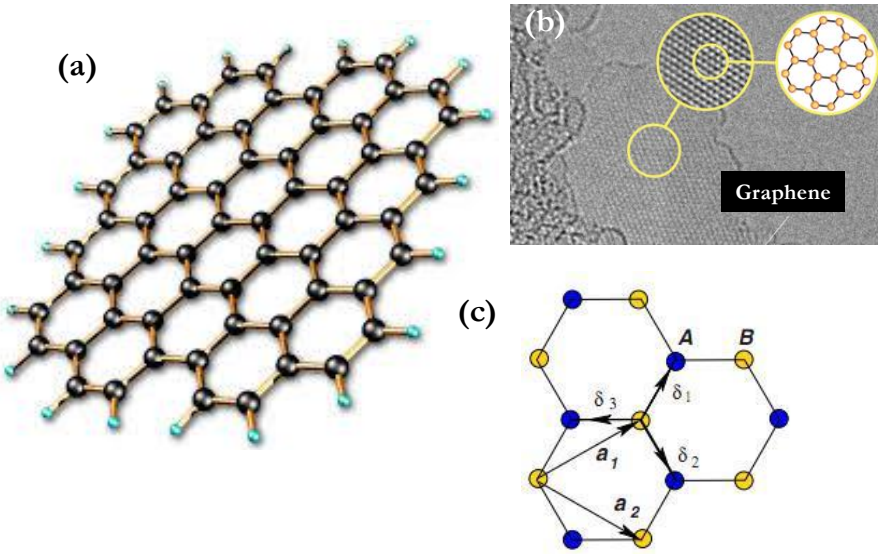

Figure 1.8 ***a)*** *Schematic of a single layer graphene b) HR-TEM image of a single layer graphene c) Crystal structure of graphene showing two interpenetrating triangular lattices with a_1 and a_2 being lattice unit vectors and $\delta_1,\delta_2,\delta_3$ being the nearest neighbor vectors.{(c) reprinted with a permission of American Physical Society @ Reviews of Modern Physics}*

graphene some intriguing properties which has raised its status as the king of all materials.[57,60–62] Being a zero gap semiconductor and a ballistic conductor simultaneously, it is only of its kind. It possesses the electrical conductivity of ~$10^8 Sm^{-1}$

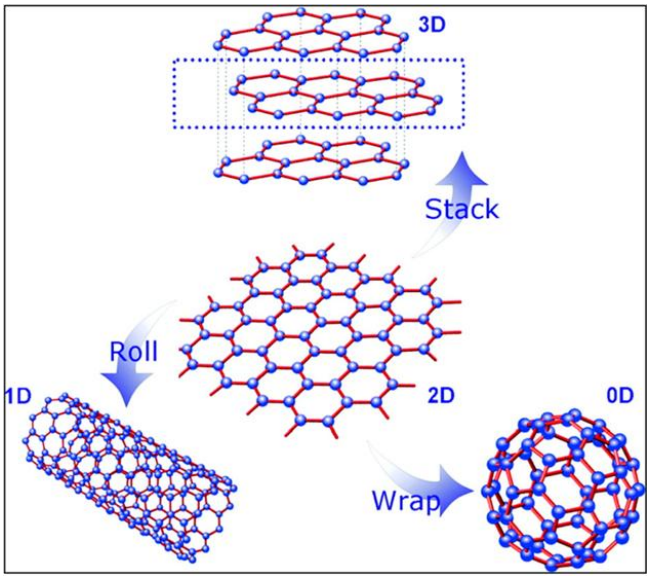

Figure 1.9 *Shows how some of the well-known allotropes are actually derivatives of basic graphene sheet. While as spherical folding leads to 0D-fullerenes, packing along an axis leads to 1D Carbon nanotubes (CNTs) and stacking along c-axis leads 3D to graphite. {Reprinted with permission of American Physical Society @ Reviews of Modern Physics}*

which is higher than some of the well known metallic conductors like copper (~6.0x $10^7 Sm^{-1}$) and silver (~6.3x$10^7 Sm^{-1}$). Carrier mobility of 10,000cm^2V^{-1} with both electron conductivity and hole conductivity makes it a promising candidate for future electronics. Additionally the defect free sp^2 bonding makes it the hardest and toughest material on Earth with tensile strength of 130GPa and Young's modulus of ~1TPa. Because of high mechanical strength and electronic properties graphene is considered the heart of flexible electronics. Besides the low absorption (~2.3%) of visible light makes it almost transparent and hence a material of choice for optoelectronics. Thermal conduction is the other field where graphene is being considered as an efficient replacement for existing thermal conductors. Graphene possesses the high thermal conductivity value of 1500 – 2500 $W \cdot m^{-1} \cdot K^{-1}$ which can be mainly attributed to its 3D acoustic modes despite being a 2D material. High surface area of 2800m^2g^{-1} makes it desirable for interface electrochemistry in storage devices.[63,64]

Graphene has been synthesized by mechanical, chemical, sono-chemical exfoliation of graphite. Besides the thermal reduction, hydrothermal reduction, chemical reduction of GO which in turn is synthesized from graphene have been employed. Chemical and electrochemical unzipping of CNT has also lead to high quality graphene.[17,65,66]

d) Nanodiamonds

These are the nano analogue of bulk single crystalline diamond with size less than 1µm**.** The nanodiamonds are reported to have formed because of explosive impacts like meteorite or explosion. Their existence was established in 1990s and now we have been able to synthesize nanodiamonds of 4-5nm. Nanodiamonds have number of exciting properties and hence corresponding applications. Being hard they have been used as abrasive. Their non toxicity allowed their use in drug delivery, surgery and skin care.[67,68]

1.3.3. Nanoengineered carbons

The engineered forms of carbon are expected to be intermediates between the bulk and nano forms as far as long range order is concerned. All carbon forms which are either obtained from assemblage of nano allotropes of carbon or by the manipulations which bring about a regular and repetitive nano structure generation in bulk allotrope of carbon can be categorised under this heading.[69–74]High temperature pyrolysis is one synthetic strategy which arrests the developing graphite structures in the semi graphitic state and hence leads to the formation of semicrystaline carbon which we classify in into hard and soft carbons.[75–77]The pyrolysis with the control over some physical parameters like growth also leads to nanocarbons (carbon nanofilms, carbon nanofibers, carbon aerogels) that can also be included in nano engineered carbon domain.[78–80]

a) Semi-graphitic soft and hard carbons

The functionally exciting and relatively more common carbon varieties like charcoals, cokes, hydrothermal carbons, porous carbons, activated carbons, low surface area carbons and carbon microspheres can be grouped under this category.[75,77,81–83,23] The striking commonality is their similar crystal ancestry as each carbon form can be considered to be structural derivative of graphite. Graphite as is known to us is a perfect 3D crystal of carbon atoms obtained by regular stacking of crystalline carbon sheets (graphene). But the structure of these carbon forms on the other hand can be thought of as randomly oriented micro crystallites of graphite (having regular stacking faults)

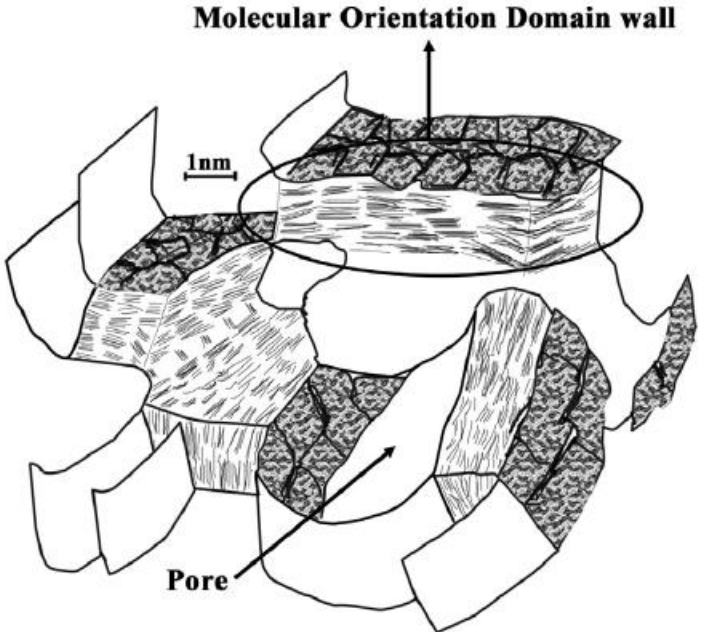

Figure 1.10 *Structure of coke is shown here with the pore wall being guarded by polyaromatic structural units with similar orientation. {Reprinted with permission of Elsevier@ Fuels publication}*

domains dispersed in a huge mass of amorphous carbon. C-axis interplanar distances for these carbons usually fall in the range of 0.34-0.42 nm.[84,85]Further one form of carbon can be differentiated from the other on the basis of presence of graphitic and non graphitic (amorphous) content. The primitive forms of carbon like charcoals and cokes possess the structure represented by huge number of small hexagonal turbostratic graphitic crystallites dispersed in sea of amorphous and sp^3 carbon of various orders and some mineral matter. The amorphous content being least in the cokes compared to chares and charcoal. Local structuring can be viewed as (*Figure 1.10*) the stacking of polyaromatic planner structures of about 1-1.5nm size heaped in the units of two or three. Carbonisation brings about the local reorientations and can lead to parallel orientations up to various length scales and thus different extent of graphitisation.[23,86]

Porous carbons include the number of carbon varieties like exfoliated graphite, carbon aerogels and activated carbons. The exfoliated graphite is synthesized by heating an intercalation compound of graphite at high temperatures that results in to breakage of crystallites into microcrystallites with the spaces generated between the graphitic

domains i.e. pores. The carbon aerogels are low density carbons obtained by super cooling process and can be considered as group assemblage of carbon nano particles with sp^2 bonding. Activated carbons are the carbon materials obtained by intermediate temperature (700^0C -1100^0C) pyrolysis of carbon precursors like synthetic polymers, oligomers, natural polymers and biomass in presence of a physical or chemical activation agent. Porous carbons possess high surface area, in the range of $600 m^2g^{-1}$ to $3500 m^2g^{-1}$, with variety of pore architectures. We have three types of porous carbons based on the pore dimensions and texture as 1) micro porous carbons (Pores <2nm) 2) mesoporous carbons (2-50 nm) 3) macro porous carbons (>50nm). [87]The various activating agents used for pore generation are KOH, NaOH, $ZnCl_2$, H_3PO_4 and physical ones like steam and CO_2. Porosity has also been generated utilising the template based synthesis strategies. In our work presented here, we have utilised the KOH activation extensively but template based pore generation was also visited for few samples.[88–94]

Structure of porous carbons can be considered close to that of coke structure with the additional features of regular pores, lesser amount of non graphitic sp^3 content and lack of mineral matter. Locally porous carbons are random packing of microcrystalline turbostratic graphite-lets which are interrupted by regular empty spaces called pores. *Figure 1.11* shows the schematic of typical porous carbon material and electron microscopy image of a representative.

Low surface area non-activated carbons have been prepared by intermediate temperature (700^0C-1100^0C) pyrolysis but in absence of activation agents, from the precursors like synthetic polymers, natural polymers and biomass. These carbon varieties lack the high surface area which is a characteristic of porous analogues. The structural differences with the porous analogues lie in the presence of more sp^3 content and better hexagonal ordering which deters pore formation in these carbon types. *Figure 1.12* shows the HR-TEM micrograph of a typical low surface non activated carbon.[23,30]

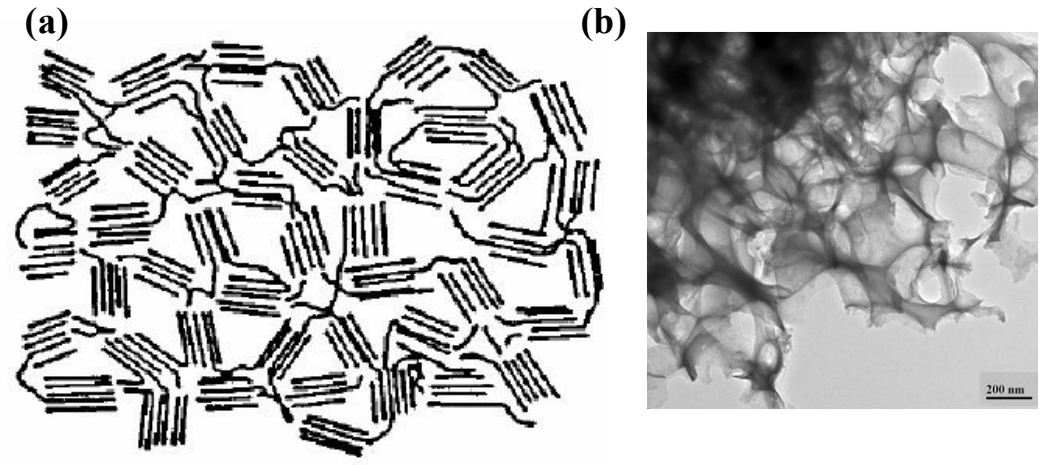

Figure 1.11 a) *Schematic representation of a porous carbon consisting of turbostratic micro graphitic domains intercepted by empty lacuna, the pores.{Reprinted with permission of Elsevier@ Fuels publication} b) HR-TEM micrograph of a porous carbon showing porosity {Activated carbon derived from bagasse synthesized in our lab }.*

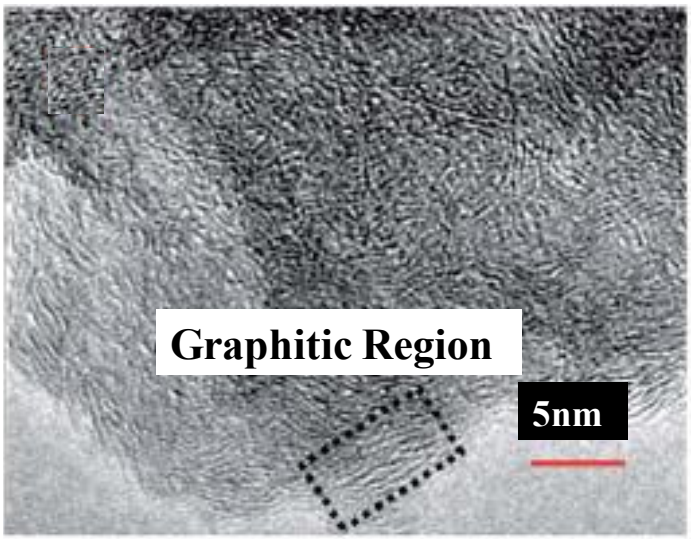

Figure 1.12 *Shows a typical HR-TEM image of a low surface area non activated carbon. {Reprinted with permission of Royal Society of Chemistry @ Journal of Materials Chemistry A}*

b) Semi-graphitic carbon nanoforms

All the carbon forms which are cut short to nano dimensions and which possess the semi crystalline turbostratic graphitic order are categorised under this heading. The carbon forms like carbon nanofibres, carbon nanofilms and carbon nanospheres are the representative examples of materials which fit under this heading. *Figure 1.13* shows

electron microscopy images of the representatives belonging to this type of carbons.[75,95–98]

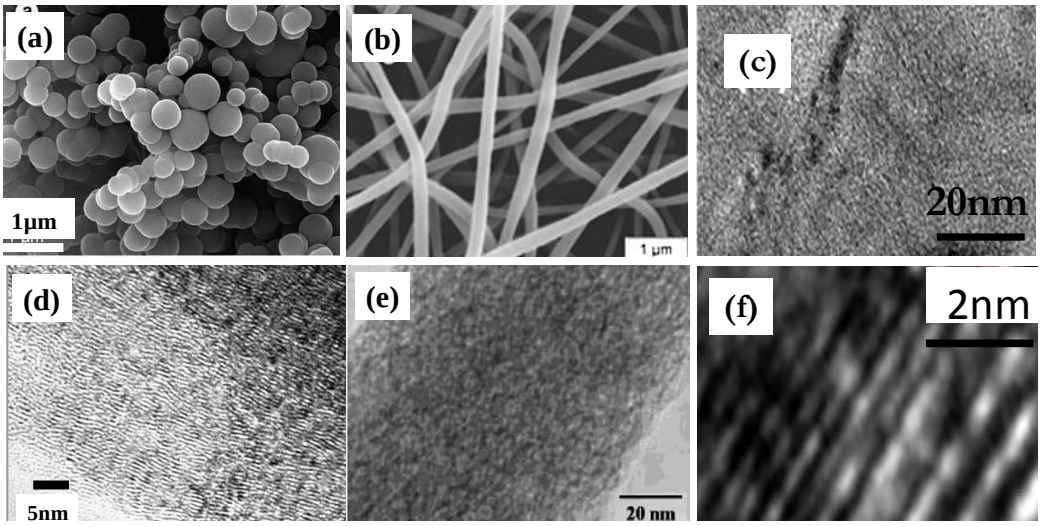

Figure 1.13 *a and d show the SEM and TEM images of carbon nanospheres synthesized by direct pyrolysis of hydrocarbons.{Reprinted with permission from Elseveir@ Carbon}. b and e show the SEM and TEM images of carbon nanofibres derived by pyrolysis of electro-spun PAN fibres. {Reprinted with permission from Springer@ Journal of Material Science} c and f show the SEM and TEM images of carbon films.{Source: Nature scientific reports*[95]*}*

1.4 Classification into hard and soft carbons.

All semi-graphitic carbon forms mentioned above can also be classified into hard and soft carbons based on tendency towards further graphitisation upon high temperature treatments. First such classification was put forward by Rosalind Franklin based on his work with the graphitisation in the primitive carbon varieties like coke, charcoal and chars. Most of the carbons synthesized by solid state pyrolysis route, the low surface area non activated carbon varieties, after attainment of microcrystalline structural order shows reluctance towards further graphitisation no matter how high we may go on temperature scale. These carbons are more popularly referred to as *hard carbons* owing to their hardness towards further graphitisation. The chars can be cited as representative example. The reluctance towards graphitisation is mainly because of extremely random arrangement of micro-crystalline graphitic domains which renders them static in the matrix of amorphous and sp^3 carbon.

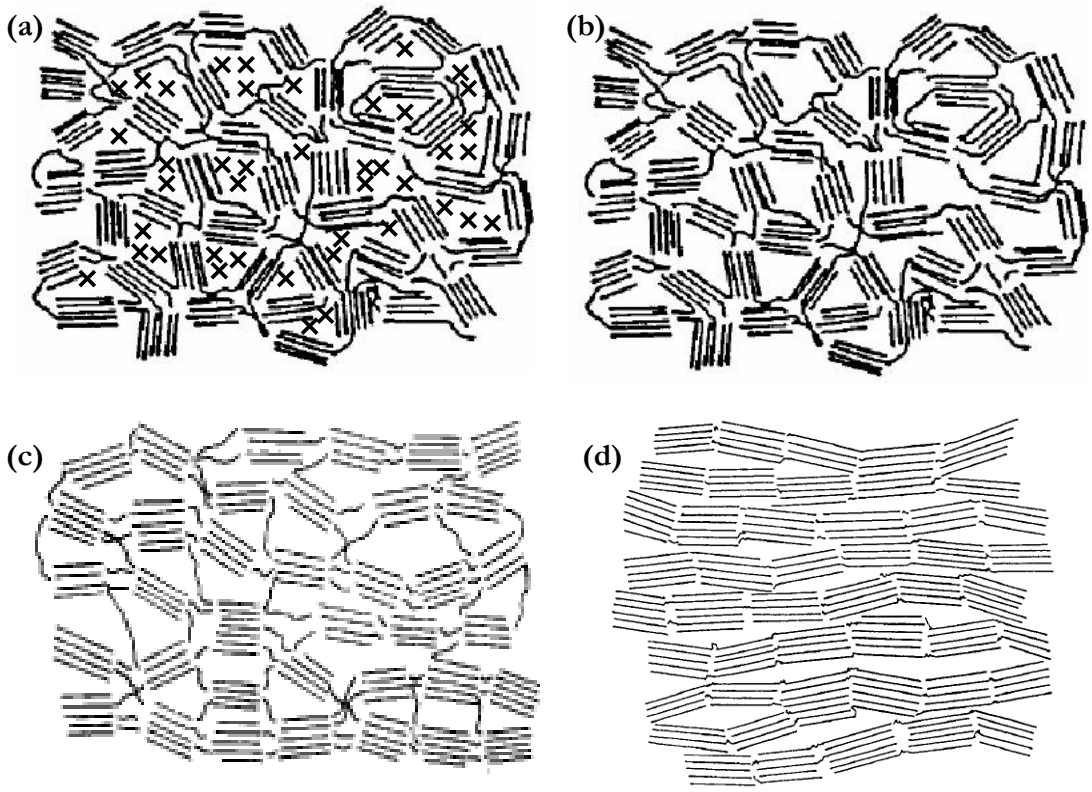

Figure 1.14 *a) Typical hard carbon with randomly oriented graphitic domains intercepted by sp3 and other amorphous carbon shown as crosses here. b) Porous activated carbon showing randomly oriented grains intercepted by open spaces. c) Typical graphitising carbon with partial alignment of graphitic grains. d) The nearly graphitised carbon obtained from high temperature pyrolysis of soft carbons.*

{Source: Reprinted and modified with permission of Elsevier@ Fuels publication}

The high temperatures (upto 3000^0C) are even insufficient to dislodge the sp^3 carbon to promote the graphitisation. The *figure 1.14* shows the graphitic ordering in typical hard carbons. As can be seen from *figure 1.14a* sp^3 carbon in between the graphitic domains arrests these microcrystallites in this irregular state thus rendering them non graphitising. The carbons have special properties of low surface area and suitable graphitic planar separation in the range of 0.36nm-0.40nm,which is typical of turbostratic carbons synthesized by pyrolysis reactions in the temperature range. The structural properties render these carbon varieties useful for Na-ion battery applications.[99–102]

Soft carbons on the other hand are the carbons whose graphitic domains are not so

randomly oriented and there is less amount of sp^3 content so that higher temperature pyrolysis can promote graphitic orientation of partially aligned grains and thus induce graphitisation**.** *Figure 1.14c* shows the typical ordering in soft carbons which can be easily moulded in to partially graphitised structure shown in *figure 1.14d*. The carbons are referred to as soft owing to its high tendency towards pyrolysis induced graphitisation. Coke can be cited as a representative example. The carbon varieties synthesized by liquid state or gas phase synthesis like CVD and laser induced deposition have the typical soft carbon features. The high surface area carbons, activated porous carbons synthesized by solid state activation cum pyrolysis owing to their free spaces and lesser sp^3 content as shown in *figure 1.14b* have been frequently listed as soft carbons. But the actual assignment must include the amount of sp^3 content in the initial carbon variety. Activation is another process of consumption of carbons for generation of pore and mostly the lose sp^3 content is susceptible to this transformation. Thus heavily activated carbons have less sp^3 content and can safely be grouped under this category. We will follow the literature trend for the assignment. Thus all the porous carbons will be referred to as soft while as the low surface area non activated carbons will be referred to as hard carbons.[27,103,104]

1.5 Energy storage applications of hard and soft carbons.

The refined carbon nanoforms (carbon nanotubes, graphene, nanoonions, nanoscrolls) together with nanoengineered carbon forms (carbon nanofibres, carbon aerogels , semi-graphitic hard and soft carbons) have found extensive applications as electrode materials in charge storage devices like super capacitors and batteries. Among them the semi-graphitic carbon types have been considered more promising owing to their easy methods of synthesis, cheap and easily available precursors and above all the lowest possible cost.[105,106] The superiority of these carbon materials to the refined and other well known carbon forms in the energy technology is primarily due to the high surface area (500-2500 m^2g^{-1}) which makes them better surface storage materials and thus materials of choice for super capacitors.[107,108] The low surface area carbons (Hard Carbons) under this category on the other hand possess open graphitic lattices with

higher interplanar separation (>0.36nm) than graphite (0.32nm) which makes them better intercalation host for Na-ion batteries. Before going into the details of charge storage mechanism in the soft and hard carbons we will establish why currently there is a desperate need of energy storage and what are different energy storage devices available to us.[109–111]

1.5.1 Need for energy storage

World energy consumption has reached to *152,777 TWh* and is estimated to increase to *305,500 TWh* by the year 2050. With the present energy sources in hand world is sure to fall in the energy crisis if the alternate sources are not explored, beside the use of coal, petroleum, natural gas are posing a threat to the environment. More of renewable sources are to be stressed upon than the traditional ones but that in turn demands efficient energy devices than anything else. Thus to meet the present global energy needs energy storage has to be focused upon than the energy production itself. The need for storing energy has arisen firstly because of the available energy locked in renewable or non renewable sources is intermittent. *Figure 1.15* lists some renewable sources of energy available to us which could simply supply energy till eternity but they inherit a basic limitation of being intermittent and can hardly be of any direct use as such. Primarily, because our needs of energy are and can never be coherent with the beat of intermittency the listed sources of energy inherit. Secondly, the energy delivery from the sources is either too fast to be directly utilised with 100% efficiency or is too slow to be of any direct use. Thus there is a formidable loss of energy when we approach the direct use of energy. Thus best approach at present is to use the stored energy available from these sources. In this regard best possible energy storage devices are in demand which in turn directly put the onus on the energy storage materials. In this thesis we portray semi-graphitic carbons as the best choice we can have for the same. With these easily synthesizable, cheap and easily processable materials we achieve the maximum storage with simplest possible device designs. [112]

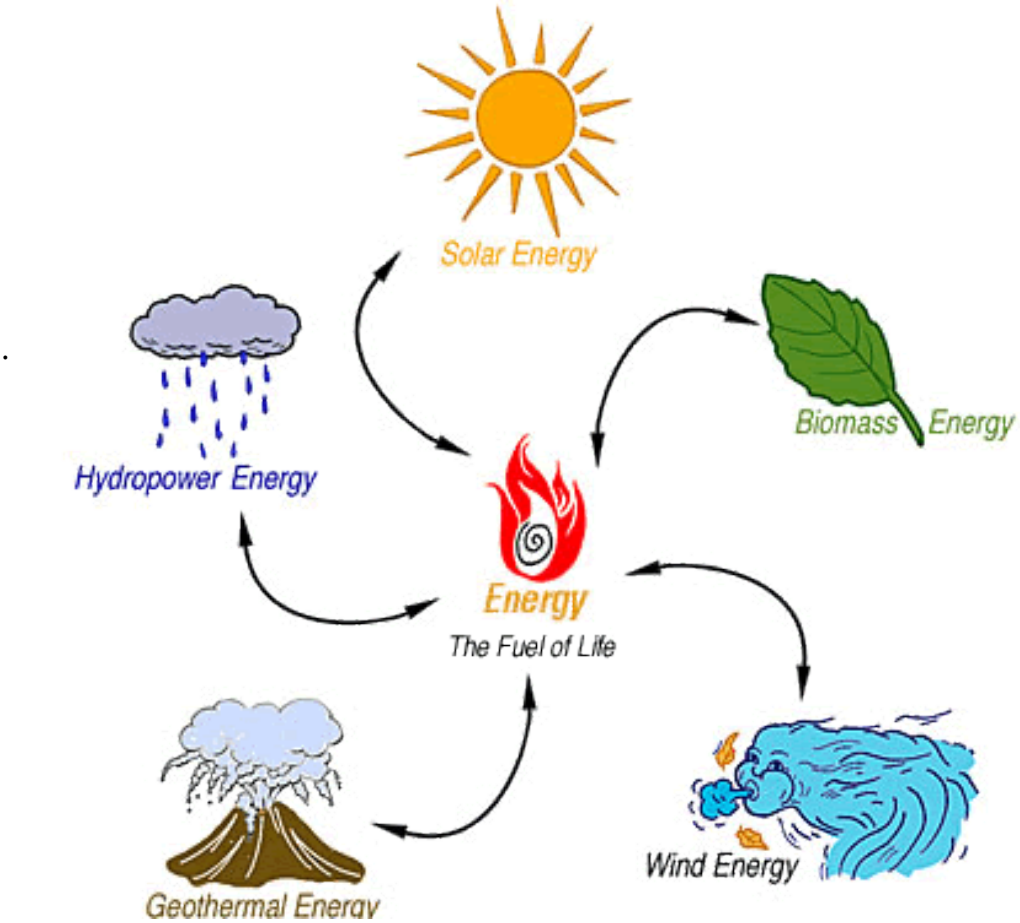

Figure 1.15 *Some common renewable sources of energy which can serve our future energy needs.* *{Source: https://reich-chemistry.wikispaces.com/Renewable+Energy}*

1.5.2 Energy storage devices

Two most common energy storage devices at service presently are capacitors and batteries. Charge being the energy storage currency in both the devices they can also be called as charge storage devices. With the different mechanisms of charge storage one device has some benefits and drawbacks over the other. Battery stores energy through chemical transformations and thus offers high energy densities while as capacitor stores energy through surface charge induction (ceramic capacitors) or ion adsorption (super-ultra capacitors) and thus offers only a low energy density.[113] The ion diffusion and charge induction being faster than chemical reactions, the capacitor delivers high

powers compared to batteries. *Figure 1.16* shows a well known energy density vs. power density plot called Ragone plot which distinguishes different energy storage devices on the basis of these two parameters.[114] Because of high power delivery

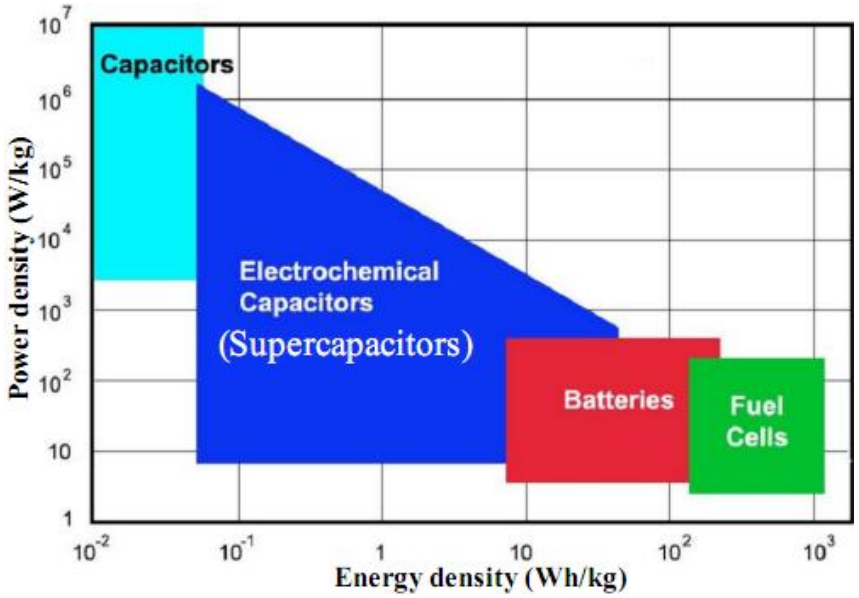

Figure 1.16 *Ragone plot showing the specific power vs. energy density plot of different energy storage devices. {Source: https://www.seas.ucla.edu/~pilon/EES.html}*

concomitant with a better energy density compared to ceramic capacitors, super-capacitors are holding a superior market compared to batteries and ceramic capacitors for high power delivery applications. On the other hand, batteries being high energy density device become important where ever amount of energy matters more than rate of energy delivery. Apart from these two parameters performance appraisal is done on the basis of parameters like capacitance/capacity, energy density, operating voltage, power density, rate stability and cyclic stability.[105,115–117] Now we will discuss the charge storage mechanisms and different variants of these energy storage devices one by one in the sections to follow.

1.5.3 Classification of charge storage devices on the basis of mechanism of charge storage

The energy storage devices can be classified into two broad categories: 1) capacitors and 2) batteries on the basis of mechanism of charge storage. While as capacitors store

charge on the surface by charge induction, surface adsorption or surface reactions the batteries storage charge exclusively by bulk chemical transformations.

1.5.3.1 Capacitors

These are the energy storage devices where charge is stored on the surface of electrodes and can be further classified on the basis of charge carriers and device designs into:

a) Dielectric capacitors (Electrostatic capacitor)

This is a simplest of a device with two conducting (usually metallic) plates held parallel to each other at certain specific distance with a polarisable dielectric in between. The application of potential difference across the terminals causes the polarisation in the dielectric with most favourable dipole alignments i.e. each charged pole faces the plate of opposite polarity. The charge storage mechanism being electro static, these capacitors are also called as electrostatic capacitors. The *figure 1.17a* portrays a design and working of simplest dielectric (electrostatic) capacitor.

Charge storage in this case is voltage dependent (higher the voltage, higher the dielectric polarisation thus higher the charge storage) and we can define a quantity called capacitance (C) which can describe the charge storage capacity of metal plates through following equation:

$$\boldsymbol{C = Q/V} \text{ ---------- (1.1)}$$

where Q is total charge at plates , V is voltage across the plates and C is capacitance. The unit of capacitance is farad (1F=1Columb/ 1V).

As the electric field developed between parallel plates of area A, having stored charge of Q coulombs is given by

$$\boldsymbol{E = Q/\varepsilon A} \text{ --------- (1.2)}$$

where ε is the permittivity of dielectric medium.

Thus capacitance equation for a parallel plate capacitor transforms to

$$\boldsymbol{C = \varepsilon A/d} \text{ ----------(1.3)}$$

where ***d*** is the separation between the plates.

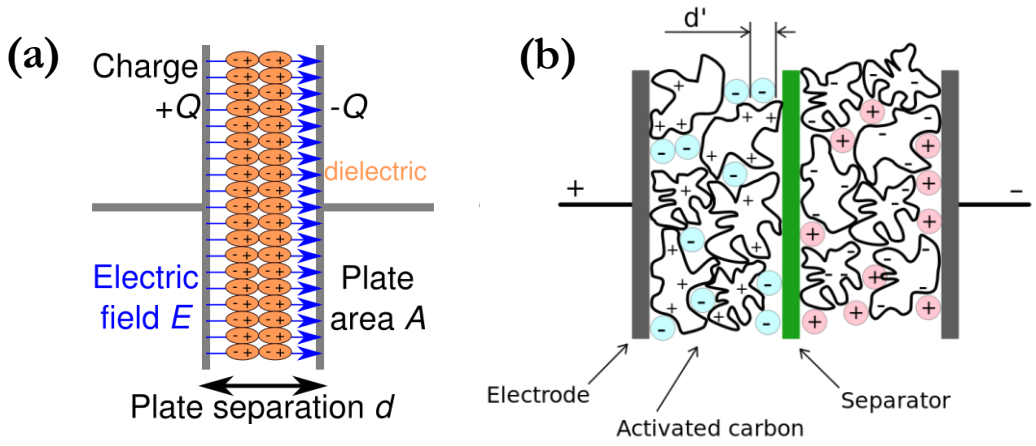

Figure 1.17 *Dielectric capacitor with a dielectric medium between metal plates. b) Corresponding double layer capacitive charge storage in porous carbon material.*

{Sources:http://www.climatetechwiki.org/technology/jiqweb-es-ec;http://large.stanford.edu/courses/2012/ph240/to1/images/f2big.png}

Thus capacitance depends upon the dimensions of electrode and not the material of the electrode and capacitance can be enhanced by increasing the area of electrodes and decreasing their separation. The other parameter which decides the superiority of a capacitor is total energy that can be stored in capacitor and is given by a familiar equation:

$$\boldsymbol{E = \frac{CV^2}{2}} \quad \text{---------- (1.4)}$$

where *E* is energy storage in a capacitor at the highest possible voltage V**.**

b) Electric double layer capacitors. (EDLCs)

Electrochemical Capacitors also called super-capacitors and ultra capacitors are the electrochemical variants of the dielectric capacitors where instead of dielectric polarisation electrolyte polarisation *(figure 1.17b)* leads to charge storage. Polarisation of ions is mediated by surface adsorption of ions at oppositely charged interfaces. The surface adsorption of ions at interface can be well understood by the electrode-electrolyte interface models discussed in next section. Because of better mobility of

ions in electrolyte than the charges in dielectric this type of charge storage is more manoeuvrable.[118] Dipping two electrodes in the solution leads to formation of two interfaces and hence two capacitors in series. *Figure 1.17b* shows the schematic of an EDLC super capacitor. The dielectric separation at the interfaces, d being very small (molecular dimensions) the capacitance of such device is enhanced substantially as can be inferred from the equation (1.3) listed above. The other manoeuvrable parameter for the device is the electrode area as capacitance is directly proportional to area of electrode as per equation (1.3). This opens new provisions of high surface area materials as electrodes in super capacitors. One such class of materials, which has really been a revelation owing to its high surface area is the engineered activated carbons. *Figure 1.18* shows working mechanism of the super capacitive charge storage in such a high surface area material. The activated carbons of this sort possess very high surface areas, in the range of 1000-3000m^2g^{-1} which can enhance the capacitance by several powers of magnitude as per the equation (1.3).

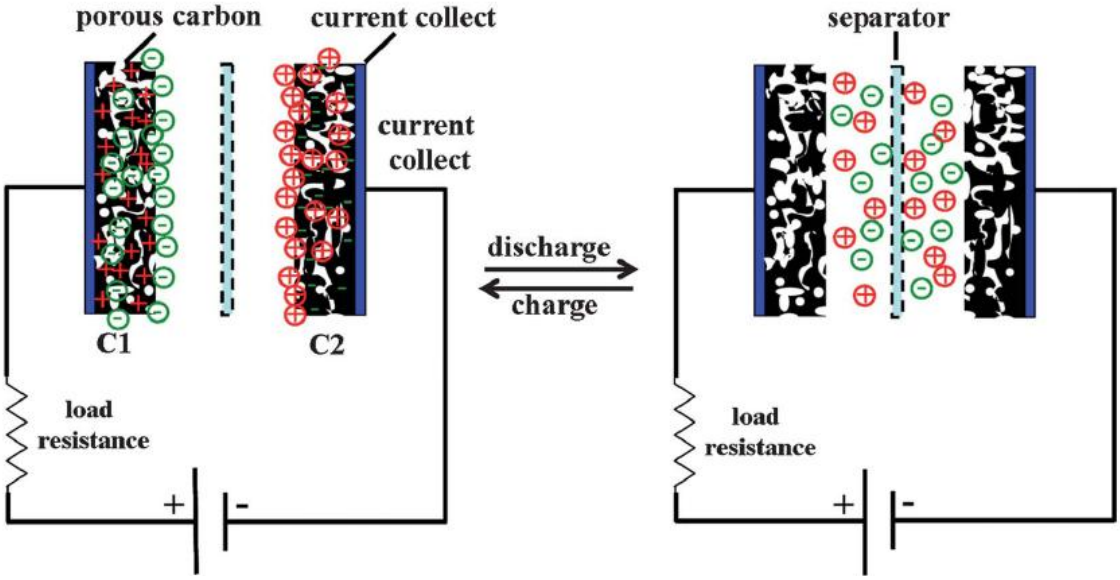

Figure 1.18 *The working mechanism of an EDLC capacitor is illustrated here. Charging and discharging state can be distinguished on the basis of polarisation upon voltage application.*
{Reprinted with permission from Royal Society of Chemistry @ Journal of Materials Chemistry A}

As the total capacitance of device is material dependant, very less can be inferred regarding the superiority of material from this capacitance value. Thus we define two

capacitances which will characterise the material rather than the device itself. The specific capacitance (C_s) or gravimetric capacitance (C_g) can be defined as the capacitance per unit mass of an electrode material. Mathematically it can be represented as:

$$\boldsymbol{C_g = C/m} \text{---------(1.5)}$$

where $\boldsymbol{C_g}$ is gravimetric or specific capacitance, $\boldsymbol{C}$ is capacitance of individual electrode measured separately (in a 3-electrode cell) and $\boldsymbol{m}$ is mass loading of material on electrode. $\boldsymbol{C_g}$ is reported in units of Fg^{-1}.

The other capacitance is the areal capacitance (C_A) which may be defined as capacitance per unit electrode area.

$$\boldsymbol{C_A = C/A}$$

where C_A is real capacitance, C is capacitance of individual electrodes measured separately(in a 3-electrode cell) and A is the area of material coating on electrode. $\boldsymbol{C_A}$ is reported in units of Fcm^{-2}. [119–121,70]

c) Pseudocapacitors.

In pseudo capacitive materials charge is stored at the surface of the electrode material but by the surface adsorption reaction instead of simple physical adsorption. *Figure 1.19* shows three types of surface redox reactions that can account for charge storage through pseudo-capacitive mechanism. As the faradic electron transfer brings about the charge storage such type of capacitors are also called as faradic capacitors. It is worth mentioning that the faradic capacitance is not actual capacitance as charge transfer here as such is not directly voltage dependent and hence the name pseudo-capacitance. Capacitance like behaviour of pseudo capacitance does come from the voltage dependant coverage of participating ions of solution. The materials which have been extensively used to good advantage as pseudo-capacitor electrode material are metal oxides and conducting polymers in aqueous acidic and basic electrolytes. Metal oxides like MnO_2, RuO_2, NiO, Co_3O_4, $NiCo_2O_4$, $NiCo_2S_4$ and other similar oxides and sulphides have shown a remarkably good performance in aqueous solution. [122–127]

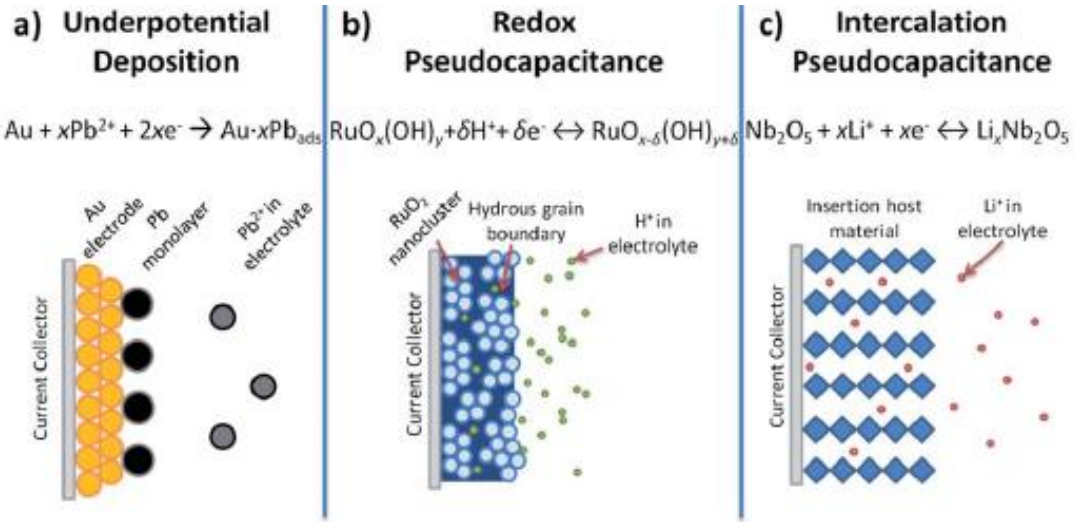

Figure 1.19 a) *Shows the under potential deposition of Pb from solution on Au surface. b) Shows the redox pseudo capacitance of RuO_2 involving reversible surface redox reaction in an acidic medium. c) Shows the intercalation super capacitance of layered Nb_2O_5 in a Li-ion electrolyte.{Reprinted with permission of Royal Sociality of Chemistry @ Energy and Environmental Science}*

Reaction sequences listed below show how RuO_2, NiO and $NiCo_2O_4$ show the Pseudo-capacitance in acidic and basic solutions respectively.

$$RuO_2 + xH^+ + xe^- \leftrightarrow RuO_{2-x}(OH)_x$$

$$NiO + OH^- \leftrightarrow NiOOH + e^-$$

$$NiCo_2O_4 + 3OH^- \leftrightarrow NiOOH + 2CoO_2 + 2H_2O + 3e^-$$

The theoretical capacitance of material can be calculated by following equation:

$$C_g = \frac{N * F}{M.W * \Delta V}$$

where N is number of electrons involved in redox reaction, F is faradays constant , ΔV is voltage window and M.W is molecular weight.

As electron can be localised in a very small space compared to an ion in solution, the capacitance of a pseudo capacitor is several order of magnitude higher than simple EDLC capacitance. Further because of involvement of chemical reaction the power

density of pseudo capacitors are considerably lower than EDLC. Additionally low conductivity of oxide materials hampers the power performance. Besides this pseudo capacitors do offer only a very low voltage window in aqueous solutions because of low over potential of oxygen evolution at the metal oxide surface than carbon materials of EDLC. Thus the huge gain in capacitance is overshadowed by huge loss in energy density because of low voltage window as per equation (1.4). This has limited their direct use as symmetric commercial devices as of yet. However the hybrid assemblies have been proposed to get the best of benefits from the high capacitance of pseudo-capacitors discussion of which will be under taken in following sub section.[120,122–124]

d) Hybrid capacitors

Different types of hybrid designs have been proposed to achieve huge pseudo-capacitance and heavy energy density. Some of them are mentioned as under:

i) Composite type

ii) Battery type hybrid

iii) Asymmetric capacitors

i) Composite type:

In this type of super capacitor designs the physical composite of metal oxide and carbon is used as an electrode material. The added carbon provides the necessary conductivity to the pseudo capacitive material but we have to compromise with the total achievable specific capacitance because carbon adds to the weight loading. Additionally, oxygen evolution potential still remains a challenge and hence limits the energy density achievable.

ii) Battery type hybrids

To increase the energy density of a supercapacitor without compromising with its power density another assembly which gained importance recently is the battery type hybrid capacitor. In this device design a super capacitor is constructed with an EDLC type electrode and a battery type counter electrode in typical battery electrolytes. The battery being a high energy density device and EDLC being a high power device their union

enables us to strike a best possible compromise of the two parameters. Lithium titanium oxide/ porous carbon can be cited as a representative example of a hybrid capacitor which exhibit high energy density in the range of 11-14Whkg^{-1} and power density of 160-2800Wkg^{-1}.

iii) Asymmetric super capacitors.

The battery type hybrids although energy efficient in comparisons to other hybrid capacitor designs but use of organic electrolytes renders them unfavourable on grounds of cost and safety. This has necessitated a mention of another and very exciting hybrid system known as asymmetric super capacitor. On contrary to symmetric capacitor design where both electrodes are derived from the same capacitive material asymmetric capacitors execute a union of two different electrode materials in a single device and hence the name. The net gains in this asymmetric design compared to a typical symmetric carbon capacitor are:

- Voltage window is enhanced.
- Energy density increases several times compared to symmetric device.
- Net weight of device for a particular capacitance will be lesser compared to symmetric one**.**

The two possible electrode unions that has resulted in desired performance from pseudo-capacitive materials is 1) Pseudo-capacitive// Pseudo-capacitive 2) Pseudo-capacitive // carbon. Various effective material combinations which have resulted in desired performance are: graphene-RuO2//graphene, CoO@polypyrrole//activated carbon, graphene $Ni(OH)_2$//graphene, SWCNT)-MnO_2//SWCNT-In_2O_3, CNT-MnO_2// CNT-SnO_2, MnO_2//Fe_3O_4. The notable achievements of the asymmetric capacitor design are the attainment of high voltage window (1.4V-2.0V) in aqueous solution. This design has thus led to energy densities in the range of 15-60 Whkg^{-1} which is quite an achievement in aqueous solution.[128–132]

Components of a super-capacitor: A typical super capacitor consists of electrodes, electrolyte and a separator as shown in *figure 1.20*. Electrodes consist of electrode materials coated on carbon coated aluminium foils separated by a polymer or paper

separator. Porous polymers like polyethylene, poly- propylene, PAN fibres, and porous cellulosic paper have performed efficiently.

Electrolyte is a very important constituent of a supercapacitor as it furnishes mobile charged ions which are polarised by application of voltage. Electrolyte should have properties of broad voltage window and high dielectric constant. In this regard various ionic salts dissolved in water or polar organic solvents like acetonitrile , EC, DMC,, DEC, PC and their mixtures have emerged as good solvents for super capacitor devices. Different aqueous electrolytes employed are 1M H_2SO_4, 6M KOH, 1M $Na2SO_4$, 1M Li_2SO_4, 1M $NaClO_4$ etc. Organic electrolytes include 1M of $LiClO_4$, $LiPF_6$, and NaClO4 in EC, DMC, PC or their mixtures. [133–135]

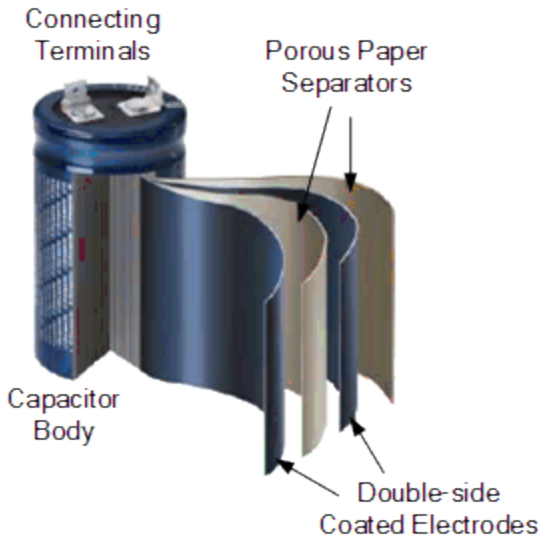

Figure 1.20 *Dissection of a commercial super-capacitor showing different components.*

{Source: https://en.wikipedia.org/wiki/Supercapacitor}

1.5.3.2 Batteries (Rocking chair batteries)

Batteries are the high energy density electrochemical storage devices that store energy by the electro chemical transformation of matter (redox reactions). The energy density of various battery designs is listed in table 1.1. The secondary batteries have a clear edge over the primary in being rechargeable.[136] Lead acid and Ni-Cd were the famous secondary batteries before the advent of Li-ion battery technology in 1991 by Sony. Li-ion battery being superior in all respects over the traditional batteries wiped out all the

other battery types and is dominating the market with *US$29.68 billion*. A close ally of Li-ion battery is Na -ion battery which is considered as only alternative to Li-ion battery. Together Li-ion and Na -ion battery are called as rocking chair batteries owing to mechanism of the charge storage which involves back and forth movement of respective ions from cathode and anode in charge discharge process.

Table 1.1 *Important performance of different battery designs are listed in this table.*

Battery Type	*Energy Density ($Whkg^{-1}$)*	*Power Density (Wkg^{-1})*	*Cycle life*	*Efficiency (%)*
Nickel Cadmium	45-80	150	1000	70
Nickel M -H	60-120	250-1000	300-500	70
Lead Acid	30-50	150-200	200-300	90
Li-ion	90-150	1800-3000	500-2000	99-100

a) Lithium ion batteries (LIB)

The Li-ion battery offers a rich energy density in the range of ~150$Whkg^{-1}$ or ~650WhL^{-1} which makes it a promising energy storage device. The lowest ionic radius *($0.76A^0$)* and highest oxidation potential *(3.045V)* makes it element of choice. The mechanism of energy storage in the LIB is the reversible movement of Li ions between anode and cathode through a Li-ion containing electrolyte like $LiPF_6$, $LiClO_4$ in organic carbonate electrolytes.[137–139] Anode provides a high energy electrochemical state for Li-ion incorporation and cathode provides a low energy electrochemical state for Li-ion. Thus extraction of Li-ions from cathode and its incorporation in anode shall be facilitated by intake of energy in the form of current and reverse will promote the release of energy in the form of same current hence reversibility. *Figure 1.21* shows the schematic of a typical Li-ion battery with four famous components i.e. anode, cathode, electrolyte and separator. As commercial Li ion battery uses $LiCoO_2$ as cathode, graphite as anode and $LiPF_6$ as electrolyte, we will explain the working by citing the reactions involved in this electrode couple. [137–139]

The reactions that enable the cell to reversibly store the charge are:

At cathode:

$$LiCoO_2 \underset{\text{Discharging}}{\overset{\text{Charging}}{\rightleftharpoons}} Li_{1-x}CoO_2 + xLi^+ + xe^-$$

At anode:

$$6C + xLi^+ + xe^- \underset{\text{Discharging}}{\overset{\text{Charging}}{\rightleftharpoons}} LixC_6$$

Net reaction:

$$LiCoO_2 + 6C \underset{\text{Discharging}}{\overset{\text{Charging}}{\rightleftharpoons}} Li_{1-x}CoO_2 + LixC_6$$

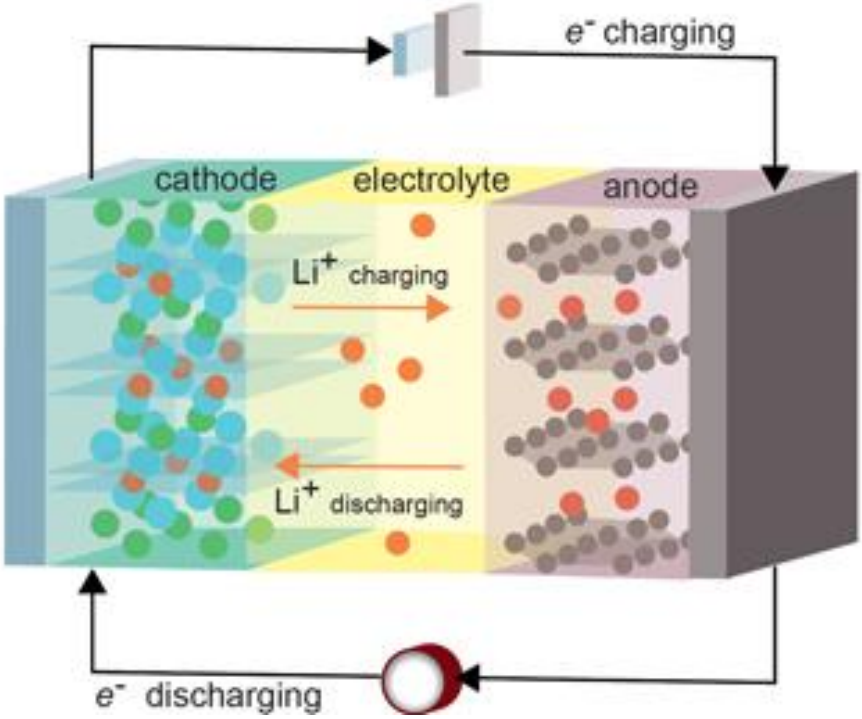

Figure 1.21 *Working of a typical Li-ion cell with layer graphite acting as anode and layered metal oxide acting as cathode is depicted here. Li-ion is shown as orange colour spheres. Li ion leave the anode during discharge (shown by left ward movement) to get incorporated in cathode and traverse a reverse path during the charging.*

{Source:www.panalytical.com/Press-room/XPress-magazine/XPress-32015-4.htm}

Thus during discharge Li^+ and an electron leave the anode and get incorporated in cathode and during charge reverse happens.

Apart from this, anode and cathode materials used in commercial battery we have host of other options for both with some advantages and disadvantages over the present combination. In the cathode many transition metal oxides possessing the NASICON type open structure like that of $LiCoO_2$ have been proposed and have yielded better results. $LiFePO_4$ is one such example, as it has high capacity, and better high temperature stability than $LiCoO_2$. Apart from this other cathode materials of this series like $LiFeO_2$, $LiMnO_4$, $LiNiO_2$, $Li_3V_2(PO_4)_3$, $Li_3V_2(PO_4)_2F_3$, $LiMn_2O_4$, V_2O_5, $LiMnPO_4$ and $LiNi_{1/3}Mn_{1/3}Co_{1/3}O_2$ have been considered. [139,140]

Similarly, for anode case we have three categories of promising materials available and have been successfully tested for the same. The anode materials are categorised as 1) insertion type, 2) conversion type and 3) alloying type.[139,141–143] Insertion type materials include graphite and $Li_4Ti_5O_{12}$ where during discharge Li ion de-intercalates from the layered lattice and while charging Li-ion intercalates into the layered lattice. The reversible reaction operative in case of $Li_4Ti_5O_{12}$ is:

$$(spinel\text{-}LTO)\ Li_4Ti_5O_{12} + 3Li^+ + 3e^- \underset{\text{Discharge}}{\overset{\text{Charge}}{\rightleftharpoons}} Li_7Ti_5O_{12}\ (\text{rock-salt-LTO})$$

Other class of materials having commendable Li-ion anode characteristics are the transition metal oxides, sulphides and phosphides like FeO, Fe_3O_4, Fe_2O_3, FeS_2, FeS, FeP, Co_3O_4,CoO, CoS,Co_3S_4, $NiFe_2O_4$, NiS_2, $CoMn_2O_4$, CuO, $MnCo_2O_4$, and MoS_2. The redox anode characteristics of these materials are called as conversion mechanism and can be understood by following representative example of Co_3O_4:

$$Co_3O_4 + 8Li^+ + 8e^- \underset{\text{Discharge}}{\overset{\text{Charge}}{\rightleftharpoons}} 4Li_2O + 3Co$$

During charge Co_3O_4 converts to Co and Li_2O and vice versa happens during discharge. Third class of anode material is called as alloying type and includes the few p-block

metals and semi metals like Si, Sn, Sb and P. Charge storage mechanism of alloying type materials can be understood by representative example of Sn.

$$4Sn + 15Li^{+} + 15e^{-} \underset{\text{Discharge}}{\overset{\text{Charge}}{\rightleftharpoons}} Li_{15}Sn_{4}$$

Thus while charging Sn forms an alloy with Li^+ by an electrochemical reaction involving $15Li^+$ and $15e^-$ and liberates 15 Li^+ and $15e^-$ while discharging. Similarly a high Li ion storage can be observed in Si because of possibility of $Li_{15}Si_4$. Electrolyte for Li-ion battery should be conducting enough to pass on Li ion to the electrodes besides being stable throughout the long voltage window of 3.0-3.5V. The electrolytes employed are 1M $LiPF_6$ in ethylene carbonate and di-methylene carbonate (1:1 weight ratio). Other electrolyte used is $LiClO_4$ in EC-DMC mixture and polymer electrolytes have also been reported. Similarly separator is equally important and should be electronically insulating.

b) Sodium ion batteries

Although Li ion technology is well established for small scale applications like laptop batteries, watches, pacemakers and other portable devices but for the large scale applications like grid storage and electric vehicles its high cost is a limiting factor. Owing to this Li ion technology is paving way for chemically similar but cost effective Na-ion battery technology to mature. The cost effectiveness comes because of huge reservoirs of sodium in the form of minerals like rock salt, sodalite and feldspars is present in Earth's crust, exact percentage being 2.5% compared to comparatively minute 0.0017% lithium. Sodium ion batteries can offer an energy density of 100-200 $Whkg^{-1}$. As far as the choice of electrodes, electrolytes and separators is concerned Na-ion battery technology can be thought of as a reciprocation of Li ion battery. *Figure 1.22* shows working of a typical sodium ion battery. For the anode side graphite has been replaced by the defective semi graphitic carbon which offers an interplanar separation in the range of 0.36-0.42nm. The greater interplanar separation of hard carbons allows easy passage for Na^+ in these carbons compared to graphite. [144,110,145]

Interplanar separation of 0.32nm in case of graphite is sufficient for Li^+ insertion and extraction but not for Na^+. As for Li ion battery, anode materials for Na ion battery can be classified into insertion, conversion and alloying type. Among the insertion type materials, hard carbons and layered $Na_2Ti_3O_7$ have shown good anode characteristics.

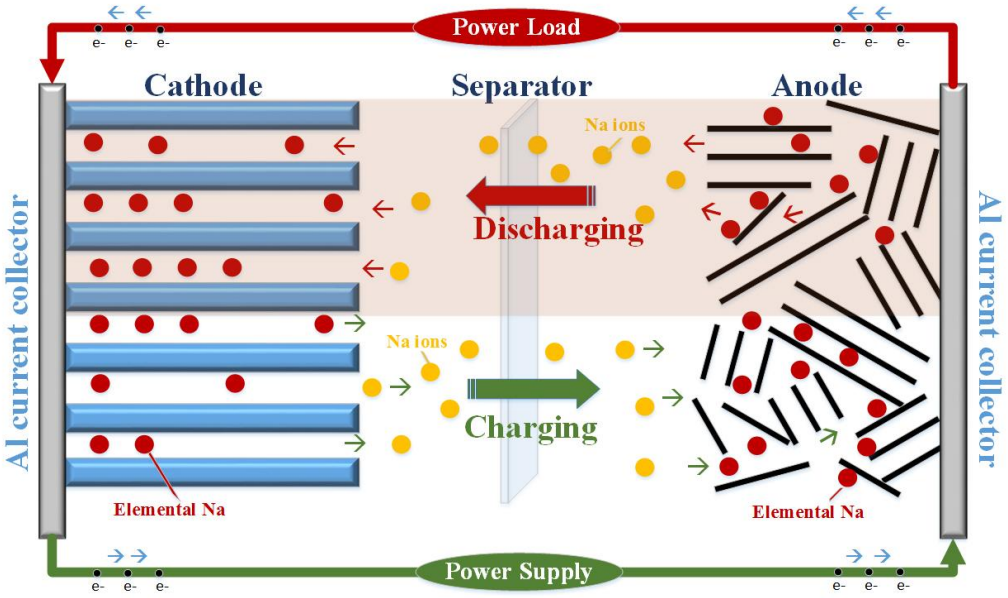

Figure 1.22 *Shows the working of a typical sodium ion cell. Anode consists of turbostratic hard carbons and cathode consists of a layered Na-transition metal oxide. The sodium in ionic state is shown as yellow colour sphere and its trapped state is shown as red colour sphere. Discharging is depicted as the movement of Na-ion from anode to cathode and charging is depicted as movement of ions from cathode to anode.*

{Source:www.purdue.edu/newsroom/releases/2015/Q3/sodium-ion-batteries-are-potential-power-technology-of-future.html}

Similarly for conversion type materials like FeS_2, CoS_2, Fe_2O_3, Co_3O_4, FeP, CoP, Sb_2O_3, and MoS_2. The conversion of Co_3O_4 can be sited as a representative example:

$$Co_3O_4 + 8Na^+ + 8e^- \underset{\text{Discharge}}{\overset{\text{Charge}}{\rightleftharpoons}} 4Na_2O + 3Co$$

Alloying materials like Sn, Sb and P have also shown excellent Na-ion anode characteristics similar to that of Li-ion. Si has been shown to have lesser storing capacity owing to existence of NaSi as the most stable phase compared to $Li_{15}Si_4$.

Anode characteristics of alloying materials can be understood by taking representative example of Sn:

$$4Sn + 15Na^{+} + 15e^{-} \underset{\text{Discharge}}{\overset{\text{Charge}}{\rightleftharpoons}} Na_{15}Sn_4$$

Performance parameters for battery: Various parameters which determine performance of battery are:

Capacity (Q): It is the measure of total charge that can be reversibly stored in an electrode material (anode/cathode). It is reported in the units of $mAhg^{-1}$. The capacity of an electrode material can be calculated by following equation:

$$\boldsymbol{Capacity}\left(\frac{\boldsymbol{mAh}}{\boldsymbol{g}}\right) = (\boldsymbol{N} * \boldsymbol{96500})/(\boldsymbol{3600} * \boldsymbol{M.W})$$

where N is number of electrons involved in charge transfer and M.W. is molecular weight of electrode material.

Rate capacity: It is a measurement which involves the capacity measurement at different currents generally starting from lower currents to higher currents (of the range of $21Ag^{-1}$-$20Ag^{-1}$) then again to the lower currents. A material is said to be rate stable if it retains the initial capacity after going through this cycle.

Cycle stability: It involves capacity measurement over hundreds of cycles at one particular current. The measurement is carried out to test the stability of material over those many cycles.

Operating voltage (O.P): It is the voltage vs. Na^{+}/ Na at which reversible electro-chemical uptake and release of Na takes place. For an anode OP closer to 0V is preferred while as for a cathode greater the voltage from 0V better is the cathode material. Electrolytic stability concerns allow maximum of 4.5V (cathode) and minimum (for anode) of 0.01V.

Energy Density (E.D): It is the total energy that can be stored in the cell per unit electrode weight and is a simple product of capacity and operating voltage of full cell.

$$\boldsymbol{E.D}\left(\frac{Wh}{kg}\right) = \boldsymbol{Q''}\left(\frac{mAh}{g}\right) * \boldsymbol{V}(V)$$

where $\boldsymbol{Q''}$ is reduced capacity of a full cell device in $mAhg^{-1}$ and $\boldsymbol{V}$ is O.P in Volts. Q' can further be defined as

$$\boldsymbol{Q''} = \frac{\boldsymbol{Q_{an}} * \boldsymbol{Q_{ca}}}{\boldsymbol{Q_{an}} + \boldsymbol{Q_{ca}}}$$

Where $\boldsymbol{Q_{an}}$ is individual capacity of anode and $\boldsymbol{Q_{ca}}$ is individual capacity of cathode.

1.5.3.3 Electrode-electrolyte interface models

Electrode electrolyte interface models describe the distribution of ions around the electrode under different potential conditions. Three such models has been proposed, the most primitive being 1) **Helmholtz model** followed by 2) **Gouy Chapman model** and finally the most accepted 3) **Stern model** as displayed in *figure 1.23***.** While as Helmholtz model advocates adsorption of all the oppositely charged ions at the outer Helmholtz plane as presented in *figure 1.23a*, Gouy Chapman model proposes

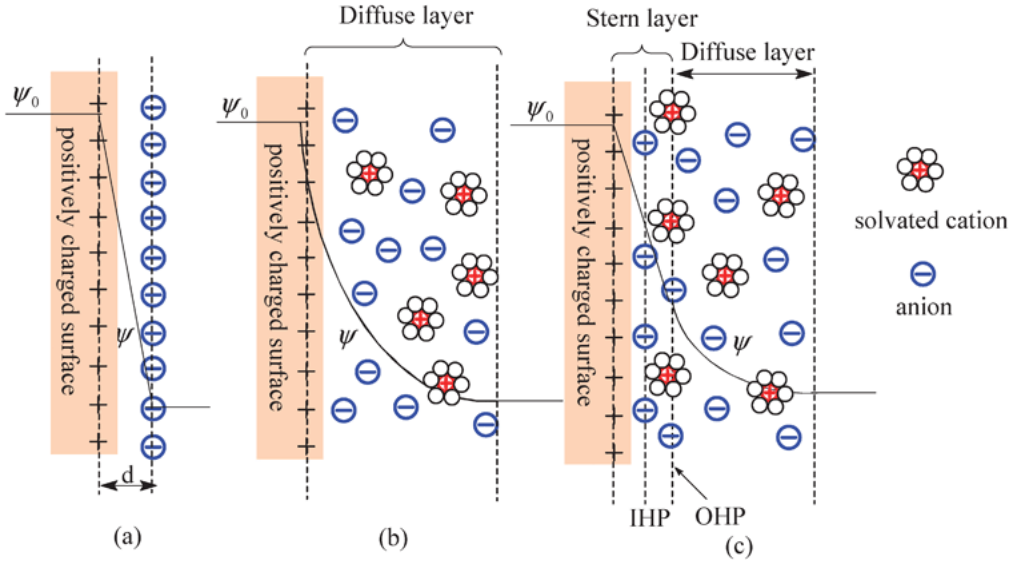

Figure 1.23 *Electric double layer models are depicted here on a positively charged electrode surface. a) Helmholtz model depicting adsorption of negatively charged ions at a plane inside electrolyte (OHP) parallel to electrode surface .b) Gouy Chapman model depicting diffuse layer of ions starting from the electrode surface itself and extending to bulk. c) Stern model depicting the diffuse layer of ions but starting from inner Helmholtz plane (IHP) inside the solution and extending to bulk. {Reprinted with permission of Royal Society of Chemistry@ Chemical Reviews}*

exponential decay of concentration of ions with respect to the distance from electrode surface as shown in *figure 1.23b*. Thus this model proposes existence of a diffuse layer

of oppositely charged ions starting directly from the electrode surface. Stern model which is considered to be the most acceptable among the three can be considered as the amalgamation of Helmholtz and Gouy Chapman model as revealed by *figure 1.23c*. It proposes the existence of Gouy Chapman type of diffuse layer with a modification that the starting point of the diffuse layer lies at the Helmholtz plane instead of metal surface as advocated by Gouy Chapman Model.[107,146–148]

1.6 Use of carbon materials as electrodes in energy storage devices

Now that we have discussed in detail about the types of carbon materials and various energy storage devices and the working principle there in, we are set to establish a relationship between the two in this section. For the super capacitor application as we know from equation (1.3) that

Table 1.2 *Table showing the specific capacitance of different carbon materials having different surface areas in organic and aqueous electrolytes.*[107]

Materials	Specific surface area $m^2 g^{-1}$	Aqueous electrolyte		Organic electrolyte	
		$F g^{-1}$	$F cm^{-3}$	$F g^{-1}$	$F cm^{-3}$
Carbon materials					
Commercial activated carbon (ACs)	1000-3500	< 200	< 80	< 100	< 50
Particulate carbon from SiC/TiC	1000-2000	170-220	< 120	100-120	< 70
Functionalized porous carbons	300-2200	150-300	< 180	100-150	< 90
Carbon nanotube (CNT)	120-500	50-100	< 60	< 60	< 30
Templated porous carbons (TC)	500-3000	120-350	< 200	60-140	< 100
Activated carbon fibers (ACF)	1000-3000	120-370	< 150	80-200	< 120
Carbon cloth	2500	100-200	40-80	60-100	24-40
Carbon aerogels	400-1000	100-125	< 80	< 80	< 40
Carbon- based composite materials					
TC- RuO_2 composite	600	630	630	_	_
CNT-MnO_2 composite	234	199	300	_	_
AC-polyaniline composite	1000	300	_	_	_

the capacitance is a direct function of surface area ; high surface area activated carbons classified under the heading of semi-graphitic soft carbons can be revolutionary prospect for said application. These carbons have an edge over the refined carbon forms like graphene, CNTs, carbon nanofibers[9], and carbononions[12] for capacitor application on account of easy synthesis and low cost. *Table 1.2* lists the capacitances furnished by different carbon materials in different electrolytes. The semi-graphitic (turbostratic) soft carbons furnish better performance compared to other refined forms of carbon. *Table 1.2* lists various carbon materials with differing capacitances with respect to their surface areas indifferent electrolytes. It can be seen that the direct relationship between capacitance

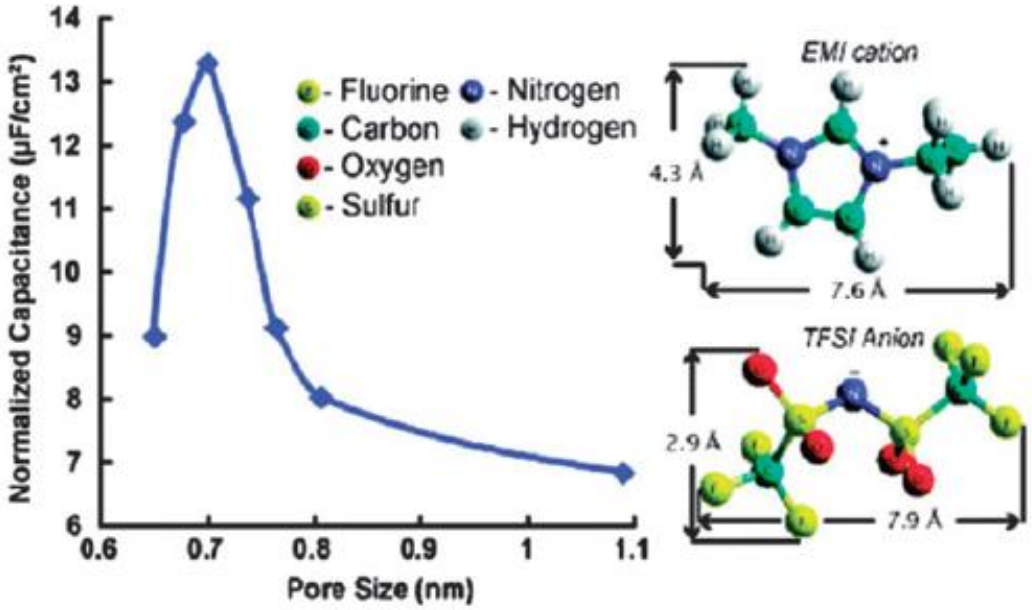

Figure 1.24 *Normalised capacitance vs. pore size plot, obtained by recording the capacitances of carbon materials with different pore sizes in ionic liquid electrolytes is presented here. The ionic liquid is so chosen that the cation (EMI) and anion (TFSI) have almost similar diameter. The maximum in the capacitance vs. pore size plot lies at the pore size of 0.72nm which happens to be the very close to the electrolyte ion size.*

{Reprinted with permission of Royal Society of Chemistry@ Chemical Reviews}

and surface area is not so direct and there is an intervention of different factors like pore size and ion size. Thus the effective surface area of a carbon material which contributes to capacitance can be said to be pore size controlled. To understand the effect of pore size on final capacitance we present work of *Largeot et al.* who

established that capacitance maximum lies at a point where pore size matches with ion size as depicted in *figure 1.24*. Based on this and other related experimental works optimal pore size for an organic electrolyte is 0.8nm and for aqueous electrolyte optimal pore size is 0.7nm.[107,149]These findings have revealed the importance of micropores for capacitance. Although mesopores are not ideally sought for high capacitance values but they have importance in bestowing the carbon materials the high power delivery by solvent buffering, as revealed by other studies.

Apart from porosity functional groups do have sizable effect on capacitance by their participation in pseudo capacitive charge transfer reactions. In this regard nitrogen, oxygen, sulphur and phosphorus doped carbons have become important.[150–152]

Semi-graphitic hard carbons on the other hand possess the required interplanar separation *(figure 1.12)* to allow easy intercalation and de-intercalation of Na ions. Na^+ intercalation and de- intercalation in hard carbons was shown by Stevens and Dahn in 2000 on the carbon derived from glucose pyrolysis. Hard carbons derived from sugars, polymers and composites of these hard carbons with CNTs and graphene have already been reported to have delivered satisfactory sodium ion performance. *Komaba et al* in 2009 showed that with proper control over the moisture content and high purity of electrolyte and solvent the cyclic stability could be increased to 50 cycles without compromising with high capacity of $300mAhg^{-1}$. Hard carbons derived from banana peels, from lotus petiole, okara by product, peanut shells, natural wood fibres and compact wood have delivered satisfactory performance as far as capacity and cycle stability is concerned.[77,144,153–157] *Figure 1.25* shows various Na ion anode materials positioned at different points in an operating potential vs. capacity plot. Position of hard carbons with low operating potential vs. Na duly justifies an intense research focus towards these semi-graphitic carbon forms.

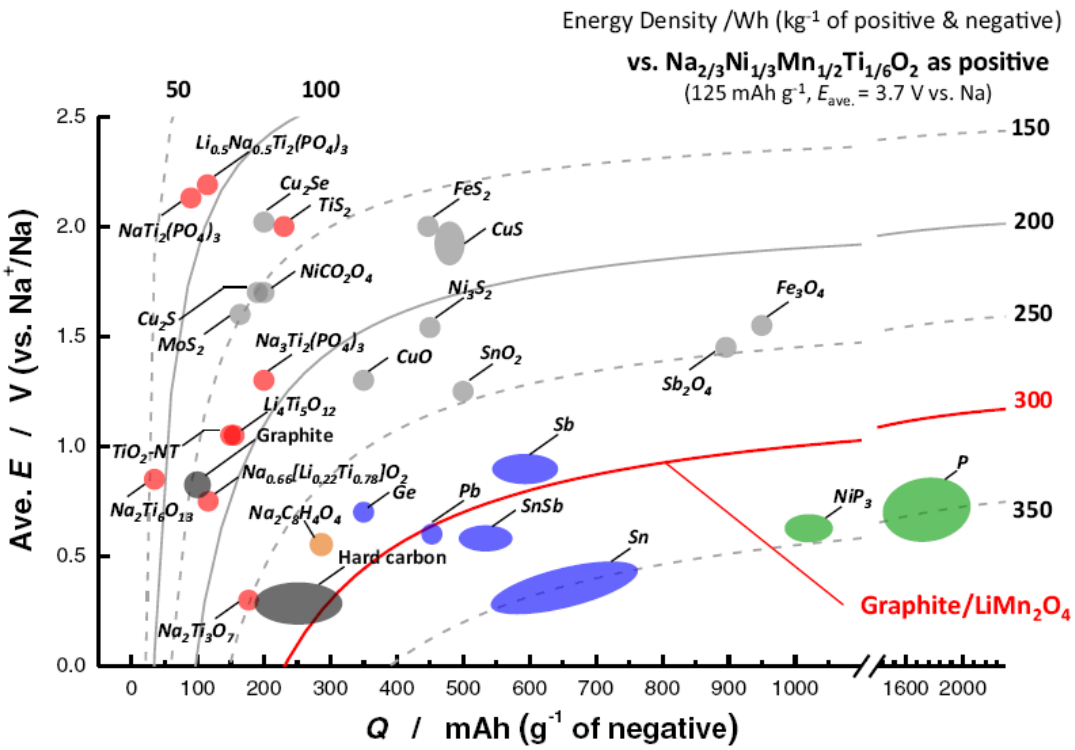

Figure 1.25 *Sodium ion anode materials discovered so far are listed in this plot. The position of a material in the plot reflects the materials capacity and operating potential vs. Na. The right side of the plot gives energy density (Whkg^{-1}) calculated with reference to $Na_{2/3}Ni_{1/3}Mn_{1/2}Ti_{1/6}O_2$ cathode.*[158] *{Reprinted with permission from American Chemical Society @Chemical Reviews}*

1.7 Plan and structure of the thesis

This thesis projects the use of cheap and easily manoeuvrable carbon materials synthesized from bio wastes and natural products for energy storage applications. The carbon materials possessing the turbostratic graphitic structure do possess suitable conductivities, surface areas and interplanar separations to be used as electrodes in super-capacitors and sodium ion batteries. Having established their structural status compared to other forms of carbon and having highlighted their structural superiorities to be used as electrode in energy storage devices in the introductory chapter. We now in the rest of the thesis provide a detailed synthesis, characterisation and then application in energy storage devices.

The ***second*** chapter firstly discusses the methods that are being employed for the synthesis with a special focus on the synthesis methods we have adopted here. Various

characterisation techniques which are indispensable for carbon material analysis have been discussed. Electrochemical tools and techniques are also discussed in detail in this chapter.

The ***third*** chapter projects the chemically activated carbon synthesized from sugar cane bagasse with a synthetic novelty of hydrothermal pre-treatment before activation pyrolysis as an efficient electrode material for a symmetric super capacitor. Further this carbon material is reported to exhibit the enhanced capacity retention of 72% and cycling stability with capacity retention of 90% after 10000 cycles.

The ***fourth*** chapter presents a non activation process for generation of porosity in a carbon material derived from a biogel, pectin. The gel infiltration inside the SBA-15 is achieved by simple dissolution which upon pyrolysis releases the interconnected carbon threads with sufficient meso/micro porosity to be used as electrode material in super capacitor. The capacitor furnishes an attractive performance with capacity of $285Fg^{-1}$ at $1Ag^{-1}$ and 96% retention of capacity after 2000 charge-discharge cycles.

The ***fifth*** chapter projects a chemically activated carbon derived from yogurt as an efficient negative electrode in the asymmetric super capacitor. The use of an asymmetric assembly with $NiCo_2S_4$ electrode grown on nickel foam as positive electrode has furnished wonderful results for this carbon with the enhancement in energy density ($21Whkg^{-1}$ in asymmetric assembly compared to $7Whkg^{-1}$ in symmetric one) by 3 folds.

The ***Sixth*** chapter deals with the low surface area non activated carbon, the hard carbon, and its application as anode material in sodium ion battery. Hard carbon derived from walnut shell is being presented as an efficient performer as sodium ion anode. Direct pyrolysis of nutshell yielded desired carbon with the suitable interplanar separation. Sodium ion anode capacity of $257mAhg^{-1}$ was observed for the wall nut derived carbons with a remarkable stability upto 300 cycles.

1.8 References

1. E. Roduner, *Chem. Soc. Rev.*, 2006, **35**, 583.
2. J. Maier, *Nat. Mater.*, 2005, **4**, 805–815.
3. W. Yang, K. R. Ratinac, S. R. Ringer, P. Thordarson, J. J. Gooding and F. Braet, *Angew. Chemie - Int. Ed.*, 2010, **49**, 2114–2138.
4. A. E. Nel, L. Madler, D. Velegol, T. Xia, E. M. V Hoek, P. Somasundaran, F. Klaessig, V. Castranova and M. Thompson, *Nat. Mater.*, 2009, **8**, 543–557.
5. R. Fisher et al., *Energy Environ. Sci.*, 2013, **3**, 4889–4899.
6. J. N. Coleman, U. Khan, W. J. Blau and Y. K. Gunko, *Carbon*, 2006, **44**, 1624–1652.
7. H. W. Kroto, J. R. Heath, S. C. OBrien, R. F. Curl and R. E. Smalley, *Nature*, 1985, **318**, 162.
8. A. W. Jensen, S. R. Wilson and D. I. Schuster, *Bioorganic Med. Chem.*, 1996, **4**, 767–779.
9. S. Iijima, *Nature*, 1991, **354**, 56–58.
10. M.F. Yu, B. S. Files, S. Arepalli and R. S. Ruoff, *Phys. Rev. Lett.*, 2000, **84**, 5552–5555.
11. J. P. Salvetat-Delmotte and A. Rubio, *Carbon*, 2002, **40**, 1729–1734.
12. J.P. Salvetat, J.-M. Bonard and N. H. Thomson, *Appl. Phys. A*, 1999, **69**, 255–260.
13. F. Kreupl, G. S. Duesberg, A. P. Graham, M. Liebau, E. Unger, R. Seidel, W. Pamler and W. Hoenlein, 2004, **8**, 1–8.
14. H. Dai, *Acc. Chem. Res.*, 2002, **35**, 1035–1044.
15. C. Mattevi et al., *J. Mater. Chem.*, 2011, **21**, 3324–3334.
16. N. Krane, *Growth Lakel.*, 1993, **4**, 1–5.

17. M. J. Allen, V. C. Tung and R. B. Kaner, *Chem. Rev.*, 2010, **110**, 132–145.

18. X. Wu, M. Sprinkle, X. Li, F. Ming, C. Berger and W. A. De Heer, *Phys. Rev. Lett.*, 2008, **101**, 1–4.

19. S. Wang, P. K. Ang, Z. Wang, A. L. L. Tang, J. T. L. Thong and K. P. Loh, *Nano Lett.*, 2010, **10**, 92–98.

20. J. Campos-Delgado, J. M. J. M. Romo-Herrera, X. Jia, D. A. Cullen, H. Muramatsu, Y. A. Kim, T. Hayashi, Z. Ren, D. J. Smith, Y. Okuno, T. Ohba, H. Kanoh, K. Kaneko, M. Endo, H. Terrones, M. S. Dresselhaus and M. Terrones, *Nano Lett.*, 2008, **8**, 2773–2778.

21. J. L. Delgado, M. Herranz and N. Martín, *J. Mater. Chem.*, 2008, **18**, 1417.

22. J. M. Sullivan, *Nature*, 1998, **392**, 237.

23. P. J. F. Harris, *Interdiscip. Sci. Rev.*, 2001, **3**, 204–210.

24. V. Sahajwalla, M. Dubikova and R. Khanna, *Proc. Tenth Int. Ferroalloys Congr.*, 2004, 351–362.

25. T. Kyotani, Z. Ma and A. Tomita, *Carbon*, 2003, **41**, 1451–1459.

26. L. Chen, X. Cui, M. Wang, Y. Du, X. Zhang, G. Wan, L. Zhang, F. Cui, C. Wei and J. Shi, *Langmuir*, 2015, **31**, 7644–7651.

27. J. Lee, J. Kim and T. Hyeon, *Adv. Mater.*, 2006, **18**, 2073–2094.

28. R. Gokhale, S. Agarkar, J. Debgupta, D. Shinde, B. Lefez, A. Banerjee, J. Jog, M. More, B. Hannoyer and S. Ogale, *Nanoscale*, 2012, **4**, 6730–4.

29. M.S. Dresselhaus, G.Dresselhaus and P. C. Eklund, *Science of Fullerenes and Carbon nanotubes*, Academic Press, New York, 1995.

30. T. D. Burchell, *Carbon Materials for Advanced Technologies*, Pergamon Press, Oxford, 1999.

31. L. Qingkun, S. Yi, L. Zhiyuan and Z. Yu, *Scr. Mater.*, 2011, **65**, 229–232.

32. B. R. Wu, *Diam. Relat. Mater.*, 2007, **16**, 21–28.

33. A. Timoshevskii, S. Kotrechko and Y. Matviychuk, *Phys. Rev. B*, 2015, **91**, 245434.

34. M. Zhou, H.-L. Wang and S. Guo, *Chem. Soc. Rev.*, 2016, **62**, 39–62.

35. J. Shui, M. Wang, F. Du and L. Dai, *Sci. Adv.*, 2015, **1**, 377–384.

36. M. S. Mauter and M. Elimelech, *Environ. Sci. Technol.*, 2008, **42**, 5843–5859.

37. D. Jariwala, V. K. Sangwan, L. J. Lauhon, T. J. Marks and M. C. Hersam, *Chem. Soc. Rev.*, 2013, **42**, 2824–60.

38. M. X. Wang, X. H. Zhang and Q. Y. Zheng, *Angew. Chemie - Int. Ed.*, 2004, **43**, 838–842.

39. I. Lamparth, C. Maichle–Mössmer and A. Hirsch, *Angew. Chemie Int. Ed. English*, 1995, **34**, 1607–1609.

40. M. Prato, *J. Mater. Chem.*, 1997, **7**, 1097–1109.

41. J. W. Mintmire, B. I. Dunlap and C. T. White, *Phys. Rev. Lett.*, 1992, **68**, 631–634.

42. V. M. Rotello, J. B. Howard, T. Yadav, M. M. Conn, E. Viani, L. M. Giovane and A. L. Lafleur, *Tetrahedron Lett.*, 1993, **34**, 1561–1562.

43. J. Hu, T. W. Odom and C. M. Lieber, *Acc. Chem. Res.*, 1999, **32**, 435–445.

44. T. Oku, T. Hirano, M. Kuno, T. Kusunose, K. Niihara and K. Suganuma, *Mater. Sci. Eng. B Solid-State Mater. Adv. Technol.*, 2000, **74**, 206–217.

45. Y. Gao, Y. S. Zhou, M. Qian, X. N. He, J. Redepenning, P. Goodman, H. M. Li, L. Jiang and Y. F. Lu, *Carbon*, 2013, **51**, 52–58.

46. Y. Moret and P. Schmid-Hempel, *Nature*, 2001, **414**, 506.

47. M. Zeiger, N. Jäckel, V. Mochalin and V. Presser, *J. Mater. Chem. A*, 2015, **4**, 3172–3196.

48. S. Fan, M. G. Chapline, N. R. Franklin, T. W. Tombler, A. M. Cassell and H. Dai, *Science* , 1999, **283**, 512–514.

49. C. Gao, Z. Guo, J.-H. Liu and X.-J. Huang, *Nanoscale*, 2012, **4**, 1948–63.

50. C.H. Liu, Y.Y. Liu, Y.H. Zhang, R.-R. Wei and H.L. Zhang, *Phys. Chem. Chem. Phys.*, 2009, **11**, 7257–7267.

51. J. V Veetil and K. Ye, *Biomed. Eng. (NY).*, 2009, **25**, 709–721.

52. E. D. Minot, A. M. Janssens, I. Heller, H. A. Heering, C. Dekker and S. G. Lemay, *Appl. Phys. Lett.*, 2007, **91**, 58–61.

53. S. Zhu and G. Xu, *Nanoscale*, 2010, **2**, 2538–2549.

54. P. S. Karthik, A. L. Himaja and S. P. Singh, *Carbon Lett.*, 2014, **15**, 219–237.

55. A. K. Geim and K. S. Novoselov, *Nat. Mater.*, 2007, **6**, 183–91.

56. E. Gerstner, *Nat. Phys.*, 2010, **6**, 836–836.

57. J. W. Suk, R. D. Piner, J. An and R. S. Ruoff, 2010, **4**, 6557–6564.

58. Y. A. Eva, L. Guohong and D. Xu, *Reports Prog. Phys.*, 2012, **75**, 56501.

59. A. H. Castro Neto, F. Guinea, N. M. R. Peres, K. S. Novoselov and A. K. Geim, *Rev. Mod. Phys.*, 2009, **81**, 109–162.

60. A. C. Ferrari, J. C. Meyer, V. Scardaci, C. Casiraghi, M. Lazzeri, F. Mauri, S. Piscanec, D. Jiang, K. S. Novoselov, S. Roth and A. K. Geim, *Phys. Rev. Lett.*, 2006, **97**, 1–4.

61. A. Gupta, G. Chen, P. Joshi, S. Tadigadapa and P. C. Eklund, *Nano Lett.*, 2006, **6**, 2667–2673.

62. M. A. Pimenta, G. Dresselhaus, M. S. Dresselhaus, L. G. Cançado, A. Jorio and R. Saito, *Phys. Chem. Chem. Phys.*, 2007, **9**, 1276–1291.

63. S. Ghosh, I. Calizo, D. Teweldebrhan, E. P. Pokatilov, D. L. Nika, A. A. Balandin, W. Bao, F. Miao and C. N. Lau, *Appl. Phys. Lett.*, 2008, **92**, 2008–2010.

64. Y. Shao, J. Wang, H. Wu, J. Liu, I. A. Aksay and Y. Lin, *Electroanalysis*, 2010, **22**, 1027–1036.

65. D. B. Shinde, J. Debgupta, A. Kushwaha, M. Aslam and V. K. Pillai, *J. Am. Chem. Soc.*, 2011, **133**, 4168–4171.

66. D. V Kosynkin, A. L. Higginbotham, A. Sinitskii, J. R. Lomeda, A. Dimiev, B. K. Price and J. M. Tour, *Nature*, 2009, **458**, 872–876.

67. V. N. Mochalin, O. Shenderova, D. Ho and Y. Gogotsi, *Nat. Nanotechnol.*, 2012, **7**, 11–23.

68. W. J. Zhang, Y. Wu, W. K. Wong, X. M. Meng, C. Y. Chan, I. Bello, Y. Lifshitz and S. T. Lee, *Appl. Phys. Lett.*, 2003, **83**, 3365–3367.

69. N. Setoyama, T. Suzuki and K. Kaneko, *Carbon*, 1998, **36**, 1459–1467.

70. D. Qu, *J. Power Sources*, 2002, **109**, 403–411.

71. K. Kaneko, C. Ishii, M. Ruike and H. kuwabara, *Carbon*, 1992, **30**, 1075–1088.

72. K. Nordlund, J. Keinonen and T. Mattila, *Phys. Rev. Lett.*, 1996, **77**, 699–702.

73. S. Tawfick, K. O'Brien and A. J. Hart, *Small*, 2009, **5**, 2467–2473.

74. J. L. Rigueur, S. A. Hasan, S. V. Mahajan and J. H. Dickerson, *Carbon*, 2010, **48**, 4090–4099.

75. Y. Z. Jin, C. Gao, W. K. Hsu, Y. Zhu, A. Huczko, M. Bystrzejewski, M. Roe, C. Y. Lee, S. Acquah, H. Kroto and D. R. M. Walton, *Carbon*, 2005, **43**, 1944–1953.

76. G. P. Hao, W. C. Li, D. Qian and A. H. Lu, *Adv. Mater.*, 2010, **22**, 853–857.

77. E. Irisarri, A. Ponrouch and M. R. Palacin, *J. Electrochem. Soc.*, 2015, **162**, 2476–2482.

78. C. Kim, K. S. Yang, M. Kojima, K. Yoshida, Y. J. Kim, Y. A. Kim and M. Endo, *Adv. Funct. Mater.*, 2006, **16**, 2393–2397.

79. X. Li, W. Cai, J. An, S. Kim, J. Nah, D. Yang, R. Piner, A. Velamakanni, I. Jung, E. Tutuc, S. K. Banerjee, L. Colombo and R. S. Ruoff, *Science*, 2009, **324**, 1312–1314.

80. M. O. Adebajo, R. L. Frost, J. T. Kloprogge, O. Carmody and S. Kokot, *J. Porous Mater.*, 2003, **10**, 159–170.

81. N. Sun, H. Liu and B. Xu, *J. Mater. Chem. A Mater. energy Sustain.*, 2015, **3**, 20560–20566.

82. V. Sahajwalla, M. Dubikova and R. Khanna, *Proc. Tenth Int. Ferroalloys Congr.*, 2004, **209**, 351–362.

83. A. J. Fletcher, *Ashleigh*, 2016, 1–7.

84. W. Luo, C. Bommier, Z. Jian, X. Li, R. Carter, S. Vail, Y. Lu, J. J. Lee and X. Ji, *ACS Appl. Mater. Interfaces*, 2015, **7**, 2626–2631.

85. J. Baek, H. M. Lee, J. S. Roh, H. S. Lee, H. S. Kang and B. J. Kim, *Microporous Mesoporous Mater.*, 2016, **219**, 258–264.

86. P. J. F. Harris, *Interdiscip. Sci. Rev.*, 1999, **24**, 301–306.

87. M. Inagaki, *Xinxing Tan Cailiao/ New Carbon Mater.*, 2009, **24**, 193–222.

88. D. Mitlin et al., *ACS Nano*, 2013, **7**, 5131–5141.

89. M. Sevilla, P. Valle-Vigon and A. B. Fuertes, *Adv. Funct. Mater.*, 2011, **21**, 2781–2787.

90. B. Sakintuna and Y. Yürüm, *Ind. Eng. Chem. Res.*, 2005, **44**, 2893–2902.

91. Y. Zhu, S. Murali, M. D. Stoller, K. J. Ganesh, W. Cai, P. J. Ferreira, A. Pirkle, R. M. Wallace, K. a Cychosz, M. Thommes, D. Su, E. a Stach and R. S. Ruoff, *Science*, 2011, **332**, 1537–1542.

92. G. S. Chai, S. B. Yoon, J.-S. Yu, J.-H. Choi and Y.-E. Sung, *J. Phys. Chem. B*, 2004, **108**, 7074–7079.

93. C. Péan, C. Merlet, B. Rotenberg, P. A. Madden, P. L. Taberna, B. Daffos, M. Salanne and P. Simon, *Energy Environ. Sci.*, 2014, **8**, 1576–1583.

94. R. Gokhale, S. M. Unni, D. Puthusseri, S. Kurungot and S. Ogale, *Phys. Chem. Chem. Phys.*, 2014, **16**, 4251–9.

95. Y. Tzeng, S. Yeh, W. C. Fang and Y. Chu, *Sci. Rep.*, 2014, **4**, 4531.

96. A. Moafi, J. G. Partridge, A. Z. Sadek and D. G. McCulloch, *J. Mater. Chem. A*, 2013, **1**, 402–407.

97. A. Nieto-Márquez, R. Romero, A. Romero and J. L. Valverde, *J. Mater. Chem.*, 2011, **21**, 1664.

98. L. Zhang, A. Aboagye, A. Kelkar, C. Lai and H. Fong, *J. Mater. Sci.*, 2014, **49**, 463–480.

99. R. Wenisch, R. Hübner, F. Munnik, S. Melkhanova, S. Gemming, G. Abrasonis and M. Krause, *Carbon*, 2016, **100**, 656–663.

100. M. Kruk, K. M. Kohlhaas, B. Dufour, E. B. Celer, M. Jaroniec, K. Matyjaszewski, R. S. Ruoff and T. Kowalewski, *Microporous Mesoporous Mater.*, 2007, **102**, 178–187.

101. B. Kwiecińska and H. I. Petersen, *Int. J. Coal Geol.*, 2004, **57**, 99–116.

102. R. J. Bowling, R. T. Packard and R. L. McCreery, *J. Am. Chem. Soc.*, 1989, **111**, 1217–1223.

103. B. Liu, H. Shioyama, T. Akita and Q. Xu, *J. Am. Chem. Soc.*, 2008, **130**, 5390–5391.

104. S. E. Skrabalak and K. S. Suslick, *J. Am. Chem. Soc.*, 2006, **128**, 12642–12643.

105. E. Frackowiak and F. Béguin, *Carbon*, 2001, **39**, 937–950.

106. C. Zhang, W. Lv, Y. Tao and Q.-H. Yang, *Energy Environ. Sci.*, 2015, **8**, 1390–1403.

107. L. L. Zhang, R. Zhou and X. S. Zhao, *J. Mater. Chem.*, 2009, **38**, 2520–2531.

108. A. G. Pandolfo and A. F. Hollenkamp, *J. Power Sources*, 2006, **157**, 11–27.

109. S. Komaba, W. Murata, T. Ishikawa, N. Yabuuchi, T. Ozeki, T. Nakayama, A. Ogata, K. Gotoh and K. Fujiwara, *Adv. Funct. Mater.*, 2011, **21**, 3859–3867.

110. S. W. Kim, D. H. Seo, X. Ma, G. Ceder and K. Kang, *Adv. Energy Mater.*, 2012,

2, 710–721.

111. D. Stevens and J. R. Dahn, *J. Electrochem. Soc.*, 2000, **147**, 1271–1273.

112. P. Viebahn et al., *Energy Policy*, 2013, **14**, 5–7.

113. M. R. Lukatskaya, B. Dunn and Y. Gogotsi, *Nat. Commun.*, 2016, **7**, 1–13.

114. T. Christen and M. W. Carlen, *J. Power Sources*, 2000, **91**, 210–216.

115. V. Johnson, *J. Power Sources*, 2002, **110**, 321–329.

116. P. Verma, P. Maire and P. Novak, *Electrochim. Acta*, 2010, **55**, 6332–6341.

117. M. D. Stoller and R. S. Ruoff, *Energy Environ. Sci.*, 2010, **3**, 1294–1301.

118. M. Mastragostino, F. Soavi and C. Arbizzani, *Adv. Lithium-Ion Batter.*, 2002, 481–505.

119. G. Madabattula and S. K. Gupta, *Comsol Conf.*, 2012.

120. P. Simon and Y. Gogotsi, *Nat. Mater.*, 2008, **7**, 845–854.

121. A. B. Cultura and Z. M. Salameh, 2015, pp. 876–882.

122. S. H. Aboutalebi, R. Jalili, D. Esrafilzadeh, M. Salari, Z. Gholamvand, S. A. Yamini, K. Konstantinov, R. L. Shepherd, J. Chen, S. E. Moulton, P. C. Innis, A. I. Minett, J. M. Razal and G. G. Wallace, *ACS Nano*, 2014, **8**, 2456–2466.

123. H. Chen, J. Jiang, L. Zhang, H. Wan, T. Qi and D. Xia, *Nanoscale*, 2013, **5**, 8879–8883.

124. P. Sun, X. Zhou, C. Wang, K. Shimanoe, G. Lu and N. Yamazoe, *Appl. Mater. Interfaces*, 2013, **6**, 12031−12037.

125. L. Yu, L. Zhang, H. Bin Wu and X. W. D. Lou, *Angew. Chemie*, 2014, **126**, 3785–3788.

126. W. Wei, X. Cui, W. Chen and D. G. Ivey, *Chem. Soc. Rev.*, 2011, **40**, 1697–1721.

127. G. P. Wang, L. Zhang and J. J. Zhang, *Chem. Soc. Rev.*, 2012, **41**, 797–828.

128. D. Ghosh, J. Lim, R. Narayan and S. O. Kim, *ACS Appl. Mater. Interfaces*, 2016, **8**, 22253–22260.

129. F. Wang, S. Xiao, Y. Hou, C. Hu, L. Liu and Y. Wu, *RSC Adv.*, 2013, **3**, 13059.

130. W. G. Pell and B. E. Conway, *J. Power Sources*, 2004, **136**, 334–345.

131. P. Yang, Y. Ding, Z. Lin, Z. Chen, Y. Li, P. Qiang, M. Ebrahimi, W. Mai, C. P. Wong and Z. L. Wang, *Nano Lett.*, 2014, **14**, 1–6.

132. K. Chiang, S. Zhang and G. Z. Chen, *Nano*, 2008, **1513**, 2008–2008.

133. R. Vali, A. Laheaar, A. Janes and E. Lust, *Electrochim. Acta*, 2014, **121**, 294–300.

134. X. Zhang, X. Wang, L. Jiang, H. Wu, C. Wu and J. Su, *J. Power Sources*, 2012, **216**, 290–296.

135. C. Zhao and W. Zheng, *Front. Energy Res.*, 2015, **3**, 1–11.

136. R. D. McKerracher, C. Ponce de Leon, R. G. a. Wills, a. a. Shah and F. C. Walsh, *Chempluschem*, 2015, **80**, 323–335.

137. R. Marom, S. F. Amalraj, N. Leifer, D. Jacob and D. Aurbach, *J. Mater. Chem.*, 2011, **21**, 9938.

138. S. Nejad, D. T. Gladwin and D. A. Stone, *J. Power Sources*, 2016, **316**, 183–196.

139. M. A. Kiani, M. F. Mousavi and M. S. Rahmanifar, *Int. J. Electrochem. Sci.*, 2011, **6**, 2581–2595.

140. Y. Wang and G. Cao, *Adv. Mater.*, 2008, **20**, 2251–2269.

141. F. Wang, R. Robert, N. A. Chernova, N. Pereira, F. Omenya, F. Badway, X. Hua, M. Ruotolo, R. Zhang, L. Wu, V. Volkov, D. Su, B. Key, M. Stanley Whittingham, C. P. Grey, G. G. Amatucci, Y. Zhu and J. Graetz, *J. Am. Chem. Soc.*, 2011, **133**, 18828–18836.

142. W. J. Zhang, *J. Power Sources*, 2011, **196**, 13–24.

143. L. Ji, Z. Lin, M. Alcoutlabi and X. Zhang, *Energy Environ. Sci.*, 2011, **4**, 2682.

144. N. Yabuuchi, K. Kubota, M. Dahbi and S. Komaba, *Chem. Rev.*, 2014, **114**, 11636–11682.

145. Y. Cao, L. Xiao, M. L. Sushko, W. Wang, B. Schwenzer, J. Xiao, Z. Nie, L. V. Saraf, Z. Yang and J. Liu, *Nano Lett.*, 2012, **12**, 3783–3787.

146. A. J. Bard and L. R. Faulkner, *Electrochemical Methods Fundamentals and Applications*, John Wiley &Sons, INC., New York, 1944.

147. J. O. M. Bockris and A. K. N. Reddy, *Modern Electrochemistry*, Kluwer Academic, New York, 1974.

148. J. O. Bockris, A. K. N. Reddy and M. Gamboa-Aldeco, *Modern Electrochemistry-Second Edition*, Kluwer Academic, New York, Second., 2002, vol. 86.

149. C. Largeot, C. Portet, J. Chmiola, P. L. Taberna, Y. Gogotsi and P. Simon, *J. Am. Chem. Soc.*, 2008, **130**, 2730–2731.

150. D. Hulicova-Jurcakova, M. Seredych, G. Q. Lu and T. J. Bandosz, *Adv. Funct. Mater.*, 2009, **19**, 438–447.

151. X. Wei, X. Jiang, J. Wei and S. Gao, *Chem. Mater.*, 2016, **28**, 445–458.

152. Y. J. Oh, J. J. Yoo, Y. Il Kim, J. K. Yoon, H. N. Yoon, J. H. Kim and S. Bin Park, *Electrochim. Acta*, 2014, **116**, 118–128.

153. F. Shen, H. Zhu, W. Luo, J. Wan, L. Zhou, J. Dai, B. Zhao, X. Han, K. Fu and L. Hu, *ACS Appl. Mater. Interfaces*, 2015, **7**, 23291–23296.

154. T. Yang, T. Qian, M. Wang, X. Shen, N. Xu, Z. Sun and C. Yan, *Adv. Mater.*, 2016, **28**, 539–545.

155. F. Shen, W. Luo, J. Dai, Y. Yao, M. Zhu, E. Hitz, Y. Tang, Y. Chen, V. L. Sprenkle, X. Li and L. Hu, *Adv. Energy Mater.*, 2016, **6**, 1–7.

156. J. R. Dahn, W. Xing and Y. Gao, *Carbon*, 1997, **35**, 825–830.

157. W. Xing, *Carbon*, 1997, **35**, 825–830.

158. K. Kubota and S. Komaba, *J. Electrochem. Soc.*, 2015, **162**, 2538–2550.

Chapter 2

Synthesis and characterization techniques

Various methods employed for the synthesis of carbon materials are presented and discussed in this chapter. An elaborate account of these methods and mechanisms involved in the carbonization process achieved through hydrothermal, microwave, CVD, laser carbonization and pyrolysis methods is illustrated in details. The second section of the chapter describes various characterization techniques like x-ray diffraction (XRD), Raman, X-ray photoelectron spectroscopy (XPS), BET, thermogravimetric analyses (TGA), electron microscopy which are very indispensable for carbon characterization. Finally, a detailed account of electrochemical methods like CV, charge-discharge and impedance measurements employed for performance monitoring of super capacitors and batteries is presented.

2.1 Synthesis of semi-graphitic high surface area activated and low surface area hard carbons.

Various techniques employed for the synthesis of semi-graphitic carbon are hydrothermal, microwave, laser, CVD, and high temperature pyrolysis. Among all these high temperature pyrolysis is considered to be a simple and economical route for the carbon synthesis. This synthetic strategy was exclusively employed in this doctoral work. Hence, after brief introductions to other methods this chapter presents more details about this pyrolysis process and its implications for the specific forms and properties of carbon obtained.

2.1.1 Hydrothermal synthesis method

Hydrothermal methods involve solution mediated syntheses carried out at high temperatures and high pressures, for crystallizing the substances from the solutions. The high pressure is maintained inside a closed vessel called autoclave which is specially designed to withstand such high pressures.[1–4] *Figure 2.1* shows the schematic of a typical autoclave. Under such high temperatures (well above the boiling points of solvents) most insoluble materials become soluble and participate in different reactions. For the solvents other than water the process is referred to as solvothermal synthesis. [5–8]

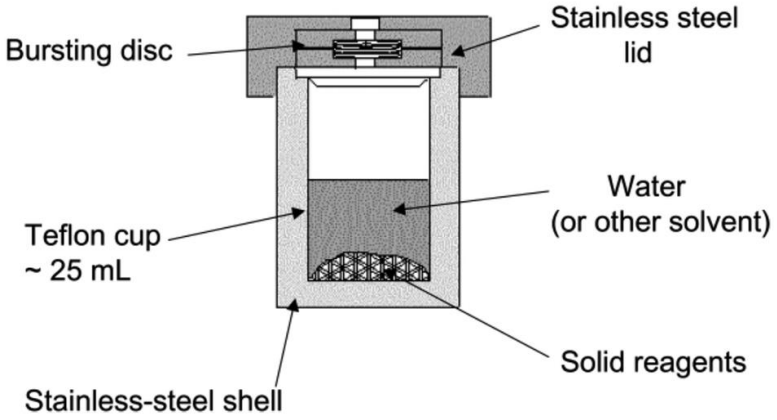

Figure 2.1 *The construction of a hydrothermal autoclave is shown here. A typical autoclave consists of a removable Teflon cup inside a stainless steel shell with tight fixable a stainless steel lid. {Reproduced with permission from Royal Society of Chemistry}*

Hydrothermal reaction may be utilized in two different ways for the synthesis of

nanonmaterials of different types. The first one may include the crystallization from a dispersion of already synthesized reaction products at high pressures inside the autoclave as in case of zeolites, SBA, MCM, other silicates and some transition metal oxides and sulphides. The other strategy may include the typical solution type reaction of practically water insoluble reactants. High temperature and pressure allows solubilization of the reactants and promotes the reaction. The advantage of hydrothermal carbonization also lies in the synthesis of larger crystals of substances below the melting point of a substance.[9–12]

Hydrothermal method applied to the synthesis of carbon materials is known as hydrothermal carbonization. The reactants of a hydrothermal carbonization reaction are

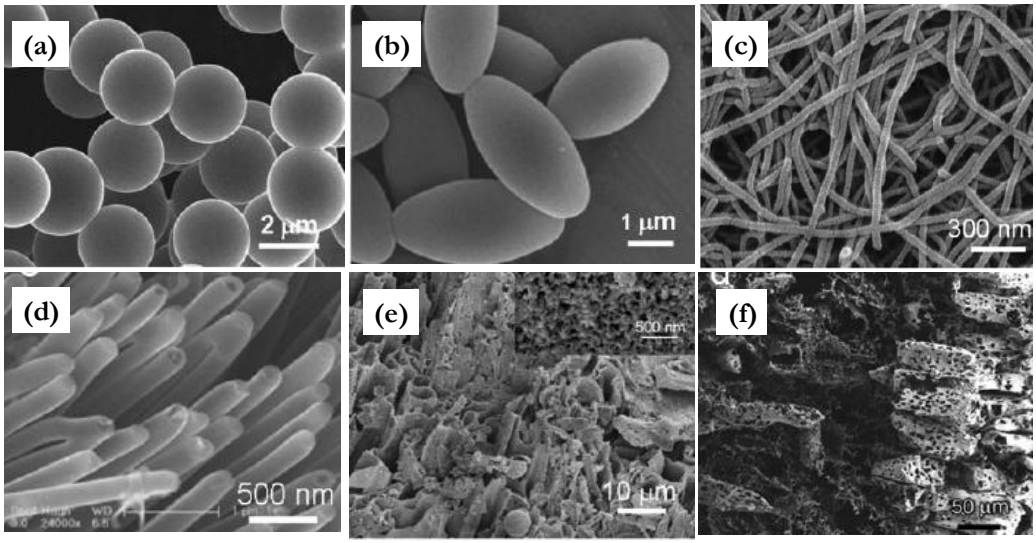

Figure 2.2 *Different morphologies of carbon materials obtained from hydrothermal carbonization. a) SEM image of spherical carbon particles.{Reprinted with permission from ref.*13*} b) SEM images of Olivine carbon particles.{Reprinted with permission from ref.* 14*} c) SEM image of a carbonaceous fibers.{Reprinted with permission from ref.* 15*} d) SEM images of carbonaceous nanotubes {Reprinted with permission from ref.* 16*} e) SEM image of hydrothermally treated oak leaf biomass.{Reprinted with permission of ref.*6*} f) SEM image of carbon scaffold.{Reprinted with permission of ref.*17*}*

sugars, cellulosic polymers, starches, waste matter and organic molecules. The high temperature and pressure inside a hydrothermal chamber promotes solubilization, initiates the melting of crystalline domains, speeds up the physical and chemical

interactions between the reactants. The undergoing chemical reaction like ionic, acid-base and polymerization type ultimately leads to precipitation of desired carbon product.[18–20] The hydrothermal reactions of carbon precursors (carbohydrates) are frequently carried out in presence of chemicals like *HCl, H_2SO_4, KOH, NaOH, Na_2CO_3*. These additives act as promoters and catalysts for dehydration and hydrolysis reactions which are indispensable for initial carbon backbone (Poly furfural alcohol) formation. *Figure 2.2* lists some interesting and useful hydrothermal carbon products with differing morphologies and thus differing applications. [7,21]

2.1.2 Microwave synthesis of carbon

Microwave synthesis has recently emerged as an energy efficient method for synthesis of various nanomaterials.[22] *Figure 2.3* shows the schematic of a typical microwave heater with its various components. Microwave method involves application of a high frequency electric/magnetic field to a system containing the electric/magnetic dipoles

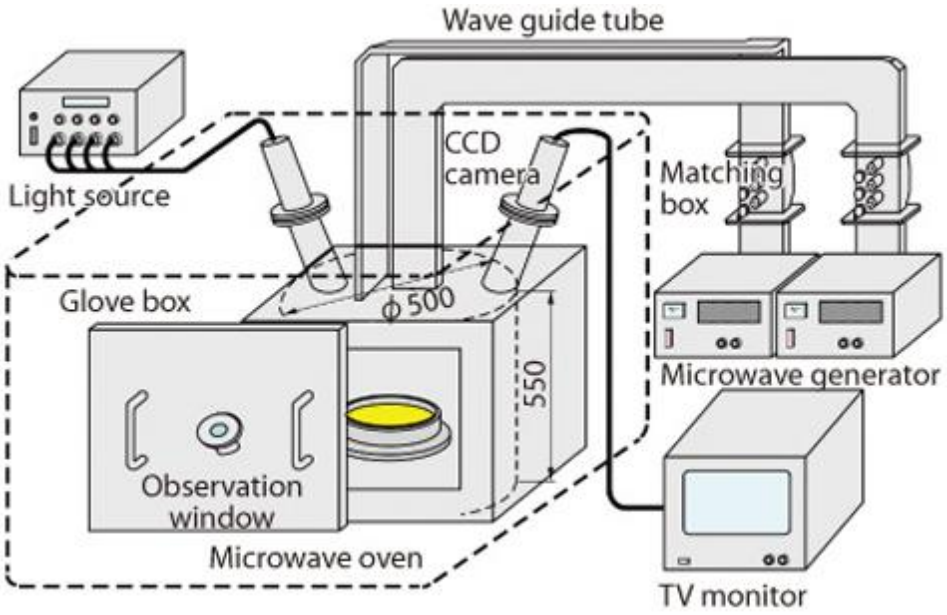

Figure 2.3 *A microwave heater with its functional parts is shown in this figure.*

{Source: http://peguc.com/diagrams-of-microwave-oven/}

and mobile charges like polar solvents, electrolytic solutions and molten salts. The allied phenomenon of dipole rotation (electric /magnetic) and ionic conduction brings about the conversion of applied electric energy to heat energy and hence gives a heating

effect. This heating mechanism involves dielectric, magnetic and conduction losses. The ability of a material to absorb microwave dictates the influence of heating effect on it. Microwave irradiation offers a uniform heating strategy unlike the conventional heating where conduction of heat occurs across the boundaries. Further high temperature can be achieved almost instantly and thus the rate of reaction shows a marked enhancement. Moreover the low reaction time scales enable us to perturb the nano level synthesis without using capping agents. Microwave strategy for the synthesis of various types of metal oxides (ZnO,TiO_2, CeO_2) sulphides, and other one dimensional structures is already well documented.[23–25]

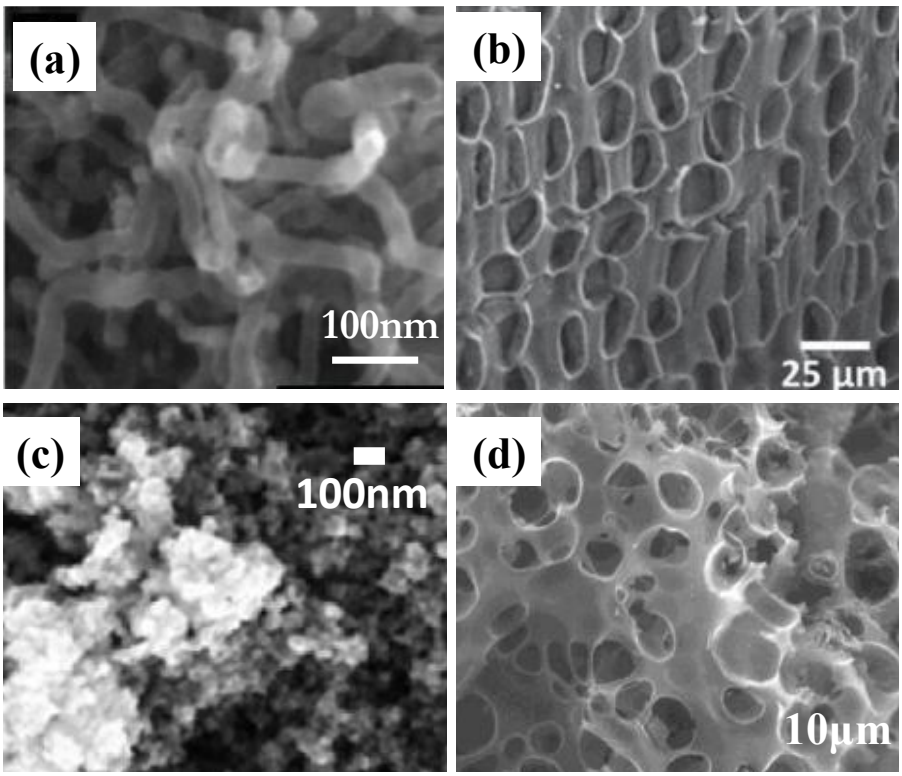

Figure 2.4 *SEM micrographs of carbon materials synthesized by microwave method. a) SEM image of CNT synthesized f by microwave method from graphene.{Reprinted with permission from ref.*26*} b) The porous carbon obtained by microwave assisted chemical activation of pineapple peels.{Reprinted with permission of ref.*27*} c) SEM images of carbon xerogels obtained by chemically activation for 6 min.{Reprinted with permission from ref.*28*} d) SEM images of hierarchically porous activated carbon obtained from lignite by microwave method.{Reprinted with permission from ref.*29*}*

Microwave assisted carbonization of polymer precursors, biomass and carbohydrates

has also lead to very interesting and functional morphologies. Precursors in different states (liquid, solid or gas) have been converted to carbon materials with different morphologies by application of microwaves. Synthesis of some refined varieties of carbon like CNT, graphene, fullerenes, carbon fibers, graphene carbon composites, carbon spheres, carbon dots and carbon nanocapsules is successfully demonstrated. Syntheses of porous carbons which are considered as back bone of energy storage technology have also been reported. For the synthesis of porous carbons by microwave process, chemical activating agents and cheap biomass precursors (palm branches, pineapple peel, orange peel, sunflower seed shells) after proper mixing have been subjected to microwave , following initial furnace treatment.[26,28–31] *Figure 2.4* shows some of the interesting carbon morphologies synthesized by microwave method.

2.1.3 Chemical vapor deposition (CVD)

Chemical vapor deposition is an industrial synthesis technique for the synthesis of carbon materials like graphene, CNT, diamond, carbon films, and porous carbons. CVD involves the decomposition of organic molecules on the surface of a catalyst/catalytic substrate under high temperature in inert atmosphere. The reaction by-products are

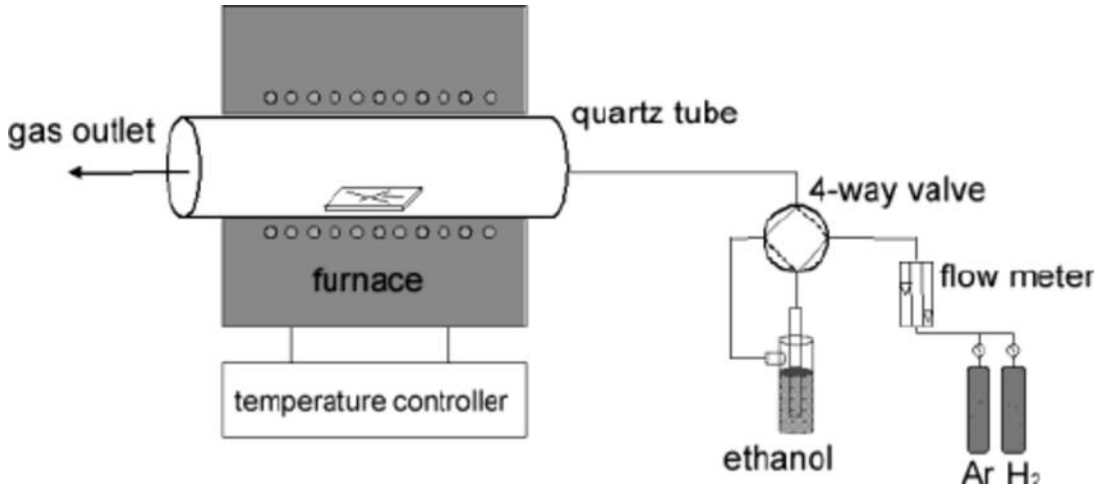

Figure 2.5 *Schematic of a CVD instrument. {Source: Journal of Physical Chemistry B}*

removed along with the gas flow. The different variants of CVD technique are plasma based plasma -enhanced CVD method, pressure mediated low pressure CVD method, and atomic layer deposition method. *Figure 2.5* shows the schematic of general CVD instrument.[32–37]

2.1.4 Laser based synthesis of carbon materials.

The laser based preparation method is a very exciting technique for the synthesis of carbon materials. The technique involves exposure of an organic molecule, a polymer or a biomass to the high energy laser for some short span of time. The local heating effect enforced on the carbon precursor leads to the removal of most of the non carbon atoms from the precursor by breaking their bonds with carbon and simultaneously initiates the formation of new carbon-carbon bonds which spreads in three dimensions to form the carbon back bone of nano/micro materials. The variety of carbon materials like SWCNTs, hydrophobic carbon films, diamond like carbon phase, graphene and carbon dots are reported to have been synthesized by this procedure.

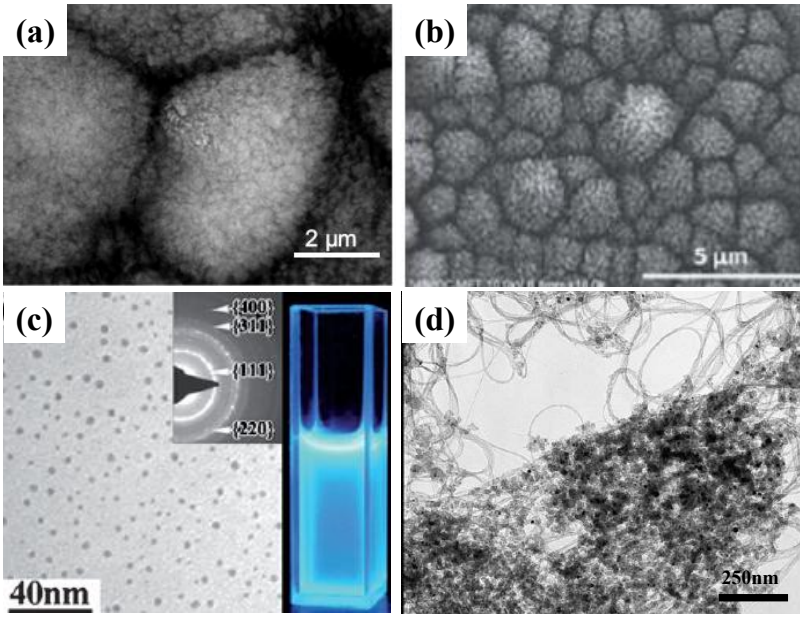

Figure 2.6 *Different carbon materials synthesized by laser irradiation. a) SEM image of diamond like carbon phase synthesized from graphite suspension. {Reprinted with permission of ref.*38*} b) SEM of broccoli type super hydrophobic carbon synthesized from DCB irradiation. {Reprinted with permission of ref.*39*} c) TEM image of fluorescent carbon nanodot synthesized from graphite suspension.{Reprinted with permission of ref.*40*} d) TEM image of SWCNT synthesized by irradiation of 20 kHz excitation laser on cylindrical graphite target. {Reprinted with permission of ref.*41*}*

Lasers with varying wavelength, energy density and power density have been employed for achieving the appropriate heating. *Sheng-Liang Hu* et al. report the use of Nd:YAG laser of 1064 nm and power density of 6×10^6 Wcm^{-2} for synthesis of carbon dots from

a graphitic suspension. While as Rohan et al. use KrF excimer of λ=248 nm, energy density of 170 mJ cm^{-2} and pulse duration 20ns for the synthesis of broccoli type hydrophobic carbon films from the DCB in liquid state irradiation process.[38–41]

2.1. 5 Pyrolysis based synthesis

Pyrolysis is a high temperature and inert atmosphere chemical reaction of organic carbonaceous precursors including simple organic molecules, synthetic and natural polymers as well as biomass to yield carbonaceous materials like charcoal, coke, char, porous activated carbons and other soft and hard carbons.[42–44] Pyrolysis process involves breaking of carbon heteroatom bonds and evaporation of heteroatoms from the carbon backbone which ultimately leads to formation of carbon materials possessing negligible number of carbon heteroatom bonds. As the carbon is the ultimate product, the process is also called as carbonization. The carbonization starts above 250^0C and full carbonized products can be achieved above 500^0C.[45–49] For achieving sufficient conductivity, temperatures above 800^0C-1000^0C are found to be instrumental. The

Figure 2.7 *Picture of tube furnace used for high temperature pyrolysis.*

{Source: http://www.mtixtl.com/1200CSplitTubeFurnacewithVacuumFlanges-OTF-1200X-4-HNGUL.aspx}

pyrolysis reaction is carried out in special furnaces called tube furnaces. The furnace has a programmable temperature control unit. There is an inlet for inert gas inflow and an outlet for inert gas outflow. Out flow of the inert gas carries with it the other gaseous products generated during pyrolysis reaction, which is very important for

subsequent steps.

Synthesis of porous carbons can be achieved by tailoring the basic pyrolysis process in different ways. Porosity can be generated in the carbon materials by the use of either activation agents or by the use of templates during pyrolysis process. [50,51]The activating agents etch the carbon atoms from the developing graphitic skeleton resulting atomic defects which ultimately aggregate and lead to formation of pores. Activation process can be carried out by use of physical agents like vapor (H_2O) and CO_2 the process is thus called as physical activation. The chemical activation is achieved by mixing the activating agent with the carbon precursor and then pyrolysis reaction is carried out. Upon removal of activation by-products with mineral acids or bases activated carbon product is obtained. The commonly used chemical activation agents (porogens) used for carbon activation are KOH, NaOH, $ZnCl_2$ and H_3PO_4. The representative example of KOH mediated chemical activation mechanism is presented below through a chemical reaction.[52–56]

$$\mathbf{6KOH + 2C \longrightarrow 2K + 3H_2 + 2K_2CO_3}$$

The process of activation reaction thus carried out by the addition of an external activating agent is called ex-situ activation. The other form of chemical activation process includes use of K and Na organic salts directly as precursors, the pyrolysis of which leads to porous carbons, as in case of *poly(4-styrenesulfonic acid-co-maleic acid) sodium salt.* [57]

Other pyrolysis strategy for synthesis of porous carbon materials is the use of template during pyrolysis process. It is much of a physical barrier mediated synthesis than chemical one. The templates possess interconnected pores which can be filled by carbon precursors to the extent of complete infiltration. The carbonization of precursor inside the template followed by template decomposition leads to porous carbon which is a negative replica of the template. The different templates that have been used so far can be categorized into hard and soft templates. The commonly used soft templates are organic molecules and polymers which decompose at certain high temperature because of their thermal instability. As the precursor material loaded in porous soft template is pyrolysed the former carbonizes and once the carbonization is achieved the later is

allowed to decompose by shifting to higher temperature that are suitable for its complete decomposition. Thus after completion of pyrolysis process the carbonaceous negative replica of template is generated which possesses pore structure complementary to the template.[58,59] Hard template pyrolysis on the other hand is a more common templating strategy than the soft template pyrolysis for porous carbon synthesis. The principle of hard templating is similar to soft template except that the hard template is temperature stable in organic material and for releasing the carbon from the template chemical dissolution of template is carried out. The commonly used hard templates include calcium carbonate, zeolites, MCM, SBA, KIT etc. These templates readily dissolve in HF and hot aqueous alkalis and thus are suitable for the porosity generation in the carbon materials.[51,60,61]

The synthesis of low surface area hard carbons on the other hand can be achieved by direct pyrolysis of carbon precursors of types mentioned above or by the direct pyrolysis of hydrothermally pretreated carbon precursor. Temperatures in the range of 1000^0C-1200^0C give preferred results. *Figure 2.8* compares the morphologies of different types of turbostratic carbons synthesized by pyrolysis method.[62–68]

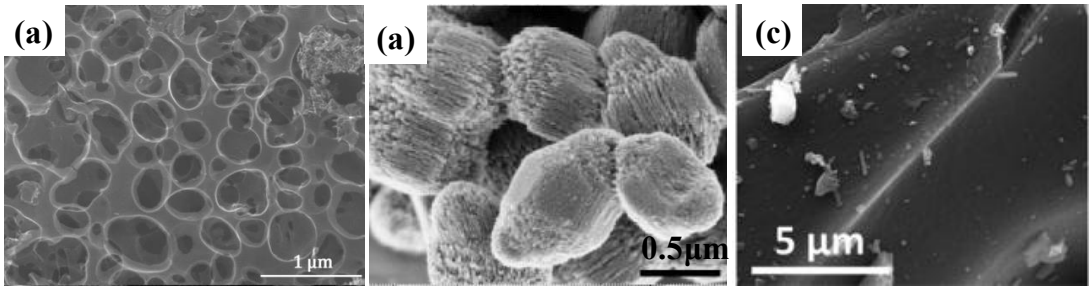

Figure 2.8 *The SEM images of carbon material synthesized by pyrolysis method is shown here, a) SEM image of KOH activated paper derived carbon.{Reprinted with permission of ref.*69*} b) SEM image of mesoporous carbon derived from cyanamide by SBA-15 mediated template pyrolysis. {Reprinted with permission of ref.*70*} c) Hard carbon derived from a biomass precursor by direct pyrolysis. {Reprinted with permission of ref.*71 *}*

2.2 Characterization Techniques

2.2.1 Powder X-ray diffraction (PXRD)

X-ray diffraction is the first go to and a trusted tool for gaining information about the crystal structure. Diffraction of X-ray by a crystal was observed for the first time by Max Van Lau in 1912 and later Bragg's proposed its use as a technique for complete crystal analysis. The principle of X-ray diffraction is that the scattering of X-rays by the atoms generate a diffraction pattern (atomic separation being comparable to X-ray wavelength) corresponding to a particular arrangement of scattering atoms.[72–74] As the atomic arrangements and inter-atomic separations vary from crystal to crystal, diffraction patterns are also expected to be different for different crystals. The mathematical modeling by Bragg's through their famous Bragg's law enabled the X-ray diffraction to be used as a trustworthy tool.[72,74]

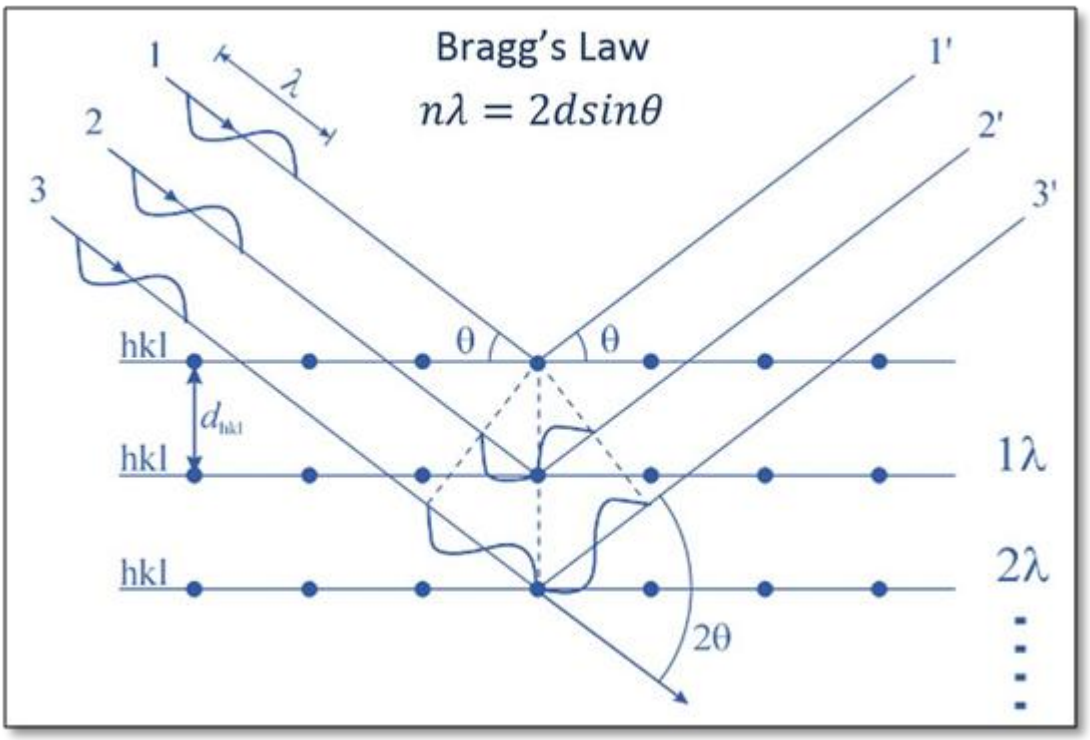

Figure 2.9 *Principle of X-ray diffraction being depicted schematically.*[75]

(Source:www.veqter.co.uk/residual-stress-measurement/x-ray-diffraction1)

Bragg's model contemplates the atoms of crystal to form one atom thick planes going through the crystal in all possible directions (*h,k,l)* as shown in *figure 2.9.*[75] Any set of parallel planes when hit by an X-ray beam falling at them at certain angle would diffract it at similar angle and the condition of constructive interference would demand the following equality called Braggs law:

$$n\lambda = 2dsin\theta \qquad \text{..... } 2.1$$

where n is order of diffraction, λ is wavelength of X-ray used (usually 0.154nm corresponding to Cu-Kα radiation) and d is interplanar separation. Considering the bright spots as products of first order reflection and knowing the wavelength of X-ray being used the only variable d can be deduced from Bragg's equation.[72–74]

There are two ways in which the X-ray diffraction data can be collected from a crystalline material. The first one being the single crystal XRD where a single micron size crystal is irradiated with X-rays and diffraction pattern of the whole crystal is acquired by rotation of sample, and stage as shown in *figure 2.10.* Although more

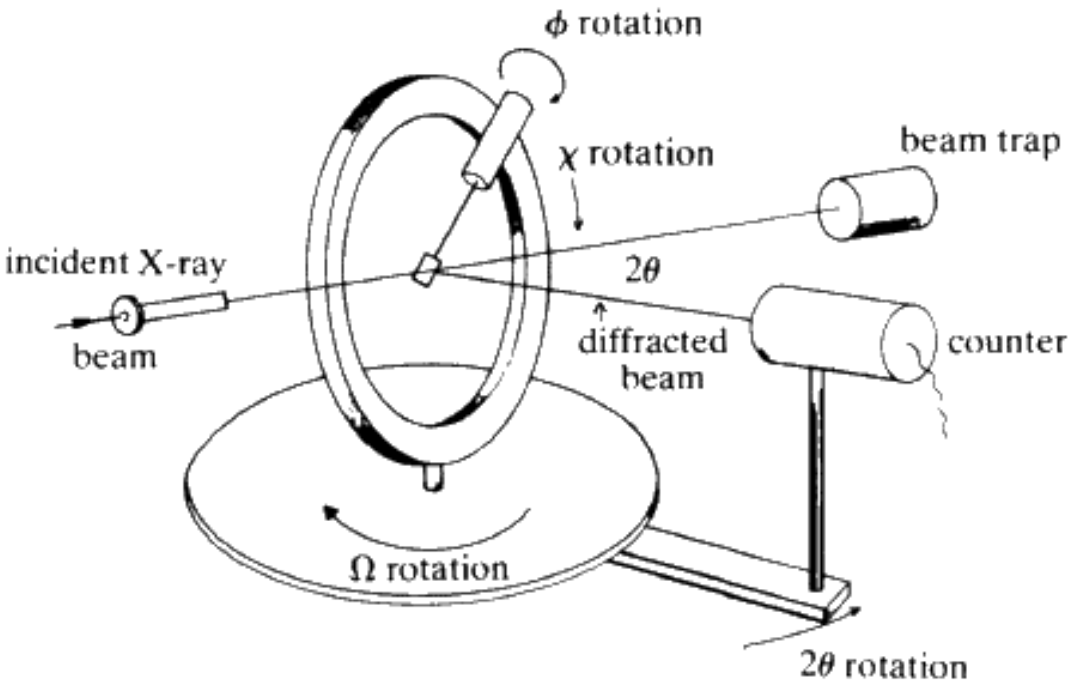

Figure 2.10 *Four circle diffractometer with four possible rotations to collect reflections from all planes.*

(Source:http://d32ogoqmya1dw8.cloudfront.net/images/research_education/geochemsheets/techniques/IUCrimg69.v2.gif)

accurate, no standards required and having the benefit of being ideal for 3D analysis of crystals; single crystal XRD suffers from some limitations like requirement of a large single crystal, optical clarity and large time for data collection. This forces a material scientist to go for the other more feasible and widely used method called powder method that requires fewer technicalities and data delivery is also rapid. The basic principle of the powder method is same as single crystal but differs in the instrument and experimental design as brought out in *figure 2.11a.* The monochromatic XRD beam is set incident to the sample which is in a powder form (randomly oriented planes) and incident beam angle with detector is scanned from 0^0 to 90^0 which brings all the oriented planes into play.

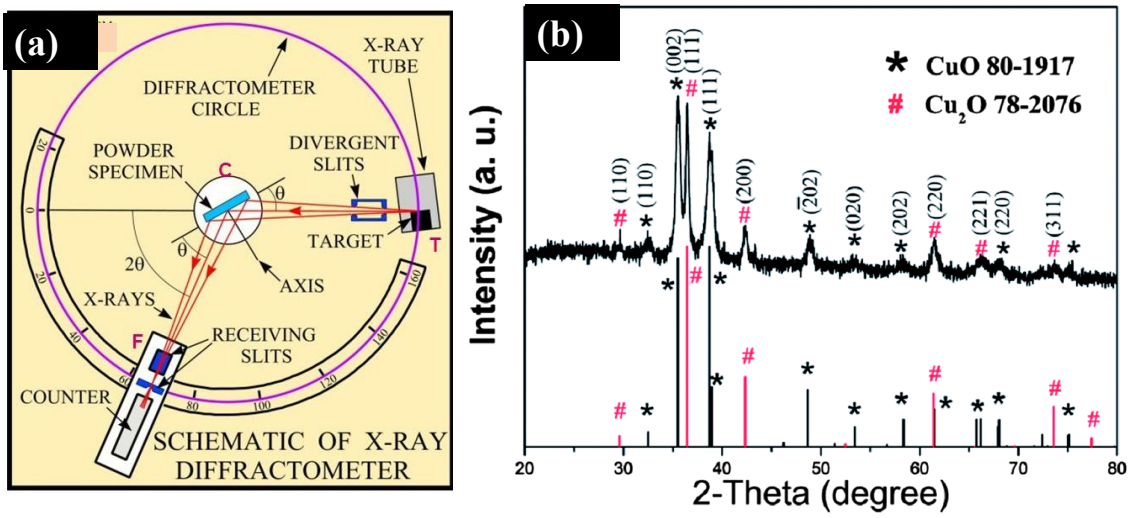

Figure 2.11 a) *Schematic of PXRD diffractometer with movable beam and detector. {Source: pubs.usgs.gov/of/2001/of01-041/htmldocs/xrpd.htm} b) Powder XRD pattern of CuO-Cu_2O hollow polyhedrons. {Reprinted with permission of ref* .11*}*

The intensity peaks at an angle which satisfies to $n\lambda=2d\sin\theta$ for any set of possible planes existent in the sample. The data collected from the powder method requires to be referenced with the standard data base available to us and is considered as the finger print of the material. A typical powder XRD graph plots intensity vs. angle between incident beam and diffracted beam expressed as 2θ and shown in *figure 2.11b.*[72–74]

Other valuable information available from the powder XRD pattern is crystallite size which is reflected in broadening of an XRD peak. The diffraction peaks broaden for the

crystallites of very small size and becomes prominent at nanolevel. The decoding the crystallite dimensions from peak broadness are achieved by a famous equality called Scherrer formula.

$$t = \frac{0.9\lambda}{\beta cos\theta} \quad \text{..... (2.2)}$$

where t is dimension of a crystallite , λ is the wavelength of X-ray, β is full width half maximum of a broadened peak.[74,76]

2.2.2 Raman spectroscopy

Raman spectroscopy is a scattering technique which entails an inelastic scattering of photons by chemical systems like molecules, polymers or crystals to obtain the information about the bonding and crystal structure. When a beam of electromagnetic radiation especially in visible or ultraviolet region is impinged on a material it can get scattered if specimen has electronic energy levels or bands that are energetically not

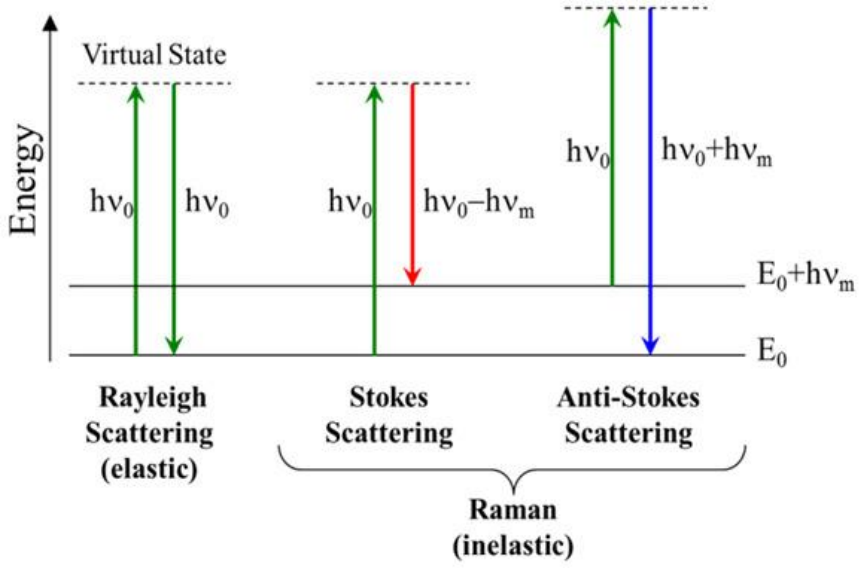

Figure 2.12 *The quantum energy transition for Rayleigh scattering and Raman scattering is depicted in this Jablonski diagram. {Reprinted with permission from ref.*77*}*

appropriately placed to absorb the frequency. The scattered beams can be of two types, the one with the same energy as the incident beam is referred to as elastic scattering or Rayleigh scattering and the other with different energy than incident beam is referred to as inelastic scattering. Inelastic scattering can be of Stokes type, if scattered light has lesser frequency than the incident light and anti Stokes if scattered light has higher

frequency than incident light.[78,79] Rayleigh scattering and Raman scattering with its Stokes and Anti-Stokes lines is depicted in *figure 2.12*.[79] The energy differences between the incident and scattered beam of light which is called as Raman shift is of the order of IR frequency ($100cm^{-1}$- $4000cm^{-1}$) and results from vibrational excitations and de-excitations accompanying the scattering phenomenon.

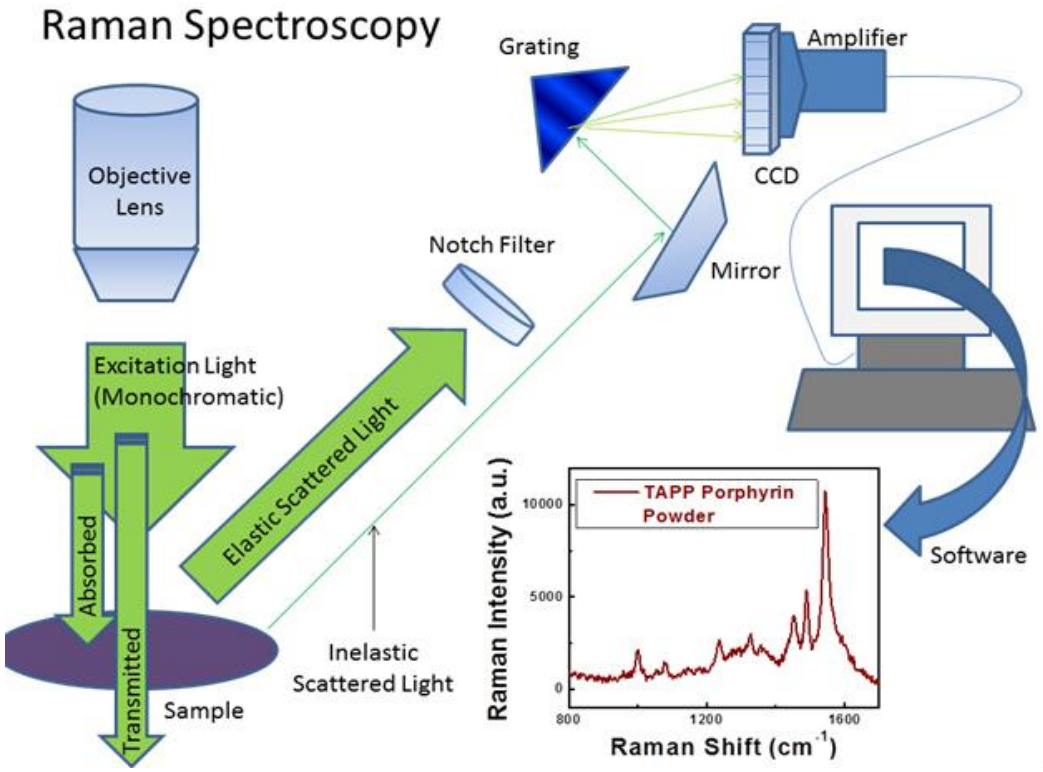

Figure 2.13 *Schematic showing working of a Raman instrument.*
(https://www3.nd.edu/~kamatlab/facilities_spectroscopy.html)

The selection rule for Raman activity is that the chemical species should be able to change the electric polarizbility with respect to vibronic co-ordinates upon irradiation. All molecules and crystal modes having permanent dipole moment are devoid of any Raman activity. Additionally the power of scattered radiation (P_S) is directly related with the intensity of incident light I_0 as $P_S = K I_0/\lambda^4$. Thus high intensity lasers are to be used as source of incident radiation than normal visible or UV radiation. *Figure 2.13* demonstrates the working of a Raman spectrometer with different types of filters to cut out the elastically scattered photons and to increase the sensitivity.[78]

Domain of Raman spectroscopy is much broader and is not restricted to molecular analysis only.[78,80–82] The lattice phonons of appropriate symmetry (polarizbility change should accompany the lattice vibrations) also equally interact with the visible /UV light to modify its frequency and thus sanctions their characterization by this technique. Scattered radiations form crystals can furnish information about the composition, crystal structure, electronic information (band gap) and magnetic properties. Traditional Raman spectroscopy and its modern variants like *SERS, RRS* have been used extensively for characterization of metal oxide,[83] metal sulphide especially transition metal oxides like TiO_2, ZnO,MoS_2, WS_2 etc. [84–87]

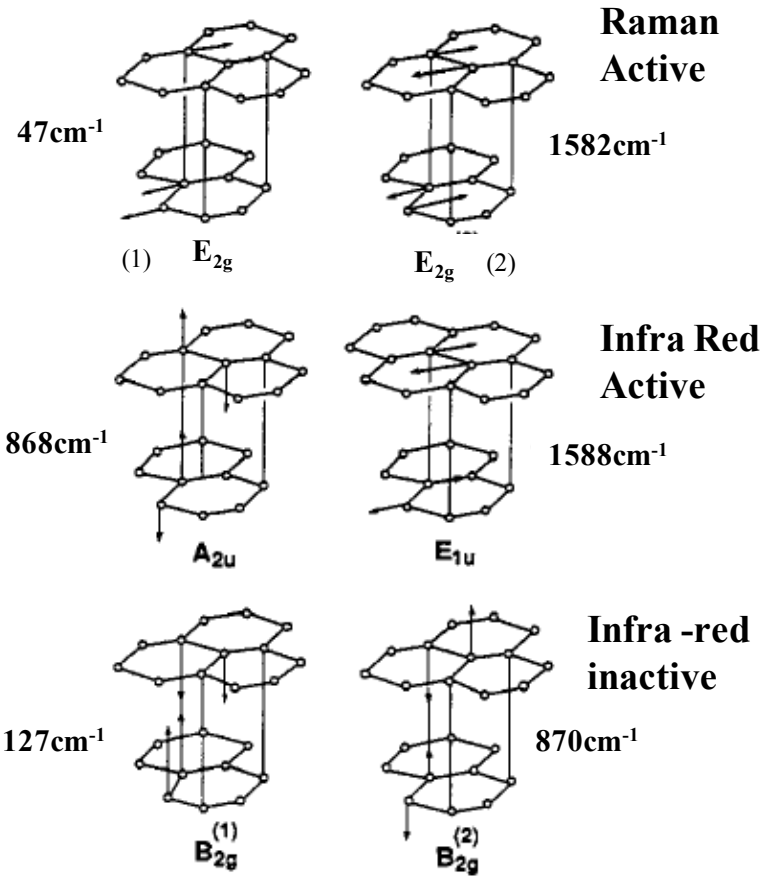

Figure 2.14 *Vibrational modes of single crystalline graphite.{Reprinted with permission of ref.*88*}*

The Raman spectroscopy being sensitive to covalent bonds of no or less dipole moment the carbon materials become the prime subjects of Raman analysis. Raman spectroscopy is able to reveal the slightest structural differences, making it a valuable

technique for carbon materials which are subject matter of this thesis. *Figure 2.14* lists various normal modes of graphite with E_{2g} (2) being the Raman active mode which is responsible for G-band of graphite.[88–91] Thus G-band results from the in-plane vibrations of graphene sheets of graphite. The Raman spectra of other bulk and nano

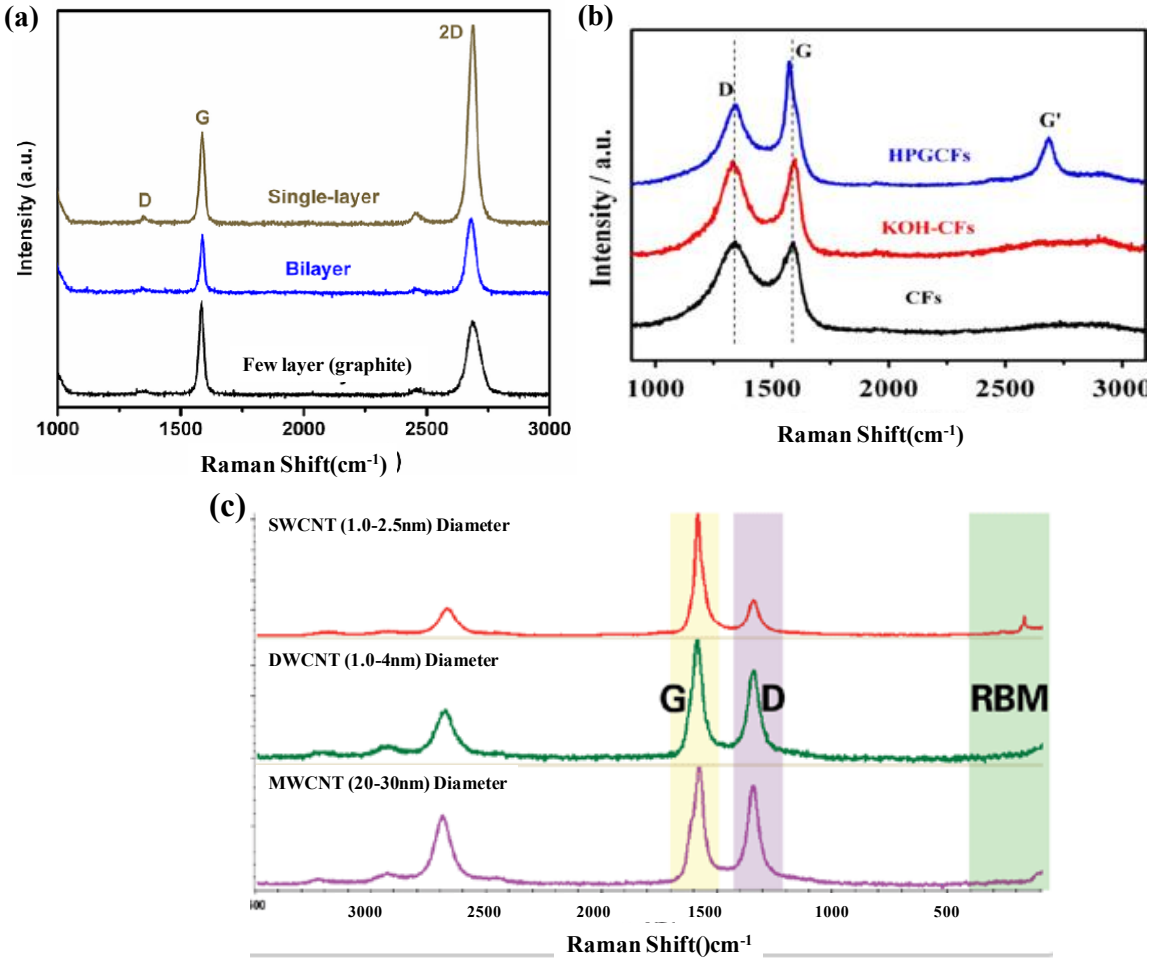

Figure 2.15 *Raman bands of graphene and its potential derivatives like CNTs , and graphite is shown here. a) Shows the evolution of Raman spectra on moving from single layer graphene towards graphite. {Reprinted with permission of ref.*92 *} b) Raman spectra of Carbon fibers (CFs), KOH activated carbon fibers (KOH-CFs) and Na activated hierarchical porous graphitic carbon fibers (HPGCFs). {Reprinted with permission of ref.* 93*} (c) Raman spectra of single, double and multi walled CNTs. {Source:open google source}*

forms of carbon which are considered to be derivatives of graphite shows emergence of some other peaks because of relaxation of selection rules and development of local structures on account of structural faults introduced therein. One such band is D-band

($1300cm^{-1}$-$1350cm^{-1}$) which shows up in the Raman spectra of semi-graphitic turbostratic carbons, defective graphenes and modified graphenes as shown in *figure 2.15*. 2D is second prominent Raman band that shows up in the region of $2600cm^{-1}$-$2800cm^{-1}$ and is attributed to c-axis faults in graphite. The *figure 2.15* depicts the systematic evolution of Raman spectra for different carbon forms reflecting the structural deviations from mother graphene.[88–91,94,95]

2.2.3 BET surface area analysis

The basic principle behind the BET technique is the famous surface science theory propounded by Brunauer, Emmet and Teller regarding the adsorption of gas molecules on solid surface. BET theory proposed some serious modifications over the age old Langmuir monolayer adsorption theory to address the adsorption phenomenon adequately.[96–98] The modification proposed by the BET surface model over that of Langmuir model are:

1) Gas molecules adsorb on the surface in multiple layers and not in a monolayer as proposed by Langmuir theory.

2) The interaction between the adsorbed layers is negligible.

3) Langmuir theory can be applied to each layer.

The graphical representation of BET model can be represented as shown in *figure 2.16.*

The application of above modification to Langmuir theory with the added assumptions of 1) adsorption at well defined sites, 2) single point interaction of each site with the upper layer, 3) dynamic equilibrium between the upper layer and gas phase and 4) desorption is kinetically limited process leads to BET equation stated below:

$$\frac{1}{v\left[\left(\frac{P_0}{P}\right)-1\right]} = (c-1)/v_m c\left(\frac{P}{P_0}\right) + 1/v_m c \quad \text{..... (2.3)}$$

where P_0 and P are the saturation pressure and equilibrium pressure of the adsorbed gas at adsorption temperature, v is the quantity of gas adsorbed, v_m is the quantity of gas adsorbed for monolayer formation and c is the BET constant. The kinetic parameter c is given by following activation type of equation:

$$c = exp^{(E1-EL)/RT} \ldots\ldots (2.4)$$

where E_1 and E_L are the adsorption energies of first and subsequent layers.[96–98]

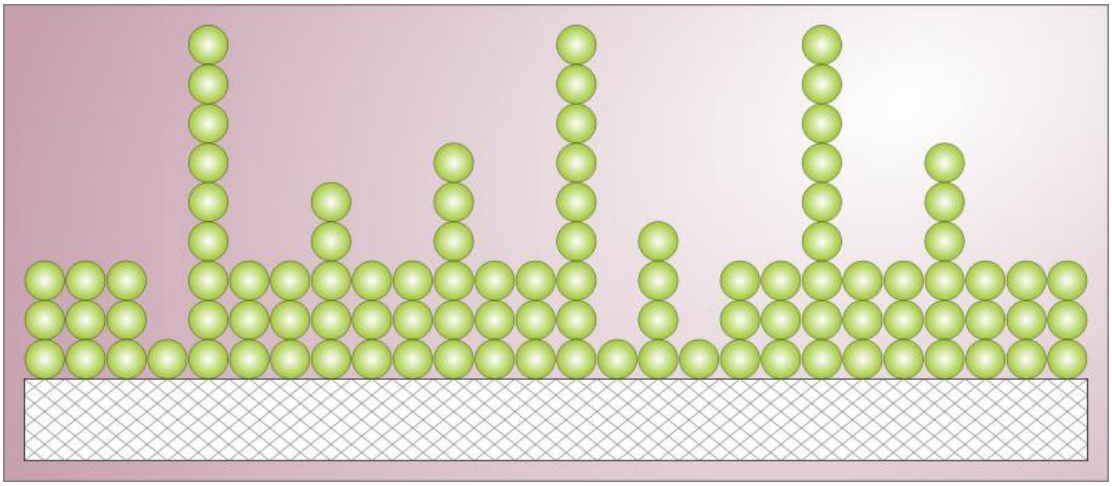

Figure 2.16 *BET model showing the multilayer adsorption of gas molecules on the solid surface. The random distribution of sites covered with different number of adsorbed molecules.* *(https://en.wikipedia.org/wiki/BET_theory)*

The plot of $\boldsymbol{v}$ vs. $\boldsymbol{P/P_0}$ is called as isotherm. The plot of $1/[v(P_0/P)-1]$ vs. (P/P_0) as *eq 2.3* will yield a straight line from the intercept and slope of which we can deduce v_m and use the following equations to calculate specific surface area and total surface area as:

$$\boldsymbol{S_t = Nsv_m/v} \text{ and } \boldsymbol{S_{BET} = S_t/a} \ldots. (2.5)$$

where S_t is total surface area occupied by gas, N is Avogadro number, s is the cross-sectional area of adsorbed gas molecule, V_m is the monolayer adsorbed volume and $\boldsymbol{a}$ is the total mass of the substance used for BET experiment.[96–98]

BET experiment is carried out at liquid nitrogen temperature (77K) and under these conditions the cross-sectional area of N_2 molecule ($0.162nm^2$) can be substituted for $\boldsymbol{s}$ in equation 2.5. *Figure 2.17* shows the construction and working design of a BET instrument. There are two operational procedures for BET, first one is known as single point BET which involves determining surface area by taking a single point on adsorption isotherm. On the other hand, multiple point BET involves the determination of surface area by taking into account minimum three points on adsorption isotherm.

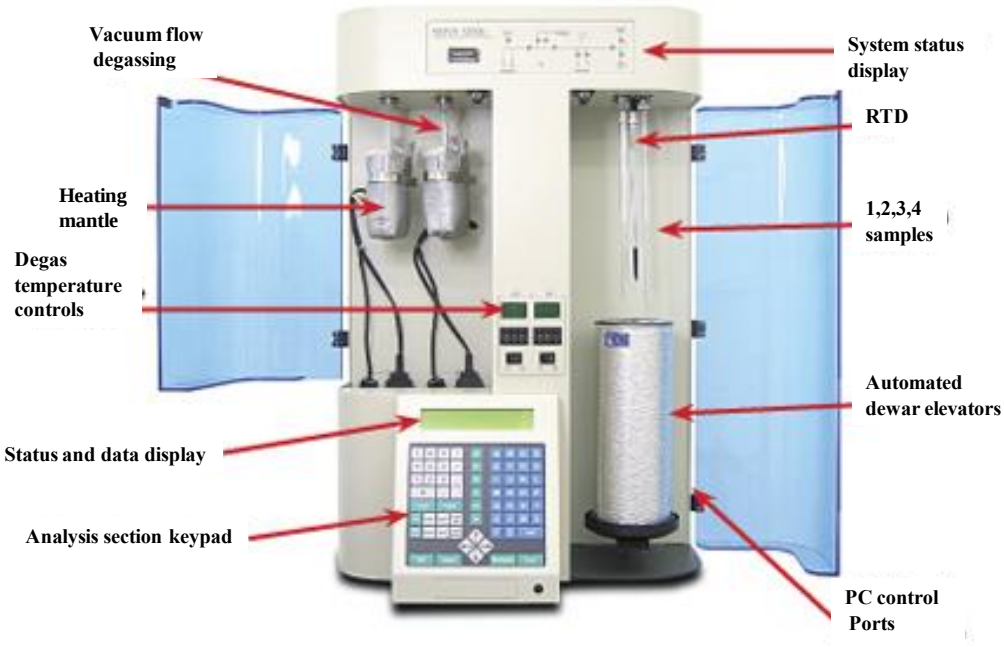

Figure 2.17 *BET Instrument with its various operational parts is shown in this figure.*

(http://www.quantachrome.com/gassorption/nova_series.html)

2.2.4 X-ray photoelectron spectroscopy (XPS)

XPS is surface analytical technique used extensively to characterize varieties of surfaces. The technique is also called as electron spectroscopy because of its working principle which involves energy analysis of photo ejected electrons. The ejection of electrons from atoms of sample by irradiation of light is called photo electric effect. The mathematical form of photoelectric effect can be stated as:

$$\boldsymbol{K.E = h\upsilon - \varphi - E_b} \ldots\ldots \textbf{(2.6)}$$

where h is Planck's constant, υ is frequency of incident X-ray light , ϕ is work function of metal, K.E is kinetic energy and E_b is binding energy of ejected electron. The working principle of XPS (photoelectric effect) is depicted in *figure 2.18.* As the inner shell electrons are knockout XPS promises to be sensitive and composition specific technique. In an XPS experiment K.E of ejected electron is measured and by using this value and further substituting the known values of ϕ, and hυ in *eq. 2.6*, the value of E_b can be acquired. *Figure 2.19* depicts the design of an XPS instrument. [98,99] The electrons ejected from the surface of the sample are made to travel through a

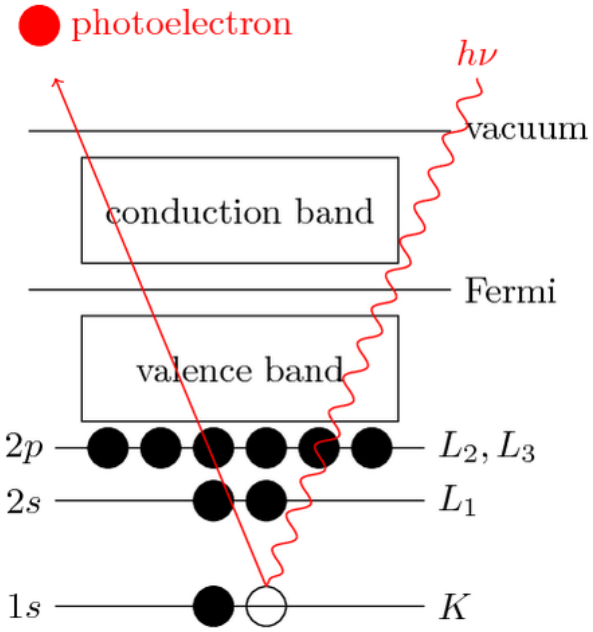

Figure 2.18 *Shows schematically of the principle of photoelectric effect and hence XPS.*

(http://www.texample.net/tikz/examples/principle-of-x-ray-photoelectron-spectroscopy-xps/)

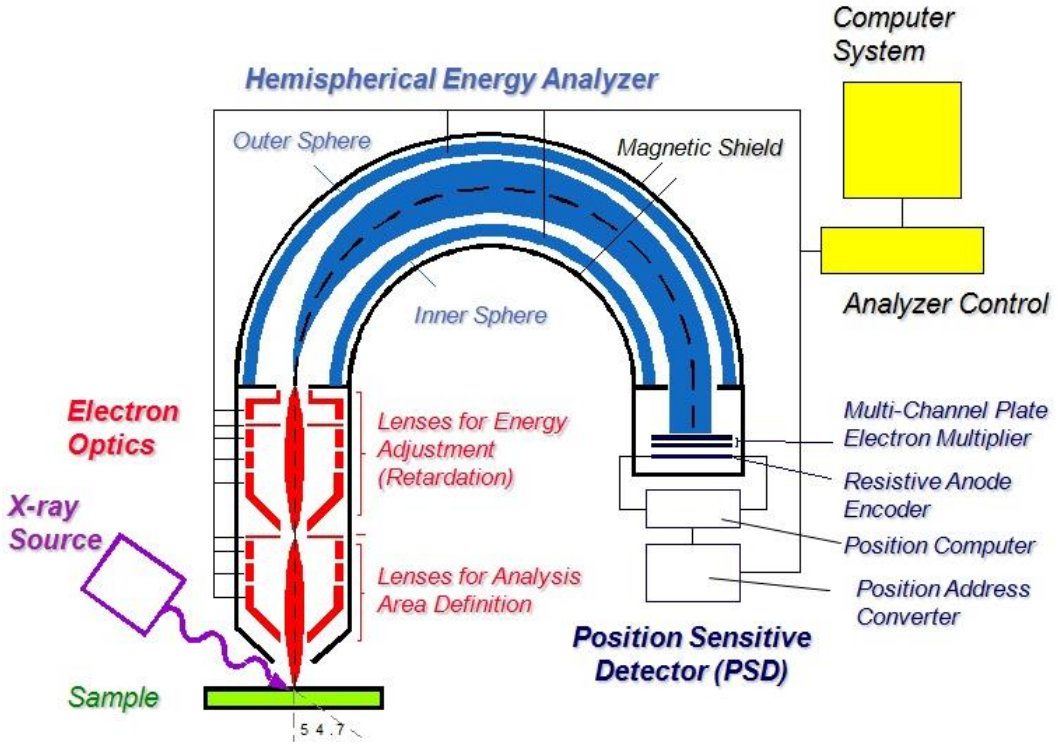

Figure 2.19 *Schematic showing the working of X-ray photo spectrometer.*

(*Reproduced from technical presentation for University of Pennsylvania, USA, © University of Pennsylvania)*

hemispherical energy analyzer by electromagnetic lenses towards the detector. The hemispherical analyzers act as energy filters and allow electrons of certain K.E only to pass through and get detected by position sensitive detectors through current multipliers located just before it. The ultra high vacuum (10^{-9}-10^{-11}) is maintained to ensure absence of energy loss events. X-rays of energy 1253.6 eV (Mg Kα) and 1486.6 eV (Al Kα) are used as incident source with which we can achieve the sample death of 10nm. XPS spectra is observed as peaks with each peak corresponding to an atomic orbital in the electron emission intensity vs. B.E plot as shown in *figure 2.20*. Further in case of orbitals with

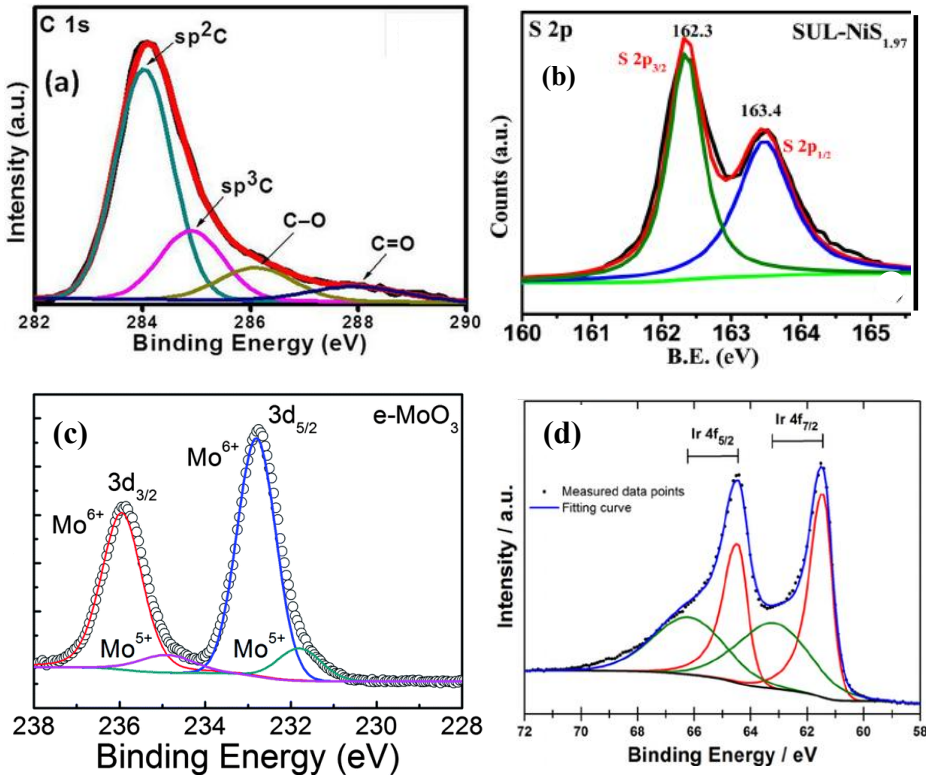

Figure 2.20 *Shows the XPS plots of different atoms in different chemical environments depicting spin orbital coupling. a) Shows the XPS spectra of carbon deconvoluted into different functional groups.{Reprinted with permission of ref.* 100*} b)Shows the XPS plot corresponding to 2p orbital of sulphur in NiS_2 showing spin orbital splitting into orbitals. {Reprinted with permission of ref.* 101*} c) XPS spectrum of 3d orbital of Mo of MoO_3 showing spin orbital splitting into orbitals. {Reprinted with permission of ref.* 102*} (d) XPS plot of 4f orbital of Ir, showing splitting into two orbitals. {Reprinted with permission of ref.* 103*}*

nonzero angular momentum quantum numbers (p, d, f) spin orbit coupling results in splitting of the spatial orbital peak into two spin orbit coupled peaks [($p_{1/2}$ and $p_{3/2}$), ($d_{5/2}$ and $d_{3/2}$) , ($f_{7/2}$ and $f_{5/2}$)] which shows up clearly in XPS spectra.[99]

2.2.5 Thermo gravimetric analysis (TGA)

Thermo gravimetric analysis is a technique used to study the thermal behavior of materials. Variety of chemical transformations like thermal decomposition, oxidation, and phase transformations can be studied with this technique. Thermal decomposition of polymers, metals and metal oxides, organic matter, plastics, glasses and carbon based compounds has successfully been studied using this technique. Besides, TGA can be helpful in elucidating reaction kinetics, mechanism and more commonly in elucidation of the organic content in inorganic materials. *Figure 2.21* shows the schematic of TGA instrument which also depicts its working principle. The main constituents include the balance, the furnace, temperature measurement device and the recording device for recording mass vs. temperature. The experiment can be carried out at different environments like Ar, N_2, O_2 etc.

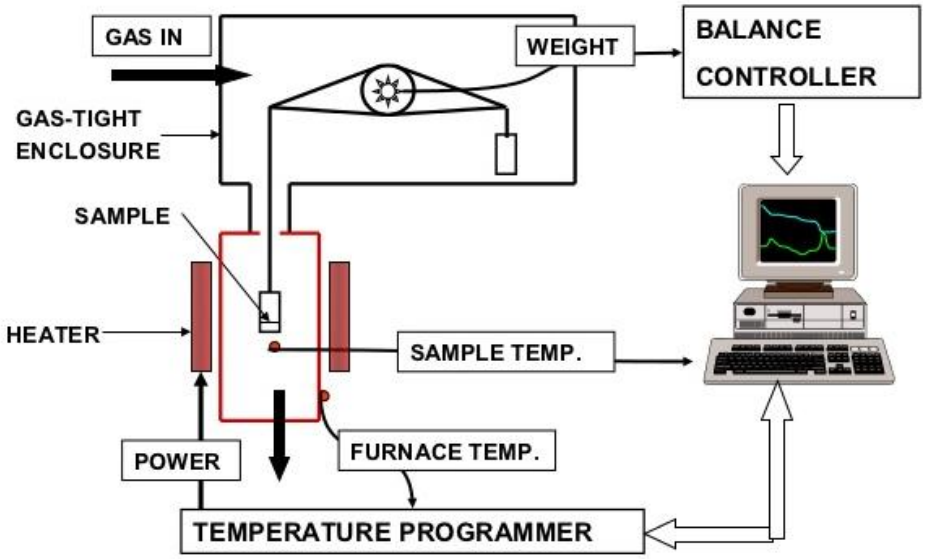

Figure 2.21 *The schematic of a TGA instrument showing its different constituents.*

{Copyright:D.M.Price@lboro.ac.uk (2006)}

Thus a *TGA* instrument measures the weight loss at different temperatures. A typical *TGA* graph plots the weight loss along the Y axis and temperature along the X axis. *Figure 2.22* shows a typical *TGA* plot of a rGO -TiO_2 in air.[104] It can be seen that in the composite case the weight loss at higher temperatures > 400^0C is greater than the bare TiO_2 which can be attributed to oxidation and evaporation of carbon into CO_2 and thus reduce the sample weight which is being recorded.[104–106]

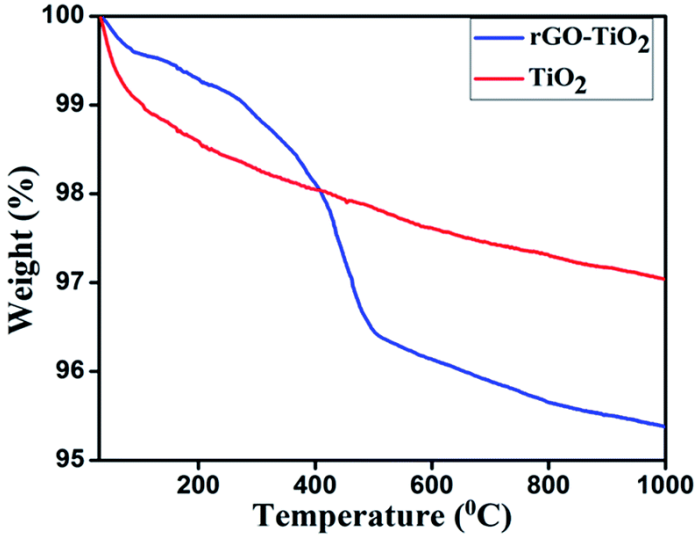

Figure 2.22 *Shows TGA plot of rGO-TiO_2 composite and bare TiO_2 in air. In the rGO-TiO_2 case larger weight loss is observed which corresponds to carbon %age in the composite. {Reprinted with permission from ref.*105*}*

2.2.6 Electron microscopy (EM)

The electron microscopy has emerged as most versatile technique for furnishing for structural and morphological information over a broad range of magnification. The two famous electron microscopy techniques namely scanning electron microscopy (SEM) and transmission electron microscopy (TEM) that have been used in this thesis extensively will be discussed in this sub section.

2.2.6.1 Transmission electron microscopy (TEM)

Transmission electron microscopy provides information at atomic scale by lattice imaging. Resolution upto 0.2nm can be achieved by high resolution transmission electron microscopy which means that individual atoms can be imaged.[74] The basic

design of a transmission electron microscope is shown in *figure 2.23.* Electrons after emission from electron source (gun) are accelerated through high voltage *(0.05MV-0.1MW)* using anodes. The electrons accelerated through such voltages possess wavelengths lower than X-rays as per following equation. Thus electrons can be diffracted by smaller structure and hence atomic level resolution.

$$\boldsymbol{\lambda = h(2meV)^{-1/2}} \text{ ..... (2.7)}$$

For using electrons for diffraction it is mandatory to focus them. Focusing of electrons is achieved by electromagnetic lenses of different types. The condenser lenses are positioned to regulate the size and angular spread of incident electron beam. The electrons that successfully transmit are directed by series of objective, intermediate and projector lenses to create a magnified image on the fluorescent screen. The movement of the screen relative to lenses can be changed to obtain a diffraction pattern rather than the image. Thus in addition to high quality image we can obtain the diffraction pattern of the sample called as SAED pattern. The technique of dark field imaging that excludes un-scattered electrons further allows a clear image with less artifacts than the common bright field mode.[74,107]

The sample preparation for TEM is little tedious than in SEM and sample thickness more than 200nm are not suitable for imaging. The sample thickness matters because of strong interaction of electron beam with the sample material where former is absorbed substantially if the sample is too thick. So generally dispersed sample solution is drop casted on carbon coated copper grids for TEM analysis. The TEM instrument can also incorporate in it the X-ray detection unit which acts as a chemical detection tool by analyzing the emitted X-ray. The technique is called energy dispersive spectroscopy (EDS). The origin of X-rays can be attributed to the energy released by electron in jumping from a higher energy level in sample atom to a hole generated by fast moving electrons of the incident beam at lower energy level. [74,107]

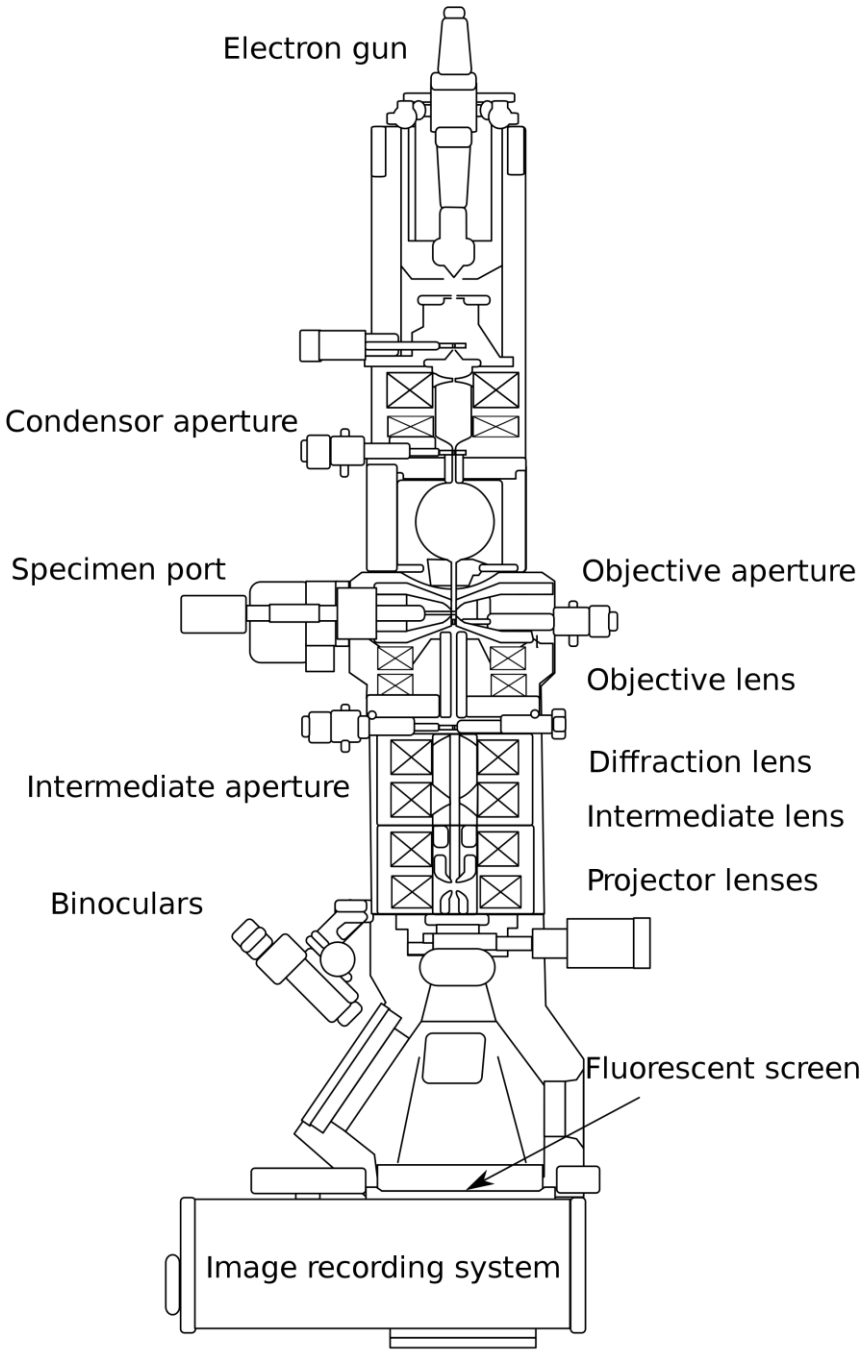

Figure 2.23 *Schematic of a high resolution transmission electron microscopy (HR-TEM) showing its different constituent parts.*[108]

(Source: https://commons.wikimedia.org/wiki/File:Scheme_TEM_en.svg)

2.2.6.2 Scanning electron microscopy (SEM)

This technique which can be considered complimentary to optical microscopy to study the topology, texture, and surface features of solid crystals and powders upto 1 micron in dimensions. *Figure 2.24* shows the schematic of constituent parts of SEM microscope. In SEM instrument an electron beam from an electron source gun (filament) is focused on a small area (5-10nm) on the surface of the sample to be imaged. The electron emission from the tungsten source of electron gun can be by thermionic emission or by field emission (electric field causes emission) and accordingly we have thermionic scanning electron microscope (TSEM) and field emission microscope (FESEM) respectively. FE-SEM is more advanced owing to the narrow distribution of electron energies triggered by electric field compared to broad distribution of electron energies in thermionic emission process. Incident high speed electrons from the electron gun in the form of a beam induce the generation of secondary electrons from the surface along with the X-rays. The electron beam is guided through the use of electric anodes (for acceleration) and magnetic lenses on the sample surface. The scanning coils make the electron beam of particular energy to scan a particular region of sample surface and generate the secondary electrons there in. The collection of all secondary electrons generated in the process of scanning are collected by detectors and sent to photo multipliers to generate the image of the sample. [74,109,110]

Thus the sample preparation for SEM is very simple and samples of any reasonable thickness can directly be used. However for the non- conducting samples which pose the problem of surface charging that in turn can cause additional electrostatic interference with the electron beam, we need to coat the sample with thin layer of inert metals like gold before actual imaging. The range of SEM instrument is very broad starting from the lowest resolving power of optical microscope (1μm) to highest resolution of transmission microscope i.e. 0.1μm.[109,110]

The emitted X-Rays can be used for chemical analysis as the energy of the X-rays corresponds to the orbital energy from which it has been ejected. The latter constitutes the principle of EDS analysis of the samples. EDS gives the valuable and accurate results for the surface composition of materials especially for the high Z elements.[109,110]

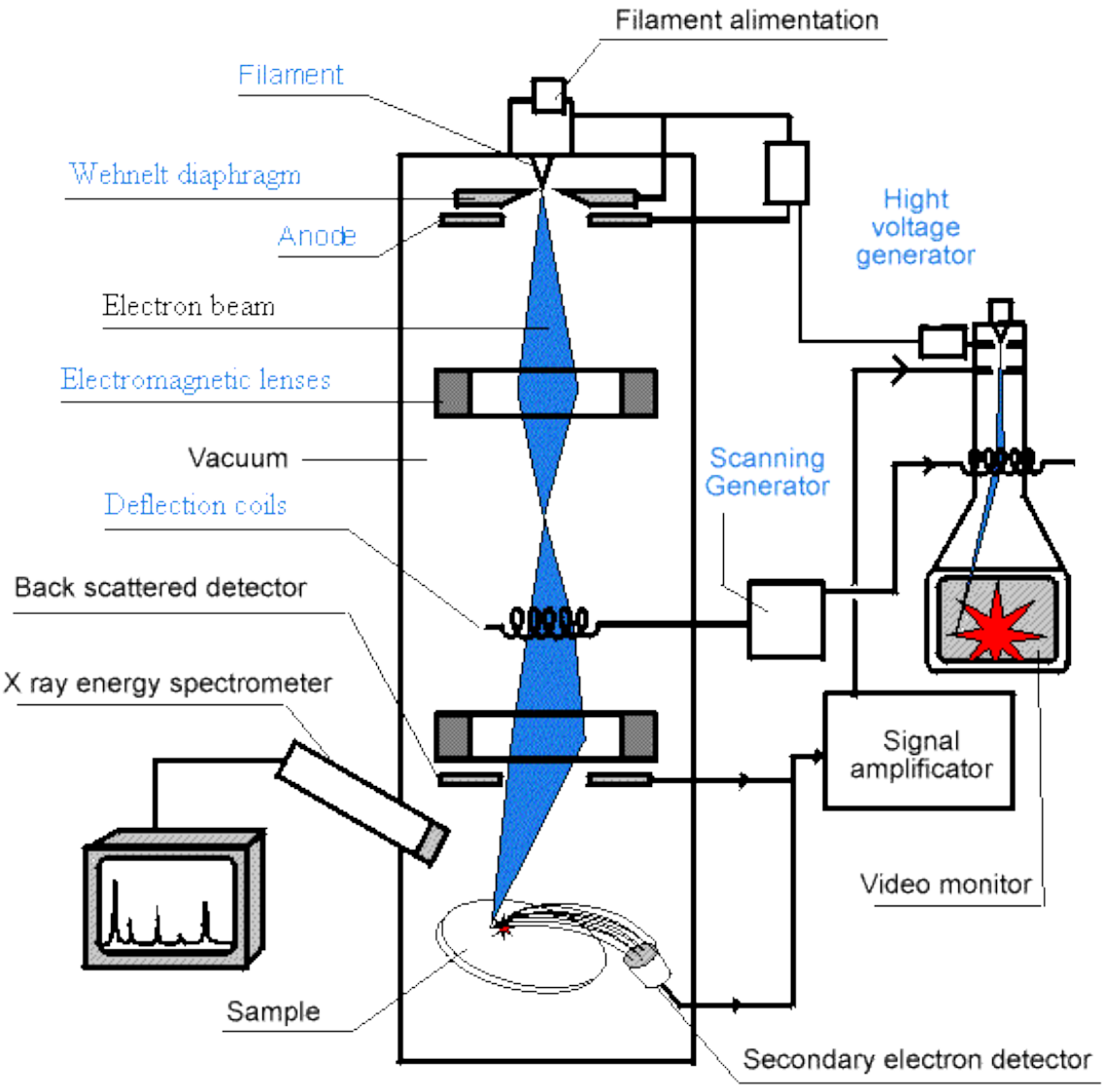

Figure 2.24 *Schematic of an FE-SEM instrument showing different constituents and working principle.*

(http://images.clipartpanda.com/microscope-diagram-and-functions-meb2.gif

2.2.7 Electrochemical measurements

The performance monitoring of energy storage materials is accomplished through three electrochemical techniques i.e. cyclic-voltammetry, charge-discharge measurements and Impedance spectroscopy. These three electrochemical techniques are sufficient tool kit for a material electrochemist to evaluate all the parameters (discussed in the previous chapter) determining the performance of energy storage devices i.e super-capacitor and battery. These techniques are discussed in detail in the following sub-sections.

2.2.7.1 Cyclic Voltammetry (CV)

The cyclic voltammetry (CV) is a potentiodynamic technique where current response to the cyclically varying potential is recorded. It differs from its closest ally, the linear sweep voltammetry in being cyclic i.e. sweep does not end at the upper vertex potential rather it goes backward to stating potential with the same sweep rate as for the forward sweep. Accordingly, current also sweeps all the possible values in the forward sweeping potentials and occasionally changes directions in the backward potential sweeps. *Figure 2.25* shows the CV plots of a faradic and a non faradic system in aqueous solution. For a faradic system, CV plot manifests itself in the form of peaks and in case of non faradic system it can be seen as a rectangular loop.[111–113]

For a faradic process, the peak currents (I_{pa} & I_{pc}) can be attributed to following equality:

$$I_P = 2.69 * 10^5\, n^{3/2} D^{1/2} V s^{1/2} A.C^* \ldots\ldots\ldots (2.8)$$

I_p is the magnitude of peak current, n is number of electrons involved in electron transfer reaction, D is diffusion coefficient, *s* is voltage scan rate, A is the area of electrode exposed to electrolyte, C^* is the concentration of analyte. Based on this I_{pa}/I_{pc} should be unity for reversible system. The peak voltages are related to number of electrons involved in the reaction by equation:

$$E_{pa} - E_{pc} = (59 * 10^{-3})/n \quad \ldots\ldots.(2.9)$$

where E_{pa} and E_{pc} are peak anodic and cathodic voltages in volts and n is number of electrons involved in charge transfer reaction.

For a non faradic system following equation is applicable for calculating the saturation currents:

$$I_{nf} = sC_{dl} \text{ …….. (2.10)}$$

where I_{nf} is non faradic current , s is voltage scan rate C_{dl} *is* double layer capacitance.

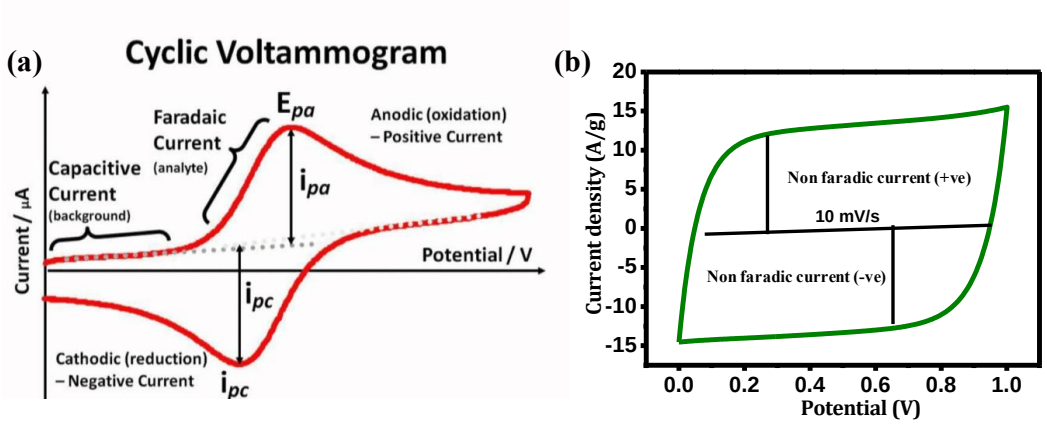

Figure 2.25 *a) Cyclic voltammetry plot of a faradic system displaying peaks corresponding to redox reactions.{Source: www.imperial.ac.uk/people/bhavik.a.patel} b) Cyclic voltametry plot of a non faradic system displaying a rectangular loop corresponding to a capacitive system.{Measurement on super capacitor assembled in our lab using carbon material synthesized from sugar cane bagasse }*

For carrying out a CV experiment a cell is assembled with electrodes dipped in a suitable electrolyte and voltage sweep is achieved by potentiostat. The analyte is either dissolved in solution or coated on electrode. Two types of electrode assemblies used commonly are 2- electrode assembly and a 3-electrode assembly. The electrodes in 3-electrode assembly are named as working, counter and reference according to their function in the cell. In 2- electrode assembly we can have a working and counter electrode. Some commonly used reference electrodes are Ag/AgCl, Hg/Hg_2Cl_2 and Hg/HgO.[111–113]

The CV has become a fundamental technique for chemical analysis of various kinds in the solid state or in the solution state. The CV analysis has proved indispensable for study of kinetics of electron transfer reactions, for detection of intermediates, for electrochemical reversibility monitoring, for elucidation of number of electrons involved in charge transfer, for formal redox potential determination, for diffusion coefficient calculation and for qualitative detection and quantitative analysis of dissolved unknown analyte. [114,115]

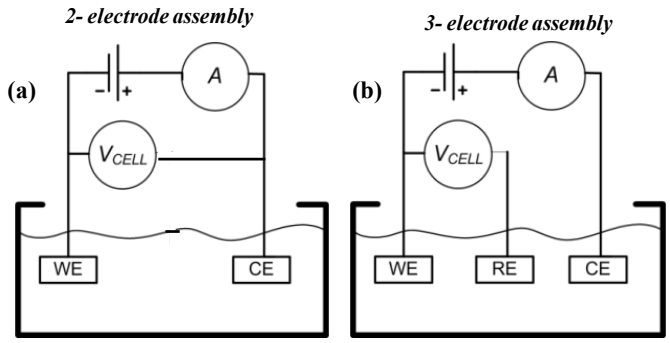

Figure 2.26 *Schematic of 2-electrode and a 3-electrode assembly. a) Working and counter electrode in action b) Working, counter and reference electrode in action.*

{Source:www.intechopen.com/books/state-of-the-art-in-biosensors-general-aspects/bioelectronics-for-amperometric-biosensors}

CV technique has been extensively used for quality evolution and quantitative determination of parameters characterizing the energy storage and conversion devices. The specific capacitance of a super capacitor material can readily obtained from the CV plot (*figure 2.25 a & b)* by using the following equality besides giving an information about the presence of peaks in if pseudo capacitance is contributing.

$$\boldsymbol{Capacitance} = (\boldsymbol{area\ under\ the\ curve})/\ (\mathbf{2} * \boldsymbol{voltage\ window} * \boldsymbol{scan\ rate})$$

This equation is for a 3-electrode system and for 2-electrode system *2* from denominator is omitted. For battery characterization CV technique provides the qualitative information about the redox phenomenon through peak positions. [114,115,116]

2.2.7.2 Charge-Discharge Measurements.

Charge discharge technique is a galvanostatic procedure where current is kept static and voltage rise to a certain fixed potential and then the reversible fall back to initial potential is measured as a function of time. The measurements can be performed in 2-electrode and 3-eelctrode assemblies exactly in the similar setup as used for CV measurements.[112–114] It has become a standard technique to test the performance of energy devices like super capacitor and battery besides being helpful in electrode kinetics study of some aqueous electrochemical reactions. The technique yields the

quantitative information about various performance parameters related to the systems besides providing some qualitative input through the peak plateaus.[114,115] The *figure 2.27* compares the charge discharge plots for three systems ie EDLC capacitor, pseudo-capacitor and battery. The reversible charge discharge plot for EDLC looks like a triangle as seen from *figure 2.27a.* The reversible charge discharge plot of a pseudo capacitor as seen in *figure 2.27b* is characterized by plateaus corresponding to a particular potential characterizing a reversible surface reaction involved. The reversible charge discharge plots of battery is characterized by plateaus as in pseudo capacitor case , but the plateaus are more in number and spread over a longer time depicting the bulk material involved in electrochemical transformations. [114,115,116]

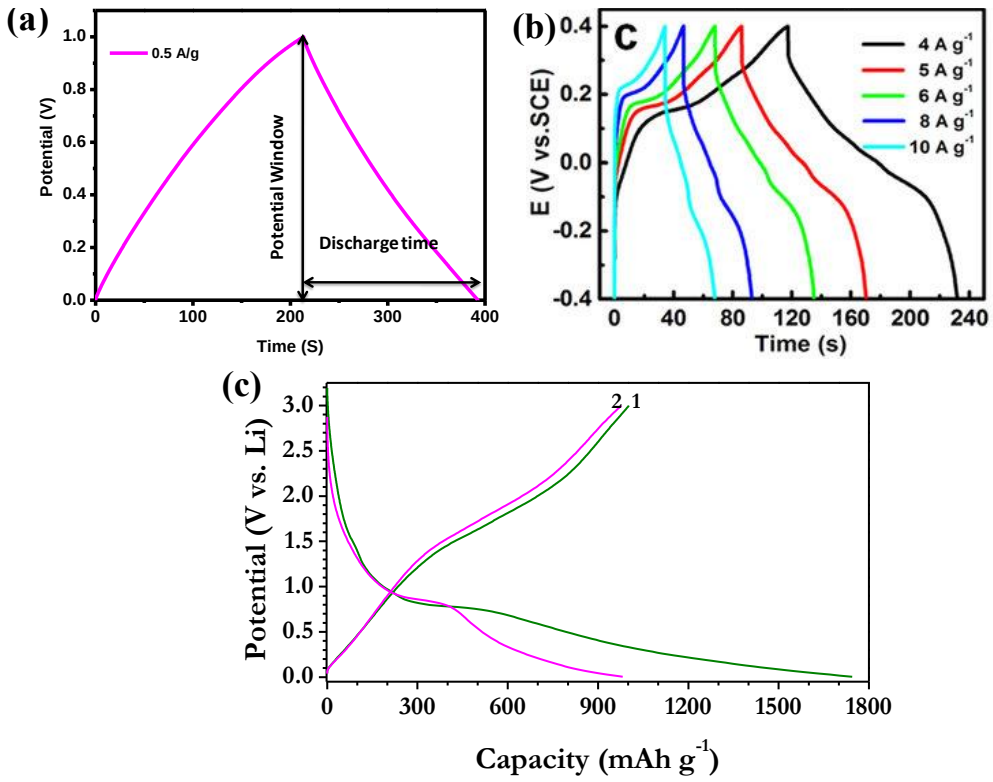

Figure 2.27 *a) Charge-discharge profile of an EDLC type capacitor.{Measurement on a super capacitor assembled in our lab using carbon material synthesized from sugar cane bagasse} b) Charge discharge profile of a pseudo-capacitor.{Reproduced from ref.* 117*} c) Charge discharge profile of a Li-ion battery. {Measurement on a lab assembled LI-ion coin cell}*

Specific capacitance (C_S) of an EDLC and pseudo-capacitor electrode material can be calculated by using following equation:

$$C_s = \frac{I}{\frac{dV}{dt} * m} \quad \text{..... (2.11)}$$

where *I* is the 3 electrode constant current applied *dV/dt* is rate of voltage change and *m* is the mass of material loaded on the electrode. For a 2-electrode measurement C_s of electrode material can be obtained by

$$C_s = \frac{I}{\frac{dV}{dt} * m} \quad \text{..... (2.12)}$$

Capacity of battery is obtained by multiplying discharge time with applied constant current (*current density*) and is plotted along the X-axis as in *figure 2.27c.*

2.2.7.3 Electrochemical impedance spectroscopy (EIS)

Electrochemical Impedance Spectroscopy is an ac voltammetry technique where current response to the frequency dependent voltage is recorded. Dependence on frequency gets the technique its name, the impedance spectroscopy, corresponding to traditional spectroscopies where frequency of electromagnetic radiations is prime parameter. In an ac circuit containing capacitor or an inductor there always exists a phase difference between current and voltage and because of which the total resistance becomes a function of phase angle and is given the name impedance.[112,114–116] EIS like other transient techniques has been used for the electrochemical study of mechanism, kinetics and thermodynamics of various redox reactions. Recently it has been used as a major electrochemical characterization tool in the charge storage devices like super-capacitors, batteries and some conversion type devices to evaluate electrochemical series resistance (ESR), charge transfer resistance (R_{CT}), Warburg impedance and double layer capacitance (C_{dl}). For highly efficient devices, resistances should be as low as possible.[112,114–116]

Impedance spectroscopy exploits phase lag condition of an ac circuit to furnish data about the electrode-electrolyte interfaces of the electrochemical devices by modeling the interfaces by appropriate ac circuits like the one shown in *figure 2.28a*. The impedance experimental data is plotted in the form of *Nyquist plot* and *Bode plot* from which ESR, charge transfer resistance and Warburg impedance can be directly obtained. *Figure 2.28b* shows the Nyquist plot, a plot of an imaginary impedance (Z_{imp}) along *y*-

axis and real impedance (Z_{re}) along x-axis, of an electrode electrolyte interface. For a double layer electrode-electrolyte circuit model shown in *figure 2.28a* the Nyquist plot manifests in the form of a semicircle with the first intercept on *x-axis* yielding ESR (shown as R_s in the plot) and the diameter of the semicircle corresponds directly to the charge transfer resistance (R_{CT}). From the intercept of Warburg line of x-axis the double layer capacitance can be calculated by equation given in plot itself.[112,114–116]

Bode plot on the other hand plots phase angle with frequency and furnishes information about behavior of interfaces at different frequencies. For an ideal capacitor bode phase is 90^0.[112,115]

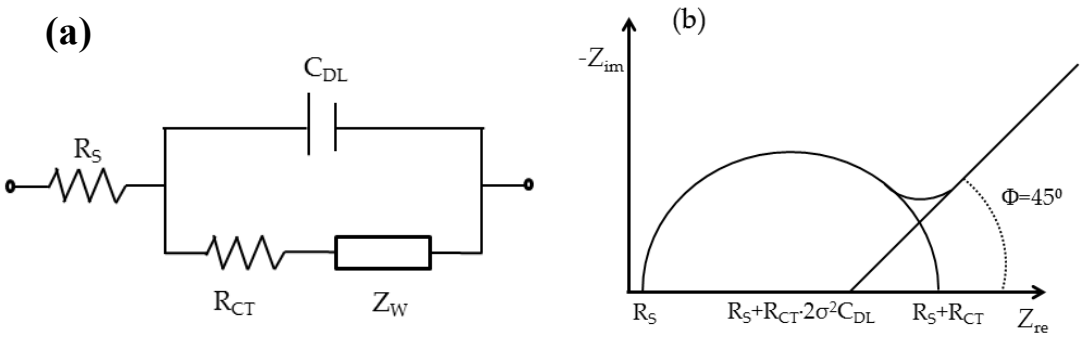

Figure 2.28 *a) Electrochemical model circuit for electrode-electrolyte interfaces encountered in energy storage devices. R_s stands for ESR, R_{CT} for charge transfer resistance, Z_W for Warburg impedance and C_{DL} for double layer capacitance.{Reproduced from ref.* 115*} b) Nyquist plot for the model the circuit showing the initial semicircle arc before going 45^0 to x-axis. {Reproduced from ref.* 118*}*

2.3 References

1. J. S. O. Evans, R. J. Francis, D. O'Hare, S. J. Price, S. M. Clark, J. Flaherty, J. Gordon, A. Nield and C. C. Tang, *Rev. Sci. Instrum.*, 1995, **66**, 2442–2445.
2. R. Ibbett, S. Gaddipati, S. Davies, S. Hill and G. Tucker, *Bioresour. Technol.*, 2011, **102**, 9272–9278.
3. N. Murayama, H. Yamamoto and J. Shibata, *Int. J. Miner. Process.*, 2002, **64**, 1–17.
4. C. S. Cundy and P. A. Cox, *Microporous Mesoporous Mater.*, 2005, **82**, 1–78.
5. A. Lagazzo, E. Finocchio, P. Petrini, C. Ruggiero and L. Pastorino, *Mater. Lett.*,

2016, **171**, 212–215.

6. M. M. Titirici, A. Thomas, S. H. Yu, J. O. Muller and M. Antonietti, *Chem. Mater.*, 2007, **19**, 4205–4212.
7. B. Hu, K. Wang, L. Wu, S. H. Yu, M. Antonietti and M. M. Titirici, *Adv. Mater.*, 2010, **22**, 813–828.
8. Y. Fang, D. Gu, Y. Zou, Z. Wu, F. Li, R. Che, Y. Deng, B. Tu and D. Zhao, *Angew. Chemie - Int. Ed.*, 2010, **49**, 7987–7991.
9. M. M. Titirici, M. Antonietti and A. Thomas, *Chem. Mater.*, 2006, **18**, 3808–3812.
10. R. Ryoo and M. J. Kim, *Chem. Commun.*, 1997, **41**, 2225–2226.
11. L. Hu and Q. Chen, *Nanoscale*, 2014, **6**, 1236–57.
12. B. Zhao, P. Liu, H. Zhuang, Z. Jiao, T. Fang, W. Xu, B. Lu and Y. Jiang, *J. Mater. Chem. A*, 2013, **1**, 367–373.
13. V. G. Pol and P. Thiyagarajan, *Ind. Eng. Chem. Res.*, 2009, **48**, 1484–1489.
14. T. Luo, L. Gao, J. Liu, L. Chen, J. Shen, L. Wang and Y. Qian, *J. Phys. Chem. B*, 2005, **109**, 15272–15277.
15. H. Qian, S. Yu, L. Luo, J. Gong, L. Fei and X. Liu, *Chem. Mater.*, 2006, **18**, 1–2.
16. Z. Wen, Q. Wang and J. Li, *Adv. Funct. Mater.*, 2008, **18**, 959–964.
17. X. Cui, M. Antonietti and S.H. Yu, *Small*, 2006, **2**, 756–759.
18. M. Sevilla and A. B. Fuertes, *Chem. A Eur. J.*, 2009, **15**, 4195–4203.
19. A. Funke and F. Ziegler, *Biofuels, Bioprod. Biorefining*, 2010, **4**, 160–177.
20. Y. Lin, X. Ma, X. Peng and Z. Yu, *Energy & Fuels*, 2016, **30**, 7746–7754.
21. L. Axelsson, M. Franzen, M. Ostwald, G. Berndes, G. Lakshmi and N. H. Ravindranath, *Biofuels, Bioprod. Biorefining*, 2012, **6**, 246–256.
22. X. Zhang and Z. Liu, *Nanoscale*, 2012, **4**, 707–714.
23. K. Murugesan, P. Sivakumar and P. N. Palanisamy, 2016, **2**, 58–66.
24. W. X. Chen, Y. Lee and Z. Liu, *Chem. Commun.*, 2002, **0**, 2588–2589.

25. S. Wang, S. P. Jiang and X. Wang, *Electrochim. Acta*, 2011, **56**, 3338–3344.

26. Z. Wang, Z. Wu, G. Di Benedetto, J. L. Zunino and S. Mitra, *Carbon N. Y.*, 2015, **91**, 103–113.

27. K. Y. Foo and B. H. Hameed, *Microporous Mesoporous Mater.*, 2012, **148**, 191–195.

28. E. G. Calvo, N. Ferrera-Lorenzo, J. A. Menéndez and A. Arenillas, *Microporous Mesoporous Mater.*, 2013, **168**, 206–212.

29. B. Xing, G. Huang, L. Chen, H. Guo, C. Zhang, W. Xie and Z. Chen, *J. Porous Mater.*, 2016, **23**, 67–73.

30. A. M. Schwenke, S. Hoeppener and U. S. Schubert, *Adv. Mater.*, 2015, **27**, 4113–4141.

31. E. G. Calvo, N. Ferrera-Lorenzo, J. A. Menéndez and A. Arenillas, *Microporous Mesoporous Mater.*, 2013, **168**, 206–212.

32. Y. Li, J. Liu, Y. Wang and Zhong Lin Wang, *Chem. Mater.*, 2001, **13**, 1008–1014.

33. D. Demarchi and A. Tagliaferro, in *Carbon for Sensing Devices*, Springer International Publishing, Switzerland, 2015, pp. 1–264.

34. G. Che, B. B. Lakshmi, E. R. Fisher and C. R. Martin, *Nature*, 1998, **393**, 346–349.

35. G. Che, B. B. Lakshmi, C. R. Martin, E. R. Fisher and R. S. Ruoff, *Chem. Mater.*, 1998, **10**, 260–267.

36. J. H. Yu, D. W. Lee, B. K. Kim and T. Jang, *J. Magn. Magn. Mater.*, 2006, **304**, 16–18.

37. M. Su, B. Zheng and J. Liu, *Chem. Phys. Lett.*, 2000, **322**, 321–326.

38. F. C. B. Maia, R. E. Samad, J. Bettini, R. O. Freitas, N. D. Vieira Junior and N. M. Souza-Neto, *Sci. Rep.*, 2015, **5**, 11812.

39. R. Gokhale, S. Agarkar, J. Debgupta, D. Shinde, B. Lefez, A. Banerjee, J. Jog, M. More, B. Hannoyer and S. Ogale, *Nanoscale*, 2012, **4**, 6730–4.

40. S.-L. Hu, K.-Y. Niu, J. Yang, S. Jing, N.-Q. Zhaoa and X.-W. Du, *J. Mater.*

Chem., 2009, **19**, 484–488.

41. C. T. Kingston, Z. J. Jakubek, S. Dénommée and B. Simard, *Carbon* , 2004, **42**, 1657–1664.
42. H. Lu, W. C. Li, E. L. Salabas, B. Spliethoff and F. Schuth, *Chem. Mater.*, 2006, **18**, 2086–2094.
43. C. Liang, Z. Li and S. Dai, *Angew. Chemie - Int. Ed.*, 2008, **47**, 3696–3717.
44. C. Pean, C. Merlet, B. Rotenberg, P. A. Madden, P. L. Taberna, B. Daffos, M. Salanne and P. Simon, *Energy Environ. Sci.*, 2014, **8**, 1576–1583.
45. Y. F. Liao, S. R. Wang and X. Q. Ma, *ACS Div. Fuel Chem. Prepr.*, 2004, **49**, 407–411.
46. J. Jones, *What is Pyrolysis*, 1997, 1–29.
47. J. Piskorz, D. Radlein and D. S. Scott, *J. Anal. Appl. Pyrolysis*, 1986, **9**, 121–137.
48. A. Demirbas, *Energy Sources, Part A Recover. Util. Environ. Eff.*, 2009, **31**, 1186–1193.
49. N. A. Rashidi, M. Mohamed and S. Yusup, *Int. J. Renew. Energy Res.*, 2012, **2**, 497–503.
50. Y. Gong, Z. Wei, J. Wang, P. Zhang, H. Li and Y. Wang, *Sci. Rep.*, 2014, **4**, 6349.
51. J. Lee, J. Kim and T. Hyeon, *Adv. Mater.*, 2006, **18**, 2073–2094.
52. K. Kierzek, E. Frackowiak, G. Lota, G. Gryglewicz and J. Machnikowski, *Electrochim. Acta*, 2004, **49**, 515–523.
53. K. Xia, Q. Gao, J. Jiang and J. Hu, *Carbon*, 2008, **46**, 1718–1726.
54. H. Teng and S. C. Wang, *Carbon* , 2000, **38**, 817–824.
55. H. Wang, Q. Gao and J. Hu, *J. Am. Chem. Soc.*, 2009, **131**, 7016–7022.
56. J. Wang, I. Senkovska, S. Kaskel and Q. Liu, *Carbon*, 2014, **75**, 372–380.
57. P. Yadav, A. Banerjee, S. Unni, J. Jog, S. Kurungot and S. Ogale, *ChemSusChem*, 2012, **5**, 2159–2164.

58. L. Chuenchom, R. Kraehnert and B. M. Smarsly, *Soft Matter*, 2012, **8**, 10801–10812.

59. Y. Deng, C. Liu, T. Yu, F. Liu, F. Zhang, Y. Wan, L. Zhang, C. Wang, B. Tu, P. A. Webley, H. Wang and D. Zhao, *Chem. Mater.*, 2007, **19**, 3271–3277.

60. X. Chen, Y.-S. Jun, K. Takanabe, K. Maeda, K. Domen, X. Fu, M. Antonietti and X. Wang, *Chem. Mater.*, 2009, **21**, 4093–4095.

61. A. Sayari and Y. Yang, *Chem. Mater.*, 2005, **17**, 6108–6113.

62. W. Lv, F. Wen, J. Xiang, J. Zhao, L. Li, L. Wang, Z. Liu and Y. Tian, *Electrochim. Acta*, 2015, **176**, 533–541.

63. P. Wang, B. Qiao, Y. Du, Y. Li, X. Zhou, Z. Dai and J. Bao, *J. Phys. Chem. C*, 2015, **119**, 21336–21344.

64. V. Simone, A. Boulineau, A. de Geyer, D. Rouchon, L. Simonin and S. Martinet, *J. Energy Chem.*, 2016, **25**, 761–768.

65. Z. Sun, X. Shi, B. K. Tay, D. Flynn, X. Wang, Z. Zheng and Y. Sun, *Diam. Relat. Mater.*, 1997, **6**, 230–234.

66. F. Shen, H. Zhu, W. Luo, J. Wan, L. Zhou, J. Dai, B. Zhao, X. Han, K. Fu and L. Hu, *ACS Appl. Mater. Interfaces*, 2015, **7**, 23291–23296.

67. F. Shen, W. Luo, J. Dai, Y. Yao, M. Zhu, E. Hitz, Y. Tang, Y. Chen, V. L. Sprenkle, X. Li and L. Hu, *Adv. Energy Mater.*, 2016, **6**, 1–7.

68. T. Yang, T. Qian, M. Wang, X. Shen, N. Xu, Z. Sun and C. Yan, *Adv. Mater.*, 2016, **28**, 539–545.

69. D. Puthusseri, V. Aravindan, B. Anothumakkool, S. Kurungot, S. Madhavi and S. Ogale, *Small*, 2014, **10**, 4395–4402.

70. Q. Shi, R. Zhang, Y. Lv, Y. Deng, A. A. Elzatahrya and D. Zhao, *Carbon* , 2015, **84**, 335–346.

71. W. Luo, C. Bommier, Z. Jian, X. Li, R. Carter, S. Vail, Y. Lu, J. J. Lee and X. Ji, *ACS Appl. Mater. Interfaces*, 2015, **7**, 2626–2631.

72. J. Patterson and B. Bailey, *Solid-State Physics*, Springer, Berlin, Heidelberg, 2010.

73. C. Kittel, *Introduction to Solid State Physics*, John Wiley &Sons, INC., New York, 2010.

74. A. R.West, *Solid State Chemistry and its Applications*, John Wiley &Sons, INC., West sussex, 2014.

75. R. S. Experts, *X-ray Diffr. Tech.*, 2005, 44, 1–2.

76. A. K. Singh and U. T. Nakate, *Adv. Nanoparticles*, 2013, **2**, 66–70.

77. K. W. Kho, Z. X. Shen, H. C. Zeng, K. C. Soo and M. Olivo, *Anal. Chem.*, 2005, **77**, 7462–7471.

78. D. A. Long, *The Raman effect: a unified treatment of the theory of Raman scattering by molecules.*, John Wiley &Sons, INC., West sussex, 2002, vol. 8.

79. C. C. Moura, R. S. Tare, R. O. C. Oreffo and S. Mahajan, *J. R. Soc. Interface*, 2016, **13**, 9–11.

80. P. R. Carey, *Annu. Rev. Phys. Chem.*, 2006, **57**, 527–554.

81. Horiba Scientific, *Raman Spectrosc. Geol. Mater. Anal.*, 2015, 2–5.

82. K. Kneipp, H. Kneipp, I. Itzkan, K. Kneipp, H. Kneipp, H. Kneipp, I. Itzkan, I. Itzkan, R. R. Dasari, R. R. Dasari, M. S. Feld and M. S. Feld, *Chem. Rev.*, 1999, **99**, 2957–2975.

83. S. Zaleski, A. J. Wilson, M. Mattei, X. Chen, G. Goubert, M. F. Cardinal, K. A. Willets and R. P. Van Duyne, *Acc. Chem. Res.*, 2016, **49**, 2023–2030.

84. B. M. Weckhuysen, J.-M. Jehng and I. E. Wachs, *J. Phys. Chem. B*, 2000, **104**, 7382–7387.

85. S. S. Chan, I. E. Wachs, L. L. Murrell, L. Wang and W. K. Hall, *J. Phys. Chem.*, 1984, **88**, 5831–5835.

86. J. Lee, M. C. Orilall, S. C. Warren, M. Kamperman, F. J. DiSalvo and U. Wiesner, *Nat. Mater.*, 2008, **7**, 222–228.

87. A. C. Ferrari, J. C. Meyer, V. Scardaci, C. Casiraghi, M. Lazzeri, F. Mauri, S. Piscanec, D. Jiang, K. S. Novoselov, S. Roth and A. K. Geim, *Phys. Rev. Lett.*, 2006, **97**, 1–4.

88. Y. Wang, D. C. Alsmeyer and R. L. Mccreery, *Carbon*, 1990, **2**, 557–563.

89. A. C. Ferrari, *Solid State Commun.*, 2007, **143**, 47–57.

90. M. S. Dresselhaus, A. Jorio and R. Saito, *Annu. Rev. Condens. Matter Phys*, 2010, **1**, 89–108.

91. P. Giura, N. Bonini, G. Creff, J. B. Brubach, P. Roy and M. Lazzeri, *Phys. Rev. B - Condens. Matter Mater. Phys.*, 2012, **86**, 1–5.

92. S. Gorantla, A. Bachmatiuk, J. Hwang, H. a Alsalman, J. Y. Kwak, T. Seyller, J. Eckert, M. G. Spencer and M. H. Rümmeli, *Nanoscale*, 2014, **6**, 889–896.

93. H. Wang, H. Yi, C. Zhu, X. Wang and H. Jin Fan, *Nano Energy*, 2015, **13**, 658–669.

94. M. S. Dresselhaus, A. Jorio, M. Hofmann, G. Dresselhaus and R. Saito, *Nano Lett.*, 2010, **10**, 751–758.

95. A. Ferrari and J. Robertson, *Phys. Rev. B*, 2000, **61**, 14095–14107.

96. C. N. C. Lam, J. J. Lu and a. W. Neumann, *Handbook of Applied Surface and Colloid Chemistry*, John Wiley &Sons, INC., West sussex, 2002, vol. 1.

97. F. Rouquerol, J. Rouquerol, K. S. W. Sing, P. Llewellyn and G. Maurin, *Adsorption by powders and porous solids*, Academic Press, London, 2014.

98. B. A. W. Allen, B. A. C. Communicated and R. T. R. R. Stebbing, *Physical Chemistry of Surfaces*, John Wiley &Sons, INC., New York, 1990.

99. J. C. V. and I. S. Gilmore, *Surface Analysis – The Principal Techniques 2nd Edition*, John Wiley &Sons, INC., West sussex, 2009.

100. N. Dwivedi, R. J. Yeo, N. Satyanarayana, S. Kundu, S. Tripathy and C. S. Bhatia, *Sci. Rep.*, 2015, **5**, 7772.

101. R. Bhosale, S. Kelkar, G. Parte, R. Fernandes, D. Kothari and S. Ogale, *ACS Appl. Mater. Interfaces*, 2015, **7**, 20053–20060.

102. Y. Zhu, Z. Yuan, W. Cui, Z. Wu, Q. Sun, S. Wang, Z. Kang and B. Sun, *J. Mater. Chem. A*, 2014, **2**, 1436–1442.

103. T. Audichon, T. W. Napporn, C. Canaff, C. Morais, C. Comminges and K. B. Kokoh, *J. Phys. Chem. C*, 2016, **120**, 2562–2573.

104. M. Das, J. Datta, A. Dey, R. Jana, A. Layek, S. Middya and P. P. Ray, *RSC*

Adv., 2015, **5**, 101582–101592.

105. A. Jitianu, T. Cacciaguerra, R. Benoit, S. Delpeux, F. Beguin and S. Bonnamy, *Carbon*, 2004, **42**, 1147–1151.

106. Z. Zhang, C. He, T. Sun, Z. Zhang, K. Song, Q. Wu and Q. Zhang, *Int. J. Hydrogen Energy*, 2016, **41**, 5234–5242.

107. B. Fultz and J. Howe, *Transmission Electron Microscopy and Diffractometry of Materials, 3rd Edition*, Springer, Heidelberg, 2008.

108. Z. Zhang, K. Yao, Y. Liu, C. Jin, X. Liang, Q. Chen and L. M. Peng, *Adv. Funct. Mater.*, 2007, **17**, 2478–2489.

109. D. Krinsley, K. Pye, S. Boggs Jr and N. Tovey, *Backscattered scanning electron microscopy and image analysis of sediments and sedimentary rocks*, Cambridge University Press, Cambridge, 1998.

110. P. Echlin, *Handbook of sample preparation for scanning electron microscopy and x-ray microanalysis*, Springer, Cambridge, 2009.

111. J. O. Bockris, A. K. N. Reddy and M. Gamboa-Aldeco, *Modern Electrochemistry*, Kluwer Academic, New York, Second., 2002, vol. 86.

112. A. J. Bard and L. R. Faulkner, *ELECTROCHEMICAL METHODS Fundamentals and Applications*, John Wiley &Sons, INC., New York, 1944.

113. P. Zanello, *Inorganic Electrochemistry*, Royal Society of Chemistry, Cambridge, 2003.

114. A. Despic and V. P. Parkhutic, *Mod. Asp. Electrochem.*, 1989, **20**, 401–503.

115. B. E. Conway, *Electrochemical Supercapacitors*, Kluwer Academic, New York, 2002.

116. W. Van Schalkwijk and B. Scrosati, *Advances in lithium-ion batteries*, Kluwer Academic, New York, 2002.

117. H. Hua, S. Liu, Z. Chen, R. Bao, Y. Shi, L. Hou, G. Pang, K. N. Hui, X. Zhang and C. Yuan, *Sci. Rep.*, 2016, **6**, 20973.

118. J. O. M. Bockris and A. K. N. Reddy, *Modern Electrochemistry*, Kluwer Academic, New York, 1974.

Chapter 3

Enhanced capacitance retention in a supercapacitor made of carbon from sugarcane bagasse by hydrothermal pretreatment.

A unique morphology controlling protocol involving hydrothermal pre-processing before pyrolysis is presented to convert cellulosic waste in the form of sugarcane bagasse into 3D interconnected, conducting and high surface area carbon nano-channels. The large buffer spaces in such a porous carbon sample yield impressive electrochemical capacitance (C_{sp}) of 280 F/g at a current density of 1A/g (and 275 F/g at 5 mV/s), with 72% retention even at a very high current density of 20 A/g. In contrast, the non-hydrothermally treated sample exhibits C_{sp} value of 180F/g at 1A/g and only 52% retention at 20A/g. The much better performance of the hydrothermally pre-processed bagasse derived carbon (BHAC) can be ascribed to the solvent retention inside the buffer spaces created, negating the diffusional limitations of pore inaccessibility at higher scan rates. The BHAC has a high surface area of 1260 m^2/g with a fairly good (11 wt%) concentration of oxygen functionality. The material furnishes good energy density of 5Wh/kg at a power density of 3.5kW/kg and shows good cyclability of 90% after 1000 charge-discharge cycles.

The content of this chapter is published in,

"*Energy Fuels*, 2014, *28* (6), pp 4233–4240".

3.1 Introduction

Porous carbon materials are the materials of choice today for high performance supercapacitor applications because of their easy synthetic protocols (such as simple pyrolysis), good charge storage capacities and low cost.[1-5] Apart from purified and refined carbon forms such as graphene[6], CNTs[7] and various other forms such as activated carbons (ACs)[8], carbon nano-fibers[9], templated carbons[10], carbide-derived carbons[11], and carbon onions[12] have been investigated for supercapacitor applications. Amongst these ACs have emerged as the most promising candidates because these materials not only offer a very large surface area for ion adsorption yielding double layer formation over a large area, but their synthesis is also relatively facile, inexpensive and scalable[13].Recent research[14] shows that carbon materials derived from cellulosic waste matter may in fact turn out to be superior to other carbon forms prepared by simple pyrolysis because of their pseudo-capacitance contribution from oxygen functionalities in addition to the contribution from the regular porous architecture. Indeed, certain low surface area carbon materials derived from cellulosic materials like gels[14], cotton[15], and cloth[16] have yielded specific capacitance values close to 180 F/g, comparable to high surface area ACs. This is because of the characteristic pseudo-capacitive redox reactions of quinol-hydroquinone type resulting from the oxygen functionalities incorporated in the carbon framework obtained by higher temperature pyrolysis[17]. Employing KOH activation over the cellulosic materials has proven profitable for the synthesis of high capacitance materials, supporting high surface area and pseudo-capacitance contributions simultaneously. This concept serves the dual goal of environmental cleaning and energy storage, as most of the domestic cellulosic wastes such as cassava peels, coffee been waste, banana fibres, coconut shells, fruit stones, dead leaves etc.[18-23] have been transformed into high capacitance functional carbon materials. In an interesting recent study[24], an initial hydrothermal treatment before the actual high temperature activation has been shown to transform the cellulosic hemp blast fibre precursor into an interesting porous carbon morphology. Such open structures have the advantage of high power delivery due to reduction in the ion transport time[25]. Such hydrothermal treatment, which has been already shown to

represent a new synthetic approach for shaping cellulosic materials into distinctly advantageous morphologies than those attainable by simple activation, deserves to be explored further for different systems. We have adopted this concept in the work reported here based on carbonization of sugarcane bagasse for supercapacitor application. Sugarcane (Saccharum barberi) is widely cultivated crop throughout the world. Brazil and India are the major producers of sugarcane with the annual production of about 7,34,000 and 3,42,382 thousand metric tons (TMT) harvest, respectively. Bagasse is the major side-product of cane sugar industry with 3 tons of wet bagasse produced on crushing 10 tons of sugar cane. The major use of the bagasse has been as a fuel, or furniture material in replacement of plywood etc. High surface area porous carbons for capacitor applications have also been derived from it by activation with $ZnCl_2$, NaOH etc.[26, 27]Capacitance as high as 250 F/g at a current density of 1 A/g has been reported with $ZnCl_2$ activation and a capacitance of 120 F/g at a current density of 1A/g has been reported with its NaOH activation. The distinctive difference of our work lies in the generation of interesting 3D channel type morphology from the same bagasse precursor by concurrent use of the separately well-established processing strategies of hydrothermal treatment and KOH activation. The maximum specific capacitance value obtained in our case is 280F/g at a current density of 1A/g. But more importantly, 72% of the capacitance retention is observed even at a current density of 20 A/g in comparison with 40% retention in the same material with $ZnCl_2$ activation under similar mass ratios of activation agent and the precursor material.

The importance of hydrothermal pre-treatment (please see scheme 3.1) lies in transforming cellulosic precursor material into a black carbon mass by dehydration and hydrolysis processes under hostile conditions, provided by the presence of acid (H_2SO_4), high temperature and high pressure. The black mass contains enough C=C carbon backbones which can be acted upon by two counter-forces of temperature induced stitching[28] and KOH induced structural breaking[29]. These finally compete and compromise into the desired morphology at the temperature of around 800^0C. Herein we have characterized the electrochemical capacitive charge storage in such hydrothermally treated and activated sample (BHAC) and demonstrated that the open-

type of structures achieved in such BHAC sample have distinct advantage(s) over the samples prepared by simple activation (BAC) or the sample prepared by initial hydrolysis step followed by direct pyrolysis (BHC).

3.2 Experimental Section

3.2.1 Synthesis of bagasse derived carbons

The processed bagasse was crushed in a mixer to cut it into small manageable pieces. It was washed with distilled water followed by drying at 90^0C in oven for 24 hours. The 3g of this bagasse mass was sealed in a 125 ml autoclave along with the 100 ml of 2M H_2SO_4 and held at 180^0 C for 20 hours. The resultant black hydrothermal product (BHP) was washed with distilled water thoroughly and followed by drying in a vacuum oven at 90^0C for 12 hours. The chemical activation of the black carbon hydrothermal product (BHP) was done with KOH. The solid KOH pellets and the hydrothermal product were mixed in 1:1 mass ratio and ground thoroughly with agate mortar and pyrolyzed at 700^0C, 800^0C, or 900^0C respectively, in argon atmosphere inside a tube furnace at temperature scan rate of 3^0C/min. The corresponding samples were named BHAC-700, BHAC-800, BHAC-900, respectively. For the synthesis of BHC-800, the hydrothermal product was directly pyrolyzed in tube furnace at 800^0C in argon atmosphere. For the synthesis of BAC-800 the washed bagasse was directly mixed with KOH (1:1 mass ratio) in agate mortar and pyrolyzed in tube furnace in argon atmosphere at 800^0C at similar temperature scans.

3.2.2 Characterization of bagasse derived carbon

The different carbon samples synthesized from sugarcane bagasse were examined by X-ray powder diffraction using Philips X'Pert PRO diffractometer with nickel-filtered Cu K_α radiation. Raman spectroscopy was performed using LabRAM HR800 from JY Horiba. High-resolution transmission electron microscopy (HR-TEM) was done using IFEI, Tecnai F30, FEG system with 300 kV. The FE-SEM was done with the help of Nova Nano SEM 450. The surface area values for all the samples were determined by Brunauer Emmett Teller (BET) adsorption method (Quadrasorb automatic volumetric instrument). Cyclic voltammetry measurements were performed by Auto Lab (model

PGSTAT 30, eco-chemie). X-ray photoelectron spectroscopy (XPS) was done on a VG scientific ESCA-3000 spectrometer using non-monochromatized Mg Kα radiation (1253.6 eV) at a pressure of about 1×10^{-9} Torr.

3.2.3 Preparation of electrodes for electrochemical measurements.

The electrodes were prepared by coating a slurry of 80 wt% carbon material, 15 wt% carbon black and 5wt% polyvinylidene diflouride (PVDF) in N-methylpyrolidine on $1cm^2$ area of graphite strips (1cm×3.5cm) and then drying at 90^0C for 24 hours. The three electrode measurements were performed with carbon coated graphite strip as working electrode, platinum strip as counter electrode and Ag/AgCl as reference electrode in 1M H_2SO_4. Two electrode measurements were performed by making a cell with the two carbon material coated graphite electrodes in 1M H_2SO_4. The gravimetric capacitance was calculated from charge-discharge and CV plots from the following equations:

$$\boldsymbol{C_g = I/(m\,dV/dt)} \quad \text{(in three electrode assembly)}$$

where m is the material loading, I is the applied current, and dV/dt is the slope of charge -discharge curve.

Also,

$$\boldsymbol{C_g = 2I/(m\,dV/dt)} \quad \text{(for 2- electrode case)}$$

Where, m is the loading on each electrode, I is the current applied, and dV/dt is the slope of charge-discharge curve. The energy density and power density were calculated on the basis of following equations for two electrode cell:

$$\boldsymbol{E = \frac{C_g * V^2}{2 * 4 * 3.6}}$$

And

$$\boldsymbol{P = E/t}$$

Scheme 3.1 *Synthesis of high capacitive carbon material (and control samples, BAC and BHC) by hydrothermal pre-processing followed by inert atmosphere KOH activation pyrolysis.*

3.3 Results and Discussion

The scanning electron microscopy (FE-SEM) images in *figure 3.1* reveal the effect of synthesis protocol on the morphology of the carbon materials prepared from the same basic sugarcane bagasse precursor. Direct pyrolysis of the hydrothermal product without using any activating agent is seen to transform it into carbon microspheres; BHC (*figure 3.1a*). The direct pyrolysis of the basic cellulosic precursor (without initial hydrothermal treatment) in the presence of activating agent transforms it into porous sheet type carbon structures, BAC (*figure 3.1b*). The combined strategy of initial hydrothermal treatment followed by pyrolysis in the presence of activating agent is seen to transform it into carbon with open channels type morphology; BHAC (*figure 3.1c*). The BHAC channels have a diameter of around 100 nm-150 nm. The formation of channels can be explained by considering the effect of two opposing forces of temperature (which tries to transform the initial hydrothermal mass into microspheres) and KOH induced etching (which tries to disrupt the structures created).

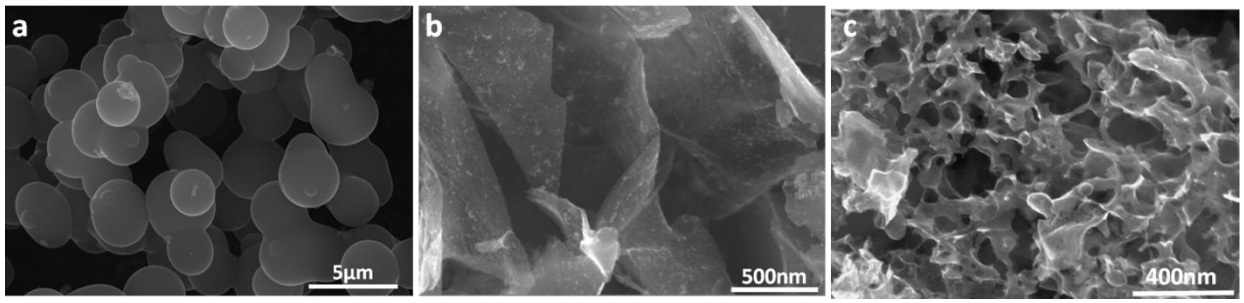

Figure 3.1 *FE-SEM images of different carbon forms synthesized from different synthesis protocols from the same basic sugarcane bagasse precursor at 800^{0}C pyrolysis (a) BHC, (b) BAC and (c) BHAC*

The channel type of morphology is further established by high resolution transmission electron microscopy (HR-TEM) images shown in *figure 3.2a* and *figure 3.2b*. The HR-TEM images reveal the presence of 100-200 nm sized channels which clearly agree with the SEM image of *figure 3.2c.*

The hydrothermal step initially creates the C=C backbone by dehydration of –OH groups which has a tendency to fold into microspheres at higher temperatures. The statement is supported by emergence of the C=C carbon content in BHP corresponding

to 284.6eV, C1s XPS peak, attributed to unsaturated carbon. XPS results are summarised in the *table 3.1*. The unsaturated content in BHP amounts to 23% of total carbon[30] (*table 3.1b*). As shown, such channel type morphology has a distinct advantage that is reflected in its significantly better electrochemical performance over the non-hydrothermally treated sample.

Figure 3.3a shows the X-ray diffraction (XRD) data for the bagasse pyrolysis products. The broad XRD peaks centred at 2θ of around 26^0 and 43^0 correspond to the graphitic (002) and (100) planes, respectively, revealing the presence of disordered carbon, as expected for pyrolysis at relatively low temperature of 800^0C[31]. The Raman spectrum (*figure 3.3b*) exhibits a broad disorder-induced D-band (1320 cm^{-1}) and an in-plane vibrational G-band (1590 cm^{-1}). The Raman data shows better graphitization in the case of hydrothermally treated samples, namely BHAC (I_G/I_D=0.76) and BHC (I_G/I_D=0.76), as compared to non-hydrothermally treated sample BAC (I_G/I_D=0.60)[32]. The XRD (002) inter-plane d-value is more for BHC (0.389 nm) pointing to more of two dimensional (2D) and less of c-axis interactions, which is also supported by higher I_G/I_D ratio. BHAC (which also has high I_G/I_D =0.76) shows similar graphitic in-plane ordering but the c-axis length (0.350 nm) is much less than BHC. This implies that in BHC the (002) planes is closer to graphitic order along the c-axis. In the case of BAC-800 lower I_G/I_D (0.60) shows lesser in-plane order and the 002 plane separation of 0.350 nm shows that the c-axis stacking close to graphite.

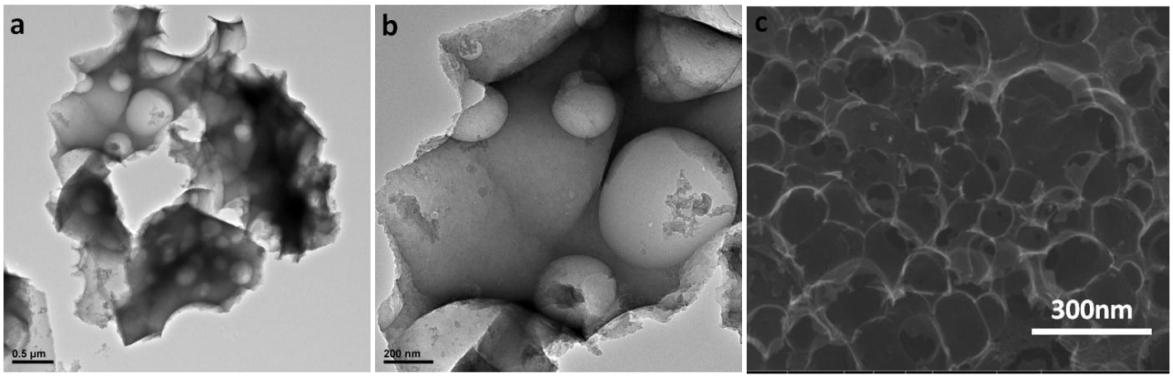

Figure 3.2 *a and b show HR-TEM images at two different resolutions; (c) FE-SEM image of BHAC-800*

Further it is useful to note that the I_G/I_D value is in between 0.52 of commercial activated carbons[33] and the case of ordered carbon nano-sheets wherein the previously

reported ratios go close to 0.90 for similar pyrolysis temperatures[24]. Also, the Raman spectra show emergence of peaks at 1230 cm^{-1}, 1385 cm^{-1} and 1550 cm^{-1} in the case of the BHAC and BHC samples. The peak at 1385 cm^{-1} can be attributed to different type of sp^2 clustering as compared to the normal sp^2 graphitic rings and chains[34, 35]. These should be responsible for holding the sheets in the folded form and creating interconnections in BHAC, and also for stitching the carbon framework into spheres in BHC. The 1550 cm^{-1} peak can be attributed to the G counterpart of the 1385 cm^{-1} peak arising from the vibrational mode of the different type of sp^2 content. The peak

Table 3.1 *XPS analysis of different carbon samples prepared by baggase pyrolysis is presented. Table 3.1a lists carbon and oxygen percentages of different samples and table 3.1b shows the functional group analysis of carbons obtained by XPS fitting.*

Element	BHAC-180	BHAC-800	BAC-800	BHC-800
C	74%	89%	93%	93%
O	26%	11%	7%	7%

	Carbon				
	C=C	C-C	C-O	C=O	COOR
BHP-180	23%	40%	37%	-	-
BHAC-800	43%	23%	9%	9%	17%
BAC-800	44%	19%	11%	9%	17%
BHC-800	49%	24%	7%	7%	13%

around 1385 cm^{-1} is seen to emerge in some nitrogen and boron doped disordered carbons as well. In the absence of such doping, its emergence can be attributed to the graphitic lattice of disordered carbon itself[36, 37]. Presence of different type of sp^2 content just helps in creating defects for relaxation of the selection rule for its excitation and itself gives a different C=C peak 1550 cm^{-1} which lies close to the main graphitic peak

of 1582 cm^{-1}.

In light of above discussion, the 1230 cm^{-1} peak can be assigned to the sp^3 content which is important for the assembly of planer graphitic domains into spherical and/or cylindrical structures. From the XRD and using Scherrer formula one can estimate the c-axis crystallite size parameter to be 0.78 nm. It implies that the walls in the 3D interconnected network are in the form of two to three layers of sheets stacked together. Thus, both, the synthetic steps and the temperature contribute to shaping the material into the desired connected channel-type morphology.

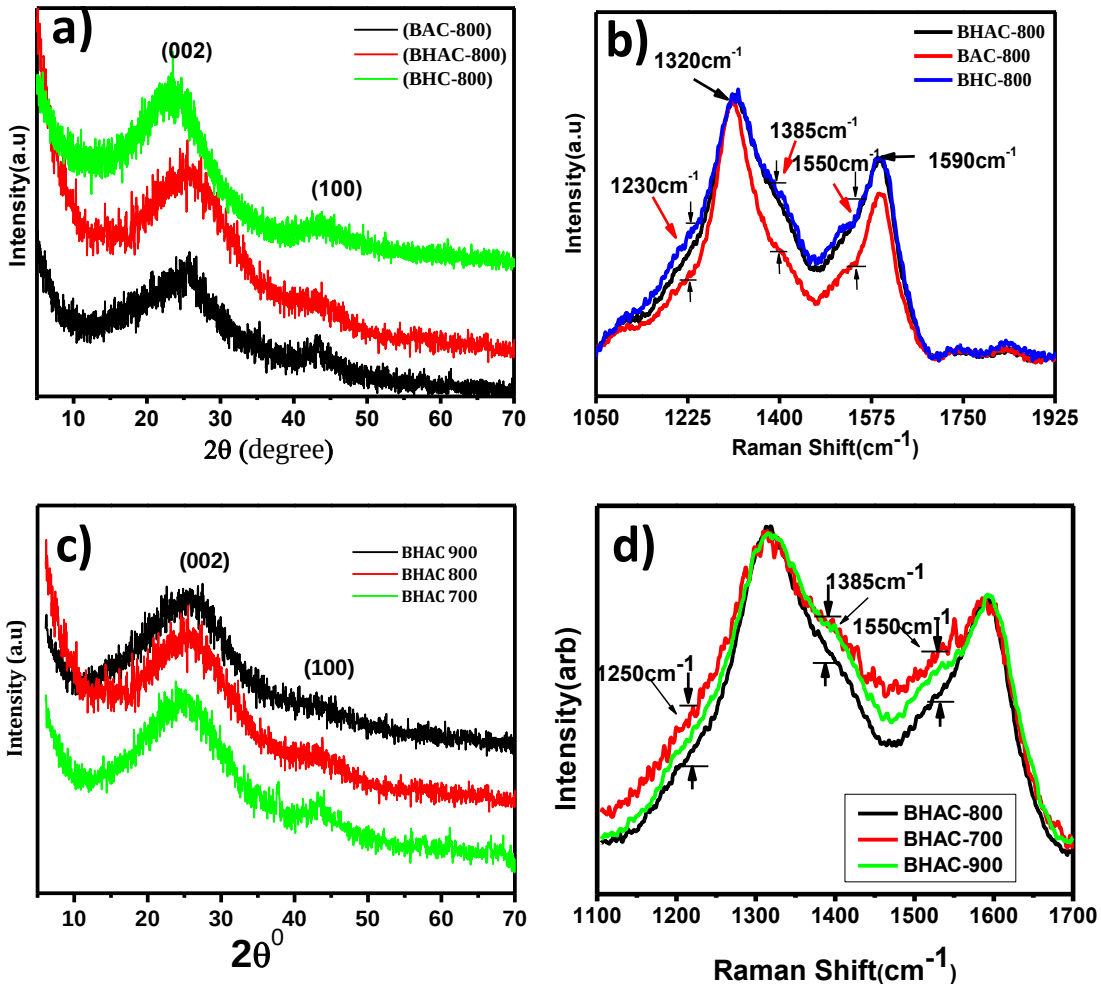

Figure 3.3 *a and b show XRD and Raman spectra of BHAC, BHC and BAC samples prepared from sugarcane bagasse, respectively; (c and d) show the processing temperature variation effects on the evolution of XRD and Raman patterns of BHAC material.*

The data on temperature variation effect on the evolution of the Raman and XRD patterns are presented in *figure 3.3c* and *figure 3.3d*. It can be seen that temperature has an effect on controlling the amount of sp^3. It can be seen that BHAC-800 has the optimum sp^3 content and non-graphitic sp^2 content as reflected in the Raman intensity enhancement at 1220 cm^{-1} and 1385 cm^{-1} respectively. To investigate the porous nature of the material BET analysis of the samples was performed. The BET isotherms for the three cases of interest are shown in the *figure 3.4a.* The BHAC-800 sample has the surface area of 1260 m^2/g with type IV isotherm, typical for materials having simultaneous presence of micro and meso porosity[38]. This is further proved by the pore size distribution plot (*figure 3.4b*) showing some pores of diameter 4-5 nm, apart from micropores, < 2nm which are abundantly present. It is useful to mention here that on increasing the final processing temperature from 700^0C to 800^0C, the surface area was seen to increase considerably from 800 m^2/g to 1260 m^2/g. This fast increase can be attributed to peak activity of KOH around this temperature[39].

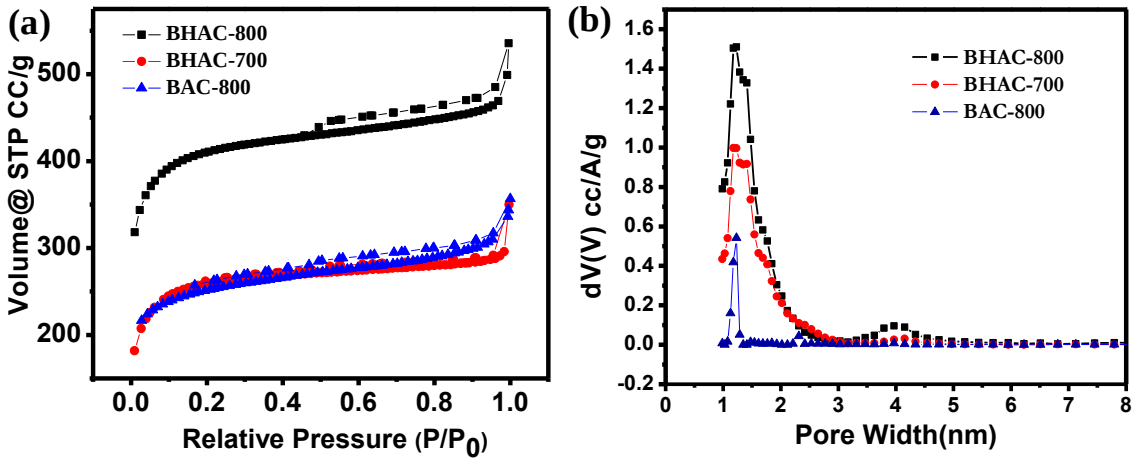

Figure 3.4 *a) Nitrogen adsorption-desorption isotherms for sugercane bagasse derived carbons. b)Pore size distribution calculated from the adsorption isotherms using density functional theory.*

The higher surface area realized in the 800^0C case may then be attributed to the larger pore volume. Thus, at high temperature KOH serves in digging deep in the pores than in increasing the pore diameter. BET surface area of 778 m^2/g of BAC-800 further brings out the importance of hydrothermal pre-processing for increasing the surface area.

The pore size distribution plots (*figure 3.4b*) show narrow pore size distribution in the case of BAC-800 as compared to BHAC-800. The widths of BHAC-800, BHAC-700 and BAC-800 pore size distribution peaks at half maxima are 0.26 nm, 20 nm, and 0.06 nm, respectively. From the pore size distribution plots it can also be observed that on going from BAC-800 to BHAC-800, the distribution is tilted towards higher mean pore size suggesting that BHAC-800 can act as a high power capacitive charge storage material. The meso-porosity of 11% (calculated roughly from peak areas) centred at a pore size of 4nm (as against only 3% for BHAC-700) suggests that BHAC-800 is suitable for high power density supercapacitor application.

The SEM, TEM, Raman, and BET characterizations together promise the superiority of BHAC-800 over the BAC sample in the context of EDLC (electric double layer capacitors) charge storage. To investigate the charge storage capability and mechanism, cyclic voltammetry (CV) was performed for the BHAC-800 and BAC-800 samples within the potential window of 0 to 1 V in a typical three-electrode cell configuration, using 1M H_2SO_4 aqueous solution as electrolyte, a Pt strip as counter electrode, and Ag/AgCl electrode as reference. *Figure 3.5a* and *figure 3.5b* compare the CVs of the BAC-800 and BHAC-800, performed at two different scan rates of 20 mV (lower) and 200mV (higher). The overall current density in the CV of the BHAC is clearly higher than that of BAC electrode. This confirms the superior capacitive property of BHAC over BAC. The CV of the BHAC electrode at different scan rates (5 to 200mV/s) was also performed. It was observed that even at the higher scan rates nearly rectangular shape is maintained which is important for practical applications (*figure 3. 5c*). Further the capacitances obtained from charge-discharge and cyclic voltammetry agree well with each other and are given in the *table 3.2a*.

Charge-discharge curves for the BAC and BHAC electrodes at a high current density of 10A/g are shown in *figure 3.5d*. The delayed discharge time of BHAC electrode confirms its better capacitance property than the BAC electrode. Also, the charge-discharge was performed at various current densities from 1 to 20A/g for both the electrodes as shown in *figure 3.5e*. The maximum specific capacitance value obtained for the BHAC electrode at a current density of 1A/g is 280F/g.

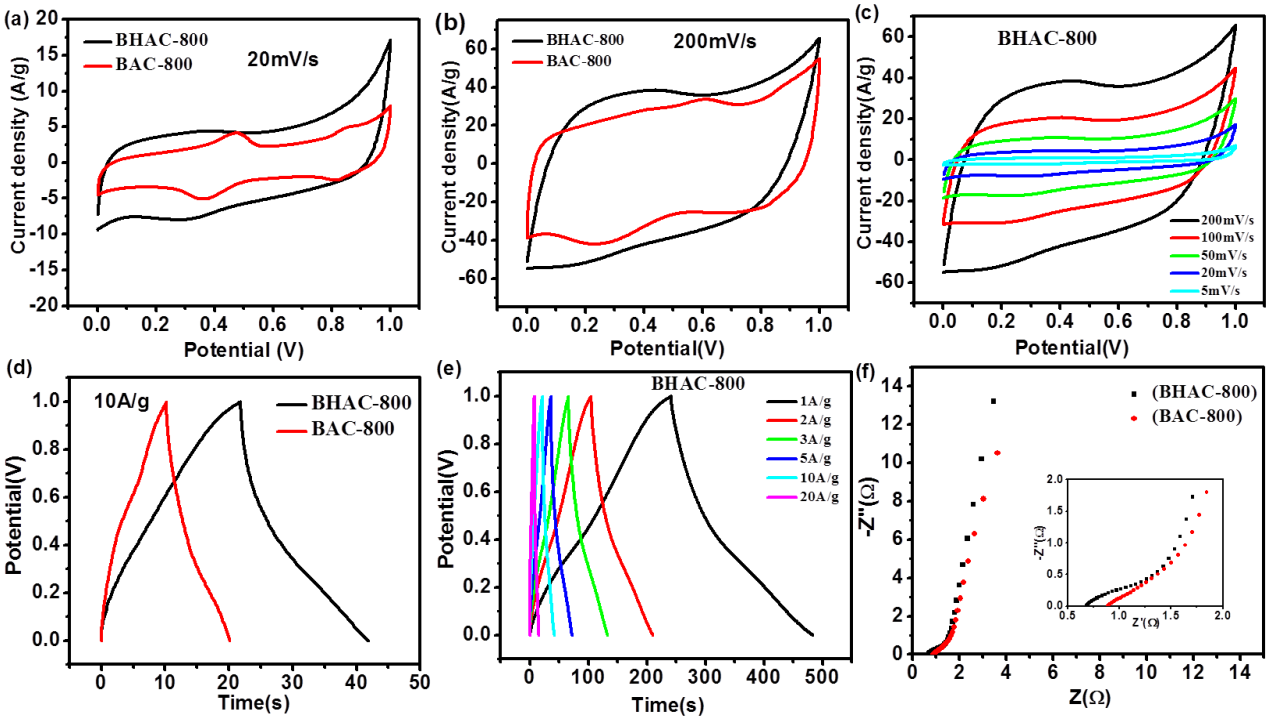

Figure 3.5 *Electrochemical characterization of sugarcane derived carbons: a) Comparison of CV curves for BHAC-800 and BAC-800 samples at the scan rate of 20mV/s; b) Comparison of CV curves for the BHAC-800 and BAC-800 samples at a scan rate of 200mV/s; c) CV curves of BHAC-800 with three electrode assembly at scan rates ranging from 5 mV/s to 200 mV/s (in 1M H_2SO_4); d) Comparative 3-electrode charge-discharge plots for the BHAC-800 and BAC-800 samples at 10A/g; e) Charge-discharge curves for BHAC-800 at different current densities with a 3-electrode assembly (in 1M H_2SO_4); f) Comparative Nyquist plots for BHAC-800 and BAC-800 over the frequency range of 100mHz to 100KHz.*

Electrochemical impedance spectroscopy (EIS) further supports the good electrical interconnectivity in BHAC-800. The Nyquist plots for BHAC-800 and BAC-800 samples are shown in *figure 3.5f*. The real axis intercepts[40] which imply Electrochemical series resistance (ESR), of 0.66 Ω (BHAC) and 0.89 Ω (BAC) can be attributed to higher conductivity in the case of BHAC-800 due to inter-connectivity, the foundation for which is laid in the initial hydrothermal treatment.

Electrochemical performance of BHAC-900, BHAC-700 and BHC-800 was also tested (*figure 3.6a* and *figure 3.6b*) and it was concluded that the 800^0C sample shows a much

better performance supporting our choice of this pyrolysis temperature as the true optimum. Very negligible capacitance value was observed for the BHC electrode (*figure 3.6b).* It is important to notice that two distinct peaks are observed for the BAC electrode, *figure 3.6c* and *figure 3.6d* (at low scan rate) which implies its pseudocapacitive nature. But in the case of BHAC, the capacitive nature mainly arises because of the electrical double layer formation. These data agree with the XPS results where pseudocapacitive surface functional group -C-O has higher concentration in BAC than BHAC (*table 3.1a* and *table 3.1b*). Yet the overall higher capacitance in BHAC can be attributed to the morphological advantage it possesses over the BAC.

In the case of the BAC electrode (*figure 3.6c* and *figure 3.6d*) the specific capacitance value of only 180F/g is observed. The variation of specific capacitance with discharge rate for BAC and BHAC is given in the *table 3.2b*. Thus, 56% of the capacitance enhancement is obtained in the hydrothermally pre-processed case, which can be directly correlated with the increase in the surface area (60% enhancement) by such processing. Importantly, this enhanced surface area is accessible for the solvated ion migration due to the unique open-type nature of porosity.

The rate capability of the BHAC electrode is much higher than the BAC electrode. After cycling the current density from 1A/g to 20 A/g, 72% of the capacitance retention is observed in the case of the BHAC electrode, whereas only 52% is retained at 20A/g in the case of the BAC electrode. Thus capacitance gain observed at 20 A/g for BHAC is 113% over that of the BAC case, which further highlights the role of channel-type of morphology. Indeed, this enhanced current response can be related to the open channel type morphology which has a role in the reduction of ion transport time ($t = l/d$, where, l is ion transport length and d is ion transport coefficient), thus maintaining high capacitance at high currents.

The cyclic stability of the BHAC electrodes, shown in *figure 3.7a,* was also evaluated at a high current density of 10A/g up to 1000 cycles. More than 90% of the capacitance retention was observed which once again confirms the superiority of this material for practical high power density applications.

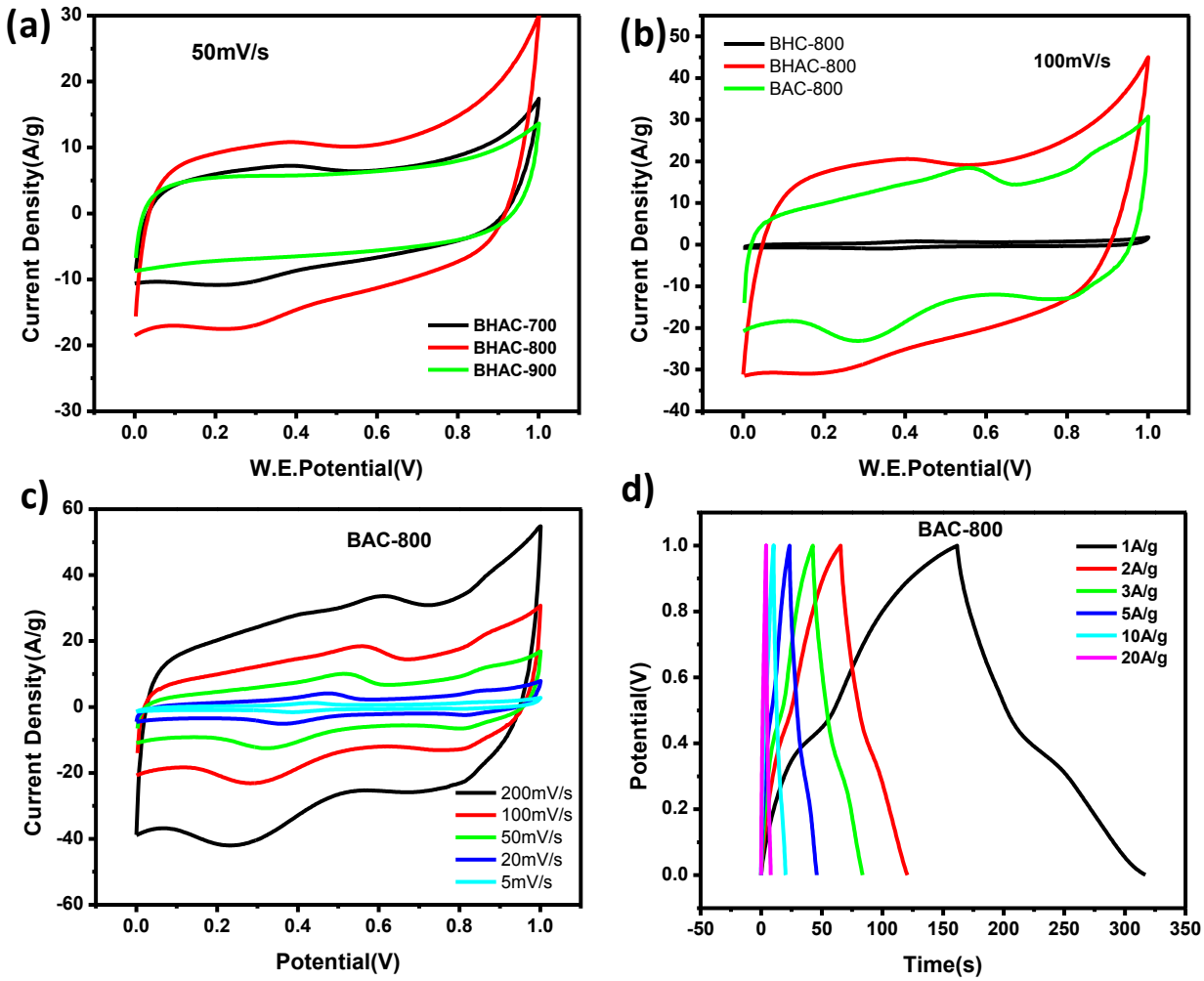

Figure 3.6 *Three electrode cyclic voltammograms in 1M H_2SO_4 using platinum strip as counter electrode and AgCl as reference electrode; a) Comparison of the performance of the samples obtained by different activation temperatures at 50mV/s scan rate; b) CV curves for BHAC-800, BAC-800, BHC-800 at 100mV/s, highlighting the importance of hydrothermal and activation steps. c) CV of plots for BAC-800 in 1M H_2SO_4. d) Charge-discharge plots for BAC-800 in 1M H_2SO_4.*

Table 3.2 *Comparison of charge-discharge capacitances of BHAC-800 and BAC-800 samples, at different current densities.*

BHAC-800 3-electrode (charge-discharge)			BAC-800 3-electrode (charge-discharge)	
Current density (A/g)	**Capacitance (F/g)**		**Current density (A/g)**	**Capacitance (F/g)**
1	**280**		**1**	**180**
2	**248**		**2**	**130**
3	**236**		**3**	**140**
5	**230**		**5**	**132**
10	**237**		**10**	**110**
20	**200**		**20**	**94**

To check the actual device characteristics, two electrode cell, cyclic voltammetry (CV) measurements were also carried out in 1M H_2SO_4 solution. *Figure 3.7 b* and *figure 3.7c* respectively show the CV and charge-discharge plots in the potential range of 0-1V. The rectangular shape of the CV curves shows the perfect double layer type charge storage. The charge-discharge capacitance of each electrode in this assembly is 225F/g at 1A/g which drops down to 165F/g at 10A/g. The deviation of the 2-electrode capacitance from the 3-electrode cell may be attributed to the asymmetry in the adsorption of positive and negative ions. Thus, with better choice of electrolytes and counter electrodes the maximum capacitance can be extracted from the material.

Figure 3.7d shows the Ragone plot for BHAC-800 with calculated power density and energy density. Although in a working symmetric cell, the material does not perform to its full potential due to asymmetry in charge storage. Still, the performance is comparable to best electrochemical capacitors and distinctly superior to activated carbons[14, 20, 26, 27, 41, 42]. Further the capacitance values obtained compare well with the other reported forms of carbon shown in *table 3.3*. The material shows a good energy density of 7Wh/kg at a power density of 571W/kg and exceptional performance of 5Wh/kg at 3.6kW/Kg. This is a huge gain in aqueous solution case when compared to activated carbons, where the pore accessibility becomes a limit on energy extraction at higher powers[43]

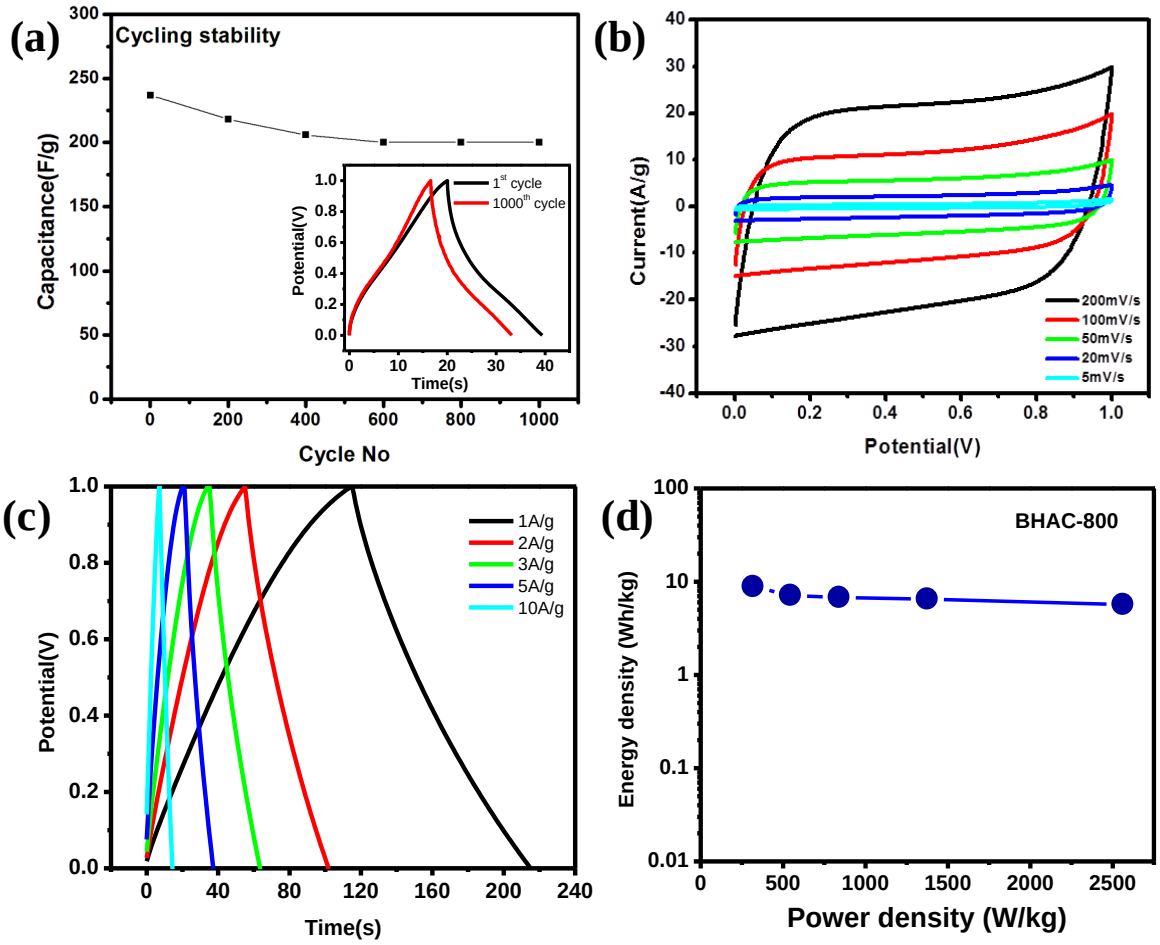

Figure 3.7 *Performance of two electrode working cell constructed from BHAC-800 coated on the graphite electrodes dipped in a beaker containing 1M H_2SO_4: a) Cycling stability of BHAC-800 at current densities of 10A/g; b) CV curves of BHAC-800; c) Charge-discharge curves with current densities ranging from 1A/g to 10A /g; and d) Ragone plot showing consistent energy delivery and storage up to very high power densities.*

Table 3.3 *Comparison of BHAC carbon with other forms of reported carbon*

Carbon Material	Activation method	S_{BET} (m^2/g)	Capacitance (F/g) Scan rate	Capacitance(F/g) current density	Electrolyte
Banana fibers	KOH $ZnCl_2$	686 1097	54 (100mV/s) 83 (100mV/s)	---	1M Na_2SO_4
Seaweed biopolymer	Thermal	273	190 (2mV/s)	198 (1A/g)	1M H_2SO_4
Waste news paper	KOH	416	---	180 ($1mA/cm^2$)	6MKOH
Sugarcane bagasse	NaOH	2871	---	109 (0.1A/g)	1M H_2SO_4
N2 +rGO + boron carbonitrides	-	527	169(10mV/s)	--	6M KOH
BHAC	***Hydrothermal***	***1260***	***275 (5mV/s)***	***200 (20A/g)***	***1M H2SO4***

3.4 Conclusion

In summary, it is shown that the functional carbon morphology attainable by hydrothermal pre-treatment of sugarcane baggase leads to significantly enhanced capacitance retention. The capacitance of 280F/g was obtained from the material at the current density of 1A/g and 72% of this value is retained at current density of 20A/g. These values are superior to the previous report on sugarcane bagasse on $ZnCl_2$ with similar activation conditions in which 40% capacitance retention was reported at same current densities.

3.5 References

1. J. R. Miller and P. Simon, *Science*, 2008, **321**, 651–652.
2. P. Simon and Y. Gogotsi, *Nat. Mater.*, 2008, **7**, 845–854.
3. E. Frackowiak and F. Beguin, *Carbon* , 2001, **39**, 937–950.
4. L. L. Zhang, R. Zhou and X. S. Zhao, *J. Mater. Chem.*, 2009, **38**, 2520–2531.
5. R. Kotz and M. Carlen, *Electrochim. Acta*, 2000, **45**, 2483–2498.
6. L. L. Zhang, R. Zhou and X. S. Zhao, *J. Mater. Chem.*, 2010, **20**, 5983-5992.
7. Y. J. Kang, S. J. Chun, S. S. Lee, B. Y. Kim, J. H. Kim, H. Chung, S. Y. Lee and W. Kim, *ACS Nano*, 2012, **6**, 6400–6406.
8. P. L. Taberna, P. Simon and J. F. Fauvarque, *J. Electrochem. Soc.*, 2003, **150**, 292-300.
9. B. Xu, F. Wu, R. Chen, G. Cao, S. Chen and Y. Yang, *J. Power Sources*, 2010, **195**, 2118-2124.
10. M. Lazzari, F. Soavi and M. Mastragostino, *Fuel Cells*, 2010, **10**, 840–847.
11. C. Largeot, C. Portet, J. Chmiola, P. L. Taberna, Y. Gogotsi and P. Simon, *J. Am. Chem. Soc.*, 2008, **130**, 2730–2731.
12. D. Pech, M. Brunet, H. Durou, P. Huang, V. Mochalin, Y. Gogotsi, P. L. Taberna and P. Simon, *Nat Nanotechnol*, 2010, **5**, 651–654.
13. D. Qu, *J. Power Sources*, 2002, **109**, 403–411.
14. E. Raymundo-Pinero, F. Leroux and F. Beguin, *Adv. Mater.*, 2006, **18**, 1877–1882.
15. L. Bao and X. Li, *Adv. Mater.*, 2012, **24**, 3246–3252.
16. Y. S. Yun, S. Y. Cho, J. Shim, B. H. Kim, S. J. Chang, S. J. Baek, Y. S. Huh, Y. Tak, Y. W. Park, S. Park and H. J. Jin, *Adv. Mater.*, 2013, **25**, 1993–1998.
17. D. Hulicova-Jurcakova, M. Seredych, G. Q. Lu and T. J. Bandosz, *Adv. Funct. Mater.*, 2009, **19**, 438–447.
18. A. E. Ismanto, S. Wang, F. E. Soetaredjo and S. Ismadji, *Bioresour. Technol.*, 2010, **101**, 3534–3540.
19. T. E. Rufford, D. Hulicova-Jurcakova, Z. Zhu and G. Q. Lu, *Electrochem. commun.*, 2008, **10**, 1594–1597.

20. V. Subramanian, C. Luo, A. M. Stephan, K. S. Nahm, S. Thomas and B. Wei, *J. Phys. Chem. C*, 2007, **111**, 7527–7531.
21. L. Sun, C. Tian, M. Li, X. Meng, L. Wang, R. Wang, J. Yin and H. Fu, *J. Mater. Chem. A*, 2013, **1**, 6462–6470.
22. H. J. Denisa, A. M. Puziy, O. I. Poddubnaya, S. G. Fabian, J. M. D. Tascón and G. Q. Lu, *J. Am. Chem. Soc.*, 2009, **131**, 5026–5027.
23. M. Biswal, A. Banerjee, M. Deo and S. Ogale, *Energy Environ. Sci.*, 2013, **6**, 1249–1259.
24. H. Wang, Z. Xu, A. Kohandehghan, Z. Li, K. Cui, X. Tan, T. J. Stephenson, C. K. King'Ondu, C. M. B. Holt, B. C. Olsen, J. K. Tak, D. Harfield, A. O. Anyia and D. Mitlin, *ACS Nano*, 2013, **7**, 5131–5141.
25. D. W. Wang, F. Li, M. Liu, G. Q. Lu and H. M. Cheng, *J. Phys. Chem. C*, 2008, **112**, 9950–9955.
26. T. E. Rufford, D. Hulicova-Jurcakova, K. Khosla, Z. Zhu and G. Q. Lu, *J. Power Sources*, 2010, **195**, 912–918.
27. K. Konno, Y. Ohba, K. Onoe and T. Yamaguchi, *Carbon* , 2008, **46**, 721–722.
28. K. Babel and K. Jurewicz, in *Journal of Physics and Chemistry of Solids*, 2004, **65**, 275–280.
29. L. Zou, B. Huang, Y. Huang, Q. Huang and C. Wang, *Mater. Chem. Phys.*, 2003, **82**, 654–662.
30. I. Retzko and W. e. s. Unger, *Adv. Eng. Mater.*, 2003, **5**, 519–522.
31. G. A. Zickler, B. Smarsly, N. Gierlinger, H. Peterlik and O. Paris, *Carbon*, 2006, **44**, 3239–3246.
32. A. C. Ferrari and D. M. Basko, *Nat. Nanotechnol.*, 2013, **8**, 235–446.
33. D. S. Knight and W. B. White, *J. Mater. Res.*, 1989, **4**, 385–393.
34. F. Tuinstra and L. Koenig, *J. Chem. Phys.*, 1970, **53**, 1126–1130.
35. A. C. Ferrari and J. Robertson, *Phys. Rev. B*, 2001, **64**, 155306-155319.
36. Y. Wang, D. C. Alsmeyer and R. L. Mccreery, *Chem. Mater.*, 1990, **2**, 557–563.
37. A. M. Rao, A. Jorio, M. A. Pimenta, M. S. S. Dantas, R. Saito, G. Dresselhaus and M. S. Dresselhaus, *Phys. Rev. Lett.*, 2000, **84**, 1820–1823.

38. J. Lee, S. Yoon, T. Hyeon, S. M. Oh and K. B. Kim, *Chem. Commun.*, 1999, **359**, 2177–2178.

39. J. Wang and S. Kaskel, *J. Mater. Chem.*, 2012, **22**, 23710-23725.

40. J. Zhang and X. S. Zhao, *ChemSusChem*, 2012, 5, 818–841.

41. M. Shimada, T. Iida and K. Kawarada, *J Mater Cycles Waste Manag.*, 2000, **2**, 100–108.

42. K. Gopalakrishnan, K. Moses, A. Govindaraj and C. N. R. Rao, *Solid State Commun.*, 2013, **175–176**, 43–50.

43. L. Zhang, X. Yang, F. Zhang, G. Long, T. Zhang, K. Leng, Y. Zhang, Y. Huang, Y. Ma, M. Zhang and Y. Chen, *J. Am. Chem. Soc.*, 2013, **135**, 5921–5929.

Chapter 4

Natural-gel derived, N-doped, ordered and interconnected 1D nanocarbon threads as efficient supercapacitor electrode material

A natural hydrogel has been successfully templated into nitrogen doped interconnected 1D nanostructure by hard templating method using SBA-15 template. With urea as nitrogen doping agent, a high nitrogen percentage of 7.0 at.% was achieved. Urea was seen to play a role in increasing the order and compactness of the final carbon product. By snipping the carbon into nano 1D threads a fairly high surface area up to 837 m^2/g was achieved with high density of mesopores characterized by pore size of 4-5 nm and pore volume of 0.87-0.89 cm^3/g. The mesoporous architecture was channel type with an average width of ~4nm. With these characteristics the material represents an architecture that is adequate for high power supercapacitor electrode application. Indeed, it was seen to deliver a capacity of 285 F/g at a current density of 1 A/g with only a small percentage loss in this initial capacitance value at a higher current density of 10 A/g (210 F/g). These values suggest a high capacity retention of 74% up to 10 A/g and 62% capacitance retention (176 F/g) at extremely high current density of 40A/g. The cycling stability of the material is also commendable as 96% capacity retention is recorded after 2000 charging-discharging cycles implemented at a high current density of 10A/g.

The content of this chapter is published in:

***RSC Adv.**, 2015,**5**, 51382-5139.*

Reproduced by permission of The Royal Society of Chemistry.

4.1 Introduction

The quest for high performance energy storage materials has put porous carbons on the forefront for various related applications, especially the fields of great current significance namely renewable energy and mobility.[1,2] Interestingly, the supercapacitor domain is still dominated by carbon materials almost exclusively despite some promising transition metal oxide options.[3,4] Indeed, the technology focus on carbon materials owes to their high surface area for ion adsorption and desorption, appropriately and easily controllable pore size distribution for ion transport, need of less intricate device design, and above all the abundance of precursors and inexpensive nature of synthetic processes.[5-9] However, these materials lack in their electrical conductivity and thereby in the ability to connect all the energy storage units to the current collectors. Additionally, lack of the desirable degree of conductivity offers resistive paths to the capacitive energy storage.[10] Inclusion of heteroatoms (N,S,B) in the semi-graphitic carbon framework is helpful in increasing the conductivity by their participation in the delocalization of electron lone pairs through unsaturated graphitic mini lattice. Among the various heteroatoms, nitrogen has been the most efficient dopant as it is similar in size to the host carbon atom.[11-20] Importantly, such heteroatom doping enables better conductivity without compromising the surface area and pore architecture.

The effective accessible surface area of carbon materials for charge storage applications can be enhanced by enforcing porosity therein. The most commonly employed strategy for generating porosity is the famous activation procedure by employing either chemical or physical activating agents which work by digging holes in the carbon matrix. Two types of activation procedures are employed: 1) *Ex-situ* activation, that is effected by carrying out pyrolysis in the presence of activation agents[19, 21-28] (KOH, NaOH, $ZnCl_2$, CO_2, and steam etc.), and 2) *In-situ* activation, which is effected by direct pyrolysis of salt of a suitable organic carbon precursor.[12, 29-34]

Besides activation the other interesting strategy employed for the generation of high surface area carbons has been the hard templating method. This method

involves infiltration of a carbon precursor inside the nano dimensional physically separated spaces followed by high temperature inert atmosphere pyrolysis. Physical barriers prevent the union of carbon-carbon grains and thus enable one to snip the carbon framework into nano-dimensional morphologies. Assembly of such nano-carbon structures ensures enough spaces which give rise to porosity and hence to high surface area.[35-40] Mesoporous silica templates like (SBA-15, KIT) have proved efficient in this respect, being chemically inert and stable up to very high temperatures.[41-46]

Template based synthesis of carbon materials started with the infiltration of sucrose inside the MCM-48 template in 1999.[40] Thereafter glucose, xylose, furfuryl alcohol and phenol resins are reported to have been successfully infiltrated and mesoporous carbon derived by this process. However, complete reverse replication of silica template by the carbon synthesized inside the porous matrix was achieved for the first time by infiltration of sucrose in SBA-15.[40] Sang Hoon Joo et al. infiltrated furfuryl alcohol inside SBA-15 and successfully carried out the polymerization inside the pores. Carbon material thus obtained by pyrolysis was a complete reverse replica of the silica template.[36] Infiltration of readymade resorcinol gel inside the mesoporous channels and the energy storage application of the corresponding carbon material has been reported very recently.[15] Gel infiltration in the channels is a slow process and needs 2-3 infiltration cycles. However, it offers the advantage of unbreakable channels which terminate into one dimensional carbon structures upon pyrolysis. One dimensionality of the final carbon product can be attributed to the poor fluidity of the gel which resists the diffusion through the complementary pores in the mesoporous channels and makes them isolated nano reactors.

Herein, we report the template based synthesis of super-capacitive carbon by infiltration of a natural hydrogel; pectin, in SBA-15 followed by pyrolysis in inert atmosphere. This is for the first time that natural gel has been directly infiltrated and pyrolysed inside a synthetic template for supercapacitive carbon preparation. Choice of pectin as precursor for the mentioned template based synthesis was

made, for it being easily available, cheap, naturally abundant and its efficient convertibility to carbon upon pyrolysis.[47] Pectin being a hydrogel, forms long unbreakable columns inside the silica channels with less sideways diffusion, fulfilling all the necessary requirements for the transformation into one dimensional carbon threads. Added superiority of pectin over other gels (like resorcinol, PVA , PVP, etc.) as a precursor for the carbon synthesis lies in the presence of enough -OH groups available for hydrogen bonding with water and with the template walls.[36,48] Close binding with solvent through such physicochemical interaction is important to achieve deep penetration. Hydrogen bonding with the -OH groups of template channel walls amplifies the advantage as it leads to close packing inside the channel.

Pectin is a biopolymer and a close ally of biopolymers agarose and alginate which form thick hydrogels in water. Chemically, pectin is a polymer of α-galacturonic acid linked together by 1,4 glucosidic linkages having its carboxylic group esterified. Commercial pectin has its carboxylic groups amidated (15%-25%) which give some percentage of nitrogen doping (1-2 at.%) into the carbons derived from it. To achieve even higher nitrogen doping urea was used as a doping agent being fairly soluble in water and having a tendency to form hydrogen bonds with the -OH groups of pectin. With the use of urea a high nitrogen percentage of 7.0 at.% could be realized. Presence of urea in the infiltration mixture leads to viscosity enhancement by attachment with polymer strands of the gel. The more viscous the infiltrating solution, more is the resistance it faces for sideways flow even at higher temperatures, leading to more compactness in the final carbon. Interconnected structure of 1D nano-threads possessing surface area of 837m^2/g is thus achieved. The porosity is mostly mesoporous with small amount of micropores. With these specifications our material offers a great promise for high power delivery super-capacitor material.

4.2 Experimental section

4. 2.1 Materials used

Pluronic 123 and tetra ethyl orthosilicate were purchased from Aldrich chemicals. Pectin and alginate were purchased from Sigma chemicals, and agarose was purchased from Invitrogen chemicals. Urea for the experiments was purchased from Merck chemicals.

4.2.2 Synthesis of template

For the synthesis of SBA-15 template an already reported procedure was followed with tri block Pluronic123 as the structure directing agent and tetra ethyl orthosilicate (TEOS) as the silica source.[44]

4.2.3 Synthesis and nomenclature of different pectin derived carbon samples

4. 2.3.1 Pectin derived carbons

Carbon samples with different percentages of nitrogen doping were prepared by varying the initial pectin to urea weight ratio. Typical synthesis involved the gelation of pectin which was effected by dissolving 2g of commercial pectin powder in 50ml of water. The mixture was stirred for 2-3 hrs at 70^0C to get a uniform fluidic gel. Few millilitres of DI water was added at the interval of 1h to counter the evaporation loss. Urea was dissolved separately in 30ml of DI water in another beaker and the solution was heated to 70^0C. To get the different concentrations of nitrogen in the final product, different amounts of initial urea (0g, 1g and 2g) were dissolved in 30ml DI water. The two solutions were mixed together, 0.6 gm of SBA-15 was added to the pectin-urea mixture solution and the final mixture was stirred under refluxing conditions at 70^0C for 6h. The quantity of SBA-15 was decided via the consideration of optimum infiltration of gel (excess gel leads to non-templated variety of carbon and less quantity reduces the yield). The final mixture solution was then taken out and stirred at 70^0C to evaporate water. This step was repeated 2-3 times to get almost complete infiltration. The resulting yellow coloured mass was dried at 60^0C in vacuum oven for 24 hrs. This final product was pyrolyzed in a tube furnace at 800^0C in Ar

atmosphere for 2h. The carbon formed inside was released into the solution by treating the pyrolysed product with 40% HF. The carbon material was obtained by vacuum filtration and subsequent drying at 90^0C in a vacuum oven for 24 h. Based on the initial pectin to urea weight ratio and on the basis of whether or not the template was used in synthesis, the carbon samples were named in series as P0-00, PU-00, P0-SBA, PU-SBA21, and PU-SBA11. P0-00 means carbon material prepared by pyrolysis of pectin alone. PU-00 means the carbon sample prepared by pyrolysis of pectin + urea mixture in weight ratio of 1:1 (i.e. addition of 2g urea in 30ml DI water to 50ml of 2g pectin gel solution) without the use of a template. P0-SBA means carbon sample prepared by pyrolysis of pectin (i.e. addition of 0g urea in 30ml DI water to 50ml of 2g pectin gel solution) inside a 0.6g SBA-15 template. PU-SBA21 means carbon material prepared by pyrolysis of 2g pectin +1g urea mixture (i.e. addition of 1g urea in 30ml DI water to 50ml of 2g pectin gel solution in the synthesis procedure) inside 0.6g of SBA-15 template. PU-SBA11 means carbon material prepared by pyrolysis of 2g pectin + 2g urea (i.e. addition of 2g urea in 30ml DI water to 50ml of 2g pectin gel solution in the synthesis procedure) inside a SBA-15 template.

4.2.3.2 Synthesis of agarose and alginate derived carbons

Similar synthesis strategy was adopted for the carbon synthesis from agarose and alginate (sodium alginate) gels. The carbons prepared were named following the same analogy. Agarose and alginate derived carbons were named as AgU-SBA11 and AlU-SBA11 in analogy with PU-SBA11 for the pectin derived one.

4.2.4 Characterization and measurements

The different carbon samples synthesized from pectin were examined by X-ray powder diffraction using a Philips X'Pert PRO diffractometer with nickel-filtered CuKα radiation. Raman spectroscopy was performed using LabRAM HR800 from JY Horiba. High-resolution transmission electron microscopy (HR-TEM) was performed using IFEI, Tecnai F30, FEG system with 300 kV. FESEM was performed with the help of Nova Nano SEM 450. The surface area values for all the samples were determined by the Brunauer–Emmett–Teller (BET) adsorption method (Quadrasorb automatic

volumetric instrument). XPS was acquired using a PHI 5000 Versa Probe II equipped with a mono-chromatic Al Ka (1486.6 eV) X-ray source and a hemispherical analyzer. Appropriate electrical charge compensation was employed. Cyclic voltammetry measurements were performed using Auto Lab (model PGSTAT 30, eco-chemie).

4. 2. 5 Electrode preparations for electrochemical measurements

The electrodes were prepared by coating a slurry of 80 wt% carbon material, 15wt% carbon-black and 5wt% polyvinylidene diflouride (PVDF) in N-methylpyrrolidine on 1cm^2 area of carbon fibre paper strips (1cm×3.5cm) followed by drying at 90^{0}C for 24h. Three electrode measurements were performed with carbon coated on a carbon fibre paper as working electrode, platinum strip as counter electrode and calomel as reference electrode in 1M H_2SO_4. Two electrode measurements were performed on a cell with the material coated on two carbon fibre paper electrodes in 1M H_2SO_4.

4.2.6 Calculations

X-ray photoelectron spectroscopy (XPS) based atomic percentage calculations were carried out by subtracting the adsorbed oxygen peak area from the total area. Atomic sensitivity factors of 0.296 for carbon, 0.477 for nitrogen and 0.711 for oxygen were taken into consideration for the calculation of relative atomic percentages.

The gravimetric capacitance was calculated from charge-discharge plots using the following equations:

$$\boldsymbol{Cg = I * t}/(\mathrm{m} * \Delta\mathrm{V}) \quad \text{and} \quad \boldsymbol{Cg = 2 * I * t}/(\mathrm{m} * \Delta\mathrm{V})$$

for 3-electrode and 2-electrode assemblies, respectively. Here m is the loading, I is the applied current, ΔV is the voltage window and t is the discharge time.

The energy density and power density were calculated on the basis of the following equations for two electrode cell:

$$\boldsymbol{E} = \frac{\boldsymbol{Cg} * \mathbf{V^2}}{2 * 4 * 3.6} \quad \& \quad \boldsymbol{P = E/t}$$

Where t is discharge time.

4.3 Results and Discussion.

The synthesis of one dimensional carbon structures was achieved inside special template, SBA-15, with mesoporous long channels. *Figure 4.1* shows the TEM micrographs of the template material at different magnifications. The continuous channel type structures are distinctly visible with no observable breaks upto 500-600 nm. SEM images of the particles are displayed in *figure 4.2* the particle size of 800nm-1µm is observed. Thus, such a material can be utilized as a hard template for the synthesis of one dimensional 100nm-150nm long carbon structures. As the synthesis involves infiltration of sufficiently fluidic gel preparations into the channels of SBA-15 and pyrolysis therein, long one dimensional threads of carbon is expected upon dissolution of the template. This is what is clearly revealed by the electron microscopy images. *Figure 4.3* shows the EM images (different magnifications) for 1:1 weight ratio sample, PU-SBA11. *Figure 4.3a* to *figure 4.3c* show the FE-SEM images of PU-SBA11. The uniformly distributed carbon nano-aggregations can be seen in *figure 4.3a*.The magnified images in *figure 4.3b* and *figure 4.3c* show that these carbon aggregates are composed of ordered nano-carbon threads bundled together.

The images clearly reveal that the morphology is complementary to the silica template used *(figure 4.1 and figure 4.2)*. The TEM images in *figure 4.3d* to *figure 4.3f* further

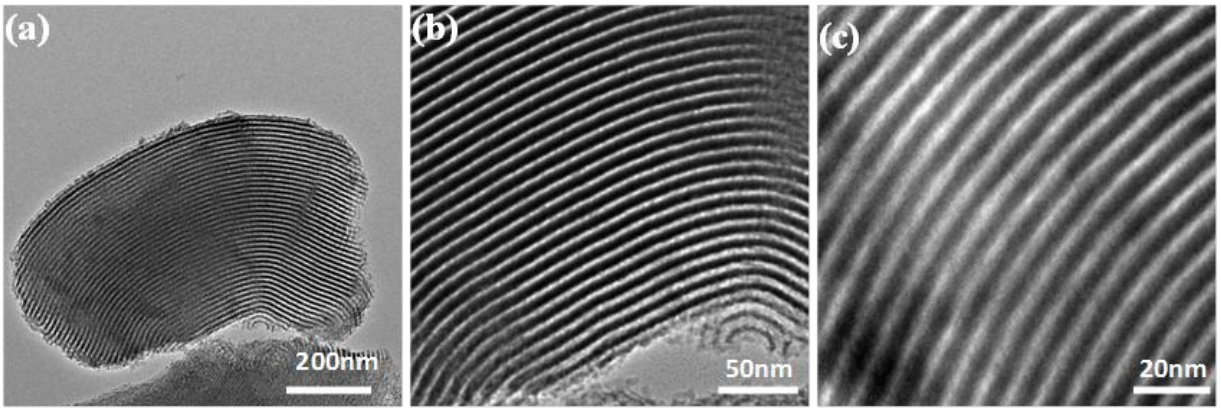

Figure 4.1 *a) to c) show the TEM images of SBA-15 template at different resolutions. Mesoporous channels are clearly visible with diameter of ~4-6nm.*

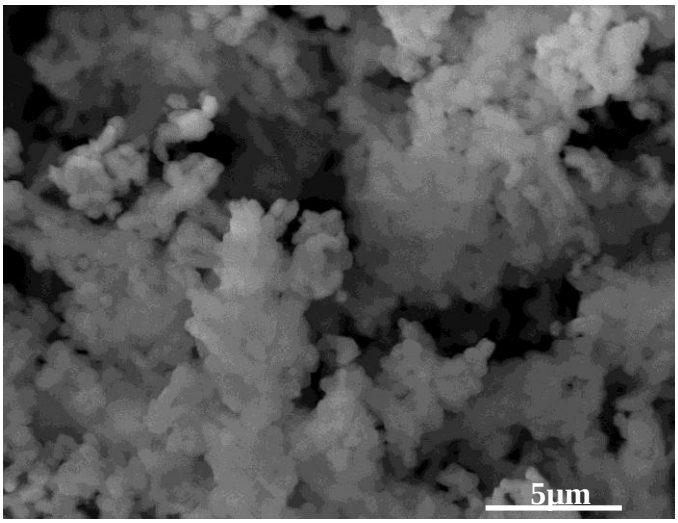

Figure 4.2 *FE-SEM image of SBA-15 particles synthesized by procedure described in experimental section*

establish the complimentary relationship between the silica template used and the carbon structures obtained. The continuous mesoporous channels are the hallmark of such morphology and distinguish it from ordered mesopores that have been obtained by templating various sugars and other natural materials inside variety of silica templates.[48]

Figure 4.4 shows the FE-SEM images for comparison. Various pectin-derived carbon samples of different denominations synthesized by varying the weight ratios of pectin and urea are displayed in the figure. It can be seen that by templating we have been able to snip micron dimensional carbon morphology (*figure 4.4a* and *figure 4.4b*) into nanoscale quasi-one dimensional structures (*figure 4.4e*). It is interesting to note that the presence of urea during pyrolysis has a marked influence on the final morphology. The compactness is observed to have increased with the increase in the urea to pectin weight ratio. This is confirmed by the morphology comparisons. The slouchy carbon morphology of P0-SBA (*figure 4.4c*) can be clearly distinguished from loosely arranged one dimensional carbon threads of PU-SBA21 (*figure 4.4d*) and well ordered compactly packed nano threads of PU-SBA11 (*figure 4.4e).*

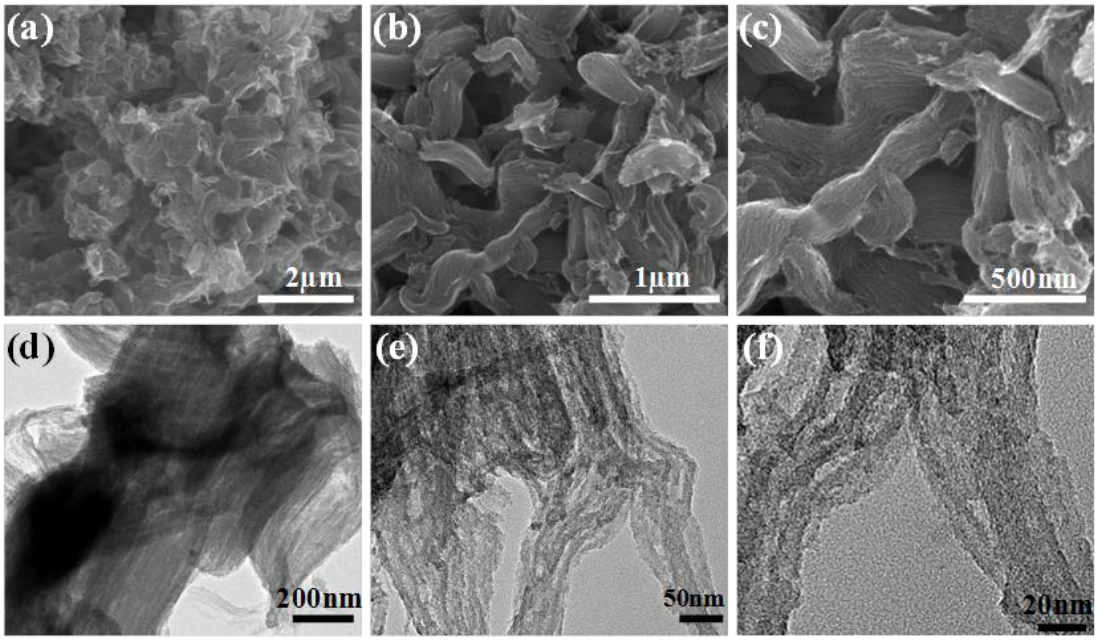

Figure 4.3 *Reveals the surface morphological characteristics and fine structuring of PU-SBA11 at different resolutions. In SEM micrographs* ***a)*** *Porous diffuse interconnected structures turn out to be composed of* ***b)*** *Uniformly arranged aggregates of 500-600nm of length 100-150nm diameter which in turn are to be composed of* ***c)*** *ordered thin carbon threads with 100-150nm length . The fine dimensions of these carbon threads with the diameter of 4-6nm is revealed by TEM micrographs* ***d)*** *to* ***f)****.*

Additionally FE-SEM images shown in *figure 4.5* display a comparison of the final morphology of carbon material prepared from pectin, PU-SBA11 with the carbon prepared from two other natural gels i.e. agarose (AgU-SBA11) and alginate (AlU-SBA11). It can be concluded that better infiltration of gel into the silica template is achieved in the case of pectin which leads to ordered and compact final carbon structure as compared to carbon from agarose and alginate. Carbon derived from pectin completely replicates the silica template which is not the case for agarose and alginate derived carbons. In order to account for the carbon morphology differences, the chemical composition and structure of three gels was surveyed. *Figure 4.6* shows the chemical structural formulae of the gels. The superiority of pectin over agarose gel for this particular synthetic strategy can be better appreciated by listing the total number of hydrogen bonding sites in

each polymer. A unit of pectin polymer (dimer) has four additional hydrogen bonding centres as compared to a similar unit (dimer) of agarose.

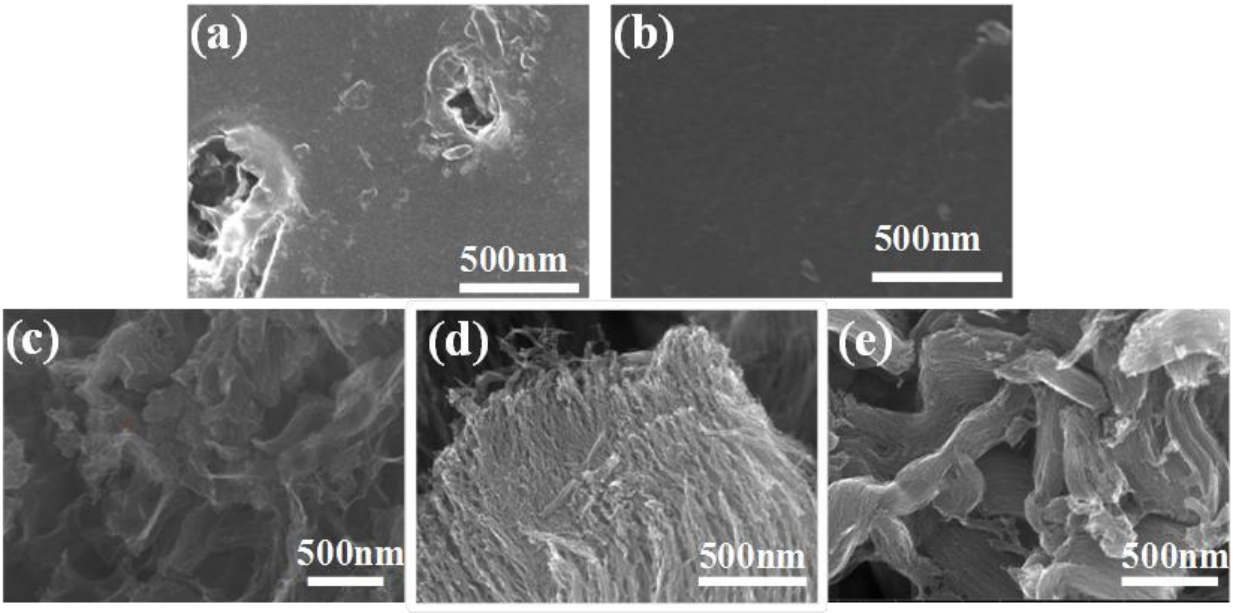

Figure 4.4 *Comparison of final morphology of pectin derived carbons at similar resolutions.* ***a)*** *and* ***b)*** *show that typical flat low surface area topography of P0-00 and PU-00 samples respectively.* ***c)*** *Shows the slouchy P0-SBA carbon.* ***d)*** *Shows relatively ordered, but loose arrangement of carbon threads in PU-SBA21.****e)*** *Shows ordered carbon threads and compactly packed in to carbon bundles.*

The additional hydrogen bonding centres in pectin lie in the polar carboxylic groups of galacturonic acid moieties at C5 position, two of which are present in each dimer. A dimer unit of agarose in comparison to pectin is composed of galactopyranose moiety which has a free OH group at C5 position, connected to 3,6-anhydro-galactopyranose which has its -OH groups at position 3 and 5 locked in an anhydrous bond. Thus in each dimeric unit pectin has four additional hydrogen bonding centres as compared to agarose. Alginate which is a polymer of α-Guluronic acid and β-Mannuronic acid possesses chemical structure similar to pectin except for the differently oriented -COOH moiety in mannuronic unit. The different spatial orientation of the -COOH group reduces the number of hydrogen bonding sites by two as compared to pectin.

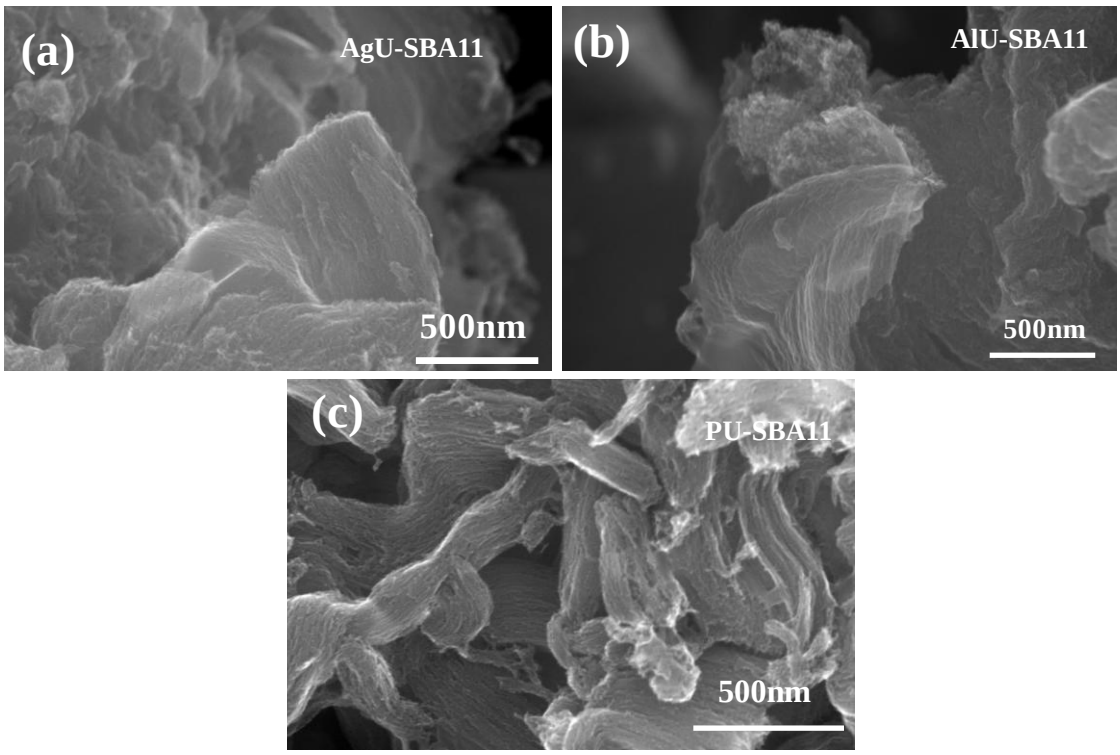

Figure 4.5 *FE-SEM images of three natural gels**.** a) Agarose-Urea gel, b) Na_Alginate-Urea gel, **c)** Pectin-Urea gel.*

Different levels of effective templating in the three cases which depends upon bonding with -OH groups of silica can be attributed to the number of these effective H-bonds.

To elucidate the order and arrangement of crystal planes X-ray diffraction (XRD) and Raman techniques were utilized. *Figure 4.7a* shows the XRD plots of the different carbon samples prepared from pectin. Two broad diffraction peaks centred at around 24.6^0 and 43.7^0 can be observed in *figure 4.4a,* corresponding to the graphitic 002 and 100 planes of carbon, respectively. The peak at 24.6^0 corresponds to the graphitic interplanar separation of 0.36nm. The XRD peaks in the case of other carbon samples fall around the same range with minor shifts pointing to basically similar atomic arrangements and similar lattice spacing in all the pectin derived samples. *Figure 4.7b* shows the Raman spectra of various carbons synthesized from pectin. All the samples exhibit the characteristic Raman disorder induced D-band and graphitic G-band in the range of 1329-1336 cm^{-1} and 1575-1585 cm^{-1} respectively.[49,50] The Raman

(a)

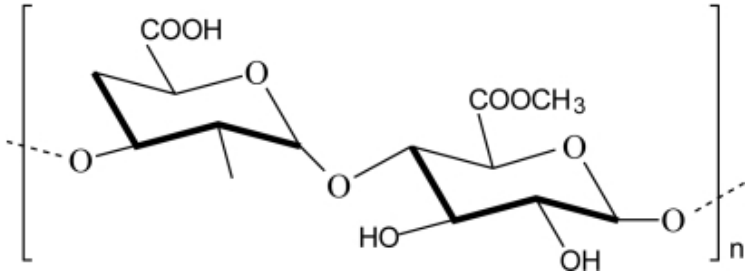

Pectin is a polymer of modified sugar, galacturonic acid and in the plant the carboxyl groups are esterified with methyl (CH3) groups which are not shown in the picture.

(b)

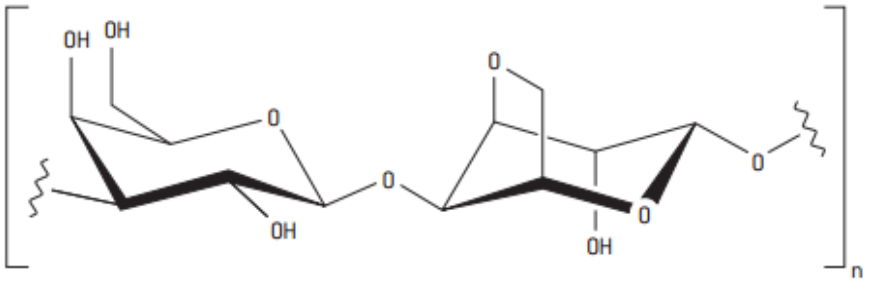

Agarose is a polysaccharide consisting of 1,3-linked β-D-galactopyranose and 1,4-linked 3,6-anhydro-α-Lgalactopyranose.

(C)

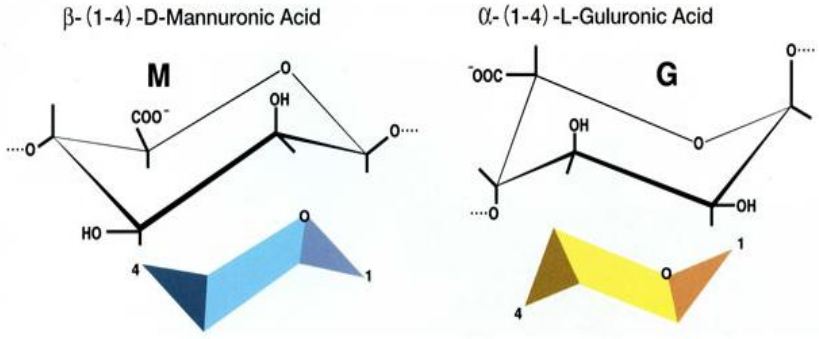

Alginic acid, a polysaccharide is composed of two types of Uronic acid.

Figure 4.6 *Shows the chemical structure of the three natural gels, a) Pectin {courtesy:http://openi.nlm.nih.gov/detailedresult.php?img=2866488_marinedrugs-08-01305f4 &req=4}b)Agarose {courtesy: http://bio.lonza.com/uploads/tx_mwaxmarketingmaterial /Lonza_ BenchGuides_ SourceBook_ Appendix_B_Agarose_Physical_Chemistry.pdf}*

c) Alginate {courtesy: http://www.kimica-alginate.com/alginate/chemical_structure.html}

parameters for all the samples derived from pectin match,*(table 4.1),* which implies similar atomic arrangements and similar kind of defects. I_D/I_G ratio of 1.4 reflects better graphitic order comparable to commercial activated carbon (Norit CA1). FWHM values for P0-SBA, PU-SBA21 and PU-SBA11 samples for the graphitic G-band stretch from 0.99, through 1.04 to 1.24. The increase in broadness can be attributed to the increase in the defect density due to N-doping.

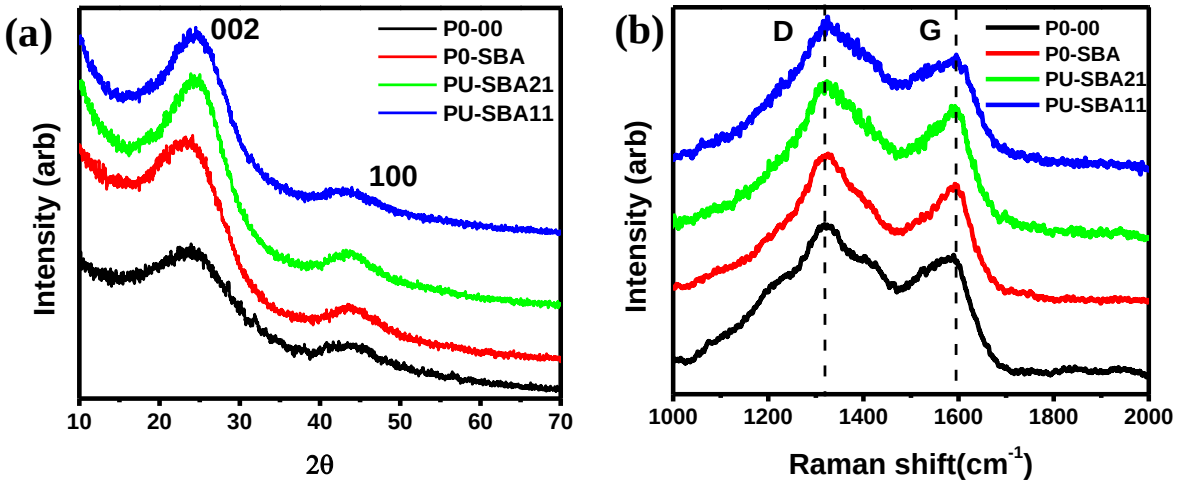

Figure 4.7.*a) XRD plots of pectin derived carbons b) Raman Plots of all pectin derived carbons*

X-ray photo electron spectroscopy was performed to check the surface layer elemental composition of different carbon samples. *Figure 4.8* shows the comparison of survey spectra of all the pectin derived carbons. As can be seen from the survey spectra, all pectin carbons show a characteristic nitrogen peak at ~400 eV besides carbon and oxygen peaks located at ~284 eV and ~531 eV.[51-53] Presence of this nitrogen peak in non-nitrogen doped samples can be traced to some amount of nitrogen present intrinsically in pectin itself and can be ascribed to certain degree of amidation in otherwise esterified carboxylic groups.[54,55] The deconvoluted carbon C1s spectra for all the pectin derived carbon forms are shown in *figure 4.9*. These are also characterized by a peak at 285.7 eV assigned to nitrogen-carbon bond. The deconvoluted individual nitrogen N1s spectra for P0-00, P0-SBA, PU-SBA21 and PU-SBA11 are shown in *figure 4.10*. In the samples P0-00 and P0-SBA where no external doping was enforced nitrogen doping percentages of 2.3 at.% and 2.6 at.% respectively, are observed. Increase in urea to pectin ratio has definitely led to increased doping of nitrogen in the

carbon lattice. Nitrogen doping %age of 7.0 at.% was detected in PU-SBA11 and nitrogen percentage of 3.4 at.% was detected in PU-SBA21. Nitrogen percentage of 3.4 at.% was also observed for PU-00.

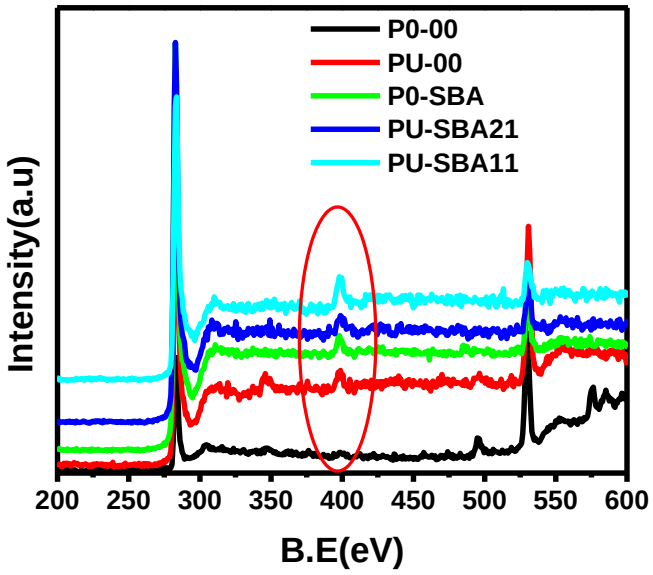

Figure 4.8 *Comparative survey XPS spectra of all pectin derived samples.*

This observation shows the positive feedback effect of confined spaces in efficient doping. To complement the XPS findings, EDS analysis of PU-SBA11, PU-SBA21, P0-SBA samples was performed. EDS data shown in *figure 4.11* reflects a similar trend for N-doping as revealed by XPS. The absolute surface concentrations of C, N and O determined from two techniques are in close agreement. As can be seen the Nitrogen XPS is dominated by Pyridinic (398.2eV), and pyrrolic (400.2eV) components both of which are essential for imparting the conductivity by participation in delocalisation.[56] In addition to these, the oxidised-nitrogen peak is observed between 403eV-405eV in some samples. N1s spectra of PU-SBA11shows the emergence of graphitic nitrogen peak at 401.1eV.[57,58] The emergence of graphitic peak can be attributed to higher urea percentage which forces the carbon rings to assemble around the nitrogen atom. Another interesting observation is that most of the nitrogen is trapped in the form of five membered pyrrolic rings. The predominance of pyrrolic and pyridinic nitrogen can be due to the urea-sugar hydrogen bonds which keep the

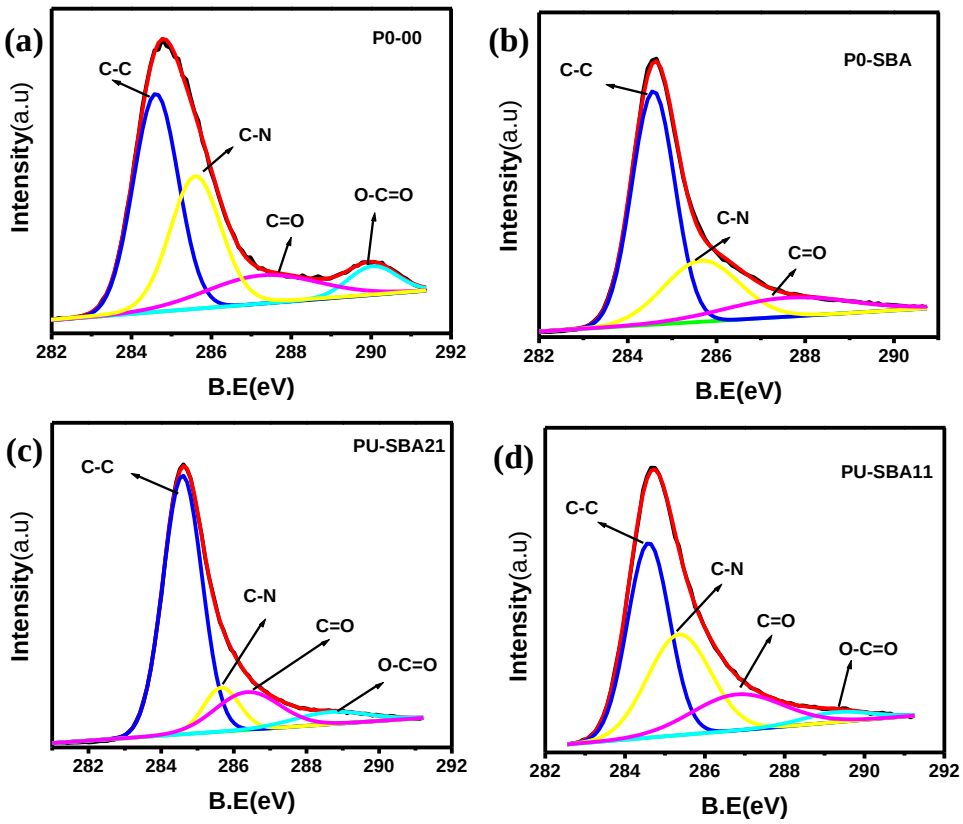

Figure 4.9 *Deconvoluted C1s spectra of all pectin derived carbons. a) P0-00, b)P0-SBA, c) PU-SBA21,d)PU-SBA11.*

nitrogen close to the ring, giving more probability for collapse into an edge nitrogen than the central graphitic nitrogen. But with the increase in urea to pectin weight ratio, as in PU-SBA11, extra urea is left out from hydrogen bonding with -OH moieties of pectin. The free urea upon decomposition releases nitrogen which is surrounded by excited carbon radicals from all sides giving better probability for getting incorporated as graphitic nitrogen.

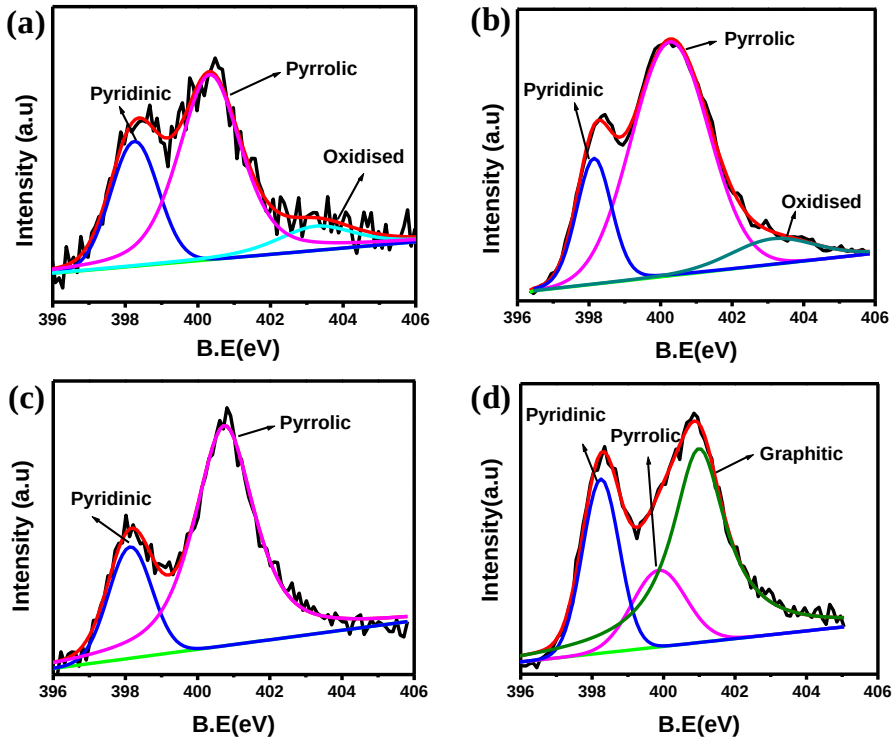

Figure 4.10 *Deconvoluted N1s XPS peak for different pectin derived carbon samples* ***a)*** *P0-00,* ***b)*** *P0-SBA,* ***c)*** *PU-SBA21* ***d)*** *PU-SBA11.*

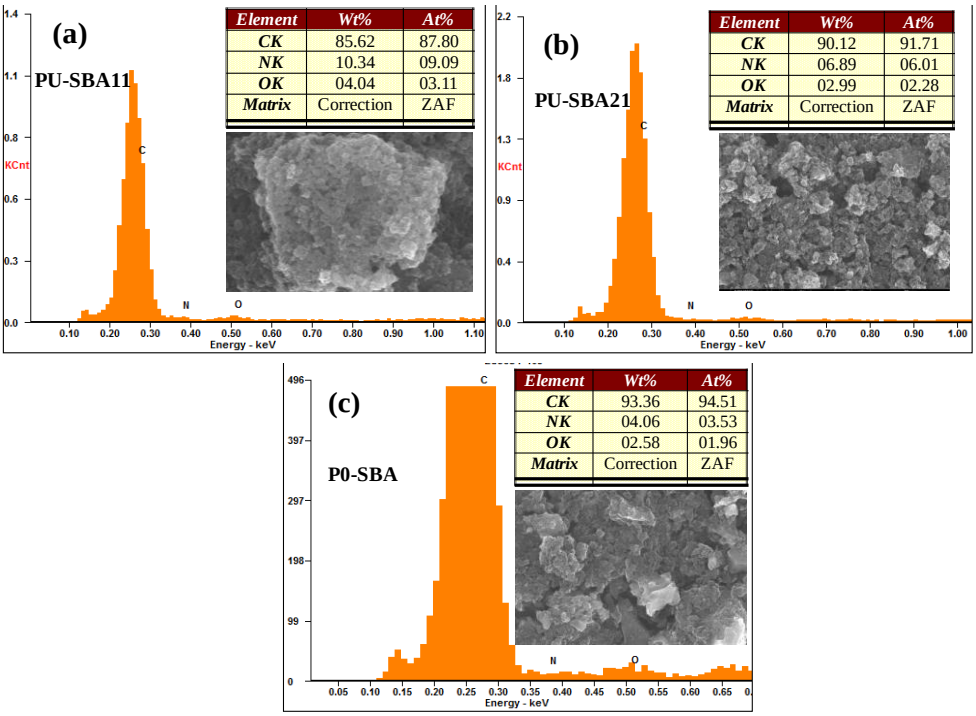

Figure 4.11 *EDS spectra of three pectin derived carbon forms along with the atomic percentage of C, O and N.* ***a)*** *PUSBA11,* ***b)*** *PUSBA21,* ***c)*** *P0-SBA.*

The pore structure was characterised by N_2 adsorption-desorption BET tests. *Figure 4.12a and figure 4.12*b show isotherm and pore size distribution for the templated and non- templated pectin derived carbons. The isotherms for all the samples show IUPAC type-IV behaviour.[59,60] This type of isotherm is characteristic of mesoporous carbons. Other interesting feature of the isotherm is the hysteresis. The samples show a clear distinction in their hysteresis differing both in the extent and the profile of hysteresis.[61]

The isotherms for the pectin sample in *figure 4.12a* reveal that interconnected pore structure evolves with increased urea to pectin ratio.[62,63] The hysteresis range for pectin derived samples, P0-00,P0-SBA, PU-SBA21, and PU-SBA11 is $0.1<P/P_0<1$, $0.1<P/P_0<1$, $0.4<P/P_0<1$, and $0.5<P/P_0<0.9$, respectively. Evolution of the hysteresis curves reveals the role of urea-assisted nitrogen doping in the morphology evolution, pore compaction and connectivity. The surface area is seen to have increased to 211m^2/g for P0-SBA from 4 m^2/g for P0-00. This increase is because of the splitting the micro-carbon to nano-carbons by physical

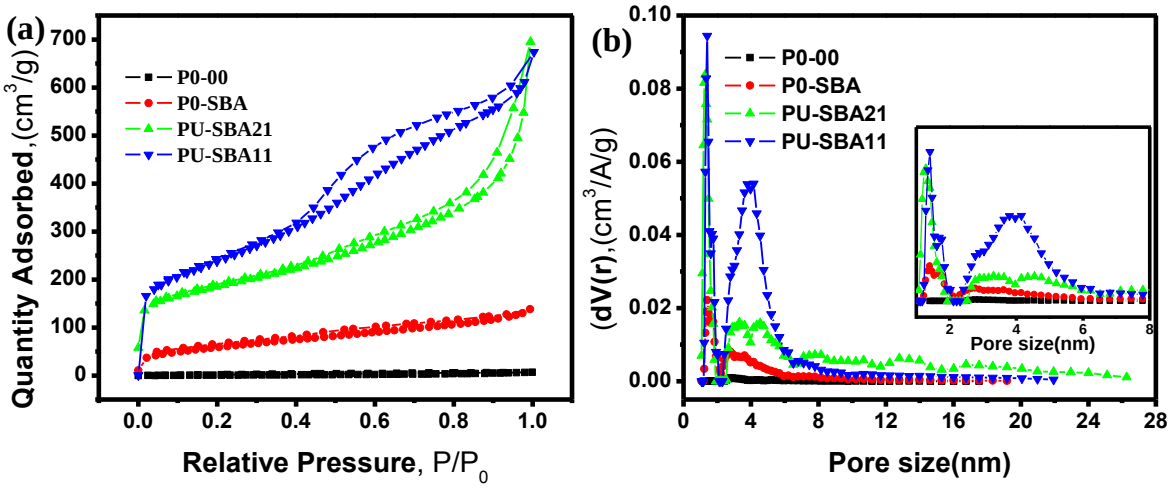

Figure 4.12 *Surface area and pore analysis using* ***N_2*** *adsorption-desorption analysis.* ***a)*** *N_2 adsorption- desorption isotherms for different pectin derived carbons with different hysteresis loops.* ***b)*** *Pore size distribution calculated using DFT calculation model.*

separation inside the template. Additionally, a surface area to 618m^2/g was observed for PU-SBA21 with the increase in urea to pectin ratio as compared to P0-SBA. Surface area of 837m^2/g was observed for PU-SBA11 with further increase in the urea to pectin ratio. Correspondingly there has been an increase in

the pore volume from 0.009cm^3/g for P0-00 to 0.87 cm^3/g for PU-SBA1. Thus increase in the urea to pectin ratio in the synthesis has led to the morphology which allows for higher surface area and beneficial pore distribution as revealed by the BET analysis.

Figure 4.12b compares the pore size distribution of the pectin derived samples. As can be seen there are two distribution maxima, located at 1.45nm and 4nm. Templating sets the foundation for the peaks at 1.45nm and 4nm. The peak at 1.45nm becomes intense with the increased urea percentage with negligible broadening, and the peak at 4nm becomes intense and broadened. With the presence and broad distribution of mesopores with a mesoporosity of 83% centered at ~4nm and a microporosity of 17% at ~1.5nm in addition to the high surface area of 837m^2/g, the sample PU-SBA11 promises a high power delivery for the supercapacitor application. *Table 4.1* Summarises the Raman, BET and XPS data. Comparing the different parameters listed in the table it can be concluded that PU-SBA11 should show the best electrochemical performance among all the samples.

Table 4.1 Summarises the Raman, BET and XPS parameters of different pectin derived carbons.

Sample		P0-00	PU-00	P0-SBA	PU-SBA21	PU-SBA11
BET analysis	*Surface area (m^2/g)*	4	-	211	618	837
	Avg. Pore width(nm)	2.7	-	1.4	1.3	1.4
	Mesoporosity (%)	99	-	71	78	83
Raman Data	*G/D band Position (cm^{-1})*	1575/1329	1575/1329	1582/1329	1581/1335	1580/1336
	I_D/I_G ratio	1.4	1.4	1.4	1.4	1.5
	FWHM (G/D) (cm^{-1})	114/280	114/280	99/238	103/250	124/275
XPS analysis	*Carbon (%)*	76.9	78.5	90.3	90.9	87.5
	Nitrogen (%)	2.3	3.4	2.6	3.4	7.0
	Oxygen (%)	20.8	18.1	7.1	5.7	5.7

The electrochemical performance of carbon materials synthesized from pectin was checked in 1M H_2SO_4 solution, in three electrode assembly, with calomel electrode as reference and platinum as the counter electrode. We first discuss the case of PU-SBA11, which was seen to perform best among all. *Figure 4.13* shows the electrochemical performance of the PU-SBA11 sample. Deviation from rectangular CV characteristics (*figure 4.13a*) is attributed to the pseudocapacitive charge transfer reactions due to nitrogen and oxygen functionalities that are especially highlighted in the three electrode measurements. Presence of these functionalities give the upper and lower wavy character to the otherwise nearly rectangular CV plot. Charge-discharge plots (*figure 4.13b*) show that capacitance of 285 F/g is observed at 1 A/g which reduces to 210 F/g at 10 A/g. Further high capacitance of 175 F/g is observed at extremely high current density of 40 A/g. Capacitance retention at higher currents (capacitance vs. current density plot, *figure 4.13c*) has thus been quite remarkable in the present material with the figures of 74% retention of 1 A/g value, at 10 A/g. Further, 62% retention was observed when the material was subjected to very extreme current load of 40 A/g. The high capacitance values can mainly be attributed to one dimensional nanocarbon morphology.[64-67]Theparticular morphology allows the maximum surface area to be presented to the electrolyte and extends the double layer over a larger surface area. The mesoporous spaces help in solvent retention and thus help in keeping ions closer to the electrode material, which in turn reflects in better performance at higher current.[68]

The impedance analysis (*figure 4.13d*) shows a close fit between experimental Nyquist plot and the corresponding simulated Nyquist plot. Zoomed higher frequency region is also shown in the inset of *figure 4.13d*. It can be seen that close fitting was observed. The electrochemical series resistance, ESR was calculated to be 1.61Ω and the corresponding double layer capacitance, C_{dl} of 207mF/cm^2 was observed. Further the nearly vertical rise (84^0) towards lower frequency side shows the typical near-ideal capacitor behaviour. Fairly small length of Warburg element (45^0 projection) in *figure 4.13d* (inset), depicts the typical mesoporous nature of the carbon material. The simulated plot sketched

together with experimental plot, in *figure 4.13d*, was constructed based on a standard circuit designs. The semicircular arc furnishes information about charge transfer resistance, R_{ct}, Warburg impedance, W and double layer capacitance, C_{dl}. The intercept of semicircular arc on real impedance axis (X-axis) provides information about electrochemical series resistance, ESR.

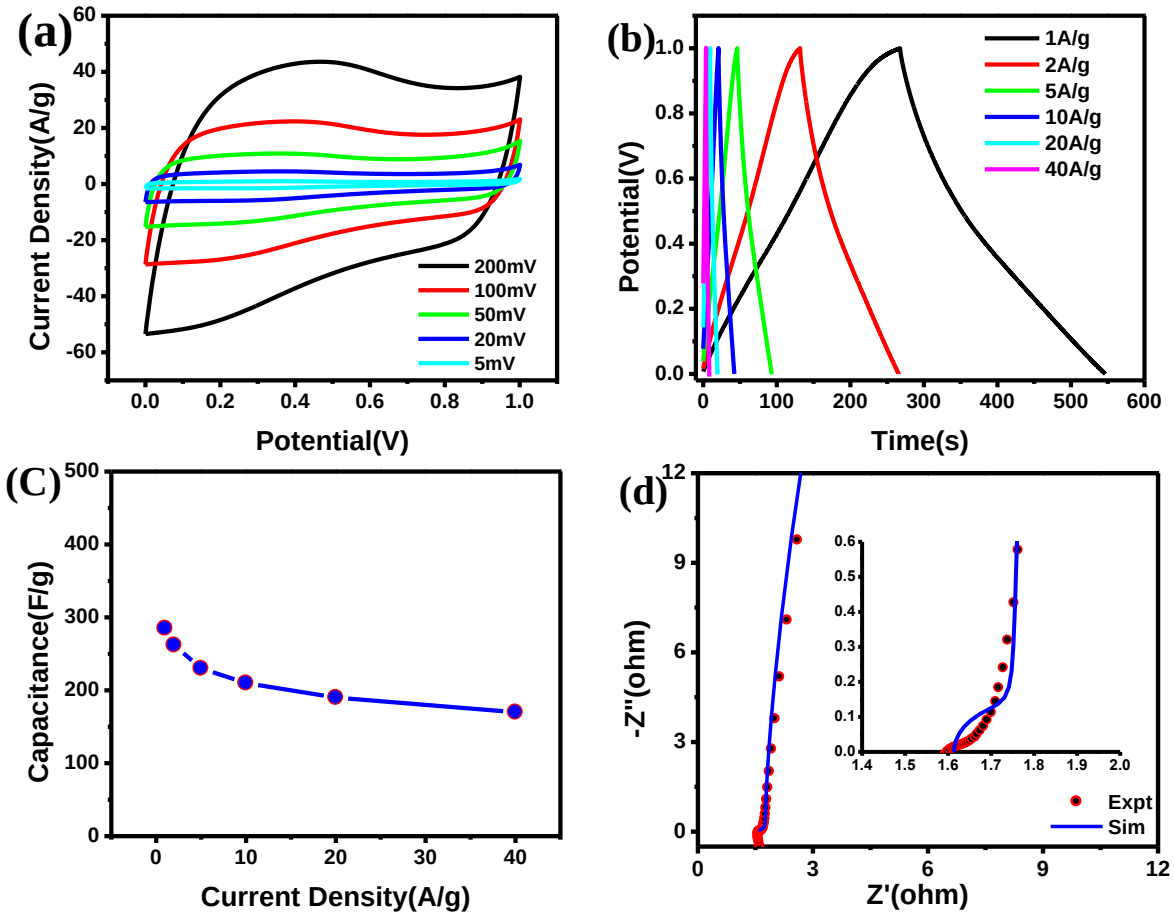

Figure 4.13 *Electrochemical characteristics of PU-SBA11 sample checked by performing CV, charge-discharge and impedance in 3-electrode assembly using IM H_2SO_4 as electrolyte and calomel electrode as reference electrode. a) CV plot of PU-SBA11 in the voltage range 0-1V at a scan rate ranging from 5mV/s to 200mV/s. b) Charge-discharge plot of PU-SBA11 at varied current density of 1A/g to 40A/g. c) Capacitance vs. current density plot showing very small loss of initial capacitance at higher current densities. d) Impedance spectra showing experimental Nyquist plot (shown by points) and corresponding simulated Nyquist plot (shown by solid blue line), simulated on the basis of standard interface circuit. The zoomed high frequency region is shown in inset.*

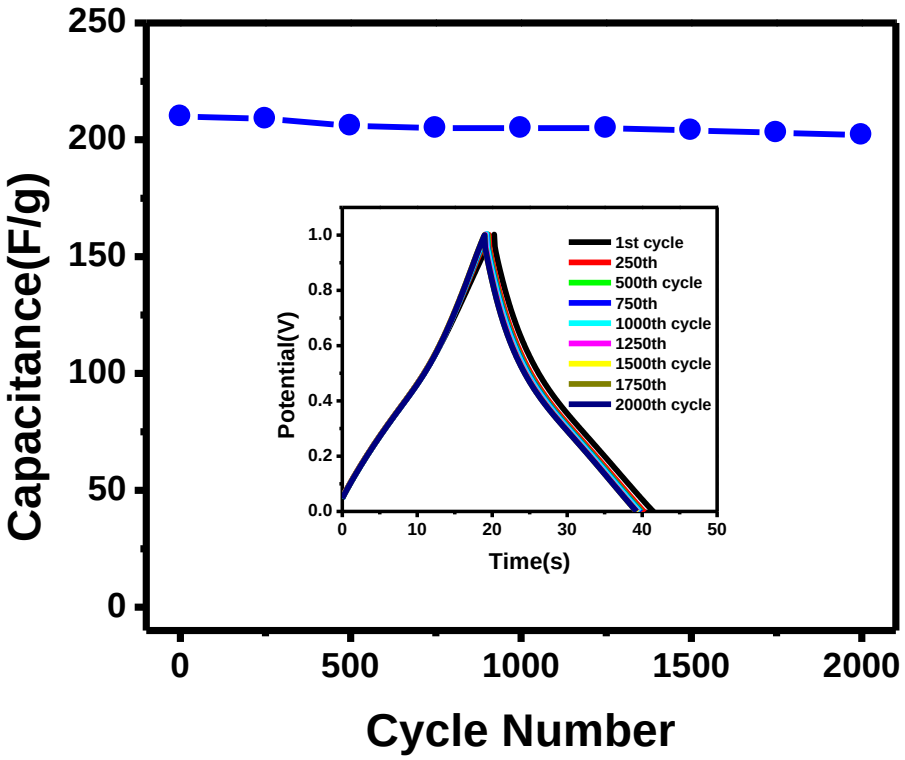

Figure 4.14 *Shows the cyclic stability measurements of PU-SBA11 at current density of 10A/g in a three electrode cell using 1M H_2SO_4 as electrolyte vs. calomel reference electrode.*

The cycling stability tests were performed at 10 A/g in 1M H_2SO_4 in a three electrode system, shown in *figure 4.14*. The material showed a negligible (only 4%) capacitance loss after 2000 cycles.

The percentage of nitrogen doping and the extent of templating are reflected in the final electrochemical performance of pectin derived carbon forms. *Figure 4.15* shows a comparative 3- electrode electrochemical performance of all pectin derived carbons. Splitting the carbon framework into nano dimensions by templating, has enhanced the capacitance by 10 folds as seen from *figure 4.15a*, *figure 4.15b* and *figure 4.15c*. Because of increased nitrogen doping, 3.8 at.% in PU-00, the capacitance has increased to 60 F/g which can be attributed to increase in conductivity.

Structural and surface morphological differences brought about by different amounts of nitrogen doping in pectin derived carbons is reflected in their electrochemical performances. *Table 4.2* summarises the electro-chemical

capacitance values of all the pectin derived carbons. The capacitance of 240 F/g was recorded for PU-SBA21 at 1 A/g in comparison to 285 F/g for PU-SBA11 at the same current density (*figure 4.15b*). Further, from *figure 4.15*b and *figure 4.15c*, for PU-SBA11 the capacitance of 285F/g at 1A/g reduced to 210F/g at 10A/g. Comparatively, for PU-SBA21 it reduced to180 F/g from 240 F/g at same current density. In the case of P0-SBA, the capacitance of 225 F/g at 1A/g

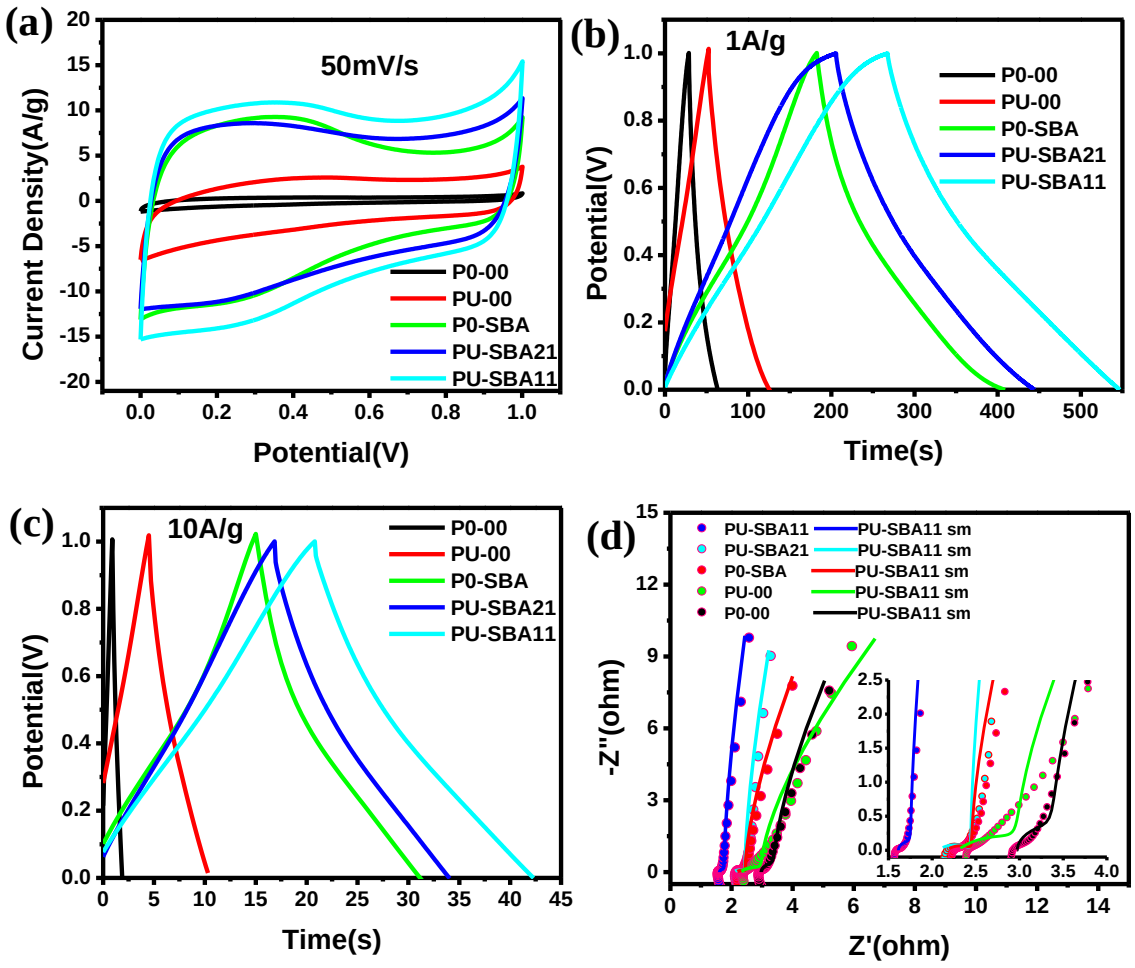

Figure 4.15 *Shows the comparative electrochemical plots for all pectin derived carbons carried out in a three electrode assembly in 1M H_2SO_4 with calomel as reference electrode. a) Shows the comparison of CV curves at scan rate of 50mV/s. b) Comparison of charge-discharge curves at 1A/g. c) Comparison of charge-discharge at 10A/g. d) Comparison in the impedance behaviour of all the pectin derived samples, dots show the experimental data while as lines show the simulated data.*

dropped to 160 F/g at 10A/g. *Figure 4.15d* compares the electrochemical impedance behaviour of all pectin derived carbons. The experimental and simulated data are plotted together. Zoomed region in the inset of *figure 4.15d* shows the close fit. The impedance data generated using standard circuit is summarised in *table 4.2*. It can be seen that PU- SBA11 stands tall, with minimum ESR of 1.61 Ω and nearly vertical line in the low frequency region, followed by PU-SBA21 and P0-SBA with ESR values of 2.07Ω and *2.26*Ω respectively. Other impedance parameters are also listed in the table. The ESR differences in case of pectin derived carbons can be related to ordered packing and substantial nitrogen concentration in the carbon lattice. The impedance data (*table 4.2*) shows a clear trend with the data collected from the CV and charge-discharge measurement. Further the polarization of the material is least in PU-SBA11 shown by vertical lines in the Nyquist plot (*figure 4.15d*) in the low frequency region. As can be seen, low surface area carbons (P0-00, PU-00 and P0-SBA) show more polarization as compared to high surface area ones. These comparisons highlight the better performance of structurally superior and heavily nitrogen doped PU-SBA11 over other pectin derived carbon samples.

Table 4.2 *Summary of the electrochemical performance of all pectin gel derived carbons.*

Samples	**Capacitance (F/g)** (charge -discharge)		**Impedance Analysis**			
	1A/g	**10A/g**	**ESR(Ω)**	**C_{dl}(F/cm^2)**	**R_{ct} (Ω)**	**W** (mMho)
P0-00	**20**	**12**	**2.97**	**11**	**0.454**	**12**
PU-00	**60**	**55**	**2.57**	**42**	**0.624**	**13**
P0-SBA	**226**	**160**	**2.26**	**104**	**0.362**	**49**
PU-SBA21	**240**	**180**	**2.07**	**154**	**0.389**	**17**
PU-SBA11	**285**	**210**	**1.61**	**207**	**0.142**	**15**

Stability comparison of the three pectin derived carbons, PU- SBA11, PU-SBA21 and P0-SBA was also carried out. *Figure 4.16* compares the stability performance

up to 1500 charge-discharge cycles. *Figure 4.16* depicts the stable charging and discharging capacities for PU-SBA11 with the retention of 97% capacity. Capacity retention of 78% and 65% was observed for PU-SBA21 and P0-SBA, respectively for the discharging case, and capacity retention of 84% and 86% was observed for the charging case. One more noteworthy observation is that the columbic efficiencies which lie close to 100% (slightly lesser) for PU-SBA11 throughout the range, lie well below 90% for the PU-SBA21 and P0-SBA. These comparisons further highlight the superiority of PU-SBA11 over other pectin derived samples.

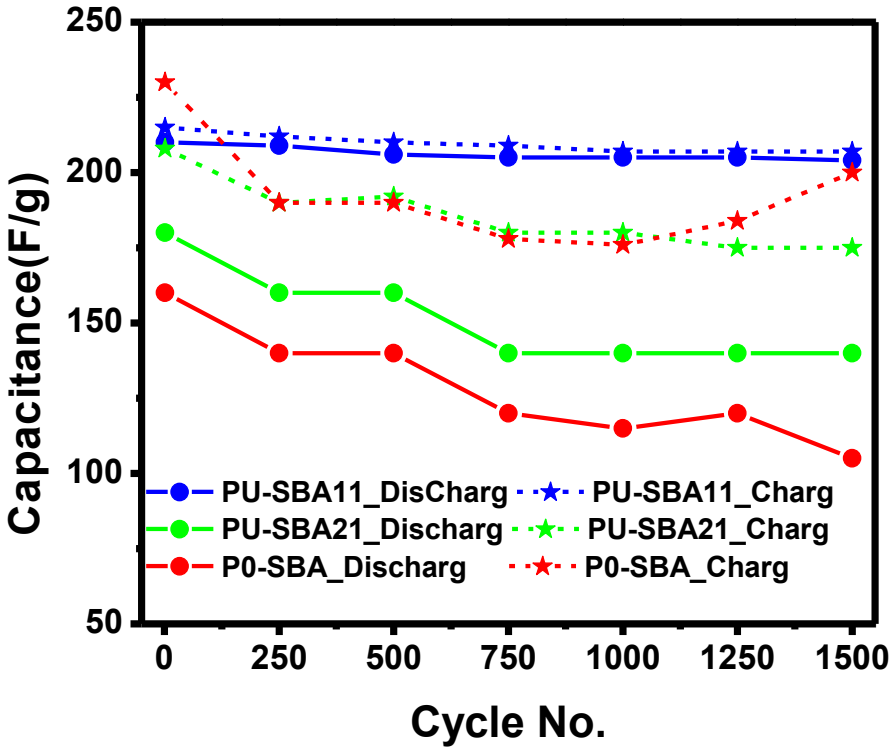

Figure 4.16 *Shows the cyclic stability data of PU-SBA11, PU-SBA21 and P0-SBA at current density of 10A/g in a three electrode cell using 1MH_2SO_4 as electrolyte vs. calomel reference electrode up to 1500 charge-discharge cycles.*

Carbon derived from two other natural gels, agarose (AgU-SBA11) and alginate (AgU-SBA11) was also tested for electrochemical performance. The carbon synthesis was achieved through the same protocol, as discussed in the experimental section. The electrochemical performance of AgU-SBA11 and AgU-SBA11 was compared with that of PU-SBA11. *Figure 4.17* shows the

comparison of the electrochemical performance (CV, CD and impedance) for these three doped carbon forms, obtained from three different hydrogels. The CV plot (*figure 4.17a*) shows that capacitance loops of pectin are comparatively broader, along current axis, pointing to considerably higher capacitance. Further, in the voltage region 0V-0.4V, the pectin CV loop is more fattened compared to other two, implying a significant pseudo capacitive contribution from nitrogen functionalities.

The templating in case of agarose and alginate has also led to improvement in capacitance values. It is interesting to compare the capacitance values (*figure 4.17b*) for the three gels. The capacitance furnished by carbon obtained from three gels, at a current density of 10A/g, is compared here. The capacitance values of 210F/g, 160F/g and 100F/g respectively for PU-SBA11, AlU-SBA11 and AgU-SBA11 clearly differentiate the carbon obtainable from three gels. The

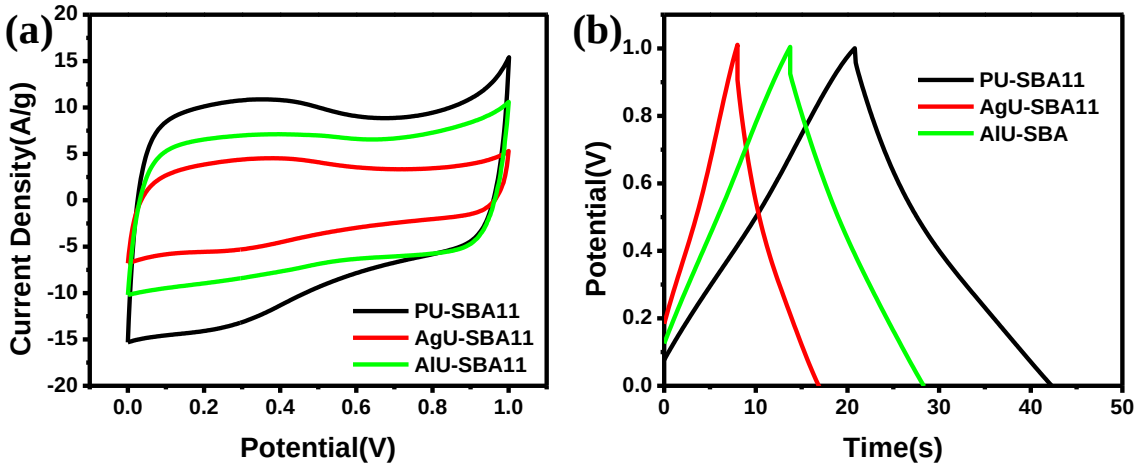

Figure 4.17 *Electrochemical performance comparison of three natural gels; agarose, alginate and pectin in a three electrode assembly in 1M H_2SO_4, with calomel as reference electrode. a) Compares the CV behaviour at scan rate of 50mV/s. b) Compares charge-discharge characteristics at 10A/g.*

distinctly better performance of PU-SBA11 over other two can be correlated to their structuring, owing to their differential response to templating and the nitrogen doping there in. The SEM comparison (***figure 4.5***) also supports the electrochemical observations. The formation of incomplete and disordered 1D threads of AgU-SBA11 and AlU-SBA11 renders the electrochemically poor

compared to PU-SBA11, where a well developed pore structure is generated. This disordered structuring of nano threads could be the result of inefficient infiltration of gel into the template.

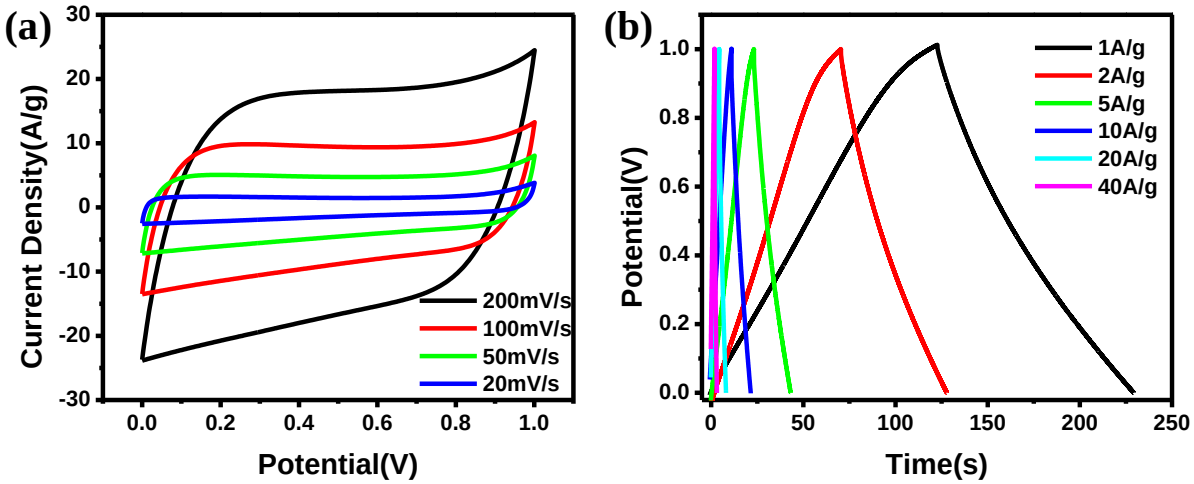

Figure 4.18 *Electrochemical two electrode performance of PU-SBA11 in 1M H_2SO_4. a) CV curves of PU-SBA11 at varied scan rates of as high as 200mV/s and as low as 20mV/s. b) Charge-discharge curves for PU-SBA11 at varied current densities ranging from lowest of 1A/g and highest of 40A/g.*

To check the symmetric characteristics of the PU-SBA material, the performance was checked in a two electrode dummy cell in 1M H_2SO_4 (*figure 4.18*). Nearly rectangular curve possess fairly sharp charging and discharging sides, depicting nearly-ideal and superior capacitance behaviour. The two electrode capacitance of 230 F/g was observed at 1A/g which decreased to 195 F/g at 10A/g and to 140F/g at 40A/g. The material provided 86% capacitance retention on going from 1A/g to 10A/g and 60% on going to 40A/g, which is comparable to well-known and efficient carbon forms.

4.4 Conclusion

In conclusion, a natural polymer hydrogel is used as a template precursor for the synthesis of porous carbon material for super-capacitor application. By use of the templating procedure, we were able to snip the carbon framework into inter-connected carbon threads. A particular morphology was seen to possess a surface

area of 837m^2/g with considerable fraction of mesopores (~4nm) with open type architecture having the pore volume of 0.87cm^3/g and mesoporosity of 83%. Urea-assisted nitrogen doping has led to doping of 7.0 at.%, distributed in pyridinic, pyrrolic and graphitic forms which add to its advantage as a supercapacitive energy storage material. The material exhibits a three electrode capacitance of 285F/g at 1A/g with the capacitance retention of 74% at 10 A/g and 63% at 40 A/g. Cycling stability is also commendable as the material exhibited only 4.0% loss after 2000 cycles at 10A/g. In a two electrode symmetric cell the material offered a capacitance of 230F/g and delivered the energy of 7Wh/kg at 2.5kW/kg in an aqueous medium.

4.5 References

1. M. Sevilla and R. Mokaya, *Energy Environ. Sci.*, 2014, **7**, 1250-1280.
2. D. Pech, M. Brunet, H. Durou, P. Huang, V. Mochalin, Y. Gogotsi, P.L. Taberna and P. Simon, Nat Nanotechnol, 2010, 5, 651–654.
3. V. Augustyn, P. Simon and B. Dunn, *Energy Environ. Sci.*, 2014, **7**, 1597-1614.
4. X. Lang, A. Hirata, T. Fujita and M. Chen, *Nat Nanotechnol*, 2011, **6**, 232-236.
5. P. Hao, Z. Zhao, J. Tian, H. Li, Y. Sang, G. Yu, H. Cai, H. Liu, C. P. Wong and A. Umar, *Nanoscale*, 2014, **6**, 12120-12129.
6. D. Mhamane, A. Suryawanshi, S. M. Unni, C. Rode, S. Kurungot and S. Ogale, *Small*, 2013, **9**, 2801-2809.
7. X. Wang, Y. Zhang, C. Zhi, X. Wang, D. Tang, Y. Xu, Q. Weng, X. Jiang, M. Mitome, D. Golberg and Y. Bando, *Nat. Commun.*, 2013, **4**, 2905-2912.
8. L. Wei, M. Sevilla, A. B. Fuertes, R. Mokaya and G. Yushin, *Adv. Energy Mater.*, 2011, **1**, 356-361.
9. T. Yang, R. Zhou, D. Wang, S. Jiang, Y. Yamauchi, S. Qiao, M. Monteiro and J. Liu, *Chem. Commun.*, 2012, **51**, 2518-2521.
10. D. Qu and H. Shi, *J. Power Sources*, 1998, **74**, 99-107.

11. V. C. Almeida, R. Silva, M. Acerce, O. P. Junior, A. L. Cazetta, A. C. Martins, X. Huang, M. Chhowalla and T. Asefa, *J. Mater. Chem. A*, 2014, **2**, 15181-15190.
12. R. Gokhale, V. Aravindan, P. Yadav, S. Jain, D. Phase, S. Madhavi and S. Ogale, *Carbon*, 2014, **80**, 462-471.
13. R. Gokhale, S. M. Unni, D. Puthusseri, S. Kurungot and S. Ogale, *Phys. Chem. Chem. Phys.*, 2014, **16**, 4251-4259.
14. J.P. Paraknowitsch and A. Thomas, *Energy Environ. Sci.*, 2013, **6**, 2839-2855.
15. Q. Shi, R. Zhang, Y. Lv, Y. Deng, A. A. Elzatahrya and D. Zhao, *Carbon*, 2014, **84**, 335-346.
16. D. W. Wang, F. Li, Z. G. Chen, G. Q. Lu and H.-M. Cheng, *Chem. Mater.*, 2008, **20**, 7195-7200.
17. J. Hou, C. Cao, F. Idrees and X. Ma, *ACS Nano*, 2015, **9**, 2556-2564.
18. K. N. Wood, R. O'Hayre and S. Pylypenko, *Energy Environ. Sci.*, 2014, **7**, 1212-1249.
19. Z. Li, Z. Xu, H. Wang, J. Ding, B. Zahiri, C. M. B. Holt, X. Tan and D. Mitlin, *Energy Environ. Sci.*, 2014, **7**, 1708-1718.
20. L. Qie, W. Chen, H. Xu, X. Xiong, Y. Jiang, F. Zou, X. Hu, Y. Xin, Z. Zhang and Y. Huang, *Energy Environ. Sci.*, 2013, **6**, 2497-2504.
21. A. B. Fuertes and M. Sevilla, *ACS Appl. Mater. Interfaces*, 2015, **7**, 4344–4353.
22. D. Puthusseri, V. Aravindan, B. Anothumakkool, S. Kurungot, S. Madhavi and S. Ogale, *Small*, 2014, **10**, 4395-4402.
23. W. Qian, F. Sun, Y. Xu, L. Qiu, C. Liu, S. Wang and F. Yan, *Energy Environ. Sci.*, 2013, **7**, 379-386.
24. M. Wahid, G. Parte, D. Phase and S. Ogale, *J. Mater. Chem. A*, 2014, **3**, 1208-1215.
25. M. Wahid, D. Puthusseri, D. Phase and S. Ogale, *Energy and Fuels*, 2014, **28**, 4233- 4240.
26. J. Wang and S. Kaskel, *J. Mater. Chem.*, 2012, **22**, 23710-23725.

27. L. Wei, M. Sevilla, A. B. Fuertes, R. Mokaya and G. Yushin, *Adv. Funct. Mater.*, 2011, **22**, 827-834.
28. Y. S. Yun, S. Y. Cho, J. Shim, B. H. Kim, S. J. Chang, S. J. Baek, Y. S. Huh, Y. Tak, Y. W. Park, S. Park and H.-J. Jin, *Adv. Mater.*, 2013, **25**, 1993-1998.
29. M. P. Bichat, E. R. Pinero and F. Beguin, *Carbon*, 2010, **48**, 4351-4361.
30. M. Biswal, A. Banerjee, M. Deo and S. Ogale, *Energy Environ. Sci.*, 2013, **6**, 1249-1259.
31. D. Puthusseri, V. Aravindan, S. Madhavi and S. Ogale, *Energy Environ. Sci.*, 2013, **7**, 728-735.
32. E. Raymundo-Piñero, M. Cadek and F. Beguin, *Adv. Funct. Mater.*, 2009, **19**, 1032-1039.
33. M. Sevilla and A. B. Fuertes, *ACS Nano*, 2014, **8**, 5069-5078.
34. P. Yadav, A. Banerjee, S. Unni, J. Jog, S. Kurungot and S. Ogale, *ChemSusChem*, 2012, **5**, 2159-2164.
35. F. Goettmann, A. Fischer, M. Antonietti and A. Thomas, *Angew. Chemie-Int. Ed.*, 2006, **45**, 4467-4471.
36. S. H. Joo, S. J. Choi, I. Oh, J. Kwak, Z. Liu, O. Terasaki and R. Ryoo, *Nature*, 2001, **412**, 169-172.
37. S. Jun, S. H. Joo, R. Ryoo, M. Kruk, M. Jaroniec, Z. Liu, T. Ohsuna and O. Terasaki, *J. Am. Chem. Soc.*, 2000, **122**, 10712-10713.
38. A. Kumar, G. Hegde, S. A. B. A. Manaf, Z. Ngaini and K. V. Sharma, *Chem. Commun.*, 2014, **50**, 12702-12705.
39. R. Ruiz-Rosas, M. J. Valero-Romero, D. Salinas-Torres, J. Rodríguez-Mirasol, T. Cordero, E. Morallon and D. Cazorla-Amoros, *ChemSusChem*, 2014, **7**, 1458-1467.
40. R. Ryoo, S. H. Joo and S. Jun, *J. Phys. Chem. B*, 1999, **103**, 7743-7746.
41. F. Chen, L. Huang and Q. Li, *Chem.Mater.*, 1997, **9**, 2685-2686.
42. T.-W. Kim, F. Kleitz, B. Paul and R. Ryoo, *J. Am. Chem. Soc.*, 2005, **127**, 7601-7610.
43. F. Kleitz, S. Hei Choi and R. Ryoo, *Chem. Commun.*, 2003, 2136-2137.

44. R. van Grieken, J. Iglesias, V. Morales and R. A. García, *Microporous Mesoporous Mater.*, 2010, **131**, 321–330..
45. P. Yang, D. Zhao, B. F. Chmelka and G. D. Stucky, *Chem. Mater.*, 1998, **10**, 2033-2036.
46. D. Zhao, P. Yang, N. Melosh, J. Feng, B. F. Chmelka and G. D. Stucky, *Adv. Mater.*, 1998, **10**, 1380-1385.
47. Y. Fan, P. F. Liu, Z. J. Yang, T. W. Jiang, K. L. Yao, R. Han, X. X. Huo and Y. Y. Xiong, *Electrochim. Acta*, 2015, **163**, 140-148.
48. H. Yang and D. Zhao, *J. Mater. Chem.*, 2005, **15**, 1217-1231.
49. Z. Zafar, Z. H. Ni, X. Wu, Z. X. Shi, H. Y. Nan, J. Bai and L. T. Sun, *Carbon*, 2013, **61**, 57-62.
50. L. G. Bulusheva, A. V. Okotrub, I. A. Kinloch, I. P. Asanov, A. G. Kurenya, A. G. Kudashov, X. Chen and H. Song, *Physica Status Solidi (B) Basic Research*, 2008, **245**, 1971-1974.
51. P. H. Matter, L. Zhang and U. S. Ozkan, *J. Catal.*, 2006, **239**, 83-96.
52. D. Hulicova-Jurcakova, M. Seredych, G. Q. Lu and T. J. Bandosz, *Adv. Funct. Mater.*, 2009, **19**, 438-447.
53. E. Desimoni, G. I. Casella, A. Morone and A. M. Salvi, *Surf. Interface Anal.*, 1990, **15**, 627–634.
54. O. Munjeri, J. H. Collett and J. T. Fell, *J. Control. Release*, 1997, **46**, 273–278.
55. G. Dongowski, B. Schnorrenberger, M. Platzer, M. Schwarz and R. Neubert, *Int. J. Pharm.*, 1997, **158**, 99–107.
56. A. G. Pandolfo and A. F. Hollenkamp, *J. Power Sources*, 2006, **157**, 11-27.
57. C. Morant, J. Andrey, P. Prieto, D. Mendiola, J. M. Sanz and E. Elizalde, *physica status solidi (a)*, 2006, **203**, 1069-1075.
58. T. Sharifi, F. Nitze, H. R. Barzegar, C. W. Tai, M. Mazurkiewicz, A. Malolepszy, L. Stobinski and T. Wagberg, *Carbon*, 2012, **50**, 3535-3541.
59. S. Brunauer, L. S. Deming, W. E. Deming and E. Teller, *J. Am. Chem. Soc.*, 1940, **62**, 1723-1732.

60. Y. Gogotsi, A. Nikitin, H. Ye, W. Zhou, J. E. Fischer, B. Yi, H. C. Foley and M. W. Barsoum, *Nat. Mater.*, 2003, **2**, 591-594.

61. G. G. Stavropoulos and A. A. Zabaniotou, *Microporous and Mesoporous Mater.*, 2005, **82**, 79-85.

62. Y. Yan, Y. Hoshino, Z. Duan, S. R. Chaudhuri and A. Sarkar, *Chem. Mater.*, 1997, **9**, 2583-2587.

63. H. J. Shin, R. Ryoo, M. Kruk and M. Jaroniec, *Chem. Commun.*, 2001, 349-350.

64. L. F. Chen, X. D. Zhang, H. W. Liang, M. Kong, Q. F. Guan, P. Chen, Z. Y. Wu and S. H. Yu, *ACS Nano*, 2012, **6**, 7092-7102.

65. Y. H. Hsu, C. C. Lai, C. L. Ho and C. T. Lo, *Electrochim. Acta*, 2014, **127**, 369-376.

66. X. Yan, Y. Liu, X. Fan, X. Jia, Y. Yu and X. Yang, *J. Power Sources*, 2013, **248**, 745-751.

67. T. Zhang, C. H. J. Kim, Y. Cheng, Y. Ma, H. Zhang and J. Liu, *Nanoscale*, 2015, **7**, 3285-3291.

68. H. Wang, Z. Xu, A. Kohandehghan, Z. Li, K. Cui, X. Tan, T. J. Stephenson, C. K. King'ondu, C. M. B. Holt, B. C. Olsen, J. K. Tak, D. Harfield, A. O. Anyia and D. Mitlin, *ACS Nano*, 2013, **7**, 5131-5141.

Chapter 5

A heavily nitrogen doped carbon material from Yogurt as an efficient negative electrode for high energy density asymmetric supercapacitor.

Yogurt is used as a novel precursor to synthesize high quality heavily nitrogen doped porous carbon for the supercapacitor application. It is an easily scalable and manufacturable food item containing casein as the major protein besides some whey proteins. The yogurt forming process is mediated by the bacteria, and hence this precursor has high nitrogen content which can get doped into carbon upon controlled precursor pyrolysis. Indeed our material retains a high (12 atm%) nitrogen percentage even after high temperature pyrolysis in the presence of an activating agent. A surface area of 1300 m^2/g is attained with a good density of mesopores, apart from abundant micropores. The material offers a high capacitance of 225 F/g at 2 A/g which falls only to 200 F/g even at a high current density of 20 A/g in aqueous electrolyte. An energy density of 7 Wh/kg is delivered at a power density of 5000 W/kg. We have also examined the cathode performance of our material vs. nickel cobalt sulfide (NCS) in an asymmetric configuration. Our energy density in asymmetric assembly goes as high as 27 Wh/kg at a power density of 364 W/kg and 17.8 Wh/kg at a power density of 6400 W/kg.

The content of this chapter is published in:

J. Mater. Chem. A, 2015,**3**, 1208-1215.

Reproduced by permission of The Royal Society of Chemistry.

5.1 Introduction

Supercapacitors are a prime research focus for high power-density energy storage applications for the past two decades. The heightened interest and activity in supercapacitor research as compared to conventional batteries is not only due to their high power capability (10 kW/kg vs. 0.1 kW/kg), but also good reversibility, and long cycle life.[1-3] With supercapacitors, a significant energy uptake and delivery is achieved within seconds.[4] However, they inherit the limitation of lower energy density of around 5 Wh/kg which makes them unsuitable for applications where long term energy delivery is sought.[5]

Supercapacitors come in two variants differing in the mechanism of energy storage. One is the EDLC-type, where energy is stored by adsorption of ions at the outer Helmholtz plane on the electrode electrolyte interface (Electric double layer). In this context, synthesis of high surface area porous carbon materials with good electrical properties are of importance.[6] Graphene like materials and graphene hydrogels have also shown considerable promise for high performance supercapacitor application in view of their high conductivity and surface catalytic properties.[7-13] The other variant is the pseudo-capacitor wherein the energy storage operates via fast surface chemical reactions. In this case high surface area forms of metal oxides like MnO_2 and RuO_2, and conducting polymers like PANI and polypyrrole have gained significant attention.[14] In pseudo-capacitors there is some contribution from the EDLC mechanism. In carbon based EDLCs involving heteroatom doping in carbon framework, significant contribution can emanate from pseudocapacitive faradic reactions.

The defining characteristics of a supercapacitor are the capacitance, power density, and energy density. The energy storage density of a supercapacitor is given by $CV^2/2$, where C is capacitance and V is the voltage window; thus by maximizing the voltage window we can increase the energy density of the supercapacitor. The maximum power density of a supercapacitor is given by $V^2/4R$, where R is the combined resistance of electrodes, contacts and the solution; thus to achieve the best capacitance from a supercapacitor this resistance should be at the minimum.[15] To address the low energy density

limitation of supercapacitors, two more variants differing in the design are also being researched. One of these is called asymmetric supercapacitor wherein one electrode is EDLC type and the other is made of a pseudocapacitive material. The second one is a hybrid capacitor which involves one battery type electrode and the other one pseudocapacitive metal oxide.[16,17]

Currently porous carbon materials prepared by pyrolysis are dominating the field at both research as well as at industrial level, in spite of having lower capacitances than the metal oxides and conducting polymers. This can be attributed to simple synthetic methods, higher power densities, long life, less intricate device requirements and low cost.[18] Among porous carbons, the biomass-derived carbons are at the focus of scientific attention because of the easy availability of the raw materials besides serving the duel goal of environmental cleaning and energy storage. Since most cellulosic biomass precursors primarily contain carbon and oxygen, they do not lend the benefits that can be gained with nitrogen incorporation in significant proportion into the functional carbon framework, such as delocalization of the electron cloud leading to higher conductivity and addition of the pseudo-capacitance contribution by participating in various electrochemical redox reactions.[19] Nitrogen doping in the carbon framework has increased the scope of applicability of porous carbon materials further in several fields including the field of supercapacitors. Both *ex-situ* doping by pyrolysing the porous carbon material with nitrogen rich precursors like melamine and urea at high temperature, and *in-situ* nitrogen doping by pyrolysis of a suitable nitrogen containing polymer such as PAN, PVA, poly acryl amide, polypyrrole, polyaniline and human hair etc. have been reported.[20-24]

In this work we show that suitably controlled pyrolysis of yogurt, a novel precursor and an easily scalable and manufacturable food item, can yield high quality heavily nitrogen doped porous carbon with excellent supercapacitor properties. Yogurt contains casein as the major protein, besides, some whey proteins. Curdling is caused by the bacteria and hence higher nitrogen content is expected from the yogurt. XPS analysis proves the high nitrogen percentage in

the carbon samples synthesized by pyrolysis of yogurt. The superior electrochemical performance of the yogurt-derived carbon over the other carbon forms derived from several natural precursors is also clearly established. Besides, high nitrogen content in the yogurt carbons, in the form of pyridinic, and pyrrolic moieties allows their use as negative electrode in asymmetric supercapacitors. Asymmetric assembly of yogurt derived carbon as negative electrode and nickel cobalt sulphide as positive electrode is demonstrated. The asymmetric assembly is shown to have lead to enhancement in energy density by several folds.

5.2 Experimental section

5.2.1. Preparation of yogurt derived carbons

For our experiments yogurt of best quality supplied by renowned Indian diary cooperative, named Amul-Masti, was purchased. The constitution of the product being:

fat(3.1%), protein (4.1%), carbohydrate (4.4%), calcium (0.183%) and rest water. The yogurt was directly sealed in a teflon lined autoclave and hydrothermal reaction was set at 180^0 for 24 hours. The importance of hydrothermal step lies in the creation of C=C back bone as already established in our previous work.[25] The hydrothermal product thus obtained was washed with copious amount of water and dried at 80^0C in a vacuum oven. The dried product was mixed with different weight ratios of KOH. The different mixtures of 1:0, 1:1, 1:2, and 1:3 of hydrothermal product: KOH were made and pyrolysed at 800^0C at the scan rate of 3^0C/ min for 2 hrs. The product was collected and washed with HCl to remove the metal and salt content. The samples were labelled as HTYC, HTYC-1:1, HTYC-2:1, HTYC-3:1 respectively. The % age yield of carbon from yogurt was 0.7%. For asymmetric supercapacitor study Ni-Co sulphide was synthesized by following an already reported procedure.[26] In a typical synthesis of Ni-Co oxide over nickel foam, 0.66g of $Ni(NO_3)_2.6H_2O$, 1.33g of $Co(NO_3)_2.6H_2O$ and 0.48g urea were dissolved in 160 ml of DI water. A 1.5 x 4 cm^2 nickel foam strip was cut and its both ends were covered (1cm on each side) by a teflon tape. The nickel foam strip and the above solution were sealed in teflon-lined stainless steel

autoclave and was put in an oven at 120 ^{0}C for 16 hrs. The sample was washed with DI water and dried in normal air. For the synthesis of Ni-Co sulfide (NCS) the sample was hydrothermally reacted with 100 mg of Na_2S in 100 ml of water at 160 ^{0}C for 6 hrs.

5.2.2 Characterization of yogurt derived porous carbons

The different carbon samples synthesized from yogurt were examined by X-ray powder diffraction using Philips X'Pert PRO diffractometer with nickel-filtered Cu Kα radiation. Raman spectroscopy was performed using LabRAM HR800 from JY Horiba. High-resolution transmission electron microscopy was done using IFEI, Tecnai F30, FEG system with 300 kV. The FESEM was done with the help of Nova Nano SEM 450. The surface area values for all the samples were determined by Brunauer Emmett Teller (BET) adsorption method (Quadrasorb automatic volumetric instrument). Cyclic voltametry measurements were performed by Auto Lab (model PGSTAT 30, eco-chemie). X-ray photoelectron spectroscopy (XPS) was done on a VG scientific ESCA-3000 spectrometer using non monochromatized Mg Kα radiation (1253.6 eV) at a pressure of about 1×10^{-9} Torr. For the calculation of relative concentration of heteroatoms present and functional group analysis, the adsorbed oxygen peak area was subtracted from total area of the mother oxygen peak. Percentage(s) of various elements and functional groups were calculated on the basis of peak areas from the deconvoluted XPS spectra.

5.2.3 Preparation of electrodes for electrochemical measurement.

The electrodes were prepared by coating a slurry of 80 wt.% carbon material, 15 wt.% carbon black and 5wt.% PVDF (in N-methylpyrolidine) on 1 cm^2 area of graphite strips (1cm×3.5cm) and then drying at 90 ^{0}C for 24 hours. The loading on the graphite strips was controlled by taking a definite volume of a known amount of carbon material in known volume of N-methylpyrolidine. A loading of 1.2mg/cm^2 was achieved on each electrode.

For asymmetric capacitor measurements the +ve electrode was directly cut from the strip having NCS grown on Ni-foam (0.5cm x 1.5cm). The negative electrode

was prepared by coating the required amount (mass balance) of HTYC-2:1 carbon on teflonised carbon fibre paper. The gravimetric capacitance was calculated from charge-discharge and the CV plots from the following equations:

$$\mathbf{Cg} = \boldsymbol{I}/(\boldsymbol{m}\,\boldsymbol{dV}/\boldsymbol{dt}) \quad \text{(for 3- electrode assembly)}$$

And

$$\mathbf{Cg} = \mathbf{2}\boldsymbol{I}/(\boldsymbol{m}\,\boldsymbol{dV}/\boldsymbol{dt}) \quad \text{(for 2- electrode case)}$$

Where ***m*** is the loading on each electrode, ***I*** is the current applied, and ***dV/dt*** is the slope of charge-discharge curve. The energy density and power density for symmetric supercapacitor, were calculated on the basis of following equation for a two electrode cell:

$$\boldsymbol{E}\left(\frac{Wh}{kg}\right) = \frac{\boldsymbol{C_g}*\boldsymbol{V^2}}{\mathbf{8}*\mathbf{3.6}} \qquad \& \qquad \boldsymbol{P}(W/kg) = \frac{\boldsymbol{E}\,(\boldsymbol{Wh/kg})}{\boldsymbol{t}(\boldsymbol{h})}$$

Where ***E*** is energy density in Wh/kg, ***Cg*** is gravimetric capacitance of electrode material in F/g, ***V*** is voltage window achievable in symmetric cell, ***P*** is power density of symmetric cell in W/kg and ***t*** is time in hours.

For asymmetric capacitor, the individual 3-electrode capacitance of negative and positive electrodes is first calculated by using above 3-electrode equation. The capacitances obtained are used for mass balancing. The energy density and power density of mass balanced asymmetric assembly is calculated by following equations:

$$\boldsymbol{E}(Wh/kg) = \frac{\boldsymbol{C_d}*\boldsymbol{V^2}}{\mathbf{2}*\mathbf{3.6}} \qquad \& \qquad \boldsymbol{P}(W/kg) = \frac{\boldsymbol{E}\,(\boldsymbol{Wh/kg})}{\boldsymbol{t}(\boldsymbol{h})}$$

where ***E*** is energy density in Wh/kg, ***V*** is voltage window in asymmetric device, ***P*** is power density of asymmetric capacitor in W/kg, ***t*** is time in hours and $\boldsymbol{C_d}$ is capacitance of device calculate from following equation.

$$\boldsymbol{C_d} = \boldsymbol{I}/(\boldsymbol{m}\,\boldsymbol{dV}/\boldsymbol{dt})$$

Where ***I*** is the capacitive (charging/discharging) current, ***m*** is the total active mass loading on both electrodes and ***dV/dt*** is the average slope of discharge curve.

5.3 Results and Discussion.

Figure 5.1 shows the morphology of dried yogurt. It is interesting to see that it is composed of agglomerates of submicron size globules which are fairly uniform in size. *Figure 5.2* shows FE-SEM images of the samples prepared from yogurt with different degrees of KOH activations. *Figure 5.2a* shows the formation of carbon

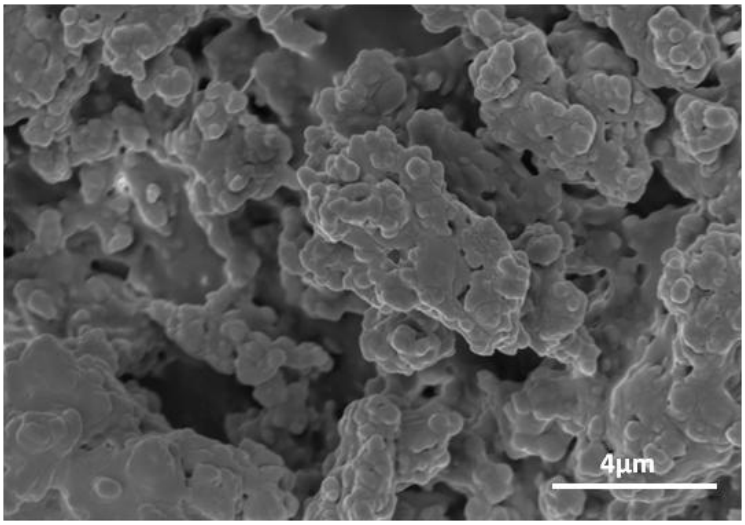

Figure 5.1 *This FE-SEM image shows the morphology of dried yogurt.*

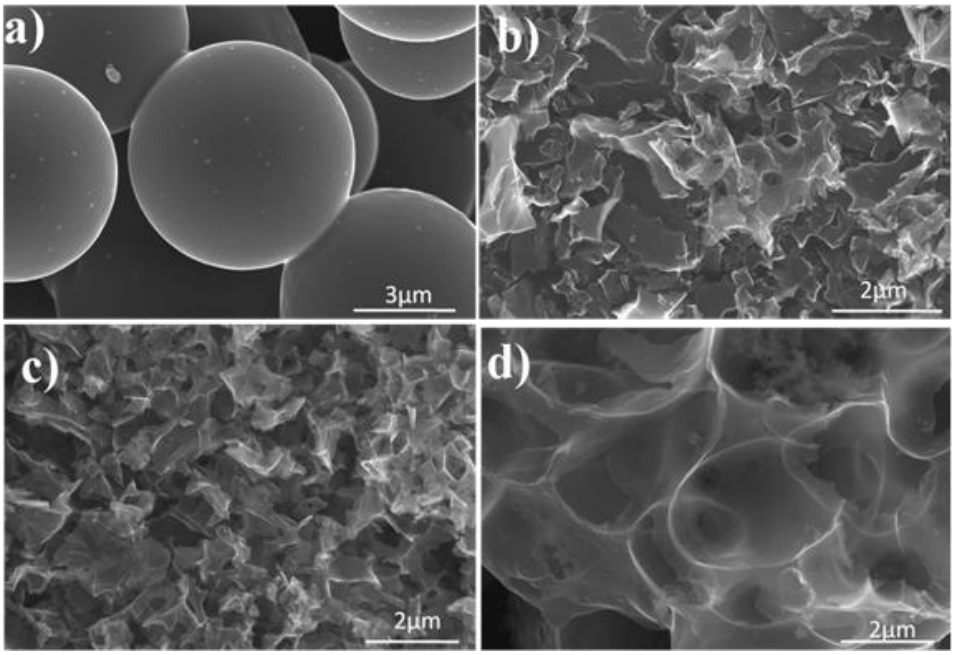

Figure 5.2 *FE-SEM images of a) HTYC b) HTYC-1:1 c) HTYC-2:1 d) HTYC-3:1*

microspheres when the hydrothermal yogurt product is subjected to direct pyrolysis without activation agent. This morphology is in itself quite interesting for other application domains. Further, *figure 5.2 (b-d)* compares evolution of morphologies with the increase in the ratio of the hydrothermal product and KOH from 1:1 to 1:3. With the increasing amounts of KOH different morphologies emerge quite interestingly, differing in sheet size and extent of folding. *Figure 5.3a* and *figure 5.3b* compare the SEM images taken at different resolutions. It can be seen from *figure 5.3b* that the individual carbon sheets have extremely porous surface structure formed by fusing of spherical carbon grains. HR-TEM images of *figure 5.3c* and d reveal the presence of mesopores in the size range of 15-20 nm besides the abundant micropores. SAED pattern is characterized by the presence of diffuse rings reflecting the turbo-stratic nature of the carbon.

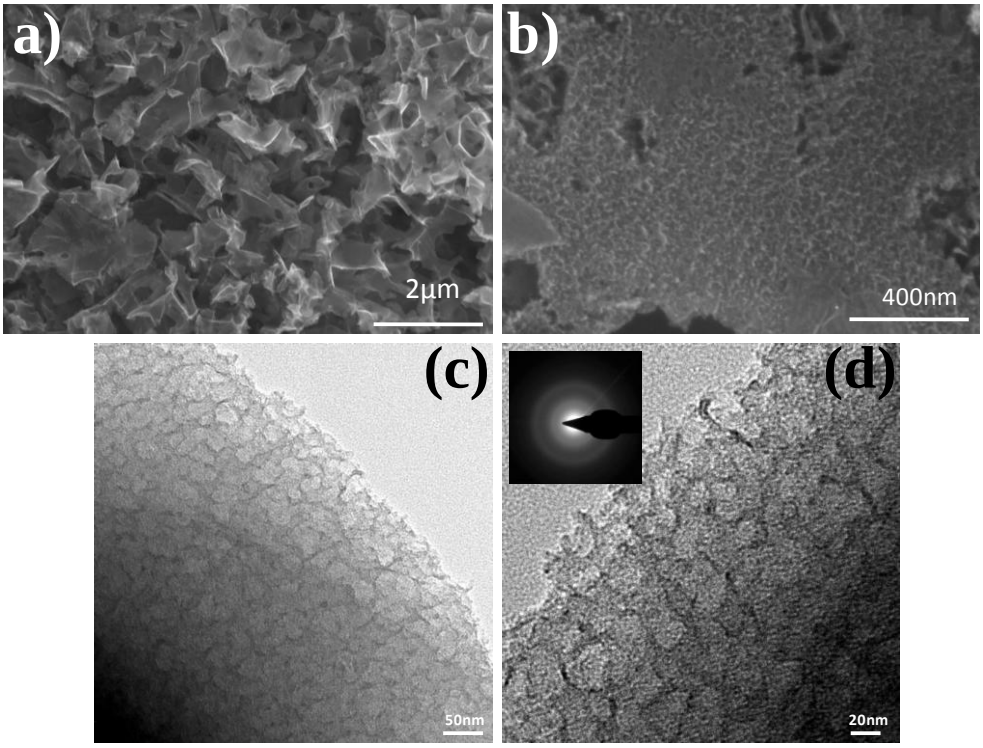

Figure 5.3 *a) and b) Show the high resolution FE-SEM images of electrochemically efficient HTYC-2:1, and c) and d) Show HR-TEM images of HTYC-2:1 at different resolutions.*

To know the extent of graphitization in the material, X-ray diffraction (XRD) and Raman spectra were recorded, and are shown in *figure 5.4*. The XRD shows two broad peaks at 26^0 and 43^0 corresponding to (002) and (101) planes of graphite. Broadness of the XRD peaks again reflects the defective nature of carbon. The Raman spectrum of HTYC-2:1 shows the presence of two peaks with the D-band intensity dominating the G band intensity with the I_G/I_D ratio of 0.70. The ratio shows better graphitization as compared to some commercially available porous

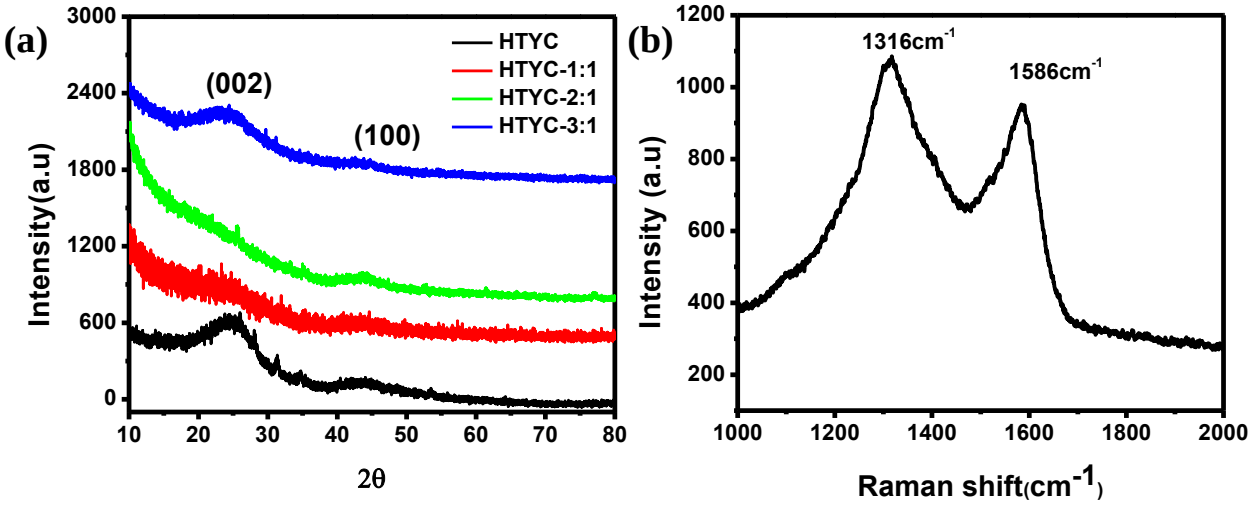

Figure 5.4 *a) XRD plots of different HTYC materials prepared from yogurt under different activation conditions, b) Raman plot of electrochemically most efficient HTYC-2:1 material.*

activated carbons. The D band is positioned at 1326 cm^{-1} and the G band is positioned at 1596 cm^{-1}.

The Brunauer-Emmett-Teller (BET) surface area analysis of the carbons shows the highest surface area of 1294 m^2/g for HTYC-2:1 among all the samples prepared from yogurt with different activations (*figure 5.5a* and *figure 5.5b*). The surface area values for HTYC, HTYC-1:1 and HTYC-3:1 being 26, 970, and 1290 m^2/g, respectively. It can also be seen that the increased activation does not lead to any further significant change in the surface area. All the carbon derivatives showed type-1 N_2 adsorption isotherm according to IUPAC classification reflecting the presence of both micro and mesopores. Pore size

distribution plots for HTYC-1:1, HTYC-2:1 and HTYC-3:1 show that all the samples exhibit peaks around the micropore dimensions of 1.2 nm-1.4 nm

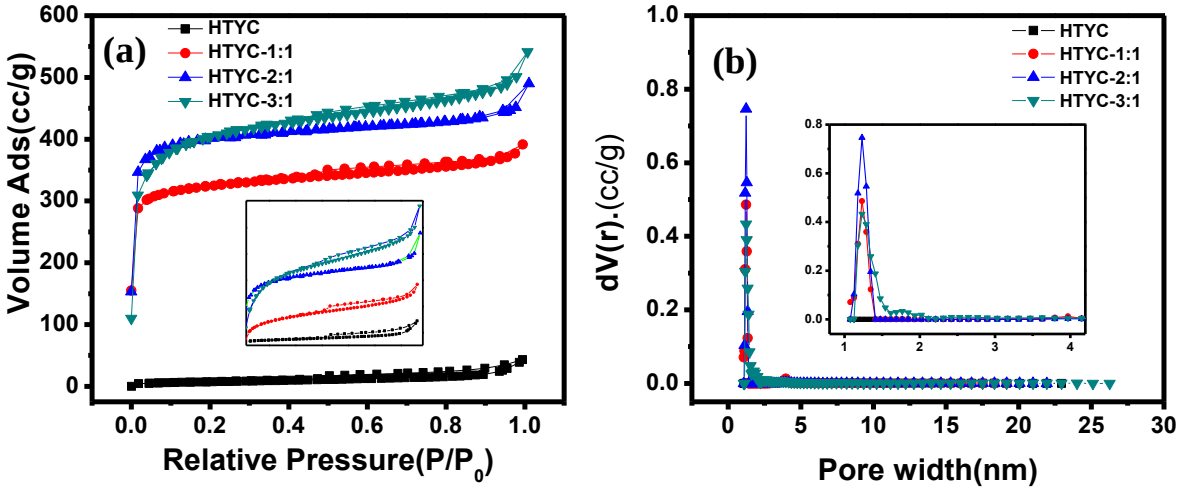

Figure 5.5 *a) Nitrogen adsorption-desorption isotherms for HTYC, HTYC-1:1, HTYC-2:1 and HTYC-3:1. The inset shows the zoomed image of the isotherm. b) The pore size distribution of HTYC materials calculated from DFT method using nitrogen adsorption isotherm; inset shows the zoomed version of original image.*

which is considered best for EDLC. Most of the nano-pores are of diameter more than 1.2 nm and there is a significant population of pores above 1nm spreading up to 1.5nm. Further mesopores distribution at pore diameter of 14nm can be seen in log scale plot of pore size distribution (*figure 5.6*) consistent with HR-TEM observation. The distribution of pores towards higher values makes such a material, a suitable candidate for higher power delivery.[27]

X-ray photoelectron spectroscopy (XPS) data was recorded to determine the surface constitution and elemental composition. Initial survey scans (representative ones for two cases shown in *figure 5.7*) taken to detect the elements present in each sample were followed by individual scans for each element present. The percentage of various elements present in the samples prepared under different activation conditions was calculated. Amongst all the samples, the highest nitrogen concentration of 28 at.% was observed in the HTYC and with the addition of KOH the percentage of nitrogen

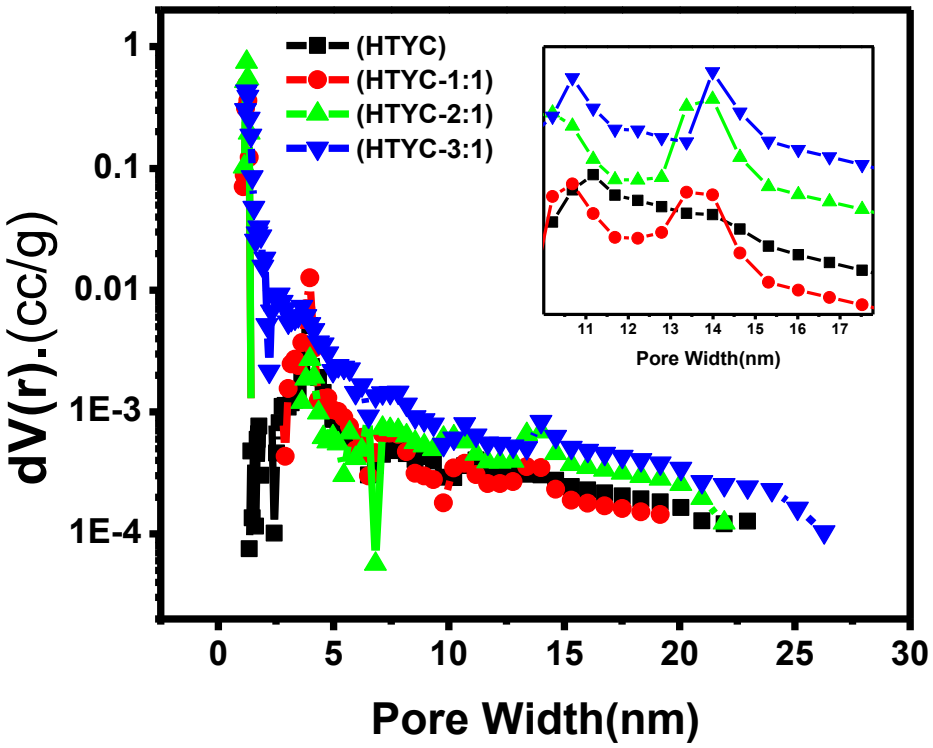

Figure 5.6 *Log sacle plot of pore size distribution of HTYC samples prepared under different activation conditions. Inset shows the zoomed plot in the range of 10nm-18nm.*

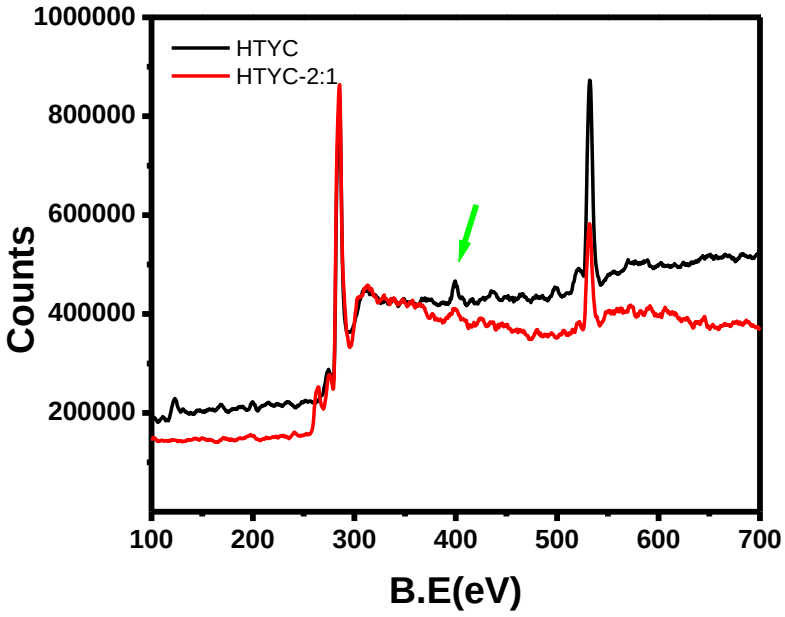

Figure 5.7 *Survey spectra of HTYC and HTYC-2:1 showing presence of nitrogen.*

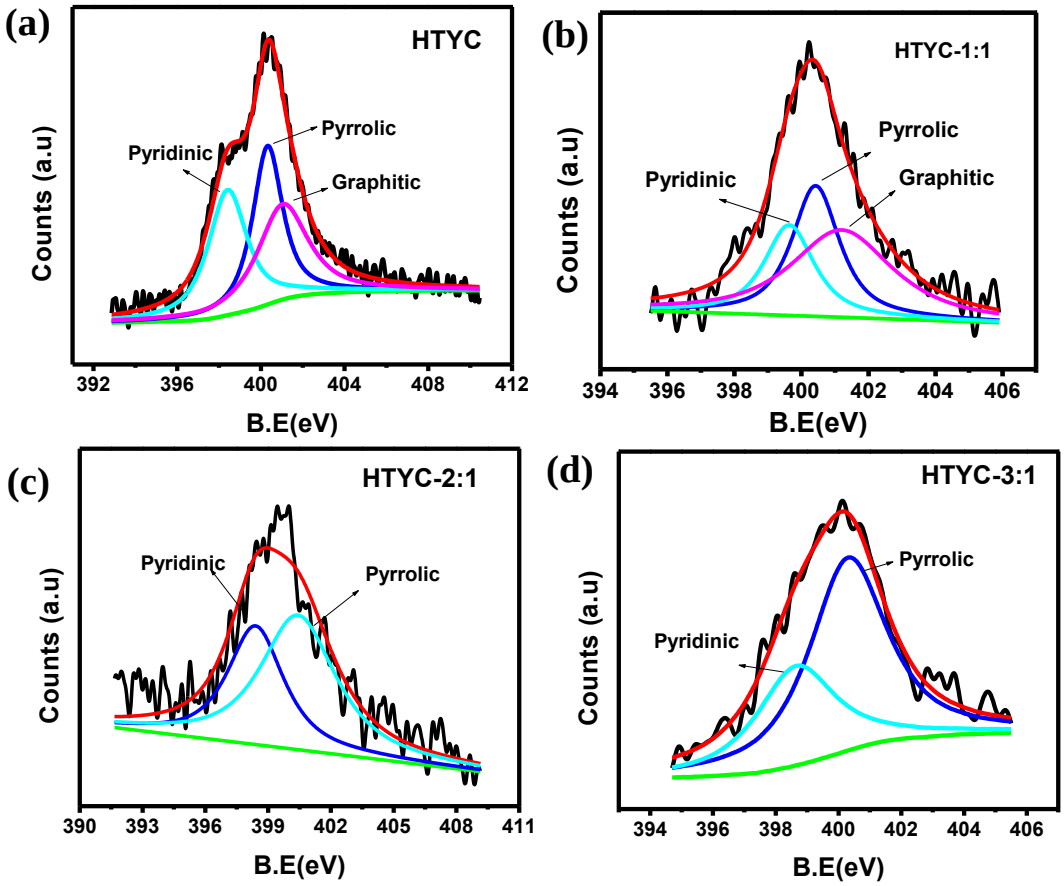

Figure 5.8 *Nitrogen XPS spectra of carbons derived from yogurt by hydrothermal pre-treatment followed by subsequent KOH activation of the product: (a) N1s spectrum of HTYC showing the presence of pyrrolic, pyridinic and graphitic nitrogen (b) N1s spectrum of HTYC-1:1 showing the presence of pyrrolic, pyridinic and graphitic nitrogen, (c) N1s spectrum HTYC-2:1 showing pyridinic and pyrrolic nitrogen, and (d) N1s spectrum of HTYC-3:1 showing the presence of pyridinic, pyrrolic nitrogen.*

decreased most probably due to partial replacement of nitrogen by oxygen from the KOH. The nitrogen and oxygen percentages in the case of HTYC-1:1 were calculated to be 15 at.% and 13 at.% respectively. The electrochemically most active sample HTYC-2:1 was noted to retain 12 at.% nitrogen and 12 at.% oxygen. The nitrogen percentage further decreased to 3 at.% for the HTYC-3:1 sample. The fitted nitrogen XPS spectra (*figure 5.8*) show the presence of pyridinic (398.4eV), pyrrolic (400.3eV) and graphitic (401.3eV) nitrogen types.[28-31]The deconvoluted oxygen 1s XPS spectra of HTYC samples were considered for estimation of adsorbed oxygen and functional oxygen. The spectra

are shown in the *figure 5.9*. As can be seen each sample contains adsorbed oxygen which shows an increase in case of high surface area samples. The relative percentages of various nitrogen and oxygen functionalities are shown in the *table 5.1*.

The electrochemical performance of HTYC materials was evaluated in 1M H_2SO_4, and 6M KOH solutions using two electrode cells with graphite electrodes as current collectors. Each electrode was controllably loaded with 1.2 mg/cm^2 of carbon material by coating a definite volume of the carbon paste made from 5 wt% binder, 15 wt% conducting carbon and 80 wt% of the carbon material.

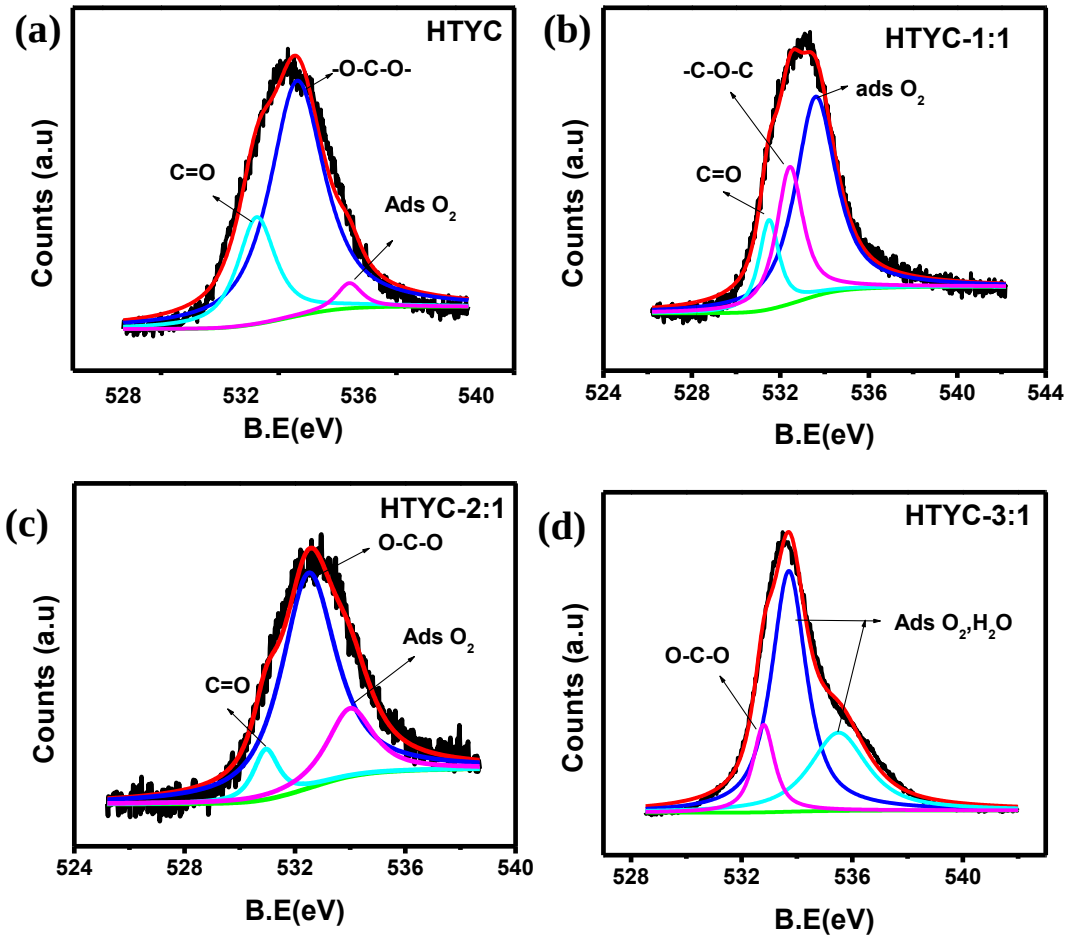

Figure 5.9 *Oxygen 1S XPS spectra of HTYC samples synthesized by activation with KOH at 800^{0}C. a) HTYC b) HTYC-1:1 c) HTYC-2:1 d) HTYC-3:1.*

Figure 5.10a shows the cyclic voltammograms of HTYC-2:1 taken at different scan rates ranging from 20 mV/s to 200 mV/s. Nearly rectangular shaped CV

curves obtained indicate that the behaviour is close to the ideal EDLC. *Figure 5.10b* shows the galvanostatic charge-discharge plots at current densities of 2, 5, 10, 20 A/g, respectively. A high capacitance of 225 F/g was observed for HTYC-2:1 at current density of 2A/g, which reduced only by a small amount to 200 F/g at a ten times high current density of 20A/g. The high capacitance values at high current densities implies the fast diffusion of ions in the electrolyte.[32] EI spectra (EIS) of the samples were recorded in a 3-electrode cell in 1M H_2SO_4 (*figure5.10c*). The EIS points to the low equivalent series resistance of 0.44 Ω and a very small contribution of resistive impedance to the capacitance. The nearly vertical line in the low frequency region of the EIS further points to the ideal capacitive behaviour.[30] Further, the small semicircle in the low frequency region points to the involvement of nitrogen functionalities of pyridenic and pyrrolic type and oxygen functionalities of quinone-hydroquinone type in the charge transfer reactions. Cycle stability is also an important issue with supercapacitors, and more importantly if there are pseudo-capacitance contributions of functional groups.

Table 5.1 *XPS functional group analysis of different carbon materials derived from yogurt by different amount of KOH activations.*

Sample	Nitrogen %			Oxygen %		
	Pyridinic	Pyrrolic	Graphitic	C=O	C-O-C	-COOH, Ad O_2
HTYC	23	39	38	17	40	43
HTYC-1:1	28	39	33	23	27	50
HTYC-2:1	41	59	-	6	26	68
HTYC-3:1	33	67	-	-	30	70

Our material offered good cyclability and capacitance retention of 91% after 5000 charge-discharge cycles which is comparable to most of the carbons obtained from polymer pyrolysis.[33,34] *Figure 5.10d* shows the cycle stability plot of HTYC-2:1 material when the two electrode cell was cycled at a high current density of 10A/g for 5000 charge-discharge cycles. The material shows remarkable stability and does not drop much even up to 5000 cycles. Electrochemical performance of the HTYC-2:1 was also tested in 6M KOH

solution in a three electrode cell using Hg/HgO as reference electrode and platinum as the counter electrode in the voltage window of -1 V to 0 V. *Figure 5.11* shows CV and charge-discharge plots of HTYC-2:1 in 6M KOH. The material shows a fairly good performance on the negative side too, offering a capacitance of 216 F/g at a scan rate of 5mV/s. Further *figure 5.12* compares the electrochemical performance of various carbon materials prepared under different activation conditions. As can be seen from the comparative plot, the best performance was delivered by the 2:1 (KOH:yogurt, hydrothermal product).

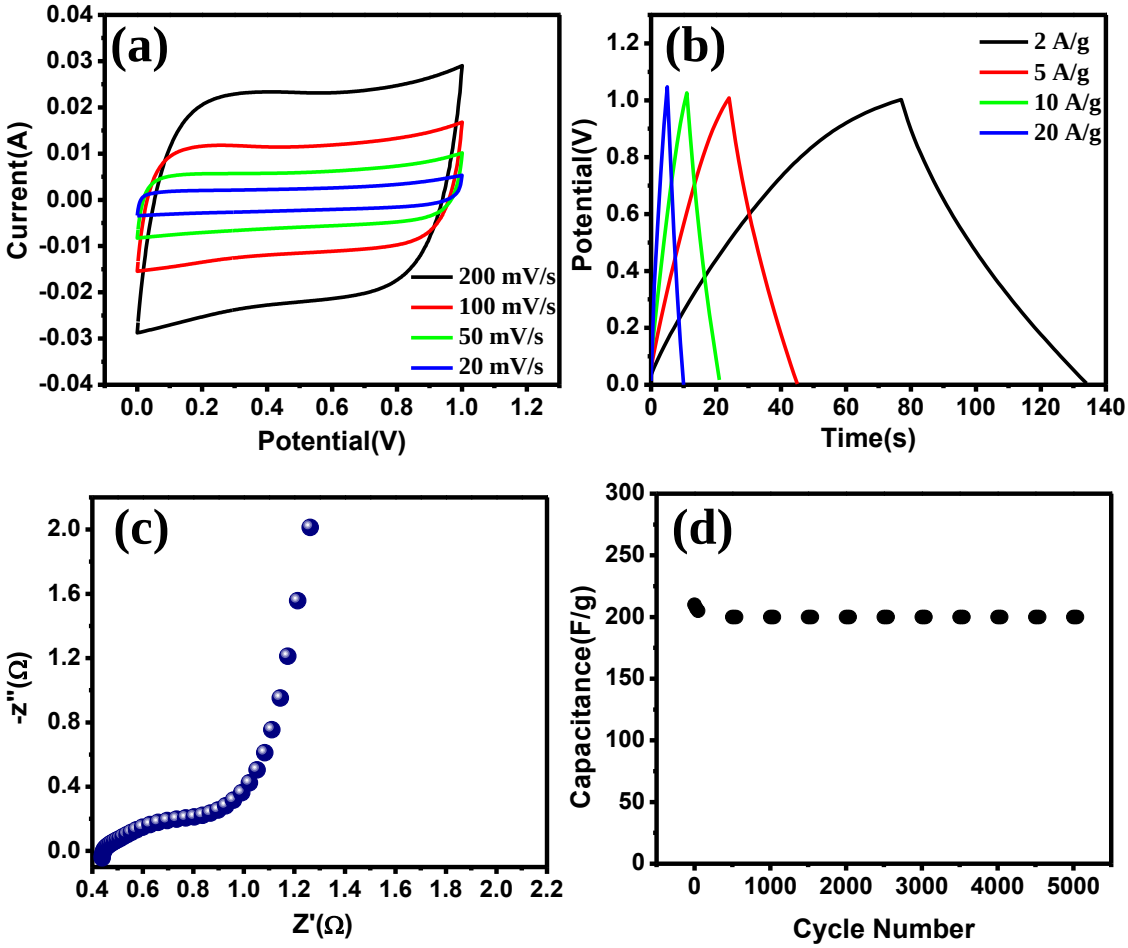

Figure 5.10 *Electrochemical performance of yogurt based porous carbons: (a) CV curves for HTYC-2:1 at different scan rates measured in a two electrode assembly in 1M H_2SO_4.(b) Charge-discharge curves of HTYC-2:1 at different current densities in a two electrode assembly in 1M H_2SO_4. (c) Nyquist plot for HTYC-2:1 measured in 1M H_2SO_4 in the frequency range of 100 mHz to 10 MHz. (d) Cycle stability of HTYC-2:1 material at current density of 10A/g for 5000 cycles.*

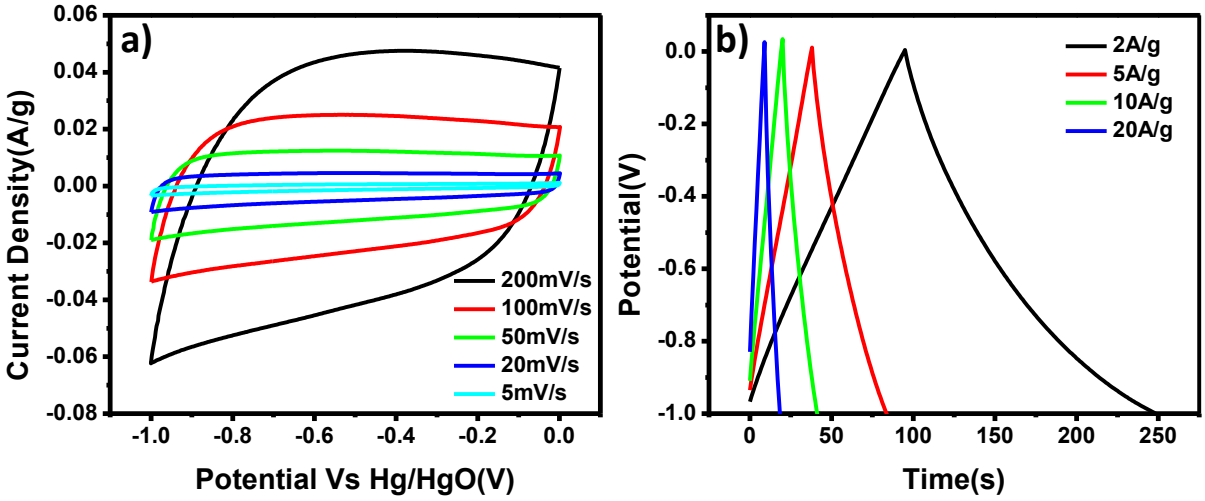

Figure 5.11 *Electrochemical performance of HTYC-2:1 in 6M KOH solution in a three electrode cell using Hg/HgO as reference electrode and carbon paper as counter electrode .a) Shows the CV plots in scan rate range of 5mV/s to 200mV/s and b) Shows the charge-discharge plots at the currents ranging from 2A/g to 20A/g.*

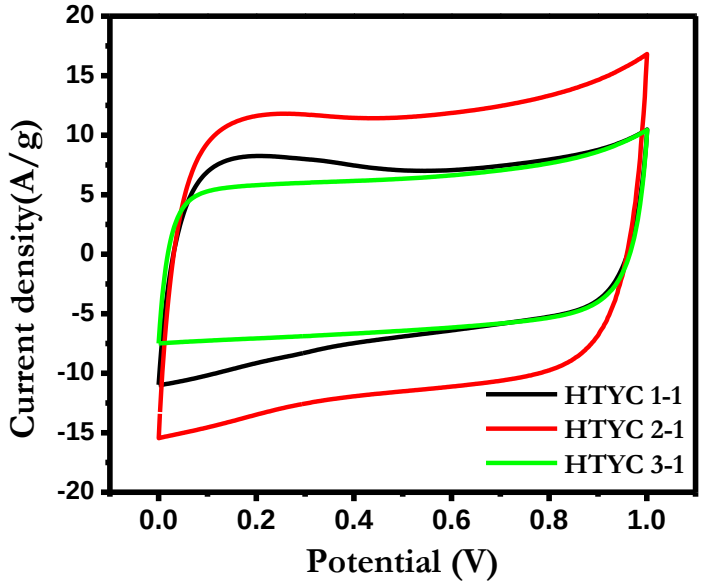

Figure 5.12 *Comparative CV plot for different carbons prepared from yogurt under different activation conditions. Measurements done in 1M H_2SO_4 at a scan rate of 50mV/s vs. Ag/AgCl, with Pt as counter electrode.*

The electrochemical performance of HTYC material is comparable and in most of the cases even better than other reported nitrogen containing carbon materials prepared from synthetic nitrogen containing polymer materials by pyrolysis and activation. *Table 5.2* (above) compares the capacitance values of different nitrogen containing carbons

prepared from synthetic polymers and biomass. It can be seen that at similar current densities our material performs better than most of other synthetic carbon materials prepared from synthetic polymers and biomass.

Table 5.2 *Capacitance values for different forms of carbon prepared by polymer pyrolysis and activation.*

Precursor	Activation/Template	Electrolyte	Electrode system	Current density	Capact. (F/g)
Natural Cotton	**-**	**1M Na_2SO_4**	**2-electrode**	**11.2µA/cm^2**	**16**
Cotton Stalk	**H_3PO_4**	**Et4NBF4**	**3-electrode**	**0.5A/g**	**114**
Cotton Shirts	**NaF**	**1M Na_2SO_4**	**3 electrode**	**2mV/s**	**70**
Silk Fibroin	**Steam- KOH**	**1M $(C_2H_5)_4NBF_4$**	**2-electrode**	**1mA/cm^2**	**52**
Seaweed	**No activation**	**1M H_2SO_4**	**2-electrode**	**1A/g**	**200**
Gelatin	**NaOH**	**6M KOH**	**2-electrode**	**5A/g**	**281**
PVA	**Mg-acetate**	**1M H_2SO_4**	**3-electrode**	**1A/g**	**210**
Gelatin	**Dual template**	**6M KOH**	**3-electrode**	**1A/g**	**284**
Melamine	**No activation**	**1M H_2SO_4**	**3-electrode**	**0.1mV/s**	**205**
poly(benzoxazine-co-resol)	**Pluronic 127**	**6M KOH**	**3-electrode**	**0.5A/g**	**274**
HTYC-2:1	**KOH/ hydrothermal**	**6M KOH**	**3-electrode**	**2A/g**	**225**

Capacitance of 225F/g at 2A/g and 200F/g at 20A/g is a good value for super-capacitors, as it stands proudly in comparison to the various nitrogen containing carbons prepared from polypyrrole microsheets (192 F/g at 10A/g), ionic liquids (196 F/g at

0.5A/g), Polyacrylonitrile (210 F/g at 0.1A/g), graphene nanoballs (206 F/g at 20A/g), block copolymer of PAN and PBA (166 F/g at 0.1A/g) and better than some advanced carbon materials like HPGC (160 F/g at 20A/g), CNT-graphene film (130 A/g at 50A/g) and 3D porous beehive carbon (140 F/g at 40 A/g) . [35-42]

HTYC-2:1 delivers high energy density of 7 Wh/kg at the power density of 5kW/kg in aqueous electrolyte. *Figure 5.13* shows the Ragone plot for the HTYC-2:1 material. The energy density compares very well with the other electrochemically valuable forms of carbon prepared from nitrogen containing

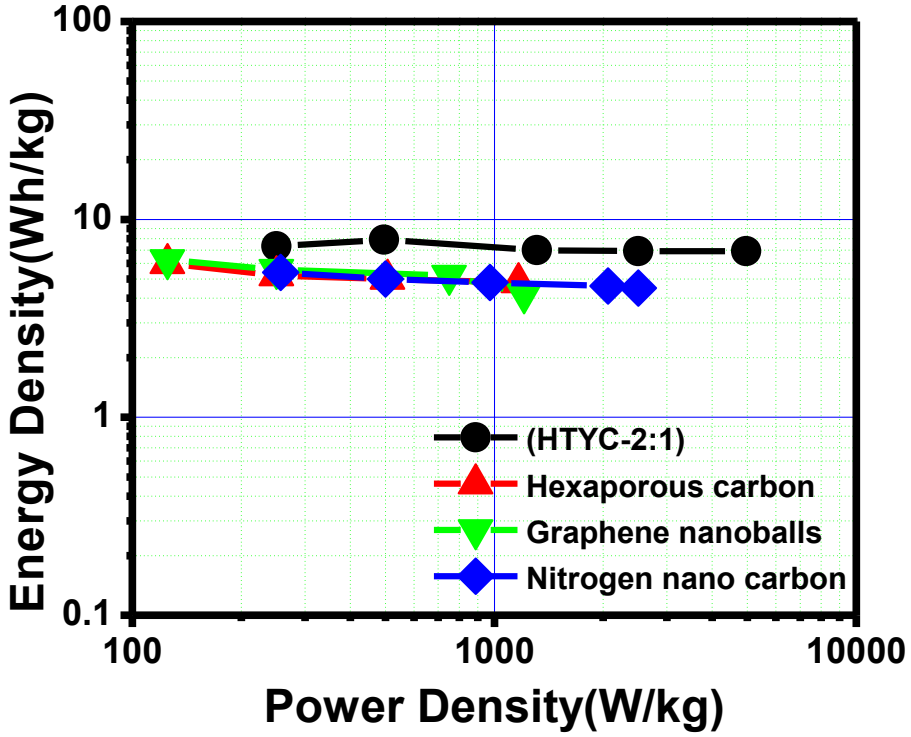

Figure 5.13 *Ragone plot compares the energy density and power density of HTYC-2:1 with other reported carbon materials in aqueous electrolyte.*

precursors. Further there is no large decrease in the energy density on going towards higher power densities thus the material promises high power delivery without a major reduction in energy density. Because of good electrochemical performance of HTYC-2:1 on negative side of the voltage (*figure 5.11*), the HTYC-2:1 material is noted to offer a good potential as cathode material for asymmetric super-capacitors.

Asymmetric performance was thus checked against a well-known anode material, Ni-Co sulphide. *Figure 5.14* shows the FE-SEM images of hydrothermally grown NCS nanowires on nickel foam. Based on the electrochemical performance in three electrode assembly a specific mass of HTYC-2:1 was loaded on carbon fiber paper so as to achieve best capacitance match (~10 mg of HTYC-2:1 to counter 1800F/g of NCS at 1A/g).

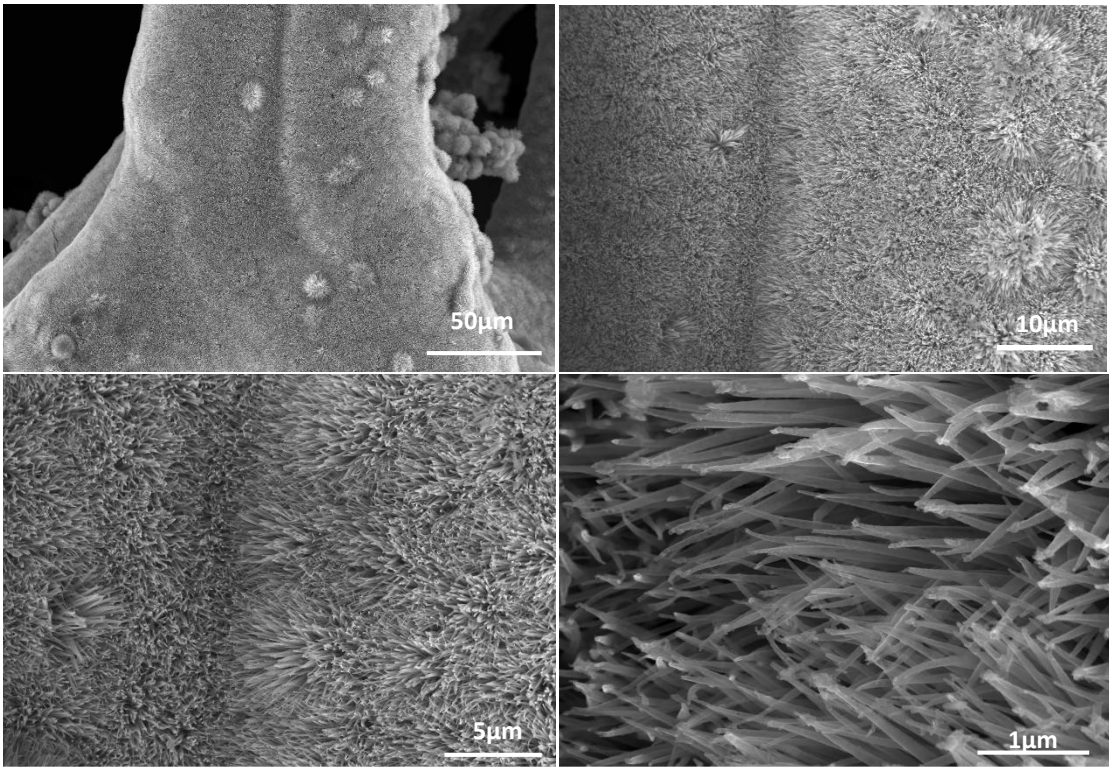

Figure 5.14 *FE-SEM images of NCS used as counter electrode in the asymmetric testing of HTYC carbon material.*

Figure 5.15 and *figure 5.16* show the asymmetric supercapacitor performance of HTYC-2:1 against NCS. *Figure 5.15a* shows three electrode CV performances after mass balance at 50mV/s. With the asymmetric assembly we could extend the voltage window up to 1.6V without any water splitting, as can be seen from *figure 5.15b* and *figure 5.15c*. A capacitance of 200 F/g at a current of 10 mA with carbon loading of 10 mg on negative electrode was noted and it was seen to decrease to 190F/g at a current of 40mA (*figure 5.16*). By this asymmetric assembly we could achieve three times increase in the energy density as shown in the Ragone plot (*figure 5.15d*). Energy

density of 27 Wh/kg was achieved at a power density of 364 W/kg; and an energy density of 17.8 Wh/kg was achieved at power density of 6400 W/kg, which is much superior to the asymmetric capacitance data reported for Ni-Co sulfide nanowires vs. commercially activated carbon asymmetric assembly. [53-55]

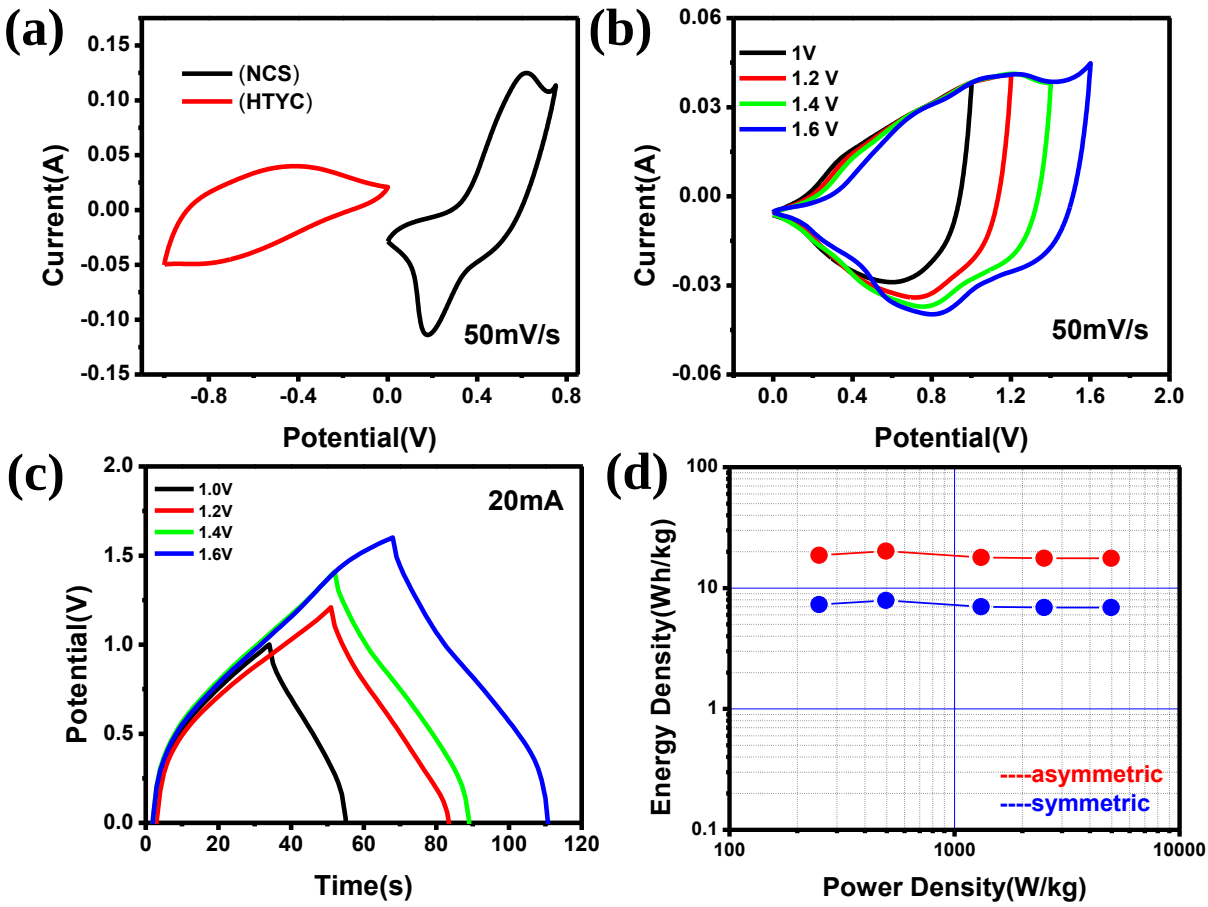

Figure 5.15 *Shows the asymmetric performance of HTYC-2:1 against NCS in 3M KOH solution. (a) Shows the individual CV performance of NCS and HTYC-2:1 at 10mV/s in 3M KOH in a three electrode assembly vs. Hg/HgO reference electrode, (b) Shows the CV plots at scan rate of 50mV/s depicting the extension in voltage window up to 1.6V in the asymmetric cell. (c) Shows the charge-discharge data of asymmetric cell at a current of 20mA. (d) Shows the Ragone plot comparing power and energy density of symmetric and asymmetric super-capacitors fabricated from HTYC-2:1.*

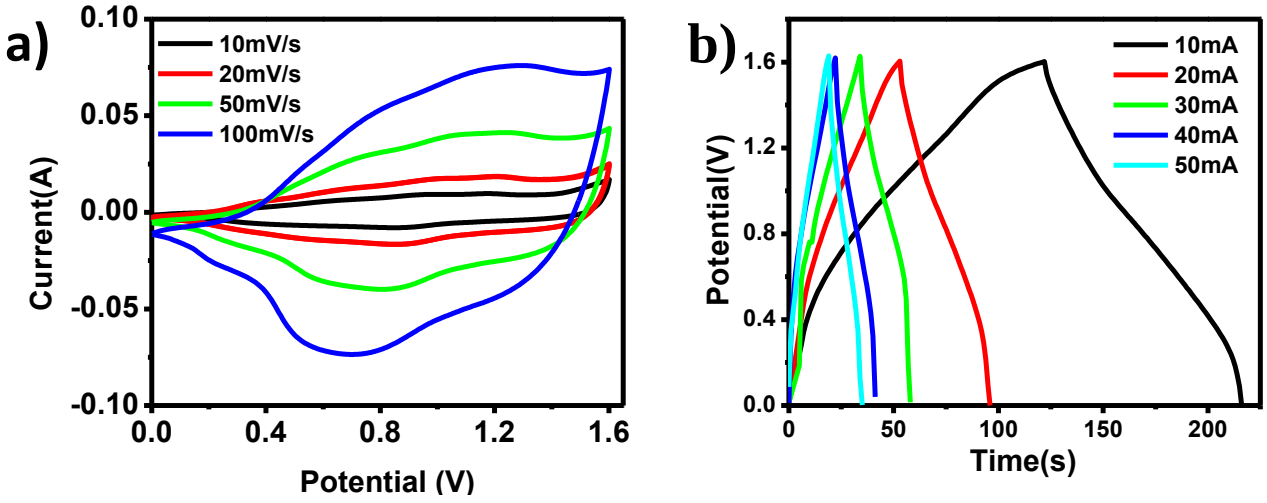

Figure 5.16 *Electrochemical performance of asymmetric cell having NCS as anode and HTYC-2:1 as cathode.* ***a)*** *Cyclic voltammetry plots at different scan rates in 3M KOH* ***b)*** *Charge-discharge plots at currents ranging from 10mA to 50mA.*

5.4 Conclusion

We report the synthesis of electrochemically efficient nitrogen containing carbon from yogurt. The material retains a high nitrogen percentage of 12 atm.% after high temperature pyrolysis in the presence of activating agent. The surface area of 1300 m^2/g was attained with a good density of mesopores, apart from abundant micropores. The material offers a capacitance of 225 F/g at 2 A/g and a capacitance of 200 F/g at large current densities of 20 A/g in aqueous electrolytes. An energy density of 7 Wh/kg is delivered at a power density of 5000 W/kg in aqueous electrolytes, which is good for several application domains. We also examined the cathode performance of our material vs. nickel cobalt sulfide (NCS) and demonstrated that our material performs better than most of the commercially available carbon materials as a cathode in asymmetric supercapacitors. Our energy density in asymmetric assembly goes as high as 27 Wh/kg at power density of 364 W/kg (and an energy density of 17.8 Wh/kg was achieved at power density of 6400 W/kg) which is comparable to or superior to other cathode materials for the different morphologies of the same NCS anode material.

5.5 References

1. B. E. Conway, *Electrochemical Supercapacitors: Scientific Fundamentals and Technological Applications*, Kluwer Academic/Plenum Publishers, New York, 1999.
2. P. Simon and Y. Gogotsi, *Nat. Mater.*, 2008, **7**, 845-854.
3. J. M. Tarascon and M. Armand, *Nature*, 2001, **414**, 359-367.
4. R. Kotz and M. Carlen, *Electrochim. Acta*, 2000, **45**, 2483–2498.
5. P. John and R. Miller, *Electrochem. Soc. Interface*, 2008, **17**, 53-58.
6. Y. Zhai, Y. Dou, D. Zhao, P. F. Fulvio, R. T. Mayes and S. Dai, *Adv. Mater.*, 2011, **23**, 4828-4850.
7. C. Huang, C. Li and G. Shi, *Energy Environ. Sci.*, 2012, **5**, 8848-8868.
8. J. Chen, K. Sheng, P. Luo, C. Li and G. Shi, *Adv. Mater.*, 2012, **24**, 4569-4573.
9. D. Puthusseri, V. Aravindan, B. Anothumakkool, S. Kurungot, S. Madhavi and S. Ogale, *Small*, 2014, **10**, 4395-4402.
10. P. Yadav, A. Banerjee, S. Unni, J. Jog, S. Kurungot and S. Ogale, *ChemSusChem*, 2012, **5**, 2159-2164.
11. D. Mhamane, A. Suryawanshi, S. M. Unni, C. Rode, S. Kurungot and S. Ogale, *Small*, 2013, **9**, 2801-2809.
12. Y. Lu, Y. Huang, M. Zhang and Y. Chen, *J. Nanosci. Nanotechnol.*, 2014, **14**, 1134–1144.
13. G. Xiong, C. Meng, R. G. Reifenberger, P. P. Irazoqui and T. S. Fisher, *Electroanalysis*, 2014, **26**, 30-51
14. Q. Lu, J. G. Chen and J. Q. Xiao, *Angew. Chemie-Int. Ed.*, 2013, **52**, 1882-1849.
15. D. Qu and H. Shi, *J. Power Sources*, 1998, **74**, 99-107.
16. G. Wang, L. Zhang and J. Zhang, *Chem. Soc. Rev.*, 2012, **41**, 797-828.
17. Y. Sun, Q. Wu and G. Shi, *Energy Environ. Sci.*, 2011, **4**, 1113-1132.
18. J. Huang, B. G. Sumpter and V. Meunier, *Chem. - A Eur. J.*, 2008, **14**, 6614–6626.
19. D. Hulicova-Jurcakova, M. Seredych, G. Q. Lu and T. J. Bandosz, *Adv. Funct. Mater.*, 2009, **19**, 438-447.

20. N. Cohen and M. S. Silverstein, *Polymer*, 2011, **52**, 282-287.
21. X. Y. Chen, C. Chen, Z. J. Zhang and D. H. Xie, *Ind. Eng. Chem. Res.*, 2013, **52**, 12025–12031.
22. T. Morishita, Y. Soneda, T. Tsumura and M. Inagaki, *Carbon*, 2006, **44**, 2360-2367.
23. L. Wei, M. Sevilla, A. B. Fuertes, R. Mokaya and G. Yushin, *Adv. Funct. Mater.*, 2012, **22**, 827-834.
24. W. Qian, F. Sun, Y. Xu, L. Qiu, C. Liu, S. Wang and F. Yan, *Energy Environ. Sci.*, 2014, **7**, 379-386.
25. M. Wahid, D. Puthusseri, D. Phase and S. Ogale, *Energy and Fuels*, 2014, **28**, 4233-4240.
26. Y. Li, L. Cao, L. Qiao, M. Zhou, Y. Yang, P. Xiao and Y. Zhang, *J. Mater. Chem. A*, 2014, **2**, 6540-6548.
27. C. Largeot, C. Portet, J. Chmiola, P.-L. Taberna, Y. Gogotsi and P. Simon, *J. Am. Chem. Soc.*, 2008, **130**, 2730–2731.
28. J. R. Pels, F. Kapteijn, J. A. Moulijn, Q. Zhu and K. M. Thomas, *Carbon*, 1995, **33**, 1641-1653.
29. F. Kapteijn, J. A. Moulijn, S. Matzner and H. P. Boehm, *Carbon*, 1999, **37**, 1143-1150.
30. D. Rosenthal, M. Ruta, R. Schlogl and L. Kiwi-Minsker, *Carbon*, 2010, **48**, 1835-1843.
31. H. Estrade-Szwarckopf, *Carbon*, 2004, **42**, 1713-1721.
32. D.W. Wang, F. Li, M. Liu, G. Q. Lu and H.-M. Cheng, *J. Phys. Chem. C*, 2008, **112**, 9950-9955.
33. E. Frackowiak and F.Beguin, *Carbon*, 2001, **39**, 937-950
34. S. Bose, T. Kuila, A. K. Mishra, R. Rajasekar, N. H. Kim and J. H. Lee, *J. Mater. Chem.*, 2012, **22**, 767-784.
35. L. Qie, W. Chen, H. Xu, X. Xiong, Y. Jiang, F. Zou, X. Hu, Y. Xin, Z. Zhang and Y. Huang, *Energy Environ. Sci.*, 2013, **6**, 2497-2504.
36. J.Y. Liu, H.Y. Chang, Q. D. Truong and Y.-C. Ling, *J. Mater. Chem. C*, 2013, **1**, 1713-1716.

37. X. Yang, D. Wu, X. Chen and R. Fu, *J. Phys. Chem. C*, 2010, **114**, 8581-8586.
38. J.S. Lee, S.I. Kim, J.C. Yoon and J.H. Jang, *ACS Nano*, 2013, **7**, 6047-6055.
39. M. Zhong, E. K. Kim, J. P. McGann, S.E. Chun, J. F. Whitacre, M. Jaroniec, K. Matyjaszewski and T. Kowalewski, *J. Am. Chem. Soc.*, 2012, **134**, 14846-14857.
40. D.W. Wang, F. Li, M. Liu, G. Q. Lu and H.-M. Cheng, *Angew. Chemie - Int. Ed.*, 2008, **47**, 373-376.
41. D. Yu and L. Dai, *J. Phys. Chem. Lett.*, 2009, **1**, 467-470.
42. D. Puthusseri, V. Aravindan, S. Madhavi and S. Ogale, *Energy Environ. Sci.*, 2014, **7**, 728-735.
43. J. Xue, Y. Zhao, H. Cheng, C. Hu, Y. Hu, Y. Meng, H. Shao, Z. Zhang and L. Qu, *Phys. Chem. Chem. Phys.*, 2013, **15**, 8042-8045.
44. M. Chen, X. Kang, T. Wumaier, J. Dou, B. Gao, Y. Han, G. Xu, Z. Liu and L. Zhang, *J. Solid State Electrochem.*, 2013, **17**, 1005-1012.
45. L. Bao and X. Li, *Adv. Mater.*,2012, **24**, 3246-3252.
46. Y. J. Kim, Y. Abe, T. Yanagiura, K. C. Park, M. Shimizu, T. Iwazaki, S. Nakagawa, M. Endo and M. S. Dresselhaus, *Carbon*, 2007, **45**, 2116-2125.
47. E. Raymundo-Piñero, F. Leroux and F. Béguin, *Adv. Mater.*, 2006, **18**, 1877-1882.
48. B. Xu, S. Hou, G. Cao, F. Wu and Y. Yang, *J. Mater. Chem.*, 2012, **22**, 19088-19093.
49. K. Shen, Z.-H. Huang, L. Gan and F. Kang, *Chem. Lett.*, 2009, **38**, 90-91.
50. X. Y. Chen, C. Chen, Z. J. Zhang and D. H. Xie, *J. Mater. Chem. A*, 2013, **1**, 10903-10911.
51. D. Hulicova, J. Yamashita, Y. Soneda, H. Hatori and M. Kodama, *Chem. Mater.*, 2005, **17**, 1241-1247.
52. D.C. Guo, J. Mi, G.-P. Hao, W. Dong, G. Xiong, W.-C. Li and A.-H. Lu, *Energy Environ. Sci.*, 2013, **6**, 652-659.
53. C. Liu, Z. Yu, D. Neff, A. Zhamu and B. Z. Jang, *Nano Lett.*, 2010,**10**, 4863-4868.

54. L. Yu, L. Zhang, H. B. Wu and X. W. Lou, *Angew. Chemie-Int. Ed.*, 2014, **53**, 3711-3714.

55. X. Wang, C. Yan, A. Sumboja and P. S. Lee, *Nano Energy*, 2014, **3**, 119-126.

Chapter 6

Low surface area, hard, carbon material derived from compactly packed walnut shells as high capacity sodium ion battery anode

Efficient sodium ion intercalation/de-intercalation in the semi graphitic lattice of hard carbon derived from walnut shell (CNS) is demonstrated in this chapter. We used high temperature pyrolysis under inert atmosphere to obtain low surface area (59m^2/g) hard carbon (CNS) from walnut shells. The CNS shows large interplanar c-axis separation of 0.39 nm - 0.36 nm as compared to 0.32 nm for graphite which, therefore, makes it suitable for sodium ion intercalation/de-intercalation. Presence of semi-graphitic domains in the carbon matrix with increased c-axis interplanar separation boosts up the sodium ion capacity for the CNSs. A stable reversible capacity of 257$mAhg^{-1}$ was observed at current density of 50mAg^{-1} for CNS-1000 (nutshell derived carbon synthesized at 1000^{0}C) with an impressive rate performance. No loss of electrochemical performance was observed for high current cycling (100mAg^{-1} → 2Ag^{-1} →100mAg^{-1}). Also, the CNS shows remarkably stable electrochemical performance up to 300 charge-discharge cycles at 100mAg^{-1} with minimal drop in capacity.

6.1 Introduction

Sodium ion batteries are emerging as new cost effective alternatives to Li-ion batteries. Similarity with lithium chemistry and natural abundance makes sodium a promising successor to lithium. Huge reservoirs of sodium in form of minerals like rock salt, sodalite and feldspars are present in Earth's crust. Abundance of sodium (2.5% for sodium vs. 0.0017% for lithium[1]) makes it economical and commercially viable alternative to lithium provided the electrochemical performance is maintained[2–4]. Since, sodium and lithium occupy same group in periodic table; their electrochemical chemistry is expected to be more or less similar. Therefore, the enormous work on lithium ion batteries in past can be the guiding force for future progress in sodium ion batteries. The ongoing research in Na-ion batteries involves discovery of efficient cathode as well as anode materials to lead the technology towards commercialization[1–4].

Replication of the lithium chemistry has been a successful ploy for the cathode. In analogy to $LiFeO_2$, $LiCoO_2$, $LiMnO_4$ and $LiNiO_2$, the binary oxides of transition metals and Na viz. $NaFeO_2$, $NaCoO_2$, $NaMnO_4$ and $NaNiO_2$ are reported to show satisfactory performance as cathode in sodium ion batteries. Similarly, sodium ion counterparts of stable polyanoinic phosphates and pyrophosphates like $LiFePO_4$, $LiMnPO_4$, $LiMn_{1/2}Fe_{1/2}PO_4$, $Li_2FeP_2O_7$, and Li2MnP2O7 are demonstrated to be useful. Also, polyanionic phosphates, fluorophosphates, carbanophosphates of lower transition metals like V and Ti show superior performance for sodium ion insertion-extraction than the lithium ion[1,5–7]. Especially, $Na_3V_2(PO_4)_3$, and $Na_3V_2(PO_4)_2F_3$ are best performing cathode materials for sodium ion battery so far[8–15]. Thus, there is a broad spectrum of choice of cathode materials available for sodium ion battery technology. However, the design of a suitable anode material is a major challenge that is impeding the further progress in this field.

Variety of anode materials including intercalation, conversion and alloying types have been proposed for Na-ion batteries. Redox alloying of Na with Si, Sn, Pb, Sb, Bi and other sodiation/de-sodiation reversible redox reactions with sulphides, selinides, phosphides, and elements like phosphorus and sulphur open a broad choice of promising anode materials for Na-ion batteries[16–24]. For alloying with Si the analogous

high Li-ion capacity phase $Li_{15}Si_4$ is not available for Na ion. Instead, NaSi exists as the highest capacity phase[1,5]. However, huge volume expansion in NaSi may make its practical realization a distant possibility. High capacity alloying with Sn does not show stable cyclability because of large volume changes[21,22,22–24] associated with formation of $Na_{15}Sn_4$. Combination of other P-block metals like Sb and Bi can take care of the volume expansion issue to some extent but it adds to the cost of manufacturing. Similarly, the use of phosphides and sulphides which seem to be promising initially are limited because of their less safe by products. Among several intercalation type materials viz. $Na_2Ti_3O_7$, MoS_2, MoO_3 and graphite, the later looks promising owing to its tremendous success in commercial lithium ion batteries[1,25–30]. However, the use of graphite has not lead to the desired performance because of some fundamental differences in the Na ion and Li ion intercalation chemistries. Although, both belong to the same group and undergo a similar one electron redox transformation, the differences in size make graphitic intercalation of Na more difficult than Li. Na ion weighs 3.2 times heavier than Li and it has 55% larger ionic size as compared to Li. Because of this , although Li ion can intercalate and de-intercalate freely in graphite, interlayer separation being 0.32nm, larger size of Na ion restricts the use of graphite as a suitable stable anodic host for Na ion battery[1,2,5,31].

Carbon provides options in variety of less ordered forms like hard carbons, rGO, graphene sheets, carbon blacks, pet cokes. These carbon forms have delivered highest reversible capacity close to $300mAhg^{-1}$, that is comparable to the Li ion capacity of graphite ($372mAhg^{-1}$). These carbon forms unlike graphite possess larger interlayer separations for free Intercalation and de-intercalation of Na ion.[32–34] Micropores further assist in reversible Na ion storage by reversible insertion and extraction through the pores which is different than conventional intercalation mechanism. High temperature pyrolysis of sugars, proteins, synthetic polymers, and biomass precursors are some of the routes to obtain hard carbons useful for Na-ion batteries[33,35]. Composites of this hard carbons with CNTs and graphene have delivered satisfactory sodium ion performance[36–40]. However, a quest for making Na-ion battery technology cheaper has shifted focus towards the use of natural precursors for hard carbon e.g. bio wastes and natural products. Hard carbons derived from banana peels, lotus petiole, okra by-product,

peanut shells, natural wood fibers or compact wood have delivered satisfactory performance[41–43,43–49].

In this chapter we report the synthesis of hard carbon by direct pyrolysis of a densely packed cellulosic precursor, the walnut shell. The milled carbon material showed an impressive initial reversible capacity of 257mAhg^{-1} at 50 mAg^{-1}. The material retains this capacity even after high current cycling at 2Ag^{-1}. The remarkable cycling stability with small initial loss and stable capacity upto 300 charging-discharging cycles was observed. The performance parameters set high standards for the current material among all recently reported hard carbons derived from biomass and synthetic polymer precursors.

6.2 Experimental Section.

6.2.1 Synthesis and nomenclature of carbon materials derived from walnut shell.

Fresh nutshells were crushed and subsequently washed thoroughly first with 2M HCl, then with DI water and ethanol to remove the mineral salts and soluble organic matter. The crushed small discs of nutshells were then dried in vacuum oven at 100^{0}C over night. The dried pieces were directly subjected to pyrolysis in a tube furnace at three different temperatures 800^{0}C, 1000^{0}C and 1200^{0}C under the flow of inert argon gas. The pyrolysis process was carried out for 6 hours with the temperature scan rate of 5^{0}C/min. After pyrolysis, the carbon samples were collected and then washed with DI water and ethanol. The washed carbon samples were dried at 60^{0}C in vacuum oven. The carbon materials resulting from the pyrolysis reactions at 800^{0}C, 1000^{0}C and 1200^{0}C are named as CNS-800, CNS-1000 and CNS-1200 respectively.

6.2.2 Physical characterization of CNS carbon samples.

The different carbon samples synthesized from walnut shell were examined by X-ray powder diffraction using Philips X'Pert PRO diffractometer with nickel-filtered Cu K_α radiation. Raman spectroscopy was performed using Lab RAM HR800 from JY Horiba. The FE-SEM was done with the help of Nova Nano SEM 450. The surface area values for all the samples were determined by Brunauer Emmett Teller (BET) adsorption method (Quadrasorb automatic volumetric instrument). Cyclic voltammetry and

impedance measurements were performed using BioLogic VMP3 multichannel potentio-galvanostat. Charge discharge measurements were performed with the help of MTI Corp. multichannel battery testing system.

6.2.3 Electrode and coin cell preparation for electrochemical measurement

The electrodes for the electrochemical analysis were prepared by coating slurry of 5% PVDF binder (*poly(vinlylidenedifluoride)), 15%* of conducting carbon *(super-P)* and 80% of CNS material (*CNS-800, CNS-1000 and CNS-1200*) prepared in NMP (*N-methylpyrrolidone)* on a carbon coated aluminum foil. The sample coated aluminum foil was dried at low temperature of 90^0C in vacuum oven for 24 hours. The material coated foil was then cut into circular discs with the help of punching machine fitted with cutters suitable for coin cells of CR2032. The CR2032 cells for electrochemical testing were assembled inside an argon filled glove box at extremely low O_2 and H_2O (*0.2 ppm-1.0 ppm*) concentrations. The metallic sodium is also cut in to discs of similar dimensions and then assembled along with the material coated aluminum electrode disk. The two electrodes are separated by a circular polyethylene separator soaked in electrolyte solution. The electrolyte used was 1M $NaClO_4$ in 1:1 volume ratio of EC (ethylene carbonate) and DMC (dimethyl carbonate) having 5% of FEC (fluoro-ethylene carbonate) already dissolved. The coin cell is sealed inside the glove box and taken outside for different electrochemical tests.

6.3 Results and Discussion.

Morphological transformation of nutshell into carbon material upon pyrolysis is depicted in *figure 6.1*. The cross-sectional morphology comparison of fresh nutshell (*figure 6.1a and figure 6.1c)* and the one pyrolysed at 1000^0C (CNS-1000, *figure 6.1 b & and figure 6.1d*) is shown here. The continuous interlayer free spaces running parallel to surface of the shell could be seen in the fresh nutshell from the figure 6.1c. Upon pyrolysis the hard shells turn in to carbonaceous products as shown in *figure 6.1b*. The SEM micrograph of pyrolysed product shown in *figure 6.1d* shows that pyrolysis into carbon product does not lead to ultimate disappearance of channels rather large

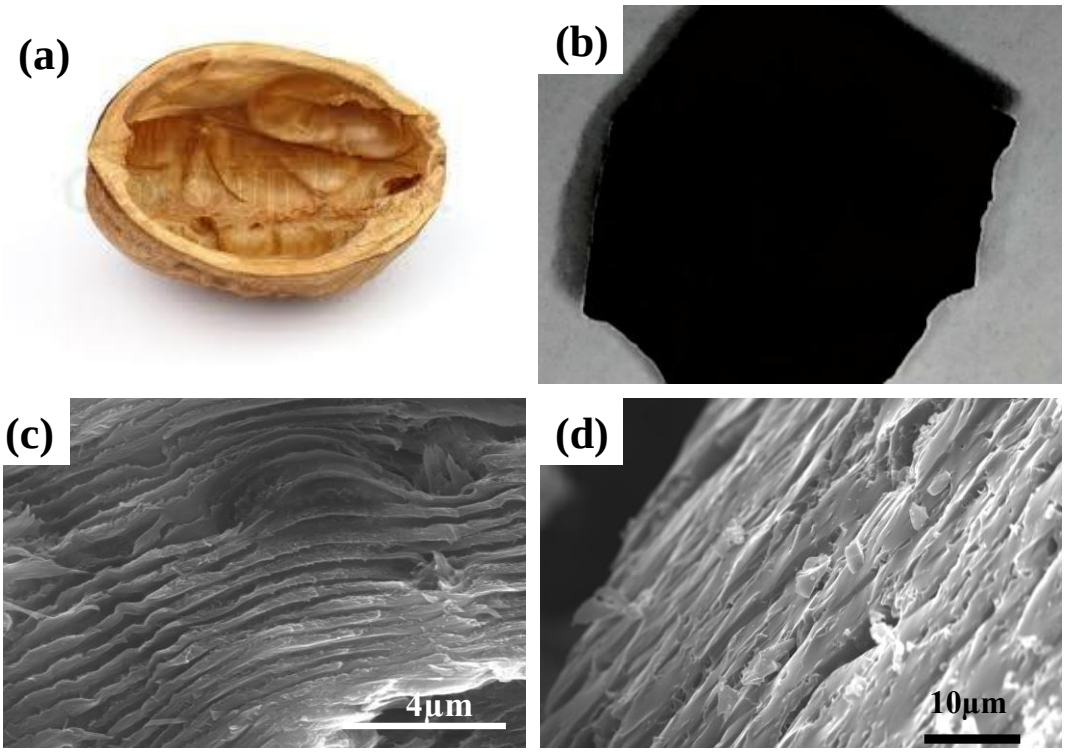

Figure 6.1 *Morphology transformation of walnut shell upon pyrolysis is depicted here. a) Picture of typical walnut shell. b) Picture of carbon chunk obtained from direct pyrolysis of smashed walnut shell. c) Cross sectional SEM image of fresh walnut shell. d) Cross sectional SEM image of carbon product obtained from walnut shell by pyrolysis at 1000^0C (CNS-1000).*

number of them can be seen in the carbon product, although in a modified form. The presence of these free spaces can be advantageous for the better electrochemical performance by maintaining the connectivity of carbon material and electrolyte over a

broad power range.[46,50]

TEM micrograph of CNS-1000 sample is shown in *figure 6.2*. The material is characterized by presence of turbo-stratic graphitic domains, scattered in non-graphitic carbon matrix, as expected for a typical hard carbon material. The interplanar separation of the order of ~0.38nm is observed by TEM fringe analysis, as can be clearly seen from *figure 6.2*. The particular separation, in the carbon material, makes CNS-1000 a suitable choice for sodium ion battery anode applications.

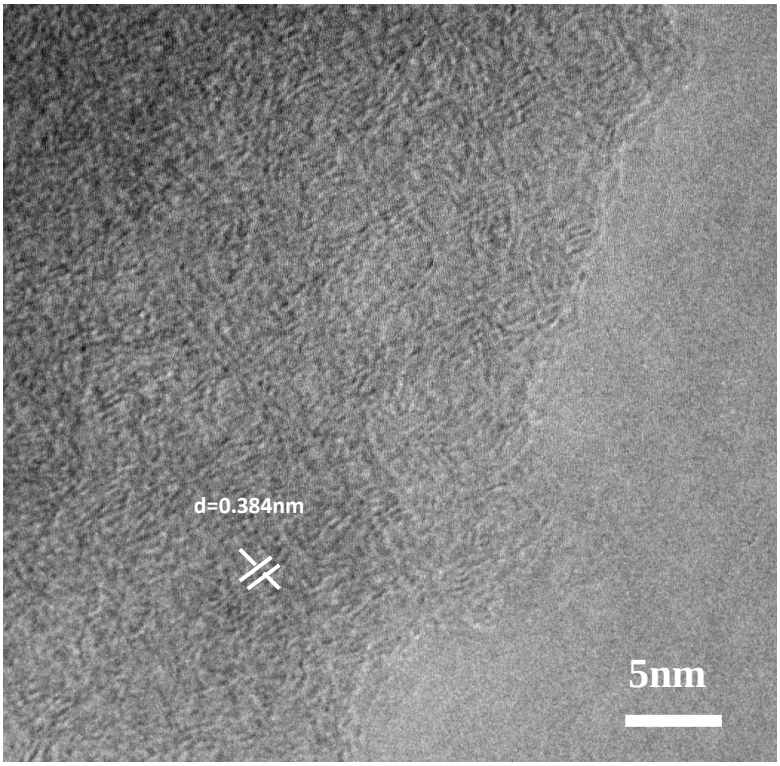

Figure 6.2. *TEM micrograph shows the turbo-stratic graphitic regions scattered in the huge matrix of non-graphitic carbon.*

The pyrolysis of nutshell was also performed at 800^0C and 1200^0C in addition to 1000^0C. It could be seen that there is no evident surface morphological distinction between CNS-800^0C, CNS-1000^0C and CNS-1200^0C samples in micron regime. *Figure 6.3* compares the FE-SEM images of three carbon samples synthesized from walnut shells at three different pyrolysis temperatures.

XRD and Raman analysis of three samples reveal that the crystal planes and atomic arrangements are not altered significantly with the increase in the pyrolysis temperature

which is characteristic of hard carbons.

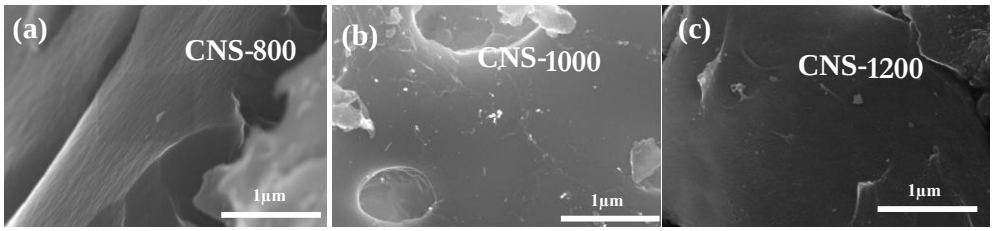

Figure 6.3 *FE-SEM images of carbon products synthesized at different temperature conditions. a) CNS-800 b) CNS-1000 c) CNS-1200*

Figure 6.4 shows the XRD and Raman plot of the CNS samples obtained at three pyrolysis temperatures. XRD analysis (*figure 6.4a*) shows that interplanar (002) separations for the three pyrolysis cases are 0.39nm, 0.37nm and 0.37nm for CNS-800, CNS-1000 and CNS-1200 respectively. The interplanar separation greater than 0.36nm, is considered favorable for efficient sodium ion intercalation/de-intercalation in the carbon lattice. Thus the CNS- materials synthesized here are promising for direct use as anode in Na-ion battery.[33]

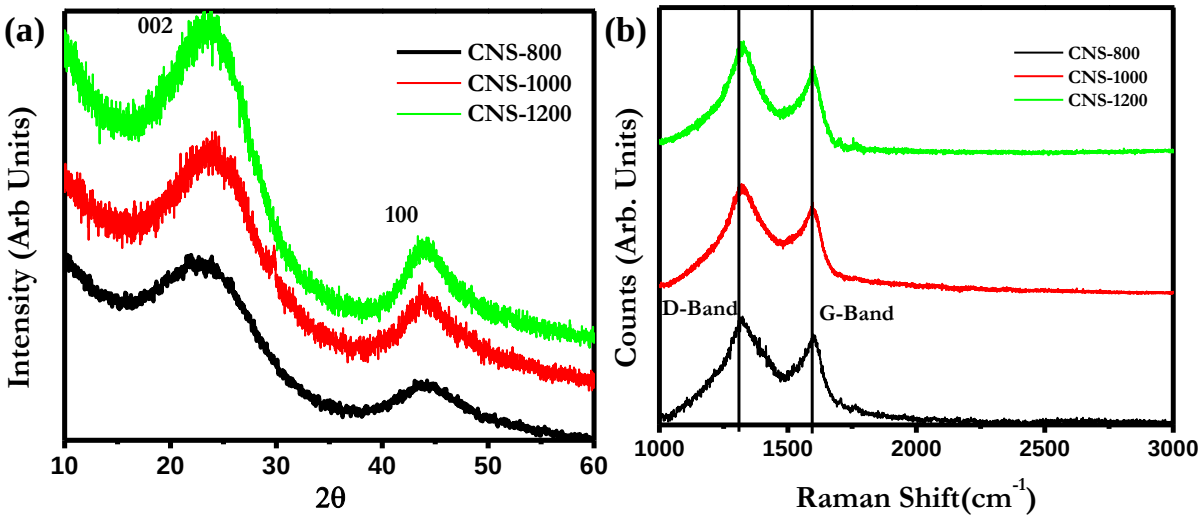

Figure 6.4 *a) XRD comparison of CNS samples synthesized at three different temperatures. b) Raman comparison of CNS samples synthesized at three different temperatures.*

Raman plots (*figure 6.4b*) further establish the fact that the nutshell carbons are the typical representative of hard carbons as there is no or negligible increase in the degree of graphitization with increase in the carbonization temperatures above 800^0C. Presence

of Raman bands at 1320cm^{-1} and 1590cm^{-1} are attributed to well known D and G bands of defective graphite.[51,52] No improvement in I_G/I_D ratios is observed at elevated temperatures which therefore establishes the hard nature of CNS carbon samples. *Table 6.1* summaries the XRD and Raman parameters of CNS samples.

Table 6.1 *Summary of XRD and Raman analysis.*

Parameter	*CNS-800*	*CNS-1000*	*CNS-1200*
XRD peak position (002)/(100)	*21.78 / 43.89*	*22.78 / 44.11*	*22.35 / 44.16*
Interplanar separation (002)	*0.39nm*	*0.37nm*	*0.37nm*
Raman G/D band position	*1594cm^{-1}/ 1331cm^{-1}*	*1586cm^{-1}/1331cm^{-1}*	*1589cm^{-1}/1322cm^{-1}*
Raman I_G/I_D ratio	*0.42*	*0.42*	*0.41*
Inplane crystallite size (100)	*1.43nm*	*2.15nm*	*2.39*

Low surface area of CNS samples was confirmed by BET analysis of CNS-1000 as a representative example. *Figure 6.5* shows the isotherm and pore size distribution plots of CNS-1000 sample. CNS-1000 shows very low surface area (59m^2/g) with no pores in

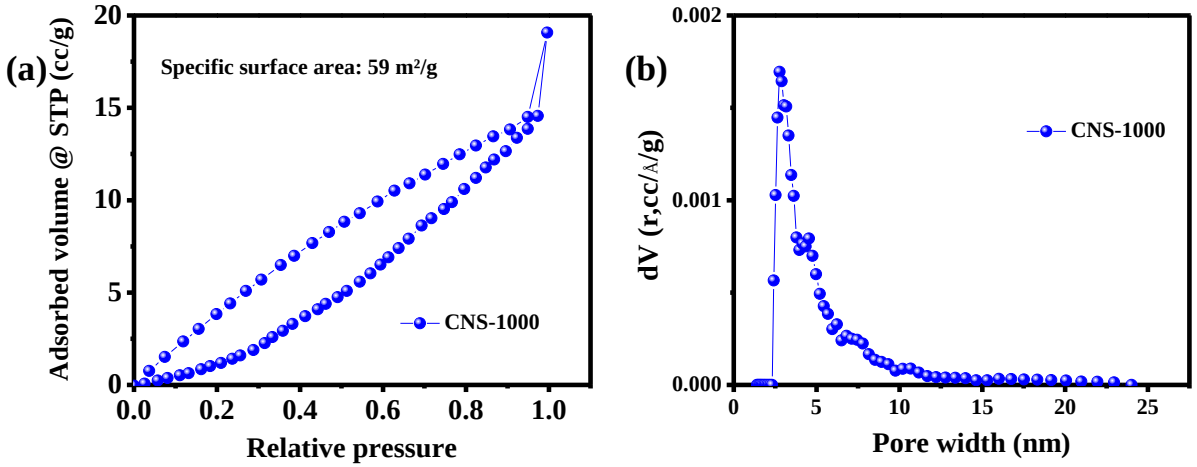

Figure 6.5 *Surface area analysis of CNS-1000. a) BET adsorption isotherm of CNS-1000. b) Pore size distribution plots of CNS-1000 constructed by the help of DFT theory.*

micropore regime (<2nm). Low surface area carbons are considered ideal for Na-ion battery because low surface area leads to less solid electrolyte interphase (SEI) formation leading to less electrolyte degradation. [30,34,53]

Electrochemical performance of CNS samples was analyzed by cyclic voltammetry (CV), charge discharge, and impedance analysis. The rate performance graphs which plot capacities calculated from charge discharge measurement at different current densities vs. cycle number furnish information about the current stability of battery material. *Figure 6.6* shows the rate stability comparisons of CNS samples. At 50mAg^{-1}, CNS-800, CNS-1000 and CNS-1200 display capacities of 165mAhg^{-1}, 257mAhg^{-1} and 254mAg^{-1} respectively. The samples showed good capacity recovery (96%, 94% and 90% respectively) after sustaining high current of 2Ag^{-1}. The capacities of CNS-1000

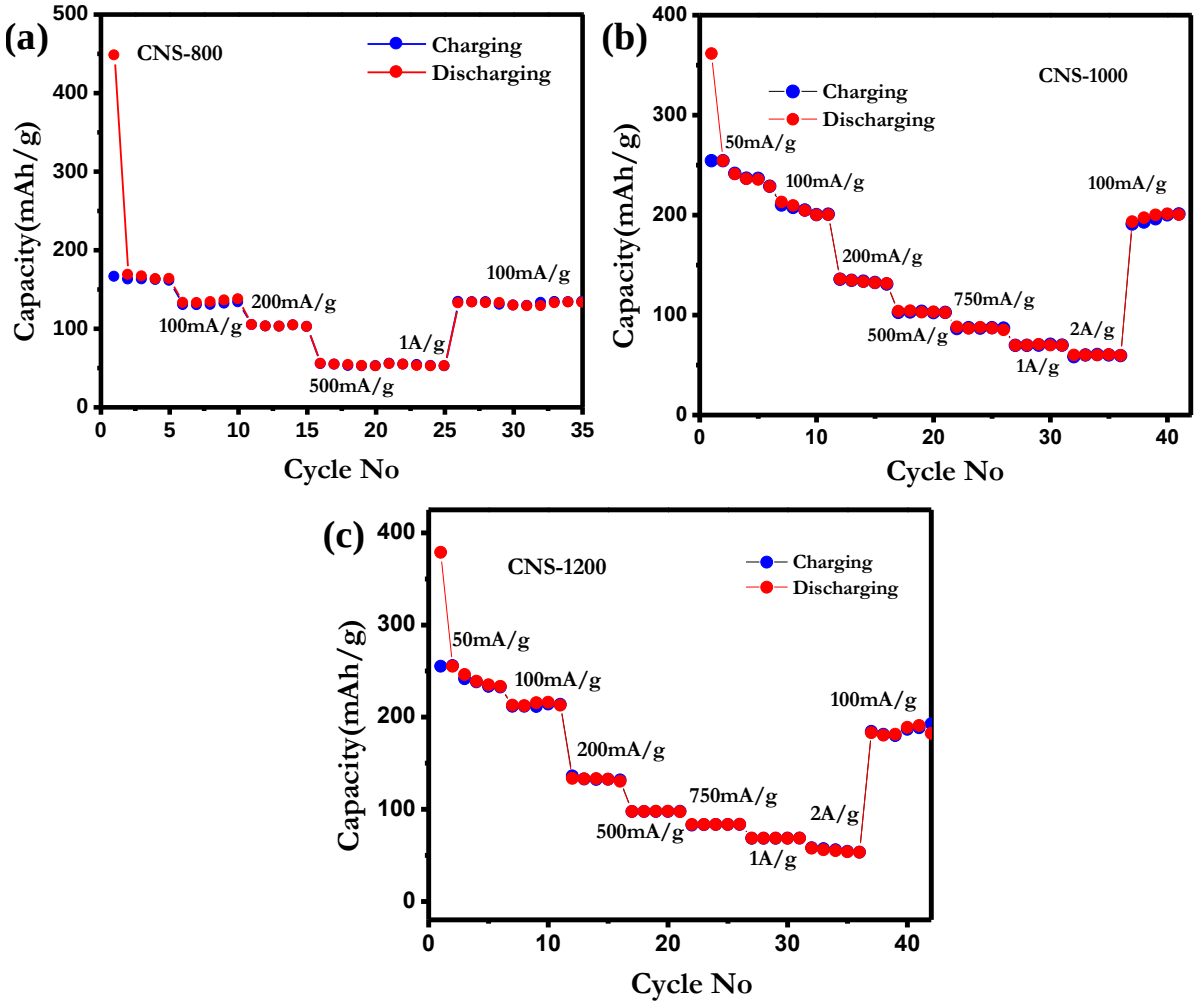

Figure 6.6 *Electrochemical rate performance plots of three CNS samples is shown here. a) CNS-800 in the range of 50mAg^{-1}-1Ag^{-1}-100mAg^{-1}, b) CNS-1000 in the range of 50mAg^{-1}-2Ag^{-1}-100mAg^{-1}, c) CNS-1200 in the range of 50mAhg^{-1}-2Ag^{-1}-100mAg^{-1}.*

and CNS-1200 at different current densities are almost the same, which further

highlight the hard nature of CNS carbons. The lower capacities of CNS-800 are attributed to low conductivities of individual graphitic domains which may due to smaller in-plane crystallites formed at this temperature (*table 6.1*). *Table 6.2* compares the capacities of various recently reported carbon materials with CNS-1000. It shows that present carbon material is superior to other reported carbon forms in terms of capacity and stability.[41,43,48,49,54–57]

The electrochemical aspects of Na^+ ion storage in CNS samples were studied with CNS-1000 as representative example. The semi-graphitic domains of CNS-1000 carbon with interplanar c-axis separation of > 0.37nm can act as a suitable host for electrochemical intercalation and de-intercalation of Na^+ and hence can display excellent anode behavior. *Figure 6.7* elucidates the electrochemical performance of CNS-1000 as an anode material in Na^+ ion cell. *Figure 6.7a* shows the CV plots (*first four cycles*) of CNS-1000 taken in the voltage range of 0.01V-3.0V in *1M $NaClO_4$* in *EC-DMC* (*1:1, 5% FEC*) solvent at a voltage scan rate of $0.1mVs^{-1}$. The cathodic peaks *I & II* observed at 1.06 V and 0.49 V respectively are seen in the first discharge cycle only and disappear in the subsequent cycles. These two peaks are attributed to the SEI (solid electrolyte interface) layer formation on the electrode surface through irreversible electrolyte decomposition at the mentioned potentials[33]. A pair of cathodic/anodic peaks is observed at 0.02V and 0.21V respectively. These are designated as peak III and peak III' in the CV plot. The cathodic peak III (0.02V) is attributed to reversible intercalation of Na^+ ions into the semi-graphitic domains of CNS-1000.[33] The peak III' (0.21V) corresponds to anodic peak of III and can be attributed to the de-intercalation of Na^+ from semi-graphitic lattices of CNS-1000. The additional pair of reversible cathodic/anodic peaks marked as peak IV and IV' is observed at 0.63V and 0.93V respectively.[33,34] The emergence of this broad peak pair is attributed to the Na^+ storage by a mechanism different than intercalation and de-intercalation, which is operative at lower voltages. The peak IV and peak IV' is attributed to the reversible insertion and extraction of Na^+ through the pores, defective regions, edges and residual functional groups of CNS-1000. Thus two mechanisms of Na^+ storage are operative as already established by CV analysis. The intercalation/de-intercalation into the graphitic lattices

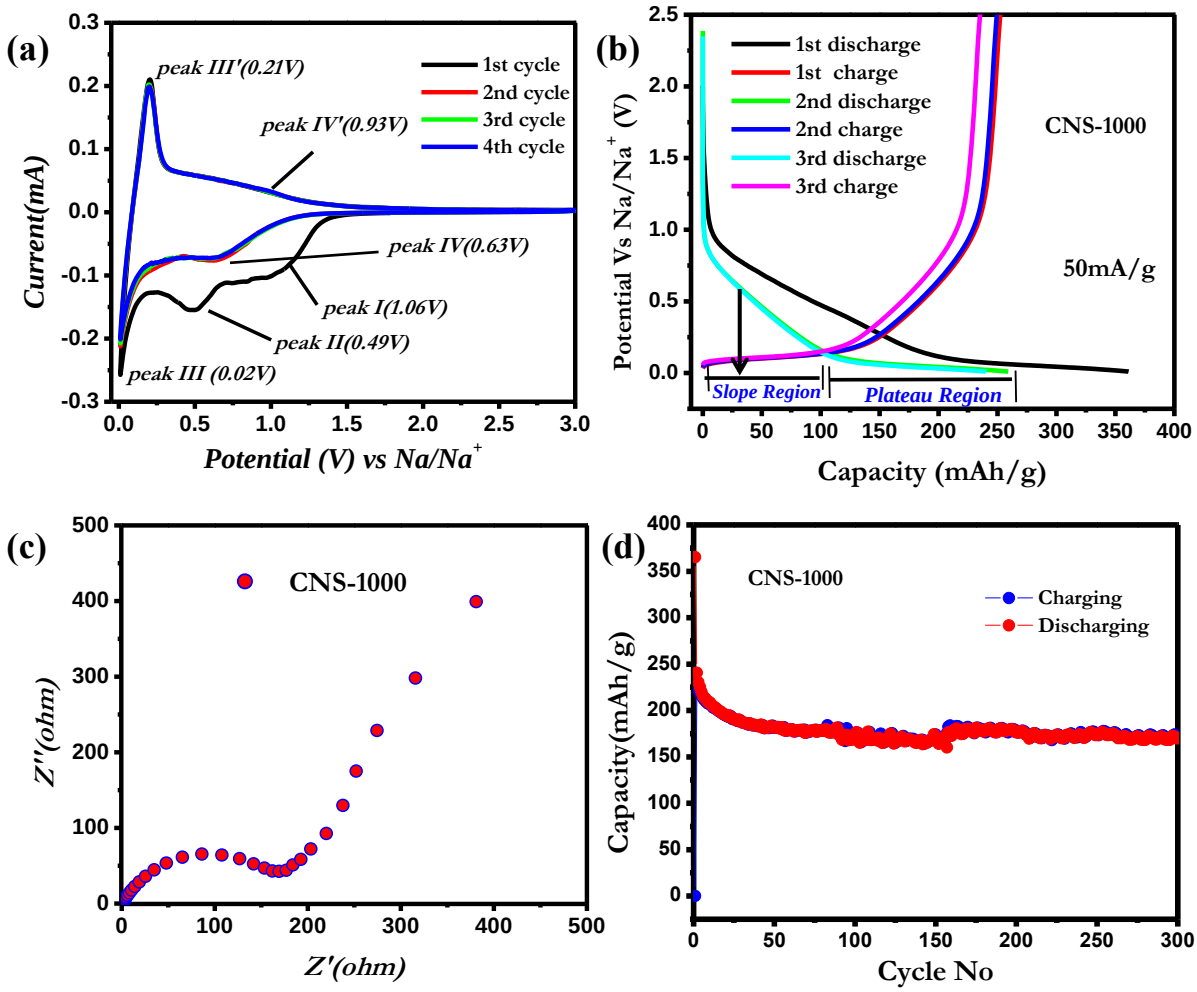

Figure 6.7 *Sodium ion storage inside CNS-1000 is explained here through CV, charge discharge and impedance measurements. a) CV profile of CNS-1000 b) Charge discharge profile of CNS-1000. c) Nyquist plot of CNS-1000 in the frequency range of 100 mHz to 1MHz. d) Long term stability of CNS-1000 in a Na ion half cell up to 300 cycles.*

still remains the dominant one, as depicted by the longer low voltage plateau and sloping regions in *figure 6.7b also*. The charge discharge profiles of CNS-1000 are shown upto three initial cycles. The higher discharge capacity (361mAhg^{-1}) of first cycle can be attributed to formation of SEI layer with minor plateaus at ~ 1.06V and ~ 0.42V which are not seen in subsequent cycles.[33,34] The reversible capacity of 257mAhg^{-1} is observed in the second discharge cycle which remains almost constant for next few cycles. The total capacity has contributions from the two operating mechanisms of Na^+ as evident from CV analysis. The second (and subsequent) discharge curves are marked into two regions with a sloping region in the voltage range

of 0.93V-0.08V and a plateau region in the voltage range of 0.08V-0.01V.[33,34] The sloping region (*figure 6.7b*) which contributes 100mAhg^{-1} to the total discharge capacity (257mAhg^{-1}) can be attributed to Na^+ storage in the defective sites, pores, edges and residual functional groups of CNS-1000 as discussed earlier. The plateau region (*figure 6.7b*) remains dominant contributor to total capacity (257mAhg^{-1}). The plateau capacity can be attributed to the Na^+ intercalation/de-intercalation in the turbostratic graphitic domains of CNS-1000 as confirmed by CV analysis earlier. The charge profiles of CNS-1000 in figure 6.7b also show similar sloping and plateau regions which agree well with the CV analysis[33,34].

Impedance analysis of CNS-1000 was performed on fresh cell that had undergone five charge discharge cycles to nullify interferences from the resistances offered by *SEI* layer formation. *Figure 6.7c* shows the *Nyquist* plot recorded on CNS-1000 in a coin cell against the Na/Na^+ electrode. The two regions in the *Nyquist* plot can be clearly distinguished. The high frequency region displays a semicircle of a smaller diameter point towards the low charge transfer resistance (R_{CT} ~ *180*Ω). Additionally *ESR* of 1.44Ω was observed from the first intercept on the X-axis which implies low material and solution resistance. Both low R_{CT} and low *ESR* project CNS-1000 as a competitive Na^+ anode material.[33,58]

Cyclic stability analysis is performed to examine the stability of material in the working condition over a period of time that in turn reflects the durability of device. Cyclic stability of CNS-1000 was monitored by capacity analysis over 300 continuous discharging and charging cycles carried out at 100mAg^{-1} and is shown in *figure 6.7d.* The material displays remarkable material stability over 300 charge /discharge cycles after initial reduction from 240mAhg^{-1} (at 100mAg^{-1}) to 170mAhg^{-1}. The cyclic stability so observed is quite comparable to the reported carbon materials for anode applications.[41,43,48,49,54–57]

Table 6.2 *A general review of sodium ion anode performance of carbon materials derived from various sources is reported in this table.*

Carbon precursor	***Capacity (50mAg^{-1})***	***Stability (cycles reported)***	***Ref.***
Lotus Petiole	**250mAhg^{-1}**	**200**	ref[43]
Okara	**290mAhg^{-1}**	**100**	ref[49]
Wood Cellulose	**240mAhg^{-1}**	**200**	ref[48]
Peat Moss	**300mAhg^{-1}**	**200**	ref[41]
Pomelo Peels	**230mAhg^{-1}**	**250**	ref[56]
Cellulose PANI Micro Spheres	**225mAhg^{-1}**	**2000**	ref[55]
N-doped Carbon Fibre	**243mAhg^{-1}**	**100**	ref[57]
N-doped Hollow Carbon Nano-fibers	**200mAhg^{-1}**	**100**	ref[54]
CNS-1000	**257mAhg^{-1}**	**300**	***Present***

6.4 Conclusion

In this chapter we report synthesis of hard carbon material from walnut shell biowaste. We show that high temperatures carbonization of compactly packed cellulose fibers in rigid walnut shell lead to hard and dense carbon materials with surface area < 60m^2g^{-1}. We further show that low surface area hard carbon is particularly advantageous in Na-ion batteries due to lesser SEI formation than high surface area amorphous carbon. Also, the hard carbon material possess sufficiently separated micro-graphene sheets (> 0.36nm in all cases) in the semi-graphitic domains to act as ideal anode material for sodium ion battery. An excellent reversible capacity of 257mAhg^{-1} is observed at 50mAg^{-1} along with good cycling stability. 71% capacity retention is observed even after 300 charge discharge cycles. Further, the carbon material (CNS-1000) shows remarkable rate performance with 96% retention after cycling at high current densities upto 2Ag^{-1}.

6.5 References

1. N. Yabuuchi, K. Kubota, M. Dahbi and S. Komaba, *Chem. Rev.*, 2014, **114**, 11636–11682.
2. S. Y. Hong, Y. Kim, Y. Park, A. Choi, N.-S. Choi and K. T. Lee, *Energy Environ. Sci.*, 2013, **6**, 2067–2081.
3. Q. Li, H. Liu, Z. Yao, J. Cheng, T. Li, Y. Li, C. Wolverton, J. Wu and V. P. Dravid, *ACS Nano*, 2016, **10**, 8788–8795.
4. E. De La Llave, V. Borgel, K. J. Park, J. Y. Hwang, Y. K. Sun, P. Hartmann, F. F. Chesneau and D. Aurbach, *ACS Appl. Mater. Interfaces*, 2016, **8**, 1867–1875.
5. C. Nithya and S. Gopukumar, *Wiley Interdiscip. Rev. Energy Environ.*, 2015, **4**, 253–278.
6. M. Giner, V. Roddatis, C. M. López and P. Kubiak, *J. Electrochem. Soc.*, 2016, **163**, A650–A653.
7. S. T. Dacek, W. D. Richards, D. A. Kitchaev and G. Ceder, *Chem. Mater.*, 2016, **28**, 5450–5460.
8. G. Longoni, J. E. Wang, Y. H. Jung, D. K. Kim, C. M. Mari and R. Ruffo, *J. Power Sources*, 2016, **302**, 61–69.
9. Y. U. Park, D. H. Seo, H. S. Kwon, B. Kim, J. Kim, H. Kim, I. Kim, H. I. Yoo and K. Kang, *J. Am. Chem. Soc.*, 2013, **135**, 13870–13878.
10. P. Singh, K. Shiva, H. Celio and J. B. Goodenough, *Energy Environ. Sci.*, 2015, **8**, 3000–3005.
11. C. W. Mason and F. Lange, *ECS Electrochem. Lett.*, 2015, **4**, A79–A82.
12. Y. Fang, L. Xiao, X. Ai, Y. Cao and H. Yang, *Adv. Mater.*, 2015, **27**, 5895–5900.
13. S. Li, Y. Dong, L. Xu, X. Xu, L. He and L. Mai, *Adv. Mater.*, 2014, **26**, 3545–3553.
14. G. Li, D. Jiang, H. Wang, X. Lan, H. Zhong and Y. Jiang, *J. Power Sources*, 2014, **265**, 325–334.
15. C. Zhu, K. Song, P. A. Van Aken, J. Maier and Y. Yu, *Nano Lett.*, 2014, **14**, 2175–2180.
16. Y. Zhu, Y. Wen, X. Fan, T. Gao, F. Han, C. Luo and S. Liou, *ACS Nano*, 2015,

9, 3254–3264.

17. M. He, K. Kravchyk, M. Walter and M. V. Kovalenko, *Nano Lett.*, 2014, **14**, 1255–1262.
18. J. Liu, Z. Yang, J. Wang, L. Gu, J. Maier and Y. Yu, *Nano Energy*, 2015, **16**, 389–398.
19. H. Wang, Y. Liu, M. Li, H. Huang, H. M. Xu, R. J. Hong and H. Shen, *Optoelectron. Adv. Mater. Rapid Commun.*, 2010, **4**, 1166–1169.
20. D. H. Nam, K. S. Hong, S. J. Lim, M. J. Kim and H. S. Kwon, *Small*, 2015, **11**, 2885–2892.
21. Y. Liu, N. Zhang, L. Jiao, Z. Tao and J. Chen, *Adv. Funct. Mater.*, 2015, **25**, 214–220.
22. W. Li, S. L. Chou, J. Z. Wang, J. H. Kim, H. K. Liu and S. X. Dou, *Adv. Mater.*, 2014, **26**, 4037–4042.
23. B. Farbod, K. Cui, W. P. Kalisvaart, M. Kupsta, B. Zahiri, A. Kohandehghan, E. M. Lotfabad, Z. Li, E. J. Luber and D. Mitlin, *ACS Nano*, 2014, **8**, 4415–4429.
24. H. Orthorhombic-sns, T. Zhou, W. K. Pang, C. Zhang, J. Yang, Z. Chen, H. K. Liu and Z. Guo, *ACS Nano*, 2014, **8**, 8323–8333.
25. X. Xie, Z. Ao, D. Su, J. Zhang and G. Wang, *Adv. Funct. Mater.*, 2015, **25**, 1393–1403.
26. W. Luo, F. Shen, C. Bommier, H. Zhu, X. Ji and L. Hu, *Acc. Chem. Res.*, 2016, **49**, 231–240.
27. P. Meduri, E. Clark, J. H. Kim, E. Dayalan, G. U. Sumanasekera and M. K. Sunkara, *Nano Lett.*, 2012, **12**, 1784–8.
28. K. Zhu, S. Guo, J. Yi, S. Bai, Y. Wei, G. Chen and H. Zhou, *J. Mater. Chem. A*, 2015, **3**, 22012–22016.
29. A. Rudola, K. Saravanan, C. W. Mason and P. Balaya, *J. Mater. Chem. A*, 2013, **1**, 2653–2662.
30. Y. Cao, L. Xiao, M. L. Sushko, W. Wang, B. Schwenzer, J. Xiao, Z. Nie, L. V. Saraf, Z. Yang and J. Liu, *Nano Lett.*, 2012, **12**, 3783–3787.
31. W. Zhou, H. Gao and J. B. Goodenough, *Adv. Energy Mater.*, 2016, **6**, 1–8.
32. Y. S. Yun, K. Y. Park, B. Lee, S. Y. Cho, Y. U. Park, S. J. Hong, B. H. Kim, H.

Gwon, H. Kim, S. Lee, Y. W. Park, H. J. Jin and K. Kang, *Adv. Mater.*, 2015, **27**, 6914–6921.

33. S. Komaba, W. Murata, T. Ishikawa, N. Yabuuchi, T. Ozeki, T. Nakayama, A. Ogata, K. Gotoh and K. Fujiwara, *Adv. Funct. Mater.*, 2011, **21**, 3859–3867.
34. E. Irisarri, A. Ponrouch and M. R. Palacin, *J. Electrochem. Soc.*, 2015, **162**, 2476–2482.
35. D. Li, H. Chen, G. Liu, M. Wei, L. X. Ding, S. Wang and H. Wang, *Carbon*, 2015, **94**, 888–894.
36. P. Papanek, M. Radosavljevic and J. E. Fischer, *Chem. Mater.*, 1996, **8**, 1519–1526.
37. H. Wang, P. Hu, J. Yang, G. Gong, L. Guo and X. Chen, *Adv. Mater.*, 2015, **27**, 2348–2354.
38. R. S. Babu and M. Pyo, *J. Electrochem. Soc.*, 2014, **161**, 1045–1050.
39. P. Thomas and D. Billaud, *Electrochim. Acta*, 2002, **47**, 3303–3307.
40. R. Alcántara, P. Lavela, G. F. Ortiz and J. L. Tirado, *Electrochem. Solid-State Lett.*, 2005, **8**, 222–225.
41. J. Ding, H. Wang, Z. Li, A. Kohandehghan, K. Cui, Z. Xu, B. Zahiri, X. Tan, E. M. Lotfabad, B. C. Olsen and D. Mitlin, *ACS Nano*, 2013, **7**, 11004–11015.
42. E. Memarzadeh Lotfabad, J. Ding, K. Cui, A. Kohandehghan, W. P. Kalisvaart, M. Hazelton, D. Mitlin, E. M. Lotfabad, J. Ding, K. Cui, A. Kohandehghan, W. P. Kalisvaart, M. Hazelton and D. Mitlin, *ACS Nano*, 2014, **8**, 7115–7129.
43. P. Wang, B. Qiao, Y. Du, Y. Li, X. Zhou, Z. Dai and J. Bao, *J. Phys. Chem. C*, 2015, **119**, 21336–21344.
44. H. Zhao, Y. Gao, J. Wang, C. Chen, D. Chen, C. Wang and F. Ciucci, *Mater. Lett.*, 2016, **167**, 93–97.
45. X. Cao, S. Chen and G. Wang, *Electron. Mater. Lett.*, 2014, **10**, 819–826.
46. F. Shen, W. Luo, J. Dai, Y. Yao, M. Zhu, E. Hitz, Y. Tang, Y. Chen, V. L. Sprenkle, X. Li and L. Hu, *Adv. Energy Mater.*, 2016, **6**, 1–7.
47. W. Lv, F. Wen, J. Xiang, J. Zhao, L. Li, L. Wang, Z. Liu and Y. Tian, *Electrochim. Acta*, 2015, **176**, 533–541.
48. F. Shen, H. Zhu, W. Luo, J. Wan, L. Zhou, J. Dai, B. Zhao, X. Han, K. Fu and

L. Hu, *ACS Appl. Mater. Interfaces*, 2015, **7**, 23291–23296.

49. T. Yang, T. Qian, M. Wang, X. Shen, N. Xu, Z. Sun and C. Yan, *Adv. Mater.*, 2016, **28**, 539–545.
50. J. Newman, K. E. Thomas, H. Hafezi and D. R. Wheeler, *J. Power Sources*, 2003, **119**–**121**, 838–843.
51. Y. Wang, D. C. Alsmeyer and R. L. Mccreery, *Carbon*, 1990, **2**, 557–563.
52. P. Giura, N. Bonini, G. Creff, J. B. Brubach, P. Roy and M. Lazzeri, *Phys. Rev. B - Condens. Matter Mater. Phys.*, 2012, **86**, 1–5.
53. M. Shirpour, X. Zhan and M. Doeff, in *Sodium-Ion Batteries : ' Beyond Lithium-Ion '*, 2015.
54. L. Zeng, W. Li, J. Cheng, J. Wang, X. Liu and Y. Yu, *RSC Adv.*, 2014, **4**, 16920–16927.
55. D. Xu, L. Fan, L. Gao, Y. Xiong, Y. Wang, Q. Ye, A. Yu, H. Dai, Y. Yin, J. Cai and L. Zhang, *ACS Appl. Mater. Interfaces*, 2016, **8**, 17090–17097.
56. K. Hong, L. Qie, R. Zeng, Z. Yi, W. Zhang, D. Wang, W. Yin, C. Wu, Q. Fan, W. Zhang and Y. Huang, *J. Mater. Chem. A*, 2014, **2**, 12733.
57. S. Wang, L. Xia, L. Yu, L. Zhang, H. Wang and X. W. Lou, *Adv. Energy Mater.*, 2016, **6**, 1–7.
58. K. Tang, L. Fu, R. J. White, L. Yu, M. M. Titirici, M. Antonietti and J. Maier, *Adv. Energy Mater.*, 2012, **2**, 873–877.

Chapter 7

Summary and future work

This chapter summarizes the entire research work besides providing an outlook regarding the future of energy storage electrode materials research.

This thesis projects the use of cheap and easily manoeuvrable carbon materials synthesised from biowastes and natural products for energy storage applications. The carbon materials possessing the turbostratic graphitic structure do possess sufficient conductivities, surface areas and interplanar separations to be used as electrodes in super-capacitors and sodium ion batteries. While high surface area carbons have been demonstrated to deliver a superior performance as supercapacitor electrode materials, the low surface area carbons have been demonstrated to deliver superior performance as sodium ion battery electrode materials.

7.1 Summary of research work

Chapters 1 and 2 present the introduction and experimental methods, respectively.

Chapter 3 projects the chemically activated carbon synthesised from sugarcane bagasse with a synthetic novelty of hydrothermal pre-treatment before activation pyrolysis as an efficient electrode material for a symmetric super capacitor. It is shown that the functional carbon morphology attainable by hydrothermal pre-treatment of sugarcane baggase leads to significantly enhanced capacitance retention. The capacitance of $280Fg^{-1}$ was obtained from the material at the current density of $1Ag^{-1}$ and 72% of this value is retained at current density of $20Ag^{-1}$. These values are superior to the previous report on sugarcane bagasse on $ZnCl_2$ with similar activation conditions in which 40% capacitance retention was reported at same current densities.

Chapter 4 presents a process for generation of porosity in a carbon material derived from a biogel, pectin, without any activation. The natural polymer hydrogel is used as a template precursor for the synthesis of mesoporous carbon for super-capacitor application. By use of the templating procedure, we were able to snip the carbon framework into inter-connected carbon threads. A particular morphology was seen to possess a surface area of $837m^2g^{-1}$ with considerable fraction of mesopores (~4nm) with

open type architecture having the pore volume of 0.87cm^3g^{-1} and mesoporosity of 83%. Urea-assisted nitrogen doping has led to 7.0% (atomic) doping, distributed in pyridinic, pyrrolic and graphitic forms which add to its advantage as a supercapacitive energy storage material. The material exhibits a three electrode capacitance of 285Fg^{-1} at 1Ag^{-1} with the capacitance retention of 74% at 10 Ag^{-1} and 63% at 40 Ag^{-1}. Cycling stability is also commendable as the material exhibited only 4.0% loss after 2000 cycles at 10Ag^{-1}. In a two electrode symmetric cell, the material offered a capacitance of 230Fg^{-1} and delivered the energy of 7$Whkg^{-1}$ at 2.5$kWkg^{-1}$ in an aqueous medium.

Chapter 5 presents research on a chemically activated carbon derived from yogurt as an efficient negative electrode in the asymmetric super capacitor. We have examined the cathode performance of yogurt derived activated carbon material Vs Nickel cobalt sulfide (NCS). It is demonstrated that the yogurt derived activated carbon performs better than most of the commercially available carbon materials as cathode in asymmetric supercapacitors. The energy density in asymmetric assembly goes as high as 27 $Whkg^{-1}$ at power density of 364 Wkg^{-1} (and an energy density of 17.8 $Whkg^{-1}$ was achieved at power density of 6400 Wkg^{-1}) which is comparable to or superior to other cathode materials for the different morphologies of the same NCS anode material.

Chapter 6 deals with the low surface area non activated carbons, the hard carbons, and their application as anode material in sodium ion batteries. The compactly packed cellulose fibers in the rigid walnut shell are made to undergo carbonization into hard and dense carbon materials at higher temperatures. Hard carbon nature of nutshell derived carbons is revealed by XRD and Raman analyses. The hard carbon materials obtained possess low surface area, < 60m^2g^{-1} and hence prove to be suitable electrode materials for sodium ion batteries. The low surface areas imply less electrolyte degradation caused by less extensive SEI layer formation. The hard carbon material possesses sufficiently separated micro-graphene sheets (> 0.36nm) in the semi-graphitic domains to act as ideal anode material for sodium ion battery. The reversible capacity of 257$mAhg^{-1}$ was observed at 50mAg^{-1}. The material displayed an excellent cycling stability with 71% capacity retention after 300 charge-discharge cycles. Further, the

carbon material exercises a remarkable rate performance with 96% retention after going through high current densities upto $2Ag^{-1}$.

7.2 Scope for future work

Because of limited reserves of Li in the Earth's crust Na ion battery is believed to be a key alternative to the existing technology. But the exact replication of Li ion battery technology for building the cheaper Na ion technology is not proving adequate enough owing to distinct charge to size ratio of Na^+ and Li^+. Thus, developing a suitable commercial electrode material (anode as well as cathode) for sodium ion battery is still a challenge.

The host of cathode materials is already available for sodium ion battery applications and only a little needs to be done on the cyclability issues to bring them to commercialization. The cyclability of cathode materials has been shown to increase with thin coatings of carbon. Either the turbostratic carbon wrapping or graphene wrapping of a cathode material ($NaFeO_2$, $NaCoO_2$, $NaMnO_4$, $NaNiO_2$, $Na_3V_2(PO_4)_3$, $Na_3V_2(PO_4)_2F_3$) can drastically increase their cycle stability and render them suitable as commercial sodium ion battery electrodes. But the anode material with required cyclability is still a challenge and field is wide open for further research.

In this thesis we have presented the use of carbon materials from natural sources and biomass as cheap materials for sodium ion anode applications. Although carbon materials of this type deliver good cyclic stability but there is more to do on capacity front to make the sodium ion battery realizable for modern applications like grid power and electric vehicles. In this regard, the conversion, alloying and intercalation materials of metals, alloys, metal oxides, sulphides and phosphides are already under study. The theoretical capacity of these materials especially the alloying ones go as high as $847mAhg^{-1}$ for Sn, $664mAhg^{-1}$ for Sb and $2596mAhg^{-1}$ for P.

These high capacity materials suffer from the low cyclability issues mainly because of size expansion upon Na^+ alloying. Thin carbon coatings can be helpful in solving the volume expansion problems and related cyclability issues. Further, the use of alloys like SnSb can also accommodate considerable Na^+ with little volume expansions, thus use of

such alloys can be significant in the field towards the goal of high capacity and high cyclability anode. Multiple metal component systems like SnSbSe, SnSbBi, SnBi, SnPb, SnP can also accommodate high sodium concentrations without significant volume changes and hence can be tested for anode applications.

The conversion cum alloying materials like Sb_2S_3, Sb_2Se_3, SnS_2, SnS, $SnSe_2$, Bi_2Se_3 also hold a promise of higher capacity owing to the two sodium storage mechanisms being operational simultaneously. These materials with the additional carbon as coatings shall furnish high capacities with enhanced cycle and rate stability.

A combination of alloying and conversion materials like MoS_2/SnS_2, $FeSnS_4$, MoS2/ Sb_2S_3 also promises a high capacity with high cyclability as anode material in sodium ion battery. These types of composite materials are least explored and shall be tried as anode materials.

Intermetallics of transition metals with P block metals like Sn, Sb, Bi can prove helpful in reducing the volume expansion related cyclic de-stability and shall be considered for the anode applications for the sodium ion batteries. Intermetallics of Sn and Sb like Ni_3Sn_4, $AuSn_2$, Cu_6Sn_5, $Co_{1-x-y}Ni_xFe_ySb_3$ etc. indeed deserve due consideration for anode applications.

List of Publications:

1. ***Malik Wahid,*** *Dhanya Puthusseri, Deodatta Phase, and Satishchandra Ogale*; Enhanced Capacitance Retention in a Supercapacitor Made of Carbon from Sugarcane Bagasse by Hydrothermal Pretreatment; Energy and Fuels 2014 28 (6), 4233-4240.*
2. ***M. Wahid,*** *G. Parte, D. Phase and S. Ogale*; Yogurt: a novel precursor for heavily nitrogen doped supercapacitor carbon ; Journal of Materials Chemistry A, 2015, 3, 1208-1215.*
3. ***M. Wahid*,*** *G. Parte, R. Fernandes, D. Kothari and S. Ogale*, Natural-gel derived, N-doped, ordered and interconnected 1D nanocarbon threads as efficient supercapacitor electrode materials, RSC Advances, 2015, 5, 51382-51391.*
4. ***Malik Wahid;*** *Dhanya Putthuseri; Ajay Kumar; Yogesh Gawli; Manjusha Shelke; Satishchandra Ogale*, Energy effective solution based synthesis of one dimensional -N doped-rGO Wrapped ultra long Sb_2Se_3 Rods: A High performance Sodium ion battery Anode. (Communicating..)*
5. ***Malik Wahid;*** *Yogesh Gawli, Ajay Kumar, Dhanya Putthuseri;; Manjusha Shelke; Satishchandra Ogale*, Hard Carbon from Hard Walnut Shell for High Capacity Sodium Ion Battery Anode: Layered Morphology Replication and Compaction. (Communicating..)*
6. *Ajay Kumar, Dhanya Putthuseri**, Malik wahid**; Satishchandra Ogale*. Aligned Nickel Cobalt Phosphide nano needle arrays uniformly grown on carbon fiber paper: An efficient catalyst for electrochemical Hydrogen evolution. (Communicating..)*
7. *Yogesh Gawli, **Wahid Malik**, Rohan Fernandez, Dushyant Kothari, Manjusha Shelke and Satishchandra Ogale*.Bio-molecule derived phosphorous incorporated carbon for Li ion battery anode. (Communicating..)*
8. *M.Thripuranthaka, **Malik Wahid**, Yogesh.Gawli, Satishchandra.Ogale*, Synthesis of Sb_2S_3/ MoS_2 Nano Composite with Flake Morphology from Sulfurisation Induced Phase Breakdown of $MoSb_2O_4$. (Under Prepration)*

Erratum